

Time-dependent multiconfiguration methods for the numerical simulation of photoionization processes of many-electron atoms

D. Hochstuhl, C.M. Hinz, and M. Bonitz^a

Institut für Theoretische Physik und Astrophysik, Universität Kiel, 24098 Kiel, Germany

Received 28 March 2013 / Received in final form 19 December 2013
Published online 5 February 2014

Abstract. Numerical simulations present an indispensable way to the understanding of complex physical processes. In quantum mechanics where the theoretical description is given in terms of the time-dependent Schrödinger equation the road is, however, difficult for any but the simplest systems. This is particularly true if one considers photoionization processes of atoms and molecules which, at the same time, require an accurate description of bound and continuum states and, therefore, an extensive region of space to be sampled during the calculation. As a consequence, direct simulations of photoionization processes are currently only feasible for systems containing up to three electrons. Despite this fundamental restriction, many physical effects can be essentially described by single- and two-electron models, among them are high-order harmonic generation and non-sequential double-ionization of atoms and molecules. A plethora of numerical investigations have been performed on atomic and molecular hydrogen and helium in the last two decades, and these have had a strong impact on the current understanding of photoionization. On the other hand, there are processes which are characterized by the interplay of a larger number of electrons, such as tunnel ionization, the Auger effect and, to give a more recent example, the temporal delay between the photo-emission of electrons from different shells of neon and krypton. The many-electron character of these effects complicates the accurate, time-resolved simulation and, so far, no universally applicable method exists. This review presents two theoretical methods which are promising candidates for closing this gap—the multiconfigurational time-dependent Hartree-Fock (MCT-DHF) method and the time-dependent restricted active space configuration interaction (TD-RASCI) method. Both represent the wavefunction in a linear subspace of the many-body Hilbert space and follow particular strategies to avoid the exponential problem. This makes it possible to treat a much larger number of electrons than with the direct techniques mentioned above.

^a e-mail: bonitz@physik.uni-kiel.de

Contents

1	Introduction	178
1.1	State of research	179
1.2	Contents of this review	183
1.3	The basic Hamiltonian	184
2	Multiconfiguration methods	186
2.1	Definitions and overview	187
2.2	The time-dependent variational principle	195
2.3	Time-dependent full configuration interaction	196
2.4	Time-dependent restricted active space configuration interaction	202
2.5	Multiconfigurational time-dependent Hartree-Fock	213
3	Numerical implementation of MCTDHF and RASCI	224
3.1	Basis sets	225
3.2	Basis transformations	233
3.3	Slater determinants	241
3.4	TD-CI equation	243
3.5	MCTDHF orbital equation	245
3.6	Time propagation	248
3.7	Analysis of the wavefunction	253
3.8	Stiffness reduction	260
3.9	Parallelization	265
3.10	Computational implementation of MCTDHF	268
4	Photoionization of atoms	270
4.1	Helium	270
4.2	Beryllium	291
4.3	Neon	297
5	Outlook and conclusions	300
5.1	Further extensions of the methods	300
5.2	Application to lattice models	309
5.3	Concluding remarks	310
Appendix A.	Determinant formulas	312
A.1	Slater determinant overlap	312
A.2	Matrix elements of single-excitations	313
A.3	Matrix elements of double-excitations	313
A.4	Autocorrelation	314
A.5	Two-time density matrix	314
Appendix B.	Basis sets	314
B.1	Discrete variable representation	315
B.2	Spherical coordinates	318
Appendix C.	Computational aspects	322
C.1	Implementation of the energy subspace projection method	322
C.2	Parallelization – Performance metrics	326
References		327

1 Introduction

Powerful new measurement techniques enable an ever deeper insight into the fundamental properties of atoms and molecules that constitute the building blocks of matter around us. One of the oldest, but still foremost approaches for their investigation is the observation of photoionization, i.e., the emission of one or more electrons induced by the absorption of one or several photons. Nowadays, a variety of different laser sources is available which provide an unprecedented experimental resolution at many frontiers. The last decade has seen the rise of high-order harmonic generated

laser pulses with attosecond duration—attoscience—offering the possibility to directly track electronic motion on an atomic scale, as well as the visionary hope to one day trigger and control chemical reactions. On the other hand, free-electron lasers all over the world are opening the doors to the use of XUV- and X-ray photons of unexplored intensities and peak brilliances. This will, in addition to physics, strongly influence and advance a variety of scientific fields, ranging from material science to biology and medical diagnostics, and will have a direct beneficial impact on human life.

The task of a theoretical physicist (or chemist) in this evolution is, on the one hand, the development of models to explain the experimental observations. This includes the promotion of intuitive pictures attributed to the physical processes at hand, which simplify the understanding and facilitate the development of new ideas. A prominent example is the three step model of high-order harmonic generation for the production of attosecond pulses. On the other hand, a theorist can employ numerical simulations with the goal of reproducing and resolving the measurements in detail and predicting results for currently inaccessible observables or parameter ranges. Other central motivations are of economical nature, since the cost and effort of computer simulations are generally much smaller than those of the corresponding *real* experiments. Naturally, in order to complement or even replace physical experiments one day, the simulations must be as reliable and accurate as possible. The present work, in which we develop simulation methods to investigate the photoionization of many-electron atoms, is intended to provide a step in this direction.

1.1 State of research

We briefly summarize our personal view on the current state of research in experimental and theoretical photoionization physics. The survey is by no means complete and will be supplemented by several details provided later in this work.

1.1.1 Experimental research

The investigation of matter via photon beams presents one of the most fundamental measuring techniques in physics. It was initiated with the investigation of cathode rays in the middle of the 19th century, which led to the discovery of X-rays by Röntgen in 1895 and, from the beginning, had a severe impact on the development of quantum mechanics. In 1917, Einstein, based on the work of Planck, provided the theoretical foundation of stimulated emission [1], which triggered a development that culminated in the realization of masers—coherent microwave radiation sources—by Townes and coworkers in 1954 [2, 3], and the invention of the laser by Maiman, Schawlow, Basov, Prokhorov and others, e.g. [4]. Soon thereafter in 1961, the concept of harmonic generation was introduced as a means to produce shorter wavelengths [5]. Since then, laser sources have become ever more efficient, realizing increased intensities, higher peak brilliance and shorter durations on the one hand, as well as smaller operating costs and improved usability as provided by table-top setups, on the other. Nowadays, a large number of different laser types is in use for various applications ranging from everyday life over industrial usage to physical imaging (for an overview see Ref. [6]). Of particular importance for this work is the vacuum and extreme ultraviolet (VUV/XUV) and X-ray light provided by synchrotrons and free-electron lasers. Particularly the free-electron lasers (FELs), which were realized for the first time in 1976 [7], have enabled access to this spectral range at unprecedented intensity regimes.

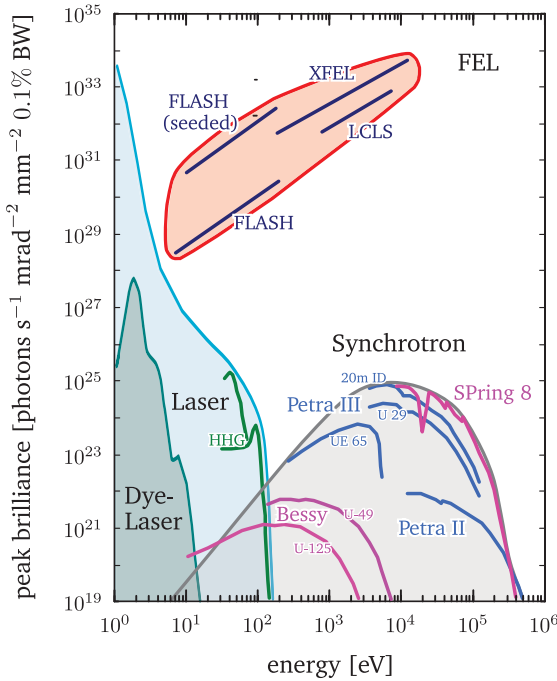


Fig. 1. Schematic comparison of the peak brilliance of various free-electron laser (FEL) facilities with a selection of synchrotrons, optical lasers and high-harmonic sources (HHG). Abbreviations: Bessy, Berliner Synchrotron; Petra, Positron Elektron Tandem Ring Anlage; SPring 8, Super Photon Ring 8 GeV. The figure has been redrawn from Fig. 1 in Ref. [8].

Currently available FELs include the Freie-Elektronen-Laser in Hamburg (FLASH), the LINAC Coherent Light Source (LCLS) at Stanford, and the Japanese Spring-8 Ångström Compact FEL (SACLA). They provide electromagnetic radiation over a large range of frequencies with intensities up to 10^{21} W/cm^2 and pulse durations down to a few tens of femtoseconds [8]. Further, several projects such as LCLS II, FLASH II and the European XFEL will become operational within the next years and further increase the spectral range, pulse durations, as well as the repetition rates. In addition to these efforts, there are complementary plans to construct table-top FELs which would enable a more wide-spread and cheaper usage [9]. Figure 1 shows a comparison of the peak brilliance of several laser sources. The advantage of the free-electron lasers is immediately obvious: in the X-ray regime, they surpass synchrotrons and conventional laser sources by up to nine orders of magnitude.

These successes enabled the measurement of several fundamental physical processes, among them the two-photon double-ionization of helium [10], which is considered theoretically in Sect. 4, the determination of the Auger spectra from aligned molecules [11] or the imaging of clusters and nano-crystals [12]. An essential technique for these studies is given by the cold target ion recoil spectroscopy (COLTRIMS) reaction microscope depicted in Fig. 2. It projects the charged fragments of an atomic or molecular reaction (such as photoionization induced by a laser pulse) onto position-sensitive detectors by a combination of electric and magnetic fields. From the measured time-of-flight of the particles and their position of impact, the momenta can be reconstructed with a resolution of up to a few hundreds atomic units [13]. This allows one to perform kinematically complete experiments, giving access to sophisticated observables such as angle-resolved differential cross sections of double-ionization processes.

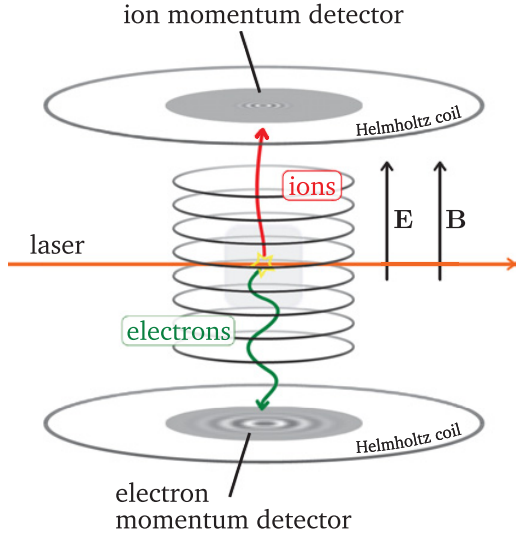


Fig. 2. Illustration of the setup of the cold ion recoil target spectroscopy (COLTRIMS) reaction microscope. By a combination of electric and magnetic fields, the fragments of an atomic or molecular reaction are guided onto position-sensitive detectors. The impact-position and the measured time-of-flight allows for a precise reconstruction of the momenta of the particles.

Another recent breakthrough is the rise of attosecond science, which was initiated in 2001 with the successful generation of ultra-short pulses of XUV light with sub-femtosecond duration by Paul et al. [14] and Hentschel et al. [15]. Attosecond laser pulses open the possibility to explore electronic motion on its natural time-scales; for instance, the oscillation period of an electron in the hydrogen ground state takes place over a time of 150 as [16]. Soon after their invention, attosecond pulses were applied to a variety of studies on topics such as the lifetime of inner-shell vacancies in krypton by Drescher et al. [17], the direct sampling of the optical waveform of an attosecond pulse in the time-domain by Goulielmakis et al. [18], or the time-resolved observation of laser-induced tunnel ionization in atoms by Uiberacker et al. [19]. The generation of attosecond pulses relies on the principle of high-order harmonic generation (HHG), which is usually explained through Corkum's semi-classical three-step model [20–22] depicted in Fig. 3: an electron is released from the atom through tunnel ionization and subsequently accelerated in the laser field. Half an optical cycle after ionization, as the electric field changes, the electron reverses its direction and is driven back towards the parent ion, where it is able to recombine. In this process, it emits a photon with an energy of an odd multiple of the frequency of the driving field. The importance of HHG for the generation of attosecond pulses stems from the fact that the illustrated process only occurs in a sharp window around the maximum of the optical cycle, so that short bursts of attosecond pulses are created periodically [23]. The extraction of isolated pulses from these pulse trains can be performed by restricting the number of driver laser cycles and other gating techniques, see Ref. [15]. In this way, attosecond pulses as short as 80 attoseconds [24] and 67 attoseconds [25] have been recorded. Also the angular distribution of the photoelectrons produced by UV and XUV pulses shows an interesting structure carrying information on the number of absorbed photons [26].

Measurements involving attosecond light pulses often rely on the *pump-probe* scheme, where the dynamics triggered by a first “pump”-pulse are probed using another laser pulse. Ideally, one desires attosecond XUV-pulses for both the pump and

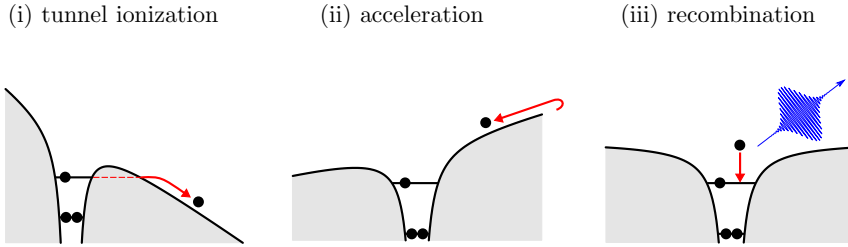


Fig. 3. Illustration of the semi-classical three-step model of high-order harmonic generation: (i) an electron is released via tunnel ionization, (ii) the liberated electron oscillates in the field, and (iii) it returns to the ion and recombines, thereby emitting a photon with an odd multiple of the frequency of the driving field.

the probe, which would enable a stroboscope-like view of the occurring processes. However, the intensities of HHG sources are currently too small to yield adequate cross sections for the XUV-XUV pump-probe process to be detected¹. A workaround is provided by the *streak camera*, which utilizes a few-cycle infrared (IR) laser pulse for the probe. Since particles acquire the momentum of the IR pulse at the time of their release, the temporal information can be extracted by measuring the energy spectra of the ionized electrons. Among several experiments, we mention that the streak camera has been applied recently by Schütte et al. to investigate the temporal and spectral characteristics of the Auger decay [28, 29]. In another recent study, Schultze et al. discovered a temporal delay in the photoionization from different shells of the neon atom. Their measurements suggest that the $2s$ electron is released 21 as earlier than the $2p$ electron [30], which triggered considerable theoretical interest [31–33]. Other techniques for the measurement of attosecond dynamics include the attoclock, where the angular distribution induced by a circularly polarized laser is used to extract time-information [34], or attosecond transient absorption spectroscopy [35–37].

1.1.2 Theoretical research

The theoretical description of non-relativistic quantum-mechanical processes is given by the time-dependent Schrödinger equation (TDSE), which can be solved analytically only for a few single-particle systems. In most practically relevant cases one must, therefore, resort either to approximate methods or to numerical solutions. The large first class contains methods such as the three-step model for high-order harmonic generation [20], the strong-field approximation (SFA) or Keldysh-Faisal-Reiss theory [38, 39], the Ammosov-Delone-Krainov (ADK) approach to tunnel ionization [40], and the description in terms of classical models or perturbation theory [41], to give a few examples. The primary goal of these methods is often not to yield exact results, but rather to give a convenient description of the arising physical processes. An important advantage is that they provide the pictures in terms of which many physicists think, and hence are well communicable and—in a certain sense—satisfying.

The second class of methods approaches the TDSE through numerical simulations. The most direct way is to represent the wavefunction in a basis set or on a grid, use a computer to find the initial state and propagate it in time, and finally extract the relevant information from the wave packet. Different methods proceed along this

¹ XUV-XUV pump-probe experiments on one-femtosecond time-scales have recently been realized to study multi-photon ionization of atoms [27].

idea, among them time-dependent configuration interaction [42], the time-dependent close-coupling method [43] or exact diagonalization [44]. While these methods are essentially exact, they share the problem that the representation rapidly becomes too complex with increasing system size (this is often termed the *exponential wall* or the *curse of dimensionality* [45]). In time-independent quantum chemistry, the attention is mainly focused on large numbers of electrons, which are described by comparably small basis sets. On the other hand, for the time-dependent photoionization processes treated in this work, the single-particle basis usually needs to be rather large in order to adequately describe the continuum states. As a result, direct calculations can currently be carried out only for systems with up to three particles, see Ref. [46]. However, these are restricted to small grids and angular expansions and are, thus, still far away from treating general processes. In contrast, the simulation of a two-particle system became routine in the last decade, and a plethora of theoretical studies on helium and molecular hydrogen have been performed, focusing on a variety of topics in photoionization, such as non-sequential double-ionization [43, 47, 48] or pump-probe ionization processes [49–51]. These approaches will be reviewed in more detail in Sect. 4.

Several workarounds have been designed to avoid the fundamental issue of direct calculations. Basically, they fall into two categories. The first employs a description of the system in terms of a quantity with reduced complexity. Among these methods are time-dependent density functional theory (TD-DFT) [52], density matrix functional theory [53] and the method of non-equilibrium Green function (NEGF) [54, 55]. They are applicable to rather large systems, but usually lack a practical way of controlling the error. Another, essentially exact approach is the variational optimization of the two-particle density-matrix [56]. The methods of the second category deal with a simplified ansatz for the wavefunction. They include time-dependent Hartree-Fock theory [57], time-dependent coupled-cluster theory [58], Møller-Plesset perturbation theory [59], the density-matrix renormalization group [60] and the closely related representation in terms of tensor-network states [61], and quantum Monte-Carlo methods [62]. Further, for the particular description of photoionization processes, single-active electron approaches [63], the time-dependent configuration interaction singles method [64] and R-matrix theory [65] have been introduced. All these methods can be applied to small and medium-sized atoms and molecules.

In this work, we consider two members of the second category, the multiconfigurational time-dependent Hartree-Fock method and the time-dependent restricted active space configuration interaction method, which are developed with a particular focus on the simulation of photoionization processes [66].

1.2 Contents of this review

As summarized before, there currently exist many well-evolved and successful theories for the ab-initio solution of the Schrödinger equation for atomic and molecular physics. In quantum chemistry, extensive computer codes are available for the stationary treatment of many-particle systems. In most cases, however, they concentrate on a time-independent description of bound states and, therefore, mainly utilize localized Gaussian basis sets which do not provide an adequate description of the continuum. Hence, these tools are inappropriate for the application to photoionization problems. On the other hand, time-dependent simulations often employ a convenient description in terms of radial grids, but are mainly restricted to the consideration of (reduced) two-particle systems. The most successful treatment of photoionization processes of many-electron systems so far is provided

by the R-matrix method, which is traditionally employed in a time-independent manner [65] and only recently has been extended to the explicitly time-dependent case [67–69].

On this basis, the principal goal of this work is the discussion of recently developed methods for the ab-initio simulation of explicitly time-dependent photoionization processes of many-electron atoms. Therefore, we extend the multi-configuration methods from quantum chemistry to the time-dependent case, and particularly optimize them for the treatment of photoionization processes. This is done in a way which combines the previously mentioned advantages: first, the methods allow for the simulation of many-particle systems and, in principle, offer a convenient mechanism for controlling the error. And second, the use of appropriate grid-like basis sets enables the efficient treatment of the possibly large grids and angular expansions needed for the description of photoionization. For this, we concentrate on two explicitly time-dependent methods: the multiconfigurational time-dependent Hartree-Fock (MCTDHF) method and the time-dependent restricted active space configuration interaction (TD-RASCI) method. The MCTDHF approach, covered in detail in Sect. 2.5, is already well established in the literature [70–72], but the application to photoionization processes of three-dimensional atoms and molecules is still in its infancy. The MCTDHF calculations of the cross-sections of atoms considered later in this work are therefore among the first published in the scientific literature². On the other hand, the TD-RASCI method presents an original contribution which has been developed in Refs. [66, 75] and which is further extended in the present work. Consequently, our goal here is to give a thorough introduction into the underlying theory, see section 2.4, and the investigation of its numerical capabilities.

Another goal of this work is the detailed application of the introduced methods to the description of photoionization processes, which is accomplished in Sect. 4. One is the two-photon double ionization of helium, which has been studied for the first time with the MCTDHF method by two of us in Ref. [76]. The advantage of helium is that it is amenable to direct solutions with the full configuration interaction method, and thereby also serves as an appropriate example for investigating the capabilities of the MCTDHF scheme. The TD-RASCI method is further applied to the photoionization of neon [77], and an X-ray–IR pump-probe process in beryllium [75]. The simulations of the latter require an explicitly time-dependent approach.

1.3 The basic Hamiltonian

In the present section, we specify the class of physical systems investigated in this work, namely few- and many-electron atoms and diatomic molecules subjected to external laser fields. The physical description is given in terms of the quantum-mechanical *wavefunction* $|\Psi(t)\rangle$, which contains the complete information on the state of the system and thus presents the analogue of a set of phase-space trajectories in classical mechanics. The wavefunction is determined by the time-dependent Schrödinger equation (TDSE) [78],

$$i \frac{\partial}{\partial t} |\Psi(t)\rangle = \hat{H}(t) |\Psi(t)\rangle, \quad (1.1)$$

² We note that concurrently with the present work, a similar approach has been developed by D.J. Haxton and C.W. McCurdy [73, 74].

which marks one of the fundamentals of quantum theory and is able to describe a large variety of physical scenarios. Note that we use atomic units throughout this work, in which $\hbar = e = m_e = 1$. Further details on the used notation are given later in Sect. 2.1. For now, we only note that the actual system is specified through the Hamiltonian $\hat{H}(t)$, which in the present work has the form

$$\hat{H}(t) = \sum_{k=1}^N \left\{ \frac{\mathbf{p}_k^2}{2} + v(\mathbf{r}_k) + \hat{v}_{\text{em}}(t) \right\} + \frac{1}{2} \sum_{k \neq l} \frac{1}{|\mathbf{r}_k - \mathbf{r}_l|}. \quad (1.2)$$

It describes N Coulomb-interacting electrons in a potential $v(\mathbf{r})$ which are exposed to the action of an electromagnetic field $\hat{v}_{\text{em}}(t)$. For the potential term, we focus on two cases, namely

- *atoms*: $v(\mathbf{r}) = -\frac{Z}{|\mathbf{r}|}$, where Z labels the positive charge of the nucleus, and
- *diatomic molecules*: $v(\mathbf{r}) = -\frac{Z_1}{|\mathbf{r}|} - \frac{Z_2}{|\mathbf{r}-\mathbf{R}|}$, where Z_1 and Z_2 denote the charge of the two nuclei, and \mathbf{R} determines the inter-nuclear distance.

In most parts of this work, we consider atoms, whereas diatomic molecules are only used for some examples. The electromagnetic field is treated semi-classically and is given in minimal coupling and the Coulomb gauge by [79]

$$\hat{v}_{\text{em}}(t) = \mathbf{A}(\mathbf{r}, t)\mathbf{p} + \frac{\mathbf{A}(\mathbf{r}, t)^2}{2}. \quad (1.3)$$

The neglect of the spatial dependence of the vector potential and, as a consequence, also the quadratic term which then affects only the global phase of the wavefunction, leads to the dipole approximation commonly stated either in *length gauge* [80],

$$\hat{v}_{\text{em}}(t) = \mathbf{E}(t)\mathbf{r}, \quad (1.4)$$

or *velocity gauge*,

$$\hat{v}_{\text{em}}(t) = \mathbf{A}(t)\mathbf{p}, \quad (1.5)$$

which may differ in approximate treatments. The behavior of the two gauges is compared in Sect. 4.

The previous specifications cover a wide range of interesting physical scenarios and constitute a standard setting in the physical literature on photoionization. However, the methods described in this work are not restricted to these special cases, but in fact work for arbitrary time-dependent single- and two-particle potentials.

The Hamiltonian (1.2) has undergone several approximations. The first and most fundamental one is the mapping from nature to a mathematical model, which is the basis of all physical studies, and which may be justified only through physical experiments, i.e., from outside the theory. Besides, we applied several approximations from within the theory by considering a description of reduced complexity. In the following, we collect these approximations and shortly discuss their ranges of validity:

- *Born-Oppenheimer*: The Hamiltonian (1.2) describes only the electrons and neglects the dynamics of the atomic nuclei. The core, therefore, remains in the state in which it was once prepared, typically the ground state. This is the Born-Oppenheimer (BO) approximation [81] which is justified in the context

of the present review as the time-scales of electronic and nucleonic dynamics differ, due to their different masses, by more than three orders of magnitude. More details and a systematic way to go beyond the BO approximation are considered in Sect. 5.1.3.

- *Non-relativistic:* The Hamiltonian is not invariant under Lorentz transformations, which is valid if the arising energies are well below the rest energy of the electron. Particularly, as a rule of thumb, the laser intensities should not exceed a value of 10^{17} W/cm^2 [82]. Further, the atomic charge Z of the atoms should not become large, since relativistic effects of valence shells increase roughly with Z^2 [83]. We note, however, that the principles of the developed methods hold as well for relativistic calculations, though with a different Hamiltonian and a more complex representation of the wavefunction.
- *Spin-free:* The Hamiltonian does not contain any effects related to spin-interactions, such as spin-orbit or spin-spin interactions [84]. Since spin-interactions consistently arise in a relativistic treatment, their neglect may be regarded as a consequence of the non-relativistic approximation. This approximation is made only on physical considerations; in fact, it would require only a minor technical effort to include spin-interactions into the description.
- *Semi-classical dipole-approximation:* The external field \hat{v}_{ext} is treated semi-classically, which is usually valid for the large photon densities produced by lasers [82]. Further, only the electric dipole approximation is considered, which is accurate if the wavelengths are way larger than the atomic dimensions [79]. An extension to a quantum-field theoretic treatment is briefly considered in Sect. 5.1.3.

Finally, in most parts of this work we employ a description in terms of a pure state, which corresponds to a restriction to the zero-temperature case. This restriction is weakened in Sect. 5.1.2, where we consider a quantum-statistical treatment of fermions trapped in a quantum dot at finite temperatures.

This review is organized as follows:

- Section 2 provides the required theoretical concepts. After a short recapitulation of the essentials of many-body quantum mechanics, the description in terms of determinants and the full CI method are derived. Thereafter, central to this work, the TD-RASCI method and the MCTDHF method are introduced.
- Section 3 collects the numerical and computational methods which are needed for the practical implementation of TD-RASCI and MCTDHF. It includes the relevant basis sets and corresponding transformation routines, the time-propagation methods, the tools for the analysis of the wavefunction, and other aspects.
- Section 4 applies the numerical methods to simulate photoionization processes of helium, beryllium and neon. The photoionization cross sections and other observables are calculated and compared to experimental and theoretical reference results. Further, the two-photon double-ionization of helium is studied. As an application which requires an explicitly time-dependent scheme, also a two-color pump-probe process in beryllium is considered.
- Finally, section 5 contains concluding remarks and gives an outlook to possible future applications.

2 Multiconfiguration methods

The present section is devoted to the theoretical concepts used in this work. We first give a short introduction into the basics of many-body quantum theory in Sect. 2.1

and summarize the time-dependent variational principle in section 2.2. Then, in sections 2.3 – 2.5, we consider the two main methods used in this work, the time-dependent configuration interaction and the multiconfigurational time-dependent Hartree-Fock method. Finally, in section 5.1, we mention possible extensions to a variety of interesting physical scenarios.

2.1 Definitions and overview

Before we consider the details of the specialized methods, in this opening section we recapitulate the essentials of many-body quantum mechanics as required for this work. For the beginning, we restrict ourselves to the description in terms of a pure state. The case of mixed states will be treated briefly in section 5.1.2, where we consider quantum statistics in the canonical ensemble. The presentation is kept rather informal from a mathematical point of view, with the focus lying on the concepts; for a rigorous introduction, see Refs. [85, 86].

2.1.1 Fermionic and bosonic Hilbert spaces

The state of a quantum-mechanical system is specified by a complete set of commuting observables. A single particle, for instance, is determined by its position $\mathbf{r} \in \mathbb{R}^3$, its total spin s (which is usually fixed), and its spin projection s_z relative to the z -axis, which can attain the $(2s + 1)$ values in $\mathbb{F}_s = \{-s, -s + 1, \dots, s\}$. The corresponding wavefunction $\psi(\mathbf{x})$ assigns a complex value to each state $\mathbf{x} = (\mathbf{r}, s_z)$ and is an element of the Hilbert space $\mathcal{H}_1 = L^2(\mathbb{R}^3 \times \mathbb{F}_s)$. Similarly, for N particles, one has to deal with a wavefunction of the N -particle Hilbert space

$$\mathcal{H}_N = \mathcal{H}_1 \times \dots \times \mathcal{H}_1, \quad (2.1)$$

which is the N -fold Cartesian product of single-particle Hilbert spaces. \mathcal{H}_N contains general square-integrable functions $\Psi(\mathbf{x}_1, \dots, \mathbf{x}_N)$ depending on a set of N complete observables and, thus, provides the appropriate framework for the description of many-particle quantum mechanics.

The fundamental indistinguishability of quantum particles has far reaching consequences for the physical properties of quantum systems, as well as for their theoretical description. In experiments, one observes either *fermions*, which satisfy Fermi-Dirac statistics, or *bosons*, which are described by Bose-Einstein statistics [87]. Examples for fermions include quarks, electrons, and muons whereas force carrier particles (such as the photon or the Higgs particle) are bosons, as are composite particles containing an even number of fermions (e.g. α -particles, excitons, or Cooper pairs).

In formal terms, the indistinguishability of particles implies that the Hamiltonian \hat{H} commutes with each permutation operator $\hat{P} \in S_N$, where S_N is the symmetric group on a set of N elements. It is therefore possible to find common eigenstates in terms of the irreducible representations of S_N , which are closely connected to the integer-partition of N and conveniently classified by *Young* diagrams [84]. From the set of irreducible representations, however, only the completely symmetric and anti-symmetric representations are suitable for describing quantum particles. Fermions possess an anti-symmetric wavefunction with respect to the interchange of any two particles,

$$\Psi^-(\mathbf{x}_1, \dots, \mathbf{x}_i, \dots, \mathbf{x}_j, \dots, \mathbf{x}_N) = -\Psi^-(\mathbf{x}_1, \dots, \mathbf{x}_j, \dots, \mathbf{x}_i, \dots, \mathbf{x}_N). \quad (2.2)$$

The fermionic wavefunction thus lies in the subspace \mathcal{H}_N^- of completely anti-symmetric functions. In this context, it is useful to define a projection operator $\hat{P}^- : \mathcal{H}_N \rightarrow \mathcal{H}_N^-$,

$$\hat{P}^- = \frac{1}{N!} \sum_{\hat{\pi} \in S^N} \text{sign}(\hat{\pi}) \hat{\pi}, \quad (2.3)$$

which filters the anti-symmetric part out of a general, non-symmetric function. The factor $\text{sign}(\hat{\pi})$ thereby denotes the parity of the permutation $\hat{\pi}$. Additionally, one introduces the *anti-symmetrization operator* \hat{A} , which acts similarly, but instead produces a normalized anti-symmetric function,

$$\hat{A} = \sqrt{N!} \hat{P}^-. \quad (2.4)$$

On the other hand, bosons are described by a wavefunction which remains identical under particle exchange,

$$\Psi^+(\mathbf{x}_1, \dots, \mathbf{x}_i, \dots, \mathbf{x}_j, \dots, \mathbf{x}_N) = +\Psi^+(\mathbf{x}_1, \dots, \mathbf{x}_j, \dots, \mathbf{x}_i, \dots, \mathbf{x}_N), \quad (2.5)$$

and which is therefore an element of the space \mathcal{H}_N^+ containing the completely symmetric functions. The corresponding projection operator $\hat{P}^+ : \mathcal{H}_N \rightarrow \mathcal{H}_N^+$ projects out the symmetric part of a general function and is defined by

$$\hat{P}^+ = \frac{1}{N!} \sum_{\hat{\pi} \in S^N} \hat{\pi}. \quad (2.6)$$

Further, its normalized version, the *symmetrization operator*, is given by

$$\hat{S} = \sqrt{\frac{N!}{n_1! n_2! \dots}} \hat{P}^+, \quad (2.7)$$

where n_k labels the occupation of the single-particle orbital with index k .

2.1.2 Basis sets of the N -particle Hilbert spaces \mathcal{H}_N and \mathcal{H}_N^\pm

In the following, we derive the basis sets of the N -particle Hilbert space \mathcal{H}_N and of its symmetric and anti-symmetric subspaces \mathcal{H}_N^\pm . This leads to Hartree products, permanents and Slater determinants, where particularly the latter are of major importance for this work. The arising basis sets are illustrated in Fig. 4 for the example of a two-particle system.

Hartree products. We begin with the expansion of a general wavefunction $|\Psi\rangle \in \mathcal{H}_N$ in terms of a single-particle basis $\{|\phi_k\rangle\} \in \mathcal{H}_1$, performed for clarity in coordinate representation,

$$\begin{aligned} \Psi(\mathbf{x}_1, \dots, \mathbf{x}_N) &= \sum_{i_1} C_{i_1}(\mathbf{x}_2, \dots, \mathbf{x}_N) \phi_{i_1}(\mathbf{x}_1) \\ &= \sum_{i_1 i_2} C_{i_1 i_2}(\mathbf{x}_3, \dots, \mathbf{x}_N) \phi_{i_1}(\mathbf{x}_1) \phi_{i_2}(\mathbf{x}_2) \\ &= \dots \\ &= \sum_{i_1 i_2 \dots i_N} C_{i_1 i_2 \dots i_N} \phi_{i_1}(\mathbf{x}_1) \phi_{i_2}(\mathbf{x}_2) \dots \phi_{i_N}(\mathbf{x}_N). \end{aligned} \quad (2.8)$$

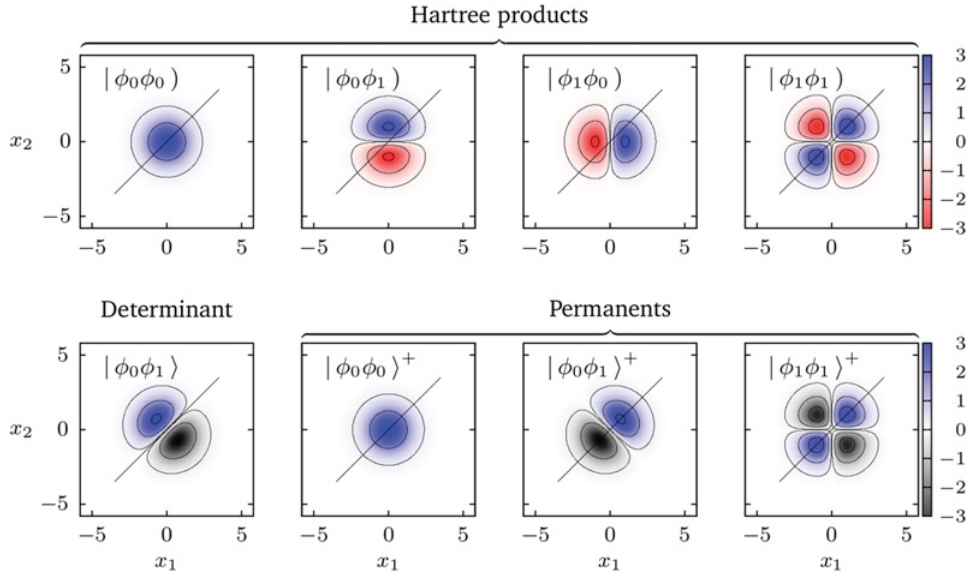


Fig. 4. Illustration of different types of Hilbert space basis sets for the example of $N = 2$ particles and the two first eigenfunctions $|\phi_0\rangle$ and $|\phi_1\rangle$ of a one-dimensional harmonic oscillator (without spin). The Hartree products in the top row are the basis states of the four-dimensional Hilbert space \mathcal{H}_2 . The Slater determinant spans the one-dimensional anti-symmetric subspace \mathcal{H}_2^- , and the three permanents the symmetric subspace \mathcal{H}_2^+ .

Hence, by successively re-expressing the variables of the expansion coefficients in the spin-orbital basis, one observes that N -fold products of single-particle functions provide a basis of the N -particle Hilbert space. In a more abstract notation, the previous result can be stated as

$$|\Psi\rangle = \sum_{i_1 \dots i_N} C_{i_1 \dots i_N} |\phi_{i_1} \dots \phi_{i_N}\rangle, \quad (2.9)$$

where we introduced the *Hartree products*³,

$$|\phi_{i_1} \dots \phi_{i_N}\rangle := |\phi_{i_1}\rangle |\phi_{i_2}\rangle \dots |\phi_{i_N}\rangle. \quad (2.10)$$

If the single-particle basis set is complete, the Hartree products form a complete basis set of \mathcal{H}_N . In numerical calculations, one naturally has to rely on a finite spin-orbital basis set of size $N_{\text{so}} = (2s + 1)N_b$, where N_b labels the spatial orbitals and s the particle spin. This also restricts the accessible subspace of \mathcal{H}_N to the span of all Hartree products with indices in the set

$$\Omega = \{(j_1, \dots, j_N) | 1 \leq j_k \leq N_{\text{so}}, k \in \{1, \dots, N\}\}. \quad (2.11)$$

The number of indices in Ω —and therefore also the number of Hartree products in the basis—is given by $N_{\text{HP}} = N_{\text{so}}^N$. Hartree products are adequate for representing general square-integrable functions without further symmetry requirements. Hence, they are particularly useful to describe *distinguishable* particles. As such, Hartree

³ For convenience, we consider only the case of identical single-particle basis sets, though the expansion of each variable x_i in a different basis set $\phi_k^{(i)}(x_i)$ can yield a significant advantage [88].

products form the building block of the multiconfigurational time-dependent Hartree method [88].

Slater determinants. On the contrary, the fermionic wavefunction obeys the anti-symmetry principle and is an element of \mathcal{H}_N^- . An expansion in terms of Hartree products is therefore inappropriate, since many basis states will give a zero contribution (those with at least two identical indices), whereas many others will contribute to only a single state. We are thus seeking for a more economic many-body basis set, which can be obtained by applying the anti-symmetrization operator $\hat{\mathcal{A}}$ onto the Hartree products and retaining only linearly independent states. This one arrives at the *Slater determinants*,

$$|\phi_{j_1} \cdots \phi_{j_N}\rangle := \frac{1}{\sqrt{N!}} \sum_{\hat{\pi} \in S_N} \text{sign}(\hat{\pi}) |\phi_{\hat{\pi}(j_1)}\rangle \cdots |\phi_{\hat{\pi}(j_N)}\rangle. \quad (2.12)$$

A maximal linearly independent set of Slater determinants is specified by the indices

$$\Omega^- = \{(j_1, \dots, j_N) | 1 \leq j_1 < \cdots < j_N \leq 2N_b\}, \quad (2.13)$$

where $N_{\text{so}} = 2N_b$ labels the size of the spin-orbital basis obtained from N_b spatial orbitals and the two spin functions. Slater determinants with a different ordering of the indices than in Ω^- differ only by a phase (± 1) from an already included determinant. By employing all linearly independent determinants, one obtains a basis of \mathcal{H}_N^- of size $N_{\text{det}} = \binom{N_{\text{so}}}{N}$, which is significantly smaller than the corresponding Hartree product basis of size N_{so}^N .

Another important notation for Slater determinants is given by the *occupation number representation*,

$$|\mathbf{n}\rangle = |n_1, \dots, n_{2N_b}\rangle, \quad (2.14)$$

where $n_P \in \{0, 1\}$ denotes the occupation of the spin-orbital $|\phi_P\rangle$. A Slater determinant $|\phi_{j_1} \cdots \phi_{j_N}\rangle$ corresponds to an occupation number vector only if

$$n_P = \begin{cases} 1, & P \in \{j_1, \dots, j_N\}, \\ 0, & \text{otherwise,} \end{cases} \quad (2.15)$$

holds for all $P \in \{1, \dots, 2N_b\}$.

Permanents. Finally, in the same manner as above, one can derive the appropriate basis set for bosonic particles. By subjecting the Hartree products to the symmetrization operator \hat{S} , one obtains the *Slater permanents* [87],

$$|\phi_{j_1} \cdots \phi_{j_N}\rangle^+ := \frac{1}{\sqrt{N! n_1! n_2! \cdots}} \sum_{\hat{\pi} \in S_N} |\phi_{\hat{\pi}(j_1)}\rangle \cdots |\phi_{\hat{\pi}(j_N)}\rangle, \quad (2.16)$$

which have a different normalization than the Slater determinants and contain no sign factor. The maximal linearly independent index set is given by

$$\Omega^+ = \{(j_1, \dots, j_N) | 1 \leq j_1 \leq \cdots \leq j_N \leq N_{\text{so}}\}. \quad (2.17)$$

The numbers $n_k \in \{0, \dots, N\}$ denote the occupation of the orbital $|\phi_k\rangle$, and can be used as well to represent the Slater determinant in an occupation number vector $|\mathbf{n}\rangle$. The total number of N -particle permanents for a basis of size N_b is given by $N_{\text{perm}} = \binom{N_{\text{so}} + N - 1}{N}$. In this work, we consider only spin-0 bosons, for which the number of spin-orbitals equals the number of spatial orbitals, $N_{\text{so}} = N_b$.

2.1.3 Second quantization

Second quantization provides a convenient reformulation of the concepts stated so far, and has several applications in almost any modern quantum mechanical theory [87]. Here, we consider the formalism only for fermionic particles. The derivation starts with the definition of the *creation operator* \hat{a}_P^\dagger , which creates the state $|\phi_P\rangle$ upon action onto a Slater determinant [59],

$$\hat{a}_P^\dagger |n_1, \dots, n_P, \dots, n_{2N_b}\rangle = \delta_{n_P, 0} \Gamma_P^n |n_1, \dots, 1_P, \dots, n_{2N_b}\rangle, \quad (2.18)$$

where the phase factor is given by

$$\Gamma_P^n = \prod_{Q=1}^{P-1} (-1)^{n_Q}. \quad (2.19)$$

Similarly, the adjoint *annihilation operator* \hat{a}_P is defined by

$$\hat{a}_P |n_1, \dots, n_P, \dots, n_{2N_b}\rangle = \delta_{n_P, 1} \Gamma_P^n |n_1, \dots, 0_P, \dots, n_{2N_b}\rangle \quad (2.20)$$

and removes the state $|\phi_P\rangle$ from the Slater determinant. Putting together Eqs. (2.18) and (2.20) readily yields the anti-commutation relations,

$$\begin{aligned} \{a_P^\dagger, a_Q^\dagger\} &= 0, \\ \{a_P, a_Q\} &= 0, \\ \{a_P^\dagger, a_Q\} &= \delta_{PQ}, \end{aligned} \quad (2.21)$$

where the anti-commutator is defined as $\{A, B\} = AB + BA$. Relations (2.21), together with the phase factors Γ_p^n , ensure that the state created by repeated application of the creation operator onto the vacuum state $|\text{vac}\rangle$ obeys the anti-symmetry constraint and the correct normalization and, therefore, is a Slater determinant,

$$|n\rangle = \left[\prod_{P=1}^{2N_b} (a_P^\dagger)^{n_P} \right] |\text{vac}\rangle. \quad (2.22)$$

A similar formalism can also be applied to the treatment of bosonic systems, with the only difference that the symmetrization rather than the anti-symmetrization must be warranted and, therefore, the repeated application of creation operators onto the vacuum yields a permanent [87].

2.1.4 The Hamiltonian in second quantization

Any operator given in first quantization can be translated to second quantization. In particular, the Hamiltonian (1.2),

$$\hat{H}(t) = \sum_{k=1}^N \left\{ \frac{\mathbf{p}_k^2}{2} + v(\mathbf{r}_k) + \hat{v}_{\text{em}}(t) \right\} + \frac{1}{2} \sum_{k \neq l} \frac{1}{|\mathbf{r}_k - \mathbf{r}_l|}. \quad (2.23)$$

attains the form [59]

$$\hat{H}(t) = \sum_{pq, \sigma} h_{pq}(t) \hat{a}_{p\sigma}^\dagger \hat{a}_{q\sigma} + \frac{1}{2} \sum_{pqrs, \sigma\tau} g_{pqrs} \hat{a}_{p\sigma}^\dagger \hat{a}_{r\tau}^\dagger \hat{a}_{s\tau} \hat{a}_{q\sigma}, \quad (2.24)$$

where we explicitly specified the spin-orbitals (previously written by upper-case indices) by their spatial and spin part, $P = (p\sigma)$. The sums extend over the N_b spatial orbitals and the two spin-components $\sigma, \tau \in \{\alpha, \beta\}$. The *single-electron matrix elements* are defined by

$$h_{pq}(t) = \int \phi_p^*(\mathbf{r}) \left\{ \frac{\mathbf{p}^2}{2} + v(\mathbf{r}) + \hat{v}_{\text{em}}(t) \right\} \phi_q(\mathbf{r}) d\mathbf{r}, \quad (2.25)$$

and are explicitly time-dependent due to the electromagnetic field term. Similarly to the full single-particle Hamiltonian, one defines the matrix representations of its contributions—the kinetic energy, potential energy and external field terms. Further, the *two-electron integrals* are given by

$$g_{pqrs} = \int \phi_p^*(\mathbf{r}) \phi_q(\mathbf{r}) \frac{1}{|\mathbf{r} - \mathbf{r}'|} \phi_r^*(\mathbf{r}') \phi_s(\mathbf{r}') d\mathbf{r} d\mathbf{r}', \quad (2.26)$$

and obey the symmetries

$$g_{pqrs} = g_{rspq}, \quad (2.27)$$

$$g_{pqrs} = g_{qpsr}^*, \quad (2.28)$$

$$g_{pqrs} = g_{qprs}, \quad (2.29)$$

where Eq. (2.29) holds only for a real basis set [59].

The previous formulas apply to the case of a spin-independent Hamiltonian, when the α - and β -spin components are treated on the same footing. Sometimes, however, it can be advantageous to describe the two spins using different spatial basis sets $\{|\phi_{k\alpha}\rangle\}$ and $\{|\phi_{k\beta}\rangle\}$ of size $N_{b,\alpha}$ and $N_{b,\beta}$, respectively. Such a case is encountered in the spin-unrestricted MCTDHF calculations considered later in this work. The Hamiltonian is then written as

$$\hat{H}(t) = \sum_{pq,\sigma} h_{pq}^\sigma(t) \hat{a}_{p\sigma}^\dagger \hat{a}_{q\sigma} + \frac{1}{2} \sum_{pqrs,\sigma\tau} g_{pqrs}^{\sigma\tau} \hat{a}_{p\sigma}^\dagger \hat{a}_{r\tau}^\dagger \hat{a}_{s\tau} \hat{a}_{q\sigma}, \quad (2.30)$$

and the corresponding one- and two-electron integrals are given by

$$h_{pq}^\sigma(t) = \int \phi_{p\sigma}^*(\mathbf{r}) \hat{h}(t) \phi_{q\sigma}(\mathbf{r}) d\mathbf{r}, \quad (2.31)$$

$$g_{pqrs}^{\sigma\tau} = \int \phi_{p\sigma}^*(\mathbf{r}) \phi_{q\sigma}(\mathbf{r}) \frac{1}{|\mathbf{r} - \mathbf{r}'|} \phi_{r\tau}^*(\mathbf{r}') \phi_{s\tau}(\mathbf{r}') d\mathbf{r} d\mathbf{r}'. \quad (2.32)$$

Hence, they are still diagonal in the spin-indices, but might be different in the two spin subspaces. Note that a Hamiltonian which explicitly depends on the spin, such as induced by an external magnetic field or spin-orbit interactions, leads to a coupling between the two spin spaces and therefore to electron integrals which are not anymore diagonal in the spin-indices.

2.1.5 Slater-Condon rules

The Slater-Condon rules constitute a set of rules to evaluate matrix elements of operators in a Slater determinant basis. They were introduced in 1929 by Slater for identical determinants [89] and completed a year later by Condon [90]. Following Ref. [59], we state them for the case of orthonormal orbitals. All Greek letters denote

spin indices and may attain either the value α or β .

(i) The Slater determinants are identical,

$$\langle \mathbf{n} | \hat{H} | \mathbf{n} \rangle = \sum_{p\sigma} n_{p\sigma} h_{pp}^\sigma + \frac{1}{2} \sum_{p\sigma, r\tau} n_{p\sigma} n_{r\tau} (g_{pprr}^{\sigma\tau} - \delta_{\sigma\tau} g_{prrp}^{\sigma\sigma}). \quad (2.33)$$

(ii) The Slater determinants differ in one pair of occupation numbers,

$$|\mathbf{n}_1\rangle = |n_1, \dots, 0_{p\sigma}, \dots, 1_{q\tau}, \dots, n_{2N_b}\rangle, \quad (2.34)$$

$$|\mathbf{n}_2\rangle = |n_1, \dots, 1_{p\sigma}, \dots, 0_{q\tau}, \dots, n_{2N_b}\rangle. \quad (2.35)$$

Then,

$$\langle \mathbf{n}_2 | \hat{H} | \mathbf{n}_1 \rangle = \delta_{\sigma\tau} \Gamma_{p\sigma}^{\mathbf{n}_2} \Gamma_{q\tau}^{\mathbf{n}_1} \left[h_{pq} + \sum_{r\gamma} n_{r\gamma} (g_{pqrr}^{\sigma\gamma} - \delta_{\sigma\gamma} g_{prrq}^{\sigma\sigma}) \right] \quad (2.36)$$

holds, where the phase factors $\Gamma_{p\sigma}^{\mathbf{n}}$ are defined in Eq. (2.19).

(iii) The Slater determinants differ in two pairs of occupation numbers,

$$|\mathbf{n}_1\rangle = |n_1, \dots, 0_{p\sigma}, \dots, 0_{r\gamma}, \dots, 1_{q\tau}, \dots, 1_{s\nu}, \dots, n_{2N_b}\rangle, \quad (2.37)$$

$$|\mathbf{n}_2\rangle = |n_1, \dots, 1_{p\sigma}, \dots, 1_{r\gamma}, \dots, 0_{q\tau}, \dots, 0_{s\nu}, \dots, n_{2N_b}\rangle. \quad (2.38)$$

In this case, the matrix element is given by

$$\langle \mathbf{n}_2 | \hat{H} | \mathbf{n}_1 \rangle = \Gamma_{p\sigma}^{\mathbf{n}_2} \Gamma_{r\gamma}^{\mathbf{n}_2} \Gamma_{q\tau}^{\mathbf{n}_1} \Gamma_{s\nu}^{\mathbf{n}_1} (\delta_{\sigma\tau} \delta_{\gamma\nu} g_{pqrs}^{\sigma\gamma} - \delta_{\sigma\nu} \delta_{\gamma\tau} g_{psrq}^{\sigma\gamma}). \quad (2.39)$$

For all other combinations of determinants which differ by more than two pairs of indices, the matrix elements of the Hamiltonian vanish. The Slater-Condon rules have been extended to non-orthonormal basis sets by Löwdin in 1955 [91].

2.1.6 Reduced density matrices

Reduced density matrices comprise parts of the information stored in the wavefunction in a compact quantity. The p -particle reduced density matrix (RDM) is obtained from the N -particle wavefunction by integrating out $(N-p)$ particle coordinates [91],

$$D^{(p)}(\mathbf{x}_1, \dots, \mathbf{x}_p, \mathbf{x}'_1, \dots, \mathbf{x}'_p; t) = \binom{N}{p} \int d\mathbf{x}_{p+1} \cdots d\mathbf{x}_N \times \Psi^*(\mathbf{x}_1, \dots, \mathbf{x}_p, \mathbf{x}_{p+1}, \dots, \mathbf{x}_N, t) \Psi(\mathbf{x}'_1, \dots, \mathbf{x}'_p, \mathbf{x}_{p+1}, \dots, \mathbf{x}_N, t). \quad (2.40)$$

From the p -particle RDM, one can obtain the expectation value of all q -particle operators with $q \leq p$. Of particular importance for the present work are the one-particle reduced density matrix, $D(\mathbf{x}, \mathbf{x}'; t)$, and the two-particle reduced density matrix $d(\mathbf{x}_1, \mathbf{x}_2, \mathbf{x}'_1, \mathbf{x}'_2; t)$. Most of the time we work in basis representation,

$$D(\mathbf{x}, \mathbf{x}', t) = \sum_{pq, \sigma} D_{pq}^\sigma(t) \phi_{p\sigma}^*(\mathbf{x}) \phi_{q\sigma}(\mathbf{x}'), \quad (2.41)$$

in which the one-particle RDM is given in terms of second quantization operators by [59]

$$D_{pq}^\sigma(t) = \langle \Psi(t) | a_{p\sigma}^\dagger a_{q\sigma} | \Psi(t) \rangle. \quad (2.42)$$

Here, $\sigma \in \{\alpha, \beta\}$ labels the particle spin and p and q the indices of the spatial orbitals.⁴ As a direct consequence of Eq. (2.42), the one-particle RDM is hermitian,

$$D_{pq}^\sigma(t) = (D_{qp}^\sigma(t))^*. \quad (2.43)$$

In addition to the spin-resolved density matrices, one further defines the spatial density matrix,

$$D_{pq}(t) = D_{pq}^\alpha(t) + D_{pq}^\beta(t), \quad (2.44)$$

which is convenient for operators which do not depend on spin. In terms of the one-particle RDM, the expectation value of a single-particle operator \hat{O} can be evaluated according to

$$\begin{aligned} \langle \hat{O}(t) \rangle &= \sum_{pq,\sigma} O_{pq}^\sigma(t) D_{pq}^\sigma(t) \\ &= \sum_{pq} O_{pq}(t) D_{pq}(t), \end{aligned} \quad (2.45)$$

where the second line refers to the case where \hat{O} does not depend on spin and the α and β spin-orbitals are identical. Similarly, the two-particle RDM is given in second quantization by

$$d_{pqrs}^{\sigma\tau}(t) = \langle \Psi(t) | a_{p\sigma}^\dagger a_{r\tau}^\dagger a_{s\tau} a_{q\sigma} | \Psi(t) \rangle. \quad (2.46)$$

It obeys the symmetries

$$\begin{aligned} d_{pqrs}^{\sigma\tau}(t) &= d_{rspq}^{\tau\sigma}(t), \\ d_{pqrs}^{\sigma\tau}(t) &= (d_{qpsr}^{\sigma\tau}(t))^*, \\ d_{pqrs}^{\sigma\sigma}(t) &= -d_{rqps}^{\sigma\sigma}(t), \end{aligned} \quad (2.47)$$

which follow directly from the anti-commutation relations (2.21). Its coordinate representation reads

$$d(\mathbf{x}_1, \mathbf{x}'_1, \mathbf{x}_2, \mathbf{x}'_2, t) = \frac{1}{2} \sum_{pqrs} d_{pqrs} \phi_p^*(\mathbf{x}_1) \phi_q(\mathbf{x}'_1) \phi_r^*(\mathbf{x}_2) \phi_s(\mathbf{x}'_2), \quad (2.48)$$

and the diagonal entry,

$$d(\mathbf{x}_1, \mathbf{x}_2, t) := d(\mathbf{x}_1, \mathbf{x}_1, \mathbf{x}_2, \mathbf{x}_2, t), \quad (2.49)$$

determines the joint probability to find one particle in the state \mathbf{x}_1 and another one in \mathbf{x}_2 . The spatial two-particle RDM is obtained by tracing over the spin coordinates

$$d_{pqrs}(t) = \sum_{\sigma\tau} d_{pqrs}^{\sigma\tau}(t), \quad (2.50)$$

⁴ Note that here we again made use of the fact that the spin spaces do not couple; otherwise, one would have to work with a more general density matrix $D_{p\sigma,q\tau}$.

The expectation value of a two-particle operator \hat{T} is given by

$$\begin{aligned}\langle \hat{T} \rangle(t) &= \frac{1}{2} \sum_{pqrs, \sigma\tau} T_{pqrs}^{\sigma\tau} d_{pqrs}^{\sigma\tau}(t) \\ &= \frac{1}{2} \sum_{pqrs} T_{pqrs} d_{pqrs}(t),\end{aligned}\quad (2.51)$$

where again the second line holds for a spin-independent operator and identical α and β spin-orbitals, and the matrix elements of the operator \hat{T} are calculated similarly to Eq. (2.32).

2.2 The time-dependent variational principle

Ever since Hero of Alexandria derived the law of reflection by assuming that light travels along the shortest distance [92], variational principles have played an important role in the evolution of physics. Their intention is to reduce the physical description to a geometric principle of finding extrema of appropriate functionals. By this, one obtains an intuitive approach which, on the one hand, may serve to identify similarities between different physical theories—compare, e.g., the role of the Hamilton principle in classical and quantum mechanics. On the other hand, as used in this work, it can be employed to simplify the derivation of differential equations of motion. A thorough introduction into the details of the time-dependent variational principle can be found in Ref. [93]. Here, we follow closely the work of Beck et al. [88].

Among the time-independent variational principles, the Rayleigh-Ritz principle is of utmost importance in quantum mechanics. It states that the ground state energy E_0 of a physical system described by the hermitian Hamiltonian \hat{H} satisfies the equality

$$E_0 = \min_{|\Psi\rangle \in \mathcal{H} \setminus \{0\}} \frac{\langle \Psi | \hat{H} | \Psi \rangle}{\langle \Psi | \Psi \rangle}. \quad (2.52)$$

Performing the variation with respect to $\langle \Psi |$, the Rayleigh-Ritz principle is readily transformed into the eigenvalue problem [59]

$$\hat{H} |\Psi\rangle = E |\Psi\rangle, \quad (2.53)$$

which is the stationary Schrödinger equation. The true ground state energy is given by the lowest eigenvalue, while the corresponding eigenfunction is the true ground state. In practice, one usually has to deal with approximate wavefunctions determined by a set of variational parameters. The Rayleigh-Ritz principle can then be used to optimize these parameters in a way that the lowest possible energy is achieved. The deviation of the resulting energy from the true ground state energy—so far it is known—can then serve to quantify the accuracy of the approximate wavefunction. Once the approximate ground state $|\Psi_0\rangle$ is at hand, the Rayleigh-Ritz principle can also be used to target the first excited state by performing the variation over the space $\mathcal{H} \setminus \{|\Psi_0\rangle\}$ orthogonal to the ground state, and so on for higher excited states. According to the Hylleraas-Undheim theorem, the energies of thus obtained excited states also provide upper bounds to the exact energies [59].

The first time-dependent variational principle (TDVP) was introduced in 1930 by Dirac [94] and by Frenkel [95] to approximately solve the TDSE and reads

$$\langle \delta\Psi | \hat{H}(t) - i\partial_t | \Psi \rangle = 0. \quad (2.54)$$

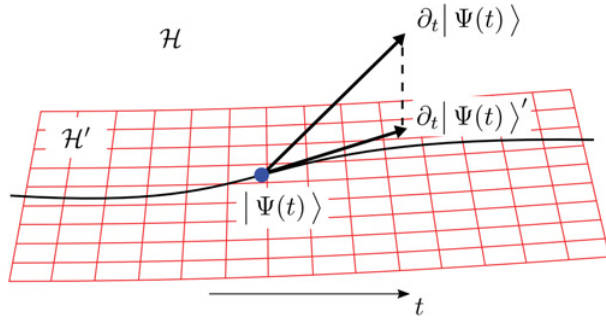


Fig. 5. Schematic illustration of the time-dependent variational principle. The wavefunction $|\Psi(t)\rangle$ is represented on the manifold \mathcal{H}' , which is a submanifold of the Hilbert space \mathcal{H} . At each instant of time, the true temporal derivative $\partial_t|\Psi(t)\rangle \in \mathcal{H}$ is approximated in the best possible way by a vector $\partial_t|\Psi(t)\rangle'$ in the tangent space of \mathcal{H}' of the point $|\Psi(t)\rangle$.

Here, δ denotes a variation on the wavefunction. Another TDVP is the McLachlan principle [96] that requires to minimize the quantity

$$\| i\partial_t\Psi - \hat{H}(t)\Psi \| . \quad (2.55)$$

Furthermore, the Lagrange formulation of the TDVP is given by [93]

$$\delta \int_{t_0}^{t_1} L(t) = 0, \quad (2.56)$$

with the Lagrangian

$$L(t) = \langle \Psi(t) | \hat{H}(t) - i\partial_t | \Psi(t) \rangle, \quad (2.57)$$

and the usual boundary conditions $\delta L(t_0) = \delta L(t_1) = 0$. All these variational principles were shown to be equivalent as long as for each allowed variation $\delta\Psi$ the variation $i\delta\Psi$ is allowed as well. This constraint is particularly satisfied if the variational parameters are complex quantities [88], which is the case throughout this work. As we are then free to choose one of the provided variational principles, following Ref. [97], we exclusively use the Lagrange TDVP in the later derivations. It can be shown that wavefunctions derived from the TDVP conserve the norm and, for a time-independent Hamiltonian, also the energy [88].

2.3 Time-dependent full configuration interaction

Full configuration interaction (FCI or exact diagonalization) theory marks one of the foundations of many-particle quantum mechanics presenting the most accurate approach to solutions of the Schrödinger equation. Due to the combinatorial growth of the numerical effort with the number of particles and basis functions, however, it constitutes an NP-hard problem⁵. Therefore, full CI methods can be applied in a reasonable way only to small systems with a moderate number of particles and basis functions. Consequently, in this work it is used exclusively for simulations of the helium atom. In the following, after giving an overview on the current state of research, we introduce the full CI ansatz and the equations of motion. Subsequently, we collect the relevant symmetry operators and show examples of how their use

⁵ This is also called *exponential wall* or *curse of dimensionality* [45].

reduces the size of the configuration space. We note that, due to the formal similarity of time-dependent and time-independent CI theory, most concepts translate directly from the stationary to the time-dependent formalism, and hence we often do not strictly distinguish between the two approaches.

2.3.1 Present state of research

Configuration interaction theory was established in 1929, when Slater introduced the description in terms of determinants and derived some of the rules for the evaluation of Hamiltonian matrix elements [89]. The early calculations employed only a few tens configurations [98]. Only with the rise of modern computers, significantly larger expansions became possible. For atomic structure calculations, the one-billion limit was first surpassed by Olsen et al. in 1990 [99], while current state-of-the-art calculations are capable of employing determinant bases of dimension up to 10^{10} [100]. Full CI has also been applied to systems such as quantum dots [44], Hubbard clusters [101], Bose-Einstein condensates [102] and several other systems. Nowadays, full CI is mainly used as a benchmark method, whereas in practical applications it is often replaced by other methods such as the Coupled-Cluster method [103], quantum Monte-Carlo full CI [62], Møller-Plesset perturbation theory [59], the density matrix renormalization group [104] or, as will be considered later in this work, the restricted active space configuration interaction method.

In contrast to the time-independent applications mentioned so far, full CI solutions of the time-dependent Schrödinger equation are usually restricted to small particle numbers as the single-particle basis often needs to be significantly larger in order to capture the arising dynamics. For photoionization applications in three-dimensional systems, direct solutions are available only for up to three particles, as has been shown by Colgan and Pindzola for the example of lithium [46]. It has to be noted, though, that these calculations present a very recent achievement and that they are restricted to grid sizes and angular momentum expansions which can be considered too small for most applications. For this reason, most photoionization studies consider two-particle systems such as helium and molecular hydrogen [43, 47, 105, 106], or, by fixing a certain set of electrons, also larger atoms such as beryllium [107, 108]. In most applications, the time-dependent close-coupling method is used, which corresponds to a full CI treatment in an angular momentum adapted basis where the angular part is described by bi-spherical harmonics, see also the subsequent discussion on symmetry restriction in paragraph 2.3.3. Time-dependent full CI calculations in the uncoupled representation have been used in our work on the two-photon ionization of helium [109].

2.3.2 TD-FCI equations

Having prepared the relevant formalism in Sect. 2.1, we are in the position to easily derive the equations of motion of the time-dependent full configuration interaction (TD-FCI) method. It starts with the expansion of the N -particle wavefunction in terms of Slater determinants,

$$|\Psi(t)\rangle = \sum_K C_K(t) |\phi_{k_1} \cdots \phi_{k_N}\rangle, \quad (2.58)$$

where the sum is running over the set Ω^- defined in Eq. (2.13), i.e., over the $N_{\text{det}} = \binom{2N_b}{N}$ indices

$$K = (k_1, \dots, k_N) \quad \text{with } 1 \leq k_1 < \cdots < k_N \leq 2N_b. \quad (2.59)$$

Insertion into the time-dependent Schrödinger equation and a subsequent projection onto $\langle \phi_{j_1} \cdots \phi_{j_N} |$ then immediately yields the TD-FCI equations,

$$i \sum_K S_{JK} \dot{C}_K(t) = \sum_K H_{JK}(t) C_K(t). \quad (2.60)$$

Here, we introduced the matrix elements of the Hamiltonian,

$$H_{JK}(t) = \langle \phi_{j_1} \cdots \phi_{j_N} | \hat{H}(t) | \phi_{k_1} \cdots \phi_{k_N} \rangle, \quad (2.61)$$

and the overlap matrix element,

$$S_{JK} = \langle \phi_{j_1} \cdots \phi_{j_N} | \phi_{k_1} \cdots \phi_{k_N} \rangle. \quad (2.62)$$

Equation (2.60) can also be stated more intuitively as a matrix equation,

$$i \mathbf{S} \dot{\mathbf{C}}(t) = \mathbf{H}(t) \mathbf{C}(t), \quad (2.63)$$

involving the coefficient vector $\mathbf{C}(t)$ of length N_{det} and the $N_{\text{det}} \times N_{\text{det}}$ dimensional Hamiltonian and overlap matrices. When applied to the stationary Schrödinger equation, the same procedure leads to the (time-independent) full configuration interaction equation,

$$\mathbf{H} \mathbf{C} = E \mathbf{S} \mathbf{C}, \quad (2.64)$$

a generalized eigenvalue problem which needs to be solved for the energies E and the coefficients \mathbf{C} . Note that in the case of orthonormal orbitals, $\langle \phi_k | \phi_l \rangle = \delta_{kl}$, also the Slater determinants are orthonormal and the many-body overlap matrix \mathbf{S} becomes the identity matrix.

The CI equation presents a mapping of the Schrödinger equation onto a discretized subspace of the anti-symmetric Hilbert space \mathcal{H}_N^- . Except for the discretization in terms of a finite basis, it provides an *exact* representation of the operators and the wavefunction (the latter may also be affected by errors of the time-integration). In particular, the full CI wavefunction contains all *correlations*, which stands in contrast to the approximate methods considered later in this work. As mentioned before, a common field of application of full CI is therefore the production of benchmark results. Furthermore, the full CI wavefunction is *size-consistent*, which means that it is able to describe molecules with different bond lengths at a consistent level of quality [59]. This feature is of major importance in quantum chemistry, for instance in the calculation of dissociation curves, see also Sect. 2.5.9. For atoms, however, it does not seem to play the same vital role.

In order to attack the CI equation, the required operator matrix elements between Slater determinants must be evaluated with the Slater-Condon rules given in Sect. 2.1.5. Next, the equation of motion needs to be integrated and the eigenvalue problem must be solved, respectively. Both tasks are usually accomplished using iterative methods such as those collected in Sect. 3.6, which require only the application of the Hamiltonian onto the state vector,

$$\sigma(t) = \mathbf{H}(t) \mathbf{C}(t). \quad (2.65)$$

This matrix-vector multiplication can be performed using two different concepts: in *conventional CI*, the Hamiltonian is constructed once and stored in a sparse matrix, which is then repeatedly applied to the coefficient vector. On the other hand, in *direct CI*, the Hamiltonian is never explicitly constructed, but only its action on the coefficient vector is evaluated [110]. This formalism is well established in quantum chemistry where usually only a small number of matrix-vector products is necessary. For the time-dependent applications considered in the present work, however, we use the conventional treatment since a much larger number of multiplications is required. In Sect. 3, we focus in detail on the arising numerical issues and present the ideas which are crucial for an efficient application to larger systems.

2.3.3 Symmetry restrictions

Symmetry restrictions play an important role in the theory of configuration interaction. The basic idea is that any symmetry can be used to reduce the complexity of the problem at hand. This reduction, however, usually comes at the cost of a more sophisticated description. A prominent example of this principle was already encountered in Sect. 2.1, where the particle interchange symmetry has been used to restrict the N -particle Hilbert space \mathcal{H}_N to the much smaller subspace of anti-symmetric functions \mathcal{H}_N^- . The price to pay is the more difficult handling of Slater determinants as opposed to Hartree products.

The foundation of symmetry reduction is given by the following classic theorem of quantum mechanics [111]: Given two operators \hat{A} and \hat{B} with $[\hat{A}, \hat{B}] = 0$ and two eigenfunctions $|a_1\rangle, |a_2\rangle$ of \hat{A} with eigenvalues a_1 and a_2 , respectively, the following implication holds:

$$a_1 \neq a_2 \implies \langle a_1 | \hat{B} | a_2 \rangle = 0. \quad (2.66)$$

Hence, the operator \hat{B} does not couple eigenfunctions belonging to different eigenvalues of \hat{A} . Consequently, using a Hilbert space basis of properly ordered eigenfunctions $\{|a_i\rangle\}$, the matrix representation of \hat{B} gets decomposed into blocks, each of which corresponds to a single eigenvalue a_i . Because each of these blocks can be treated independently of the others, one often obtains a valuable reduction in complexity. In practical calculations, it is hence convenient to specify a certain set of symmetry quantum numbers, construct the Hilbert space with the corresponding eigenstates, and work exclusively in the thus obtained subspace.

In the following, we particularly discuss the single- and two-particle symmetry operators of the Hamiltonian (1.2),

$$\hat{H}(t) = \sum_{k=1}^N \left\{ \frac{\hat{\mathbf{p}}_k^2}{2} - \frac{Z}{r_k} + \hat{V}_{\text{ext}}(t) \right\} + \frac{1}{2} \sum_{k \neq l} \frac{1}{|\mathbf{r}_k - \mathbf{r}_l|}.$$

These are the spin operators \hat{S}^2 and \hat{S}_z , the angular momentum operators \hat{L}^2 and \hat{L}_z and the parity operator $\hat{\Pi}$. In case of broken spherical symmetry, which occurs under action of a laser field or in the case of diatomic molecules, the \hat{L}^2 symmetry is violated and the related angular momentum quantum number is not conserved. Further, for an elliptically polarized field, and also for general molecules, the \hat{L}_z -symmetry is broken. For a general introduction into quantum-mechanical group theory, which provides the mathematical foundation of symmetries, see Ref. [112].

Single-particle operators. We first consider the treatment of single-particle operators \hat{O} , for which the construction of eigenstates is comparably easy. In fact, it is sufficient to work in a single-particle basis of eigenstates of the symmetry operator,

$$\hat{O}|\phi_k\rangle = o_k|\phi_k\rangle. \quad (2.67)$$

In this basis, the operator is represented as

$$\hat{O} = \sum_k o_k \alpha_k^\dagger \alpha_k, \quad (2.68)$$

and application to a Slater determinant straightforwardly leads to

$$\hat{O}|\mathbf{n}\rangle = \left(\sum_k o_k n_k \right) |\mathbf{n}\rangle. \quad (2.69)$$

Slater determinants are therefore eigenvectors of \hat{O} , as long as they are set up in terms of the corresponding single-particle eigenstates.

One important example for this concept is the *spin projection operator* \hat{S}_z , which commutes with the spin-free Hamiltonian (1.2). By working in a single-particle basis in which the spin-part is described by either α - or β -spin functions,

$$\phi_{p\sigma}(\mathbf{r}) = \phi_{p\sigma}(\mathbf{r}) \sigma(s_z), \quad \sigma \in \{\alpha, \beta\}, \quad (2.70)$$

the representation of \hat{S}_z becomes

$$\hat{S}_z = \frac{1}{2} \sum_p (a_{p\alpha}^\dagger a_{p\alpha} - a_{p\beta}^\dagger a_{p\beta}). \quad (2.71)$$

As this operator includes only diagonal terms, Slater determinants are simply eigenfunctions,

$$\hat{S}_z |\mathbf{n}\rangle = \frac{N_\alpha - N_\beta}{2} |\mathbf{n}\rangle, \quad (2.72)$$

where N_α (N_β) denotes the number of particles with α -spin (β -spin).

Regarding the angular momentum projection \hat{L}_z , it is advantageous to describe the angular part of the orbitals by spherical harmonics,

$$\phi_{klm\sigma}(\mathbf{r}) = R_{klm\sigma}(r) Y_{lm}(\theta, \phi), \quad (2.73)$$

such that the angular momentum projection operator becomes

$$\hat{L}_z = \sum_{klm\sigma} m \hat{a}_{klm\sigma}^\dagger \hat{a}_{klm\sigma}. \quad (2.74)$$

As before, Slater determinants $|\mathbf{n}\rangle$ are then trivially eigenfunctions,

$$\hat{L}_z |\mathbf{n}\rangle = \left(\sum_{klm\sigma} m n_{klm\sigma} \right) |\mathbf{n}\rangle. \quad (2.75)$$

Finally, to ensure that Slater determinants are also parity eigenfunctions, it suffices to work in a single-particle basis $\{\phi_p(\mathbf{r})\}$ which is symmetric or anti-symmetric with respect to inversion relative to the origin,

$$\hat{\pi} \phi_{p\sigma}(\mathbf{r}) = \phi_{p\sigma}(-\mathbf{r}) = \xi_p \phi_{p\sigma}(\mathbf{r}). \quad (2.76)$$

Here, $\xi_p = +1$ for symmetric orbitals and $\xi_p = -1$ for anti-symmetric orbitals. The parity of a determinant $|\mathbf{n}\rangle$ is then given by

$$\hat{\pi} |\mathbf{n}\rangle = \left(\prod_{p\sigma} \xi_p^{n_p} \right) |\mathbf{n}\rangle, \quad (2.77)$$

where the exponent n_p ensures that the product is taken only over the occupied spin-orbitals. Note that the parity is already accounted for when working in the basis (2.73), as the spherical harmonics are also parity eigenfunctions [113],

$$\phi_{klm\sigma}(-\mathbf{r}) = (-1)^l \phi_{klm\sigma}(\mathbf{r}). \quad (2.78)$$

Two-particle operators. For two-particle operators, the construction of eigenstates is significantly more difficult than in the single-particle case. In principle, the problem can be addressed by calculating the matrix representation of a two-particle operator \hat{T}

in the Slater determinant basis,

$$T_{\mathbf{n}, \mathbf{m}} = \langle \mathbf{n} | \hat{T} | \mathbf{m} \rangle. \quad (2.79)$$

Subsequently, this matrix has to be diagonalized to obtain the eigenvalues τ , of which only a selected subset is retained. The corresponding eigenvectors \mathbf{U}_τ are then used to set up the symmetry-adapted eigenbasis,

$$|\Phi_{\tau, i}\rangle = \sum_{\mathbf{n}} U_{\tau, i\mathbf{n}} |\mathbf{n}\rangle, \quad (2.80)$$

which consequently consists of a linear superposition of Slater determinants. Whether this approach is feasible, however, depends heavily on the operator at hand and on the related ability to keep the matrices small by exploiting further convenient properties.

The procedure becomes clear by considering the basic example of the total spin operator \hat{S}^2 , which trivially commutes with the spin-independent Hamiltonian (1.2). The many-body eigenstates of the total spin are called *configuration state functions* (CSFs). Being a standard problem in quantum chemistry, several works are dedicated to the construction and use of CSFs. Among the applied methods are projection methods [114, 115], the genealogical coupling scheme [59] or symmetric group approaches [116]. A thorough review has been given by Pauncz [84]. In this work, we apply a variant of the basic method mentioned before which has been described by Slater [111]. It proceeds by constructing the matrix representation of

$$\hat{S}^2 = \hat{S}_+ \hat{S}_- + \hat{S}_z (\hat{S}_z - 1) \quad (2.81)$$

in an appropriate subspace of the Hilbert space which consists of all determinants having the same *orbital configuration* [59]. The orbital configuration of a determinant $|\mathbf{n}\rangle$ is the vector

$$|m_1, \dots, m_{N_b}\rangle, \quad m_p = n_{p,\alpha} + n_{p,\beta}, \quad (2.82)$$

where $m_k \in \{0, 1, 2\}$ labels the occupation of the spatial orbital $|\phi_k\rangle$. It can be shown that two determinants $|\mathbf{n}_\gamma\rangle$, $|\mathbf{n}_\mu\rangle$ belonging to different orbital configurations γ and ν , respectively, do not couple under the total spin operator,

$$\langle \mathbf{n}_\gamma | \hat{S}^2 | \mathbf{n}_\mu \rangle = 0, \quad \text{for } \gamma \neq \mu. \quad (2.83)$$

It is therefore sufficient to construct the matrix representation of \hat{S}^2 only in the subspace of determinants belonging to a specified orbital configuration, the dimension of which is significantly smaller than the total Hilbert space. This makes it easy to determine the eigenvalues $S(S+1)$ and eigenvectors \mathbf{U} of this matrix and retain only selected values of S . Doing so for each arising orbital configuration, one obtains the representation of the configuration state functions in terms of (usually a few) Slater determinants,

$$|\text{CSF}_{\gamma, i}\rangle = \sum_{\mathbf{n}_\gamma} U_{i\mathbf{n}_\gamma} |\mathbf{n}_\gamma\rangle. \quad (2.84)$$

The expansion coefficients $U_{i\mathbf{n}_\gamma}$ are eigenvectors of the spin matrix and are formally given by products of Clebsch-Gordan coefficients. Matrix elements of the Hamiltonian between CSFs can then be calculated as

$$\langle \text{CSF}_{\gamma, i} | \hat{H} | \text{CSF}_{\nu, j} \rangle = \sum_{\mathbf{n}_\gamma \mathbf{n}_\nu} U_{i\mathbf{n}_\gamma}^* U_{j\mathbf{n}_\nu} \langle \mathbf{n}_\gamma | \hat{H} | \mathbf{n}_\nu \rangle. \quad (2.85)$$

For further details on the construction of spin eigenstates, we refer to Ref. [59].

In a very similar way, one can also construct common eigenfunctions of the total spin and the total angular momentum operator

$$\hat{L}^2 = \hat{L}_+ \hat{L}_- + \hat{L}_z (\hat{L}_z - 1). \quad (2.86)$$

The procedure we describe is due to Schaefer and Harris [117]. For its application it is highly advantageous to work in a basis of angular momentum eigenfunctions $\psi_{klm\sigma}(\mathbf{r})$ as given in Eq. (2.73). Then, similar to the total spin case, one constructs the *radial configurations*,

$$|r_{11}, \dots, r_{N_{\text{rad}} N_l}\rangle, \quad (2.87)$$

where

$$r_{kl} = \sum_{m\sigma} n_{klm\sigma} \quad r_{kl} \in \{0, 1, \dots, 2(2l + 1)\}, \quad (2.88)$$

and determines the matrix representation of $\hat{L}^2 + \lambda \hat{S}^2$ in the complete set of determinants contributing to a single radial configuration. Here, λ is a small parameter which serves to disentangle the eigenvalues of the spin and angular momentum operator (of the order $\lambda \approx 0.001$). Diagonalization of this matrix for each arising radial configuration then yields the symmetry-adapted eigenfunctions, which are represented through an expansion similar to Eq. (2.85). A more elaborate treatment for the construction of combined spin- and angular momentum eigenfunctions can be found in Ref. [118].

Example: Symmetries of the helium atom. We give an example of the introduced concepts by means of the calculation of the helium ground state, which has ${}^1S^e$ symmetry. Thereto, we use a spatial basis given by

$$\psi_{klm}(\mathbf{r}) = R_{klm}(r) Y_{lm}(\theta, \phi). \quad (2.89)$$

The explicit form of the radial functions $R_{klm}(r)$ is not important here, but only that we use $N_{\text{rad}} = 49$ radial functions for each value of (lm) . We further include spherical harmonics up to $l \leq 6$, which yields a number of $N_{\text{ang}} = 49$ angular basis functions. The total number of basis functions is thus $N_b = N_{\text{rad}} N_{\text{ang}} = 2401$, and the number of spin-orbitals is $2N_b = 4802$.

Table 1 shows the results. Starting from the number of possible Hartree-products, the successive restriction to fixed symmetry quantum numbers leads to a significantly smaller Hilbert space. In particular, the angular momentum symmetries yield the largest reduction. For this set of symmetry quantum numbers, the approximately 10^7 Slater determinants reduce to merely 14406 symmetry-adapted configurations. This is small enough to allow for a diagonalization by dense matrix methods, through which the complete spectrum of ${}^1S^e$ symmetry becomes accessible. For other choices of the symmetry quantum numbers, however, as well as for larger radial basis sets, the subspaces can become significantly larger (e.g., 79233 for the same parameters but $L = 4$). This prevents one from obtaining a complete spectrum of the helium atom, which would enable an accurate characterization of singly- and doubly-ionized states.

2.4 Time-dependent restricted active space configuration interaction

The time-dependent restricted active space configuration interaction (TD-RASCI) method presents a way to reduce the exponential problem occurring in direct solutions of the time-dependent Schrödinger equation. The idea is to retain in the full CI expansion only those determinants which are expected to be important for the

Table 1. Reduction of the full configuration interaction problem for the $^1S^e$ ground state of helium. N_{conf} denotes the number of remaining configurations which span the symmetry-restricted subspace of the Hilbert space.

level	symmetry	N_{conf}	reduction
Hartree products		23 059 204	
Slater determinants		11 527 201	$\times \frac{1}{2}$
Spin projection	$S_z = 0$	5 764 801	$\times \frac{1}{2}$
Angular mom. projection	$L_z = 0$	554 631	$\times \frac{1}{10}$
Total spin	$S = 0$	277 487	$\times \frac{1}{2}$
Total angular mom.	$L = 0$	14 406	$\times \frac{1}{16}$

physical process under investigation and by this—hopefully—obtain a calculation that is manageable and sufficiently accurate at the same time. In the following, we summarize the state of research, the goals of the present work, and give a detailed survey on the TD-RASCI method and its efficient application to photoionization processes.

2.4.1 State of research

The idea to reduce the effort of direct calculations by including only important determinants is present since the invention of the configuration interaction method. The early atomic structure CI calculations were restricted to a few dozens of determinants which, in order to provide a reasonable description, have been selected individually on the basis of physical considerations or by trial and error [98]. With increasing computer power and the related growth of the determinant spaces, however, the individual selection procedure quickly became impracticable. Nowadays, calculations instead apply restrictions which are often classified by the *excitation level*. The full CI wavefunction is therefore set up in terms of excited determinants from a reference state [119],

$$|\Psi\rangle = c_0|\Phi_0\rangle + \sum_{a,r} c_a^r |\Phi_a^r\rangle + \sum_{\substack{a < b \\ \mathbf{r} < s}} c_{ab}^{rs} |\Phi_{ab}^{rs}\rangle + \sum_{\substack{a < b < c \\ \mathbf{r} < s < t}} c_{abc}^{rst} |\Phi_{abc}^{rst}\rangle + \dots \quad (2.90)$$

The reference state $|\Phi_0\rangle$ is usually a single Slater determinant or configuration state function constructed from Hartree-Fock or multiconfigurational Hartree-Fock orbitals. Further, the excited determinants are defined by

$$|\Phi_a^r\rangle = \hat{a}_r^\dagger \hat{a}_a |\Phi_0\rangle, \quad (2.91)$$

$$|\Phi_{ab}^{rs}\rangle = \hat{a}_s^\dagger \hat{a}_b |\Phi_a^r\rangle, \quad (2.92)$$

and so on. They are constructed from the reference state by raising one or more particles from the occupied orbitals a, b, \dots to the virtual orbitals r, s, \dots , the indices of which are ordered in the summations so as to produce only different determinants.

Truncation of the series (2.90) at the level of single-excitations leads to the *configuration interaction singles* (CIS) approximation, at the level of double-excitations to *configuration interaction singles/doubles* (CISD), and so on. Generally, the scheme

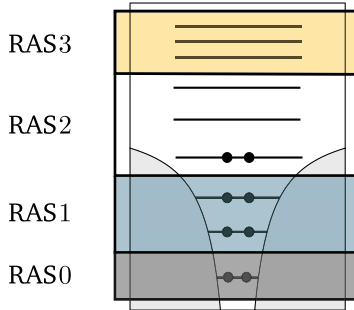


Fig. 6. Illustration of the original restricted active space scheme introduced by Olsen et al. [122]. The single-particle basis is divided into 4 partitions. The electrons in RAS0 are assumed to be fixed, in RAS1 a chosen number of at most n_h holes is allowed, the electrons are not restricted in RAS2, and in RAS3, at most n_e electrons are allowed.

obtained by restriction to the n -th excitation level leads to a determinant basis of size

$$N_{\text{det},n} = \binom{N}{n} \binom{2N_b - N}{n} \approx (2N_b)^n, \quad (2.93)$$

and thus for small n to a convenient polynomial scaling. Approximations of this kind are ubiquitous in quantum chemistry and physics. They include applications to atoms and molecules, quantum dots [120], or Bose-Einstein condensates [121], to mention only a few examples. A similar type of approximation is presented by multi-reference configuration interaction, where instead of the single-reference expansion (2.90) a number of reference states $|\Phi_\gamma\rangle$ plus their excitations are employed,

$$|\Psi\rangle = \sum_\gamma c_\gamma |\Phi_\gamma\rangle + \sum_\gamma \sum_{a,r} c_{\gamma a}^{r,a} |\Phi_\gamma^{r,a}\rangle + \frac{1}{2} \sum_\gamma \sum_{ab,rs} c_{\gamma ab}^{rs} |\Phi_\gamma^{rs}\rangle \dots \quad (2.94)$$

Multi-reference approaches are essential if a single reference state is not able to provide an appropriate representation of the system, such as, for instance, for the ozone molecule [59].

The reduced-excitation methods covered so far present only a rough guideline for the selection of determinants. A more sophisticated strategy is given by the *restricted active space* method introduced to quantum chemistry by Olsen et al. in the context of CI and MCHF calculations [122], where it is also called restricted active space self-consistent field (RASSCF) method. In its original formulation, the single-particle basis space is divided into four partitions named RAS0 to RAS3, and certain restrictions are imposed onto the occupation of the partitions, see Fig. 6. The advantage of the RAS scheme is that one can adjust the wavefunction expansion in a more controlled way, and by this, e.g., treat core and valence electrons with a different level of accuracy. The original RAS idea has also been straightforwardly extended to a larger number of partitions [123].

Up to now, we have considered only time-independent applications. For solutions of the time-dependent Schrödinger equation and, particularly for the treatment of photoionization processes, specialized variants of the previous ideas have been examined. An important role is played by the single-active electron (SAE) approximation introduced by Kulander and coworkers [63, 124], which has been applied to a variety of topics including photoionization of atoms [125] and molecules [126], high-order harmonic generation [127], and others. Further, the two-active electron (TAE) approximation has been applied by Laulan and Bachau [107] and by Yip et al. [108] to

the single- and double-photoionization of beryllium, as well as by Kamta and Starace to the negatively charged lithium ion [128]. The time-dependent configuration interaction singles (TD-CIS) method has been introduced to strong-field physics by Rohringer et al. [129] and found successful application to high-order harmonic generation [130] or the decoherence in the photoionization of xenon [131]. Further, Krause et al. have used Gaussian basis sets to consider the excitation of lithium cyanide within TD-CIS [42]. Another approach similar to TD-CIS has been introduced by Spanner and Patchkovskii to describe single-ionization [132].

2.4.2 TD-RASCI – applications

This work discusses a time-dependent version of the restricted active space configuration interaction method that was first presented by Hochstuhl and Bonitz in Ref. [75] and applied to photoionization processes in multi-electron atoms. The TD-RASCI method presents a general approach to time-dependent ab-initio simulations of few-particle systems which, as will be covered in detail below, incorporates all the time-dependent methods mentioned in the previous subsection in a single framework. TD-RASCI is, at the same time, a conceptually simple method, as can be seen from the derivation of the equation of motion in the next subsection. For the efficient application to photoionization processes, the RAS scheme, which is traditionally formulated in energy space, is further extended to the coordinate space, using an appropriate mixed single-particle basis introduced in Sect. 3.1.3. Finally, in Sect. 4, the TD-RASCI method is applied to atoms in order to demonstrate its outstanding capabilities in describing correlated photoionization processes.

2.4.3 TD-RASCI equations of motion

The TD-RASCI ansatz for the N -particle wavefunction is given by

$$|\Psi(t)\rangle = \sum_{I \in \Omega} C_I(t) |\psi_{i_1} \cdots \psi_{i_N}\rangle, \quad (2.95)$$

and looks almost identical to the time-dependent full CI ansatz (2.58). The only difference is the index set Ω , which specifies the included Slater determinants. In full CI, it is given by Eq. (2.13),

$$\Omega^- = \{(j_1, \dots, j_N) \in \mathbb{N}^N \mid 1 \leq j_1 < \dots < j_N \leq 2N_b\}. \quad (2.96)$$

In contrast, the index set applied in TD-RASCI calculations is only a subset of Ω^- , the selection of which is considered in the next subsection. Here, let us assume for the moment that Ω is already determined. Then, a straightforward insertion of the ansatz into the time-dependent Schrödinger equation yields the TD-RASCI equations of motion,

$$i \sum_{J \in \Omega} S_{IJ} \dot{C}_J(t) = \sum_{J \in \Omega} H_{IJ}(t) C_J(t), \quad (2.97)$$

or equivalently in matrix notation,

$$i \mathbf{S} \dot{\mathbf{C}}(t) = \mathbf{H}(t) \mathbf{C}(t), \quad (2.98)$$

where the overlap matrix \mathbf{S} and Hamiltonian matrix \mathbf{H} have been defined in Eqs. (2.62) and (2.61), respectively. Note that these equations are formally identical to the TD-FCI equations, but involve another choice for the discretized subspace of the Hilbert space and therefore matrices and vectors of smaller dimension.

These lines illustrate several convenient properties of the TD-RASCI scheme:

- The derivation of the equation of motion is extraordinarily simple, and the whole task is the appropriate selection of the index set Ω to describe the physical process at hand.
- Since the formalism is independent of the actual content of Ω , a single implementation can be set up which is able to treat a variety of different RAS approximations.
- The TD-RASCI equations require only the evaluation of matrix-vector products which is a computational standard task, and therefore greatly simplifies the efficient implementation, such as the use of parallelization schemes.

2.4.4 Determinant selection

The TD-RASCI method is determined by the included Slater determinants in the wavefunction expansion (2.95), i.e., by the set Ω of determinant indices. Generally, the choice of determinants should reflect the physical problem at hand and include those states which are expected to dominantly contribute to the process. On the other hand, the number of determinants should not be too large such that the calculations remain feasible. To accomplish both requirements, one needs to have an efficient selection procedure available. Such has been proposed in Ref. [75] and is described in the following:

- (i) Divide the single-particle basis,

$$\mathcal{B} = \{|\psi_1\rangle, \dots, |\psi_{2N_b}\rangle\}, \quad (2.99)$$

into an arbitrary number P of partitions \mathcal{B}_i ,

$$\mathcal{B} = \mathcal{B}_1 \cup \dots \cup \mathcal{B}_P, \quad (2.100)$$

with

$$\mathcal{B}_i = \{|\psi_{p_{(i-1)}}\rangle, \dots, |\psi_{p_i-1}\rangle\}. \quad (2.101)$$

The partitioning is thus defined by the $P + 1$ numbers

$$(p_0 = 1, p_1, \dots, p_{P-1}, p_P = 2N_b), \quad (2.102)$$

i.e., by $P - 1$ free parameters. The number of orbitals in the partition \mathcal{B}_i is denoted by $N_{b,i}$; by definition, one has $\sum_j N_{b,j} = 2N_b$. The partitions are visualized by the four black boxes in Fig. 7.

- (ii) Impose restrictions on the particle numbers allowed in the partitions. Therefore, for each partition \mathcal{B}_i , one specifies the minimal and maximal particle number, $N_{\min,i}$ and $N_{\max,i}$, and allows only for particle numbers N_i inbetween these two values, $N_{\min,i} \leq N_i \leq N_{\max,i}$. The restrictions should be assigned to match the occurring physical processes as good as possible but, at the same time, lead to only a moderate number of determinants.

Each allowed pair (\mathcal{B}_i, N_i) obtained this way is related to a discrete full CI Hilbert space $\mathcal{H}_i(N_i)$, which is the span of all N_i -particle Slater determinants constructed with the truncated single-particle basis \mathcal{B}_i . For an example, see the right-hand part of Fig. 7. The restricted Hilbert space \mathcal{H}_{RAS} is thus decomposed as

$$\mathcal{H}_{\text{RAS}} = \bigcup_{\substack{N_{\min,i} \leq N_i \leq N_{\max,i} \\ \sum_j N_j = N}} \mathcal{H}_1(N_1) \times \dots \times \mathcal{H}_P(N_P), \quad (2.103)$$

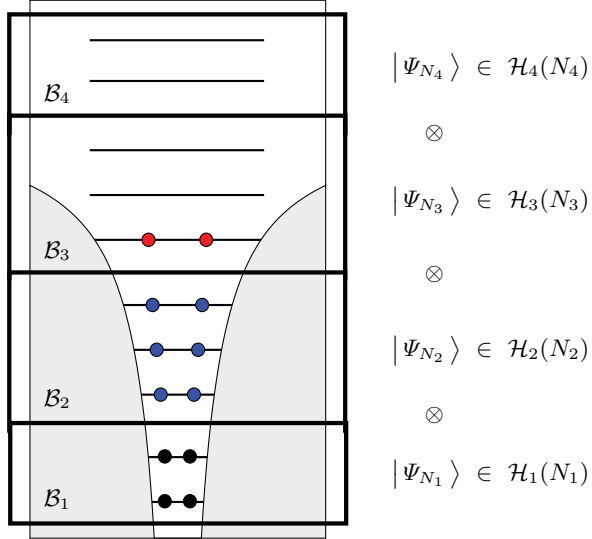


Fig. 7. Illustration of the restricted active space scheme for a number of $P = 4$ partitions of the single-particle basis \mathcal{B} . In each partition, one imposes certain restrictions on the allowed particle numbers. The total N -particle wavefunction $|\Psi\rangle$ is constructed as the tensor product of the N_i -particle wavefunctions $|\Psi_i\rangle$, with $\sum_i N_i = N$. Figure from Ref. [75].

i.e., as the unification of the Cartesian products of all subspaces which satisfy the RAS constraints and together have the correct total particle number N . It has the dimension

$$\dim(\mathcal{H}_{\text{RAS}}) = \sum_{\substack{N_{\min,i} \leq N_i \leq N_{\max,i} \\ \sum_j N_j = N}} \binom{N_{\text{b},1}}{N_1} \cdots \binom{N_{\text{b},P}}{N_P}. \quad (2.104)$$

The wavefunction is set up as the anti-symmetrized product of the given Slater determinants (which is just a determinant in the original Hilbert space),

$$|\Psi(t)\rangle = \sum_{|I_i\rangle \in \mathcal{H}_i(N_i)} C_{I_1, \dots, I_P}(t) \hat{\mathcal{A}} |I_1\rangle \cdots |I_P\rangle. \quad (2.105)$$

Finally, in order to bring the wavefunction into the form of Eq. (2.95), one needs to specify the index set of the thus included Slater determinants,

$$\Omega = \{(i_1, \dots, i_N) | \forall j \in \{1, \dots, P\} : N_{\min,j} \leq N_j \leq N_{\max,j}\}. \quad (2.106)$$

Here, the occupation N_j of the j -th partition \mathcal{B}_j is given by

$$N_j(I; p_0, \dots, p_P) = \sum_{k=1}^N \begin{cases} 1, & p_{j-1} \leq i_k < p_j \\ 0, & \text{else} \end{cases}. \quad (2.107)$$

Note that the notation for the index set Ω does not explicitly indicate the strong dependence on the RAS parameters, i.e., on the partitioning (p_0, \dots, p_P) and the range of allowed particle numbers, $N_{\min,i}$ and $N_{\max,i}$.

If we made no restriction on the particle numbers, i.e., allowed for $0 \leq N_i \leq N$ in each partition \mathcal{B}_i , we would recover the full configuration interaction method.

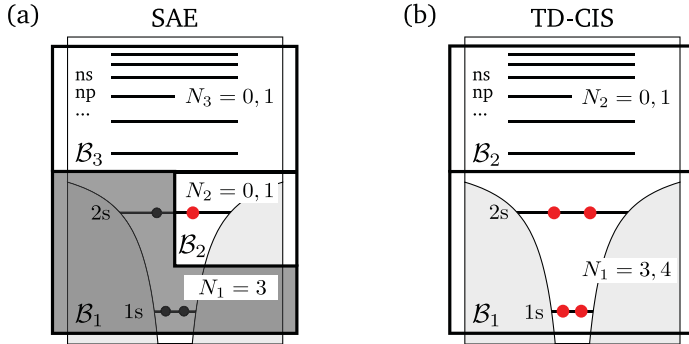


Fig. 8. Special cases of the TD-RASCI scheme for the example of beryllium. The numbers N_i label the allowed particle numbers in the partitions \mathcal{B}_i (black boxes). Active electrons are plotted in red. (a) Single-active electron approximation with an active 2s orbital. The gray-shaded orbitals are fixed, and at most a single electron is allowed in the continuum. (b) Time-dependent configuration interaction singles. All electrons are active, but only single-excitations from the ground state are included. Figure from Ref. [75].

By restricting the accessible many-body Hilbert space in the way just presented, one can significantly reduce its dimension and thus enable time-dependent configuration interaction calculations which are far beyond reach of the full CI scheme.

2.4.5 Relation to existing methods

As has been mentioned previously, the TD-RASCI scheme is a very general method which incorporates a variety of time-dependent approaches of strong-field physics. In the following, we prove this statement by explicitly specifying the RAS parameters required to obtain the single- and two-active electron approximation and the time-dependent configuration interaction singles method.

We begin with the single-active electron approximation. In its basic form, e.g. Ref. [63], it reduces the N -particle TDSE to an equation for a single particle,

$$i \frac{\partial}{\partial t} \psi_{\text{SAE}}(\mathbf{r}, t) = \left\{ -\frac{1}{2} \nabla^2 + v_{\text{SAE}}(\mathbf{r}) \right\} \psi_{\text{SAE}}(\mathbf{r}, t), \quad (2.108)$$

where the pseudo-potential $v_{\text{SAE}}(\mathbf{r})$ models the ionic background felt by the active electron. Common choices for the pseudo-potential include spherically symmetric potentials [133] and angular momentum dependent expansions [134]. However, as pointed out by Rohringer et al. [129], the ambiguous choice for the pseudo-potential prevents the basic SAE approximation from being an ab-initio method. In the TD-RASCI method, the SAE approximation is easily realized by fixing all orbitals except one, see the graphical representation shown in Fig. 8. The corresponding wavefunction is given by

$$|\Psi_{\text{SAE}}(t)\rangle = c_0(t) |\Phi_0\rangle + \sum_{r \in \text{virt.}} c_a^r(t) |\Phi_a^r\rangle. \quad (2.109)$$

Note that the index a of the active orbital is fixed and the index r runs over the virtual, i.e., unoccupied, orbitals. $|\Phi_0\rangle$ denotes an appropriate reference determinant, which is usually constructed with Hartree-Fock orbitals. As for the basic SAE approximation, the corresponding TD-RASCI single-active electron treatment reduces the N -particle problem to a description with $\mathcal{O}(N_b)$ free parameters, and therefore requires an effort

which is comparable to the solution of a single-particle Schrödinger equation. Besides, the TD-RASCI scheme has the advantage that the interaction with other atomic shells—including the exchange potential—is modeled consistently and hence there is no need to rely on pseudo-potentials. We note that SAE approximations of this kind have already found application to strong-field processes [64, 129].

A similar ansatz is made in the time-dependent configuration interaction singles (TD-CIS) method [64, 129], where now each occupied orbital is considered to be active,

$$|\Psi_{\text{CIS}}(t)\rangle = c_0(t)|\Phi_0\rangle + \sum_{a \in \text{occ.}} \sum_{r \in \text{virt.}} c_a^r(t)|\Phi_a^r\rangle. \quad (2.110)$$

A graphical illustration is given in Fig. 8. The TD-CIS approximation requires a total effort of $\mathcal{O}(N \cdot N_b)$. Note that, when working in a Hartree-Fock orbital basis, the Brioullin theorem holds [59],

$$\langle \Phi_0 | \hat{H} | \Phi_a^r \rangle = 0, \quad (2.111)$$

which implies that the ground state is not improved by single-excitations and, consequently, the ground state energy is the Hartree-Fock energy. As an intermediate between the CIS and SAE approximation, one can also treat only a selected subset of the occupied orbitals as active, e.g., fix the core electrons and allow only the valence electrons to become ionized.

The two-active electron approximation usually applied in photoionization studies, e.g. [108, 128], proceeds in a similar way as the SAE approximation. It reduces the description to a two-particle wavefunction which is governed by the equation

$$i \frac{\partial}{\partial t} \psi_{\text{TAE}}(\mathbf{r}_1, \mathbf{r}_2, t) = \left[\sum_{i=1}^2 \left\{ -\frac{1}{2} \nabla_i^2 + v_{\text{TAE}}(\mathbf{r}_i) \right\} + \frac{1}{|\mathbf{r}_1 - \mathbf{r}_2|} \right] \psi_{\text{TAE}}(\mathbf{r}_1, \mathbf{r}_2, t). \quad (2.112)$$

While the Coulomb interaction between the active electrons is treated in an ab initio fashion, the interaction with the residual atom is approximated by a pseudo-potential $v_{\text{TAE}}(\mathbf{r}_i)$ (which does not need to be the same for both electrons). Common choices include the Hartree potential [107], the Slater $X\alpha$ -potential [135] or, simpler, screened Coulomb potentials which match the ionization potential of the modeled electrons [32]. The advantage of the TD-RASCI two-active electron ansatz,

$$|\Psi_{\text{TAE}}(t)\rangle = c_0(t)|\Phi_0\rangle + \sum_{r \in \text{virt.}} \left(c_a^r(t)|\Phi_a^r\rangle + c_b^r(t)|\Phi_b^r\rangle \right) + \sum_{r < s} c_{ab}^{rs}(t)|\Phi_{ab}^{rs}\rangle, \quad (2.113)$$

where a and b denote the indices of the active orbitals, is again that the inter-shell interaction is treated consistently and no pseudo-potentials must be introduced. Further, the required total effort of $\mathcal{O}(N_b^2)$ is the same as for Eq. (2.112). Among other examples, this enables a consistent time-resolved consideration of double-ionization processes of many-electron atoms.

In a similar way, one can create other approximations. The selection of determinants can be based to a large extent on physical considerations, with the only restriction being imposed by the size of the determinant basis and the sparsity of the arising Hamiltonian matrix. This opens the door to simulations of a variety of explicitly time-dependent physical processes which can be approached with the TD-RASCI method. As a final example how physics translates into TD-RASCI constraints, we mention the KLL-Auger process in neon, see also Fig. 9. On the one hand, the process requires the $1s$ shell to be active, such that the K-shell ionization can occur. On the

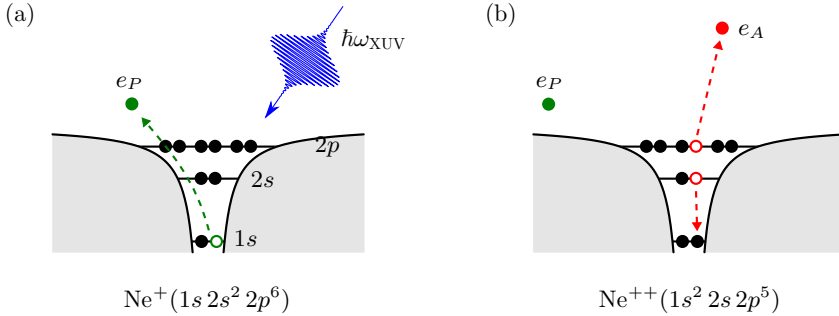


Fig. 9. Illustration of the minimal model for simulating the KLL-Auger process of neon in the ground state. Inactive electrons are depicted in black. (a) Core-electron ionization via absorption of an XUV photon leaves the ion in the $\text{Ne}^+(1s 2s^2 2p^6)$ state. (b) Subsequent inner atomic decay leads to the final ionic state $\text{Ne}^{++}(1s^2 2s 2p^5)$. The Auger process is triggered by the Coulomb interaction between the Ne^+ and Ne^{++} ion, which can be described on first principles in the TD-RASCI method.

other hand, a final state must be present with two holes in the L-shell, say in the 2s and 2p₀ orbital. The minimal ansatz to the wavefunction therefore looks like

$$|\Psi_{\text{Auger}}(t)\rangle = c_0(t)|\Phi_0\rangle + \sum_{r \in \text{virt.}} c_{1s}^r(t)|\Phi_{1s}^r\rangle + \sum_{r < s} c_{2s,2p_0}^{rs}(t)|\Phi_{2s,2p_0}^{rs}\rangle. \quad (2.114)$$

The idea is that once the laser pulse has ionized an electron from the 1s shell, the Coulomb coupling between the states $|\Phi_{1s}^r\rangle$ and $|\Phi_{2s,2p_0}^{rs}\rangle$ is able to trigger the Auger decay. Under the usually valid assumption that the doubly-ionized state does not get excited by the laser pulse, the number $\sum_{rs} |c_{2s,2p_0}^{rs}(t)|^2$ can then be used as an estimate for the fraction decayed via the Auger process. Further, in a similar way as before, correlations could be added to the description by allowing also for other excited states. Such an approach would provide a valuable alternative to the time-resolved description introduced by Kazansky and Kabachnik [136], and improve the latter by adding a consistent treatment of the ionic background as well as of post-collision interactions.

2.4.6 Treatment of photoionization

So far, we considered the TD-RASCI approach in a general basis set, but, for the examples, mainly focused on Hartree-Fock orbitals, or equivalently, other kinds of optimized orbitals such as those arising from a MCHF or Kohn-Sham treatment. The reason is that, in order to be efficient, RAS schemes require an appropriate reference determinant (or more than one in the case of multi-reference calculations) based on which the Hilbert space is constructed. The concept of relating to a reference determinant in fact works well for many applications and constitutes the foundation of a variety of correlated treatments such as Coupled-Cluster or Møller-Plesset theory [59]. For photoionization problems requiring large basis sets, however, the use of Hartree-Fock orbitals becomes difficult due to the number of $\mathcal{O}(N_b^4)$ two-electron integrals that must be handled. This issue has been faced in Ref. [64] by truncating the two-electron integrals in a way similar to semi-empirical calculations [137]. In contrast, the strategy we describe in the following employs a mixed basis set and is capable of using the full, unrestricted Coulomb interaction.

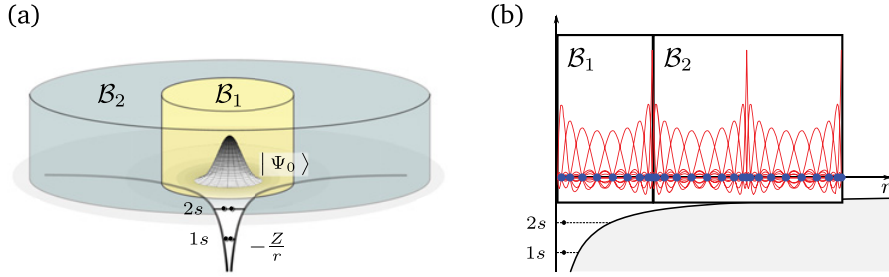


Fig. 10. Partitioning of the coordinate space used in the TD-RASCI treatment of photoionization. (a) The coordinate space is divided into two (or more) spatial partitions, where \mathcal{B}_1 contains the ground state $|\Psi_0\rangle$ and \mathcal{B}_2 models the continuum. Figure from Ref. [75]. (b) In practice, the partitioning is achieved by using a spatially localized basis set, which allows for the application of the same constraint selection procedure as before in energy space. For example, the restriction to single-ionization corresponds to allowing only for a single electron in \mathcal{B}_2 .

Generally, for large basis expansions, it is advantageous to employ localized (or nearly-localized) basis sets which have the property to be non-zero only in a certain region of the coordinate space. Localized basis sets include finite-difference and finite-element representations [138], B-splines [139], wavelets [140], or, as used in this work and detailed in Sect. 3.1, discrete variable representations. The advantage of localized basis sets is, first, a sparse representation of the two-electron integrals with typically only a number of $\mathcal{O}(N_b^2)$ terms, which makes it possible to handle also large expansions without approximation. Next, what is even more important for the TD-RASCI scheme, localized basis sets allow one to introduce a division of the coordinate space which can be treated in the same manner as before the division in energy space. As illustrated in Fig. 10, this enables the distinction of an atomic region and the continuum which can be straightforwardly exploited, for instance, by allowing only for single-ionization (one electron in the continuum region), double-ionization (two electrons in the continuum region), and so on.

On the other hand, localized basis sets have the disadvantage that they do not resemble atomic orbitals, such that a single reference determinant usually does not provide an adequate representation of the ground state wavefunction. As a solution to this problem, we introduce a mixed basis set which consists of Hartree-Fock or similarly optimized orbitals in the atomic region, and of localized orbitals in the continuum region. This allows for the construction of an appropriate reference state that is localized in the atomic region. Moreover, in the remaining coordinate space—which usually presents the by far larger region—the advantages of the localized basis set can be exploited. In particular, it is possible to include the Coulomb interaction in a consistent manner. The actual construction of the basis set in terms of a discrete variable representation is topic of Sect. 3.1.3.

In summary, we have introduced a scheme which allows for the efficient application of the usual RAS ideas to photoionization problems and, further, is capable of treating large basis sets without approximation to the Coulomb interaction.

2.4.7 Relation to the time-dependent R-matrix method

The R-matrix method can be considered the most successful approach to the ab-initio simulation of many-electron atoms taken so far. It is traditionally employed either in time-independent calculations [65] or together with the Floquet ansatz [141], and has

produced several benchmark results for the photoionization of atoms such as neon and argon. Recently, Lysaght et al. [67], as well as Guan et al. [68, 69], have also introduced an explicitly time-dependent R-matrix variant for the treatment of atoms. It has been successfully applied to the calculation of correlated high-order harmonics generation [142] or the study of time-delays in the photoionization of different shells in the neon atom [33].

The time-dependent R-matrix method as described in Ref. [67] employs the *division-of-space* concept to construct the $(N+1)$ -electron wavefunction by an expansion into $(N+1)$ -particle wavefunctions localized in the inner region, and products of N -particle wavefunction in the inner region and a single-particle function in the continuum. The wavefunctions in the inner region are chosen as angular momentum and spin eigenstates. There, in the inner region, the TD-RM method accounts for electron exchange and correlation effects, while in the outer region exchange and correlation effects between the ejected electron and the remaining N electrons are considered to be negligible. Hence, the ejected electron moves in the local long-range potential of the residual N -electron ion, which is obtained via a multipole expansion. The discretized wavefunction is then propagated in time via the Crank-Nicolson algorithm. For further details, we refer to the original work [67].

The R-matrix division-of-space concept closely resembles the partitioning that is usually applied in this work. For this particular setting, the R-matrix and the TD-RASCI method in fact constitute very similar approaches, which should also provide comparable results. However, they significantly differ in the underlying concepts: the R-matrix method is built on the assumption of two distinct spaces, which are then equationed to each other at the boundary by enforcing the wavefunction to be continuously differentiable. In contrast, the TD-RASCI method starts from the full, connected Hilbert space, which is then reduced by the RAS constraints in order to arrive at a feasible approximation. This makes it easy to consistently include exchange effects or to model the ionic potential without multipole approximations.

2.4.8 Summary and extensions of the TD-RASCI method

Let us summarize some of the advantageous properties and possible extensions of the TD-RASCI method:

- It is not necessary to restrict oneself to the two-fold division of space that is used throughout this work. In fact, the TD-RASCI method can handle an arbitrary set of constraints and thus allows for a great freedom in the parametrization of the wavefunction. Hence, one can employ as many divisions as are useful for the problem at hand.
- The TD-RASCI method comprises a variety of different methods in a single framework, from the SAE approximation to the full CI method. Therefore, in principle, any physical process can be addressed. For example, to switch from single-ionization to double-ionization, a simple change of the corresponding input parameters is sufficient.
- The derivation of the equations of motion is completely straightforward, and their solution presents a standard problem of computational physics for which a variety of efficient algorithms are available.
- The TD-RASCI method treats the Coulomb interaction in an ab-initio fashion in the whole coordinate space, including correlation and exchange effects. It is not required to employ a multipole expansion to model the ionic potential experienced by the ejected electron. However, it is possible to do so by approximating the two-electron integrals, which is likely to reduce the effort of the simulation.

- Spin and angular momentum symmetries can be exploited in TD-RASCI by using standard algorithms such as those collected in Sect. 2.3.3.
- The extension from atoms to diatomic molecules is straightforward and amounts only to a change from the spherical to the prolate spheroidal single-particle basis, which are both covered later in Sect. 3.1.

These features render the TD-RASCI method highly appropriate for the simulation of photoionization processes in atoms and molecules. To confirm these statements by physical results is the goal of Sect. 4.

2.5 Multiconfigurational time-dependent Hartree-Fock

The multiconfigurational time-dependent Hartree-Fock (MCTDHF) method is another versatile tool for the numerical simulation of few-particle systems. It presents, on the one hand, an extension of the Hartree-Fock method using more than a single determinant, thus adding correlations to the mean-field description. On the other hand, it can be considered as an extension of the full configuration interaction method, in which the exponential problem is reduced by using a smaller but optimized single-particle basis set. In the following, after giving an overview on the state of research and the goals of this work, we focus in detail on the idea underlying MCTDHF and the various possibilities for its implementation. Subsequently, we derive the equations of motion and show their connection to time-dependent Hartree-Fock and configuration interaction theory. We close this section with a comparison of spin-restricted and spin-unrestricted treatments in molecular hydrogen.

2.5.1 State of research

The first multiconfigurational Hartree-Fock (MCHF) calculation has been published by Hartree et al. in 1939 [143]. Since then, the MCHF method has evolved into a standard tool in chemical physics, see, e.g., the monograph of Froese-Fischer [144]. In relation to photoionization, it has been used to calculate photoionization cross sections and angular distributions of atoms and molecules [145, 146]. Time-dependent generalizations of the MCHF method were considered the first time around 1980 by Daalgard [147], Yeager et al. [148] and McWeeny [149].

A particularly successful variant is the multiconfigurational time-dependent Hartree (MCTDH) method introduced by Meyer, Manthe and Cederbaum in 1990 [150, 151]. The MCTDH approach has found applications to a variety of physical scenarios, among them photoexcitation of polyatomic molecules, scattering of atoms and molecules, or the spin-boson model, to name a few. A thorough introduction into the MCTDH formalism and its applications is given in Refs. [88, 152]. In the MCTDH method, the wavefunction is expressed by a superposition of time-dependent Hartree products and therefore does not incorporate the particle exchange symmetry.

The extension to the multiconfigurational time-dependent Hartree-Fock method has been derived in several works published around 2004 by Scrinzi and coworkers [70, 153], Nest et al. [72] and Kato et al. [71]. These works consider fermionic particles and consequently apply Slater determinants instead of Hartree products. Shortly thereafter, also the extension to bosonic particles named MCTDHB has been given by Alon et al., who employed a basis of permanents [154]. As was further pointed out by the same authors, the fermionic and bosonic theories are very similar and differ only in the handling of the many-particle configurations [97]. In addition, both these extensions are rather similar to the MCTDH treatment, which consequently ever had and still has a great impact on the development of the MCTDHF and MCTDHB

methods. Another, complementary approach is the non-variational formulation of MCTDHF given by Nguyen-Dang et al. [155]. Further, extensions were made to the usage of selected configurations in MCTDH [156, 157], which closely resembles the restricted active space idea. Moreover, recently also a RAS treatment considering double-excitations was tailored explicitly to the MCTDHF model by Miyagi and Madsen [158]. Another promising idea of Kvaal combines the coupled-cluster approach with the principle of using time-dependent orbitals [58].

In the context of photoionization, the MCTDHF method has been applied to atoms and diatomic molecules by Haxton et al. [74]. Jordan and Scrinzi studied photoionization of the hydrogen molecule in cylindrical coordinates using a model interaction [159]. Further, Gaussian basis sets have been used by Nest et al. [160] to study photoexcitation of lithium hydride as well as by Klamroth et al. [161] to sodium clusters. Kato and coworkers applied a set of numerical orbitals to the hydrogen molecule to investigate excited state dynamics [162, 163]. Nguyen-Dang et al. introduced a partitioning scheme to obtain an improved description of the continuum [164]. Further, molecular dynamics beyond the Born-Oppenheimer approximation have been considered by Nest [165] and Haxton [73]. Another recent development by Kvaal in the context of MCTDH is the combination of wavefunction and density matrix methods to describe particle absorption in a Lindblad approach [166]. The approach in this work bears several similarities to the one taken by Haxton et al. [73, 74].

2.5.2 MCTDHF – goals of this work

One goal of this work is to review applications of the MCTDHF formalism to photoionization processes in three-dimensional atoms and molecules. Therefore, a new computer code has been implemented to solve the MCTDHF equations, the first results were published in Ref. [76]. Particular attention is payed on the usage of appropriate basis sets and the development of efficient algorithms. The resulting code is highly appropriate for studying photoionization and is optimized for the treatment of atoms and diatomic molecules.

Another goal is practical investigation of the capabilities of MCTDHF which is performed in Sect. 4. Therefore, the method is applied to the single-ionization and two-photon double-ionization of helium, which provides an ideal test case since it is amenable to full CI calculations [75], as well as the photoionization of beryllium. We further present applications of the MCTDHF method to the photoionization of one-dimensional model atoms [109, 167] and the breathing mode of harmonically confined interacting particles [168–171].

2.5.3 General idea of the MCTDHF method

Before we consider the mathematical details, let us shortly highlight the beautiful idea underlying the MCTDHF method. To this end, consider again the full configuration interaction expansion taken in Sect. 2.3, where the N -particle wavefunction was expressed in a basis of Slater determinants,

$$|\Psi(t)\rangle = \sum_{1 \leq i_1 < \dots < i_N \leq 2N_b} C_I(t) |\psi_{i_1} \dots \psi_{i_N}\rangle. \quad (2.115)$$

Although it is essentially exact this ansatz is, most of the times, unnecessarily complex as it does not take advantage of the characteristics of the physical problem. It works regardless of whether the Hamiltonian contains N -particle operators or only one-particle operators, or whether the Coulomb interaction is strong or weak, but the

exponential scaling is a high price to pay for this guarantee. The disadvantage becomes particularly vivid if the Hamiltonian consists only of a single-particle operator,

$$\hat{H} = \sum_{i=1}^N \hat{h}(\mathbf{x}_i, t). \quad (2.116)$$

For this scenario, the exact wavefunction is given by a Slater determinant,

$$|\Psi(t)\rangle = |\phi_1(t) \phi_2(t) \cdots \phi_N(t)\rangle, \quad (2.117)$$

where the time-dependent orbitals $|\phi_k(t)\rangle$ satisfy the single-particle Schrödinger equation,

$$i \frac{\partial}{\partial t} |\phi_k(t)\rangle = \hat{h}(t) |\phi_k(t)\rangle, \quad (2.118)$$

with appropriate initial conditions. The full CI method would proceed here by constructing the complete Hilbert space of size $\binom{2N_b}{N}$ —which can be huge—and then employ the whole basis to represent the single determinant (2.117).

In contrast, the MCTDHF ansatz uses a set of *time-dependent* Slater determinants,

$$|\Psi(t)\rangle = \sum_{1 \leq i_1 < \dots < i_N \leq 2M} C_I(t) |\phi_{i_1}(t) \cdots \phi_{i_N}(t)\rangle, \quad (2.119)$$

which inherit their time-dependence from the orbitals. Note that the indices of the time-dependent orbitals extend only up to the number $2M$, which is usually much smaller than the number of time-independent basis functions $2N_b$ in the full CI expansion. Consequently, also the Slater determinant basis is considerably reduced to $\binom{2M}{N}$ which allows a larger number of particles to be treated. Even more convenient is that the number of spatial orbitals M provides the chance to adjust the accuracy of the wavefunction. One thereby usually starts with the single determinant obtained for $M = N/2$ and, if possible, increases M until convergence is obtained. For $M \rightarrow \infty$, one essentially recovers the exact result. Figure 11 illustrates the difference between the CI and MCTDHF approach again in a graphical way.

For the previous one-particle Hamiltonian example, a single determinant is sufficient to obtain the exact result. Therefore, the MCTDHF method converges already at the lowest possible choice of M and requires an effort which is identical to the solution of Eq. (2.118). Further, for the more realistic scenario of weakly interacting particles, one often obtains a convergence for small M . In both cases, the MCTDHF method is able to recognize and exploit the uncorrelated or weakly-correlated nature of the wavefunction. The full CI method does not offer a similar feature, and, hence, requires a significantly higher effort.

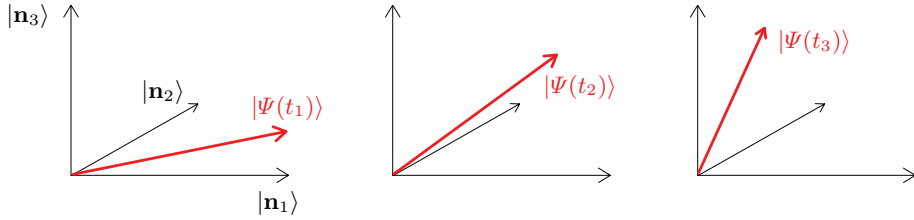
2.5.4 Different levels of MCTDHF approximations

The multiconfigurational time-dependent Hartree-Fock ansatz, Eq. (2.119),

$$|\Psi(t)\rangle = \sum_I C_I(t) |\phi_{i_1}(t) \cdots \phi_{i_N}(t)\rangle, \quad (2.120)$$

is determined by two sets of variational parameters, the wavefunction coefficients $\{C_I(t)\}$ and the time-dependent orbitals $\{|\phi_i(t)\rangle\}$. The coefficients are complex numbers which label the occupation of the determinants in a time-dependent full CI space. The orbitals are elements of a single-particle Hilbert space which, for electrons, consists of a spatial and a two-dimensional spin space. Various choices are possible for the variation of the orbitals, which are discussed in the following.

Configuration interaction



Multiconfigurational time-dependent Hartree-Fock

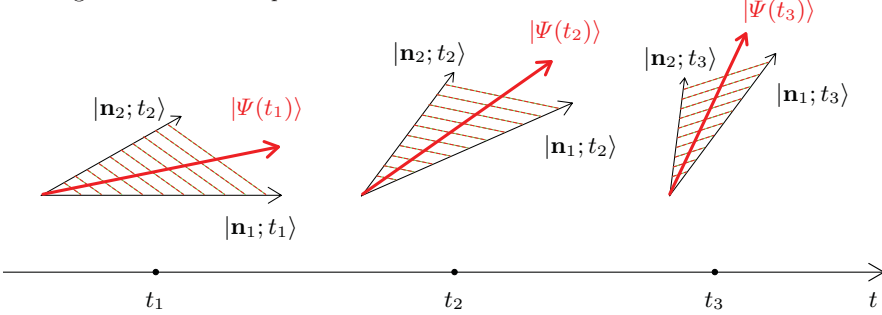


Fig. 11. Illustration of the idea underlying the multiconfigurational time-dependent Hartree-Fock theory. Whereas in CI, the wavefunction $|\Psi(t)\rangle$ is expanded in a static Slater determinant basis set, in MCTDHF the determinants vary in time in order to provide an adequate representation of the wavefunction with a reduced number of determinants.

Generally, a greater variational freedom leads to a better approximation of the wavefunction. However, it is often convenient to restrict the form of the orbitals and accept a slightly less accurate representation, as the wavefunction thereby becomes able to satisfy certain symmetry requirements⁶. Furthermore, as the variational space is smaller, the solution of the corresponding equations of motion is usually simplified.

- *Spinor.* The most general ansatz to the orbitals consists of a spinor

$$\phi(\mathbf{x}, t) = \phi_\alpha(\mathbf{r}, t) \alpha(m_S) + \phi_\beta(\mathbf{r}, t) \beta(m_S). \quad (2.121)$$

Beside the exchange symmetry, determinants constructed from spinors in general exhibit no further symmetry.

- *Spin-unrestricted.* The spin-unrestricted ansatz is given by

$$\phi(\mathbf{x}, t) = \phi_\sigma(\mathbf{r}, t) \sigma(m_S), \quad (2.122)$$

where $\sigma \in \{\alpha, \beta\}$. The spin-functions are restricted to spin-eigenfunctions, but the spatial orbitals may differ for different spin projection. Determinants using this kind of orbitals are eigenfunctions of the spin projection operator \hat{S}_z .

- *Spin-restricted.* In the spin-restricted ansatz, orbitals belonging to different spin projections are identical, i.e., $\phi_\alpha(\mathbf{r}) = \phi_\beta(\mathbf{r}) = \phi(\mathbf{r})$, and the corresponding spin-orbitals read

$$\phi(\mathbf{x}, t) = \phi(\mathbf{r}, t) \sigma(m_S). \quad (2.123)$$

⁶ This fact is sometimes termed *symmetry dilemma*, and its earliest formulation is attributed to Löwdin [172].

Determinants constructed with them are eigenfunctions of \hat{S}_z , and, in case one considers a closed-shell or spin-polarized determinant, also eigenfunction of the total spin \hat{S}^2 .

- *Angular momentum-restricted.* One can further impose restrictions onto the spatial part of the orbitals. A common choice for atoms is to fix the angular part and retain as variational parameter only the radial wavefunction, which can depend either on the quantum numbers (l, m) ,

$$\phi(\mathbf{x}, t) = R_{lm}(r, t) Y_{lm}(\theta, \phi) \sigma(m_S), \quad (2.124)$$

or only on l ,

$$\phi(\mathbf{x}, t) = R_l(r, t) Y_{lm}(\theta, \phi) \sigma(m_S). \quad (2.125)$$

In the latter ansatz, it is further assumed that the radial parts of all orbitals in an atomic shell are identical. The corresponding determinants are eigenfunctions of \hat{S}_z , of \hat{S}^2 in the closed-shell case, and of the angular momentum projection \hat{L}_z .

Further choices are possible, but are not relevant for this work. In addition to the functional form, it is also important whether the orbitals are orthogonal to each other or whether they are allowed to be non-orthogonal, which has a major impact on the way the wavefunction can be represented. Here, we mainly focus on the orthogonal spin-restricted ansatz and occasionally also on the spin-unrestricted ansatz. A comparison between the two is given at the end of the present section for the example of the dissociation of molecular hydrogen. The angular momentum-restricted variant has been implemented on the time-independent Hartree-Fock level, in order to serve as an orbital generator for the TD-RASCI scheme.

2.5.5 Ansatzes used in this work

In this work, we consider both the spin-restricted and spin-unrestricted ansatz. As particles with different spin projection are essentially distinguishable for the spin-free Hamiltonian (1.2), the Slater determinants can be conveniently set up in terms of products of so-called *spin strings* $|I_\sigma\rangle$, which are Slater determinants comprising the orbitals of σ -spin [59]. In the spin-restricted case, the MCTDHF wavefunction is thus given by

$$|\Psi\rangle = \sum_{I_\alpha I_\beta} C_{I_\alpha I_\beta}(t) |\phi_{i_{\alpha,1}}(t) \cdots \phi_{i_{\alpha,N_\alpha}}(t)\rangle |\phi_{i_{\beta,1}}(t) \cdots \phi_{i_{\beta,N_\beta}}(t)\rangle, \quad (2.126)$$

which we also simply write as

$$|\Psi\rangle = \sum_{I_\alpha I_\beta} C_{I_\alpha I_\beta}(t) |I_\alpha\rangle |I_\beta\rangle = \sum_I C_I(t) |I\rangle. \quad (2.127)$$

The sum runs over all Slater determinants constructed from N_α particles with α -spin, N_β particles with β -spin, and M spatial orbitals. Their number is $\binom{M}{N_\alpha} \binom{M}{N_\beta}$. The spin-restricted wavefunction presents a rather general ansatz, which includes several special cases encountered in the quantum-chemical literature. For example, on the Hartree-Fock level, it is easy to treat spin-polarized, closed-shell and open-shell systems simply by adjusting the particle numbers N_α and N_β . In particular, there is no need to explicitly distinguish between methods such as spin-restricted Hartree-Fock

and restricted open-shell Hartree-Fock⁷. Further, by increasing the number of time-dependent orbitals M , one can adjust the number of Slater determinants and thus account for the correlation between particles. In the limit $M \rightarrow \infty$, the wavefunction essentially becomes exact.

The spin-unrestricted MCTDHF wavefunction looks very similar,

$$\begin{aligned} |\Psi\rangle &= \sum_{I_\alpha J_\beta} C_{I_\alpha I_\beta}(t) |\phi_{\alpha,i_{\alpha,1}}(t) \cdots \phi_{\alpha,i_{\alpha,N_\alpha}}(t) \phi_{\beta,i_{\beta,1}}(t) \cdots \phi_{\beta,i_{\beta,N_\beta}}(t)\rangle \\ &= \sum_{I_\alpha I_\beta} C_{I_\alpha I_\beta}(t) |I_\alpha I_\beta\rangle = \sum_I C_I(t) |I\rangle, \end{aligned} \quad (2.128)$$

except that the spin-strings are constructed from different orbital sets $\{|\phi_{\alpha,k}\rangle\}$ and $\{|\phi_{\beta,k}\rangle\}$ of size M_α and M_β , respectively. The dimension of the Slater determinant basis is correspondingly given by $\binom{M_\alpha}{N_\alpha} \binom{M_\beta}{N_\beta}$. The numbers M_α and M_β of time-dependent orbitals can be adjusted to treat the two spin projections with different accuracy. For an example, consider the lithium atom in its $1s^2 2s$ ground state. Here, it is sufficient to choose $M_\beta = 1$, which represents the single β -electron exactly. On the other hand, $M_\alpha \geq 2$ can be chosen to appropriately account for the correlation between the α -electrons, as well as to provide an accurate potential energy surface for the β -electron.

2.5.6 Spin-restricted MCTDHF equations

For the derivation of the spin-restricted MCTDHF equations, we start from the ansatz (2.126) and employ the Lagrange formulation of the time-dependent variational principle, which requires a minimization of the action functional [97, 109],

$$\begin{aligned} S &= S[\{C_I(t)\}, \{|\phi_p(t)\rangle\}] \\ &= \int dt \left\{ \langle \Psi | \hat{H}(t) - i \frac{\partial}{\partial t} | \Psi \rangle - \sum_{kl} \mu_{kl}(t) (\langle \phi_k | \phi_l \rangle - \delta_{kl}) \right\}, \end{aligned} \quad (2.129)$$

with respect to the variational parameters (2.126). The Lagrange multipliers $\mu_{kl}(t)$ are introduced in order to allow only for orthonormal time-dependent orbitals. In the following, we perform the minimization separately, starting with the equation of motion for the orbitals.

Orbital equation. For the derivation of the orbital equation, it is useful to express the expectation value in the action functional in terms of the reduced density matrices (2.44) and (2.50),

$$\langle \Psi | \hat{H}(t) - i \frac{\partial}{\partial t} | \Psi \rangle = \left\{ \sum_{pq} D_{pq} \left[h_{pq} - \left(i \frac{\partial}{\partial t} \right)_{pq} \right] + \frac{1}{2} \sum_{pqrs} d_{pqrs} g_{pqrs} \right\}. \quad (2.130)$$

Note that in addition to the single-particle Hamiltonian matrix element h_{pq} and the two-electron integrals g_{pqrs} , we introduced the matrix element of the time-derivative

⁷ The difference arises because in quantum chemistry these Hartree-Fock methods are usually formulated as *orbital* theories, which hardly ever deal with the underlying configuration [119]. In MCTDHF, on the other hand, one has the opportunity to first determine the form of the wavefunction, and then let the algorithm find the appropriate, optimized orbitals.

operator, which can be considered a unitary operator as long as the orbitals remain normalized [97],

$$\left(i \frac{\partial}{\partial t} \right)_{pq} = i \int d\mathbf{x} \phi_p^*(\mathbf{x}, t) \frac{\partial}{\partial t} \phi_q(\mathbf{x}, t). \quad (2.131)$$

Taking the functional derivative with respect to the orbitals and setting it equal to zero leads to

$$\begin{aligned} 0 &\equiv \frac{\delta}{\delta \langle \phi_p |} S \left[\{C_I(t)\}, \{|\phi_p(t)\rangle\} \right] \\ &= \left\{ \sum_q D_{pq} \left[\hat{h}(t) - i \frac{\partial}{\partial t} \right] |\phi_q\rangle + \sum_{qrs} d_{pqrs} \hat{g}_{rs} |\phi_q\rangle \right\} - \sum_m \mu_{pm}(t) |\phi_m\rangle, \end{aligned} \quad (2.132)$$

where we made use of the symmetries of the two-particle density matrix and the two-electron integrals. Moreover, we introduced the mean-field integrals \hat{g}_{rs} given in coordinate representation by

$$g_{rs}(\mathbf{r}) = \int d\bar{\mathbf{r}} \phi_r^*(\bar{\mathbf{r}}) \frac{1}{|\mathbf{r} - \bar{\mathbf{r}}|} \phi_s(\bar{\mathbf{r}}). \quad (2.133)$$

Particularly in the quantum chemistry literature, the quantities $g_{rs}(\mathbf{r})$ are also called Coulomb-integrals (for $r = s$) and exchange-integrals (for $r \neq s$). It is further important to realize that, due to the orthonormality of the orbitals, the derivative of the density matrices with respect to the orbitals vanishes. This is not anymore the case for a non-orthogonal basis set, see Ref. [173]. From Eq. (2.132), it is easy to solve for the Lagrange multipliers,

$$\mu_{pm}(t) = \sum_q D_{pq} \left\langle \phi_m \left| \hat{h}(t) - i \frac{\partial}{\partial t} \right| \phi_q \right\rangle + \sum_{qrs} d_{pqrs} \langle \phi_m | \hat{g}_{rs} | \phi_q \rangle. \quad (2.134)$$

Reinsertion of the Lagrange multipliers into Eq. (2.132) yields

$$0 = \hat{\mathbf{P}} \left\{ \sum_q D_{pq} \left[\hat{h}(t) - i \frac{\partial}{\partial t} \right] |\phi_q\rangle + \sum_{qrs} d_{pqrs} \hat{g}_{rs} |\phi_q\rangle \right\}, \quad (2.135)$$

where we introduced the projection operator

$$\hat{\mathbf{P}} = \mathbf{1} - \sum_m |\phi_m\rangle \langle \phi_m|, \quad (2.136)$$

which projects onto the orthogonal complement of the subspace spanned by the orbitals $|\phi_m\rangle$. Solving for the term with the time-derivative, multiplying by $(\mathbf{D}^{-1})_{np}$ and summing over p yields

$$i \hat{\mathbf{P}} \frac{\partial}{\partial t} |\phi_n\rangle = \hat{\mathbf{P}} \left\{ \hat{h}(t) |\phi_n\rangle + \sum_{pqrs} (\mathbf{D}^{-1})_{np} d_{pqrs} \hat{g}_{rs} |\phi_q\rangle \right\}. \quad (2.137)$$

Due to the projection operator $\hat{\mathbf{P}}$ appearing on both sides, equation (2.137) is an integro-differential equation the solution of which can be cumbersome.

In order to obtain equations which are numerically more appropriate, one can apply a unitary transformation to the orbitals in order to satisfy [154]

$$\langle \phi_p | i \frac{\partial}{\partial t} |\phi_q\rangle \equiv \langle \phi_p | \hat{Q}(t) |\phi_q\rangle, \quad (2.138)$$

where $\hat{Q}(t)$ is an arbitrary time-dependent hermitian operator. This transformation is valid due to the invariance of the MCTDHF wavefunction under unitary transformations, which is considered later in Sect. 3.2.6. Briefly, we will see there that for any rotation of the orbitals, a corresponding rotation of the expansion coefficients exists such that the wavefunction remains identical. The variational space is therefore invariant under unitary transformations of the orbitals, and the MCTDHF equations give exactly the same result for any hermitian operator $\hat{Q}(t)$.

By application to Eq. (2.137), the projection operator on the left-hand side vanishes and one immediately obtains the *spin-restricted orbital equations*

$$i \frac{\partial}{\partial t} |\phi_n\rangle = \hat{Q}(t) |\phi_n\rangle + \hat{\mathbf{P}} \left\{ (\hat{h}(t) - \hat{Q}(t)) |\phi_n\rangle + \sum_{pqrs} (\mathbf{D}^{-1})_{np} d_{pqrs} \hat{g}_{rs} |\phi_q\rangle \right\}. \quad (2.139)$$

They constitute a set of first-order differential equations for the time-dependence of the M MCTDHF orbitals. Reasonable choices for the constraint operator $\hat{Q}(t)$ are considered below.

Coefficient equation. For the coefficient equation, the derivative with respect to the expansion coefficients is set equal to zero. Therefore, we insert the MCTDHF expansion (2.126) into the action functional to obtain a form which explicitly depends on the coefficients,

$$\langle \Psi | \hat{H}(t) - i \frac{\partial}{\partial t} | \Psi \rangle = \sum_{IJ} C_I^*(t) C_J(t) \langle I | \hat{H}(t) - i \frac{\partial}{\partial t} | J \rangle. \quad (2.140)$$

The functional derivative then directly yields

$$\begin{aligned} 0 &\equiv \frac{\delta}{\delta C_I^*} S[\{C_J\}, \{|\phi_p\rangle\}] \\ &= -i \frac{\partial C_I(t)}{\partial t} + \sum_J C_J(t) \langle I | \hat{H}(t) - i \frac{\partial}{\partial t} | J \rangle. \end{aligned} \quad (2.141)$$

With the property (2.138), the time-derivative of the Slater determinants can be expressed in terms of the gauge operator $\hat{Q}(t)$, and one arrives at the MCTDHF *coefficient equation*,

$$i \frac{\partial}{\partial t} C_I(t) = \sum_J \langle I | \hat{H}(t) - \hat{Q}(t) | J \rangle C_J(t), \quad (2.142)$$

which is just the TD-FCI equation in the basis of the time-dependent Slater determinants. The operator $\hat{Q}(t)$ arises here in order to compensate for the unitary transformation in the orbital equation.

Working equations. In practical calculations, one further needs to specify the constraint operator $\hat{Q}(t)$. In principle, any hermitian operator is possible and leads to identical results, but the actual choice can affect the numerical behavior. Most of the time, we consider the case $\hat{Q}(t) = 0$, which leads to the form of the MCTDHF equations used throughout this work,

$$i \frac{\partial}{\partial t} C_I(t) = \sum_J \langle I | \hat{H}(t) | J \rangle C_J(t), \quad (2.143)$$

$$i \frac{\partial}{\partial t} |\phi_n\rangle = \hat{\mathbf{P}} \left\{ \hat{h}(t) |\phi_n\rangle + \sum_{pqrs} (\mathbf{D}^{-1})_{np} d_{pqrs} \hat{g}_{rs} |\phi_q\rangle \right\}. \quad (2.144)$$

As induced by the projection operator, the orbitals remain constant as long as there are only rotations in the orbital space involved. Instead, these rotations are processed by variation of the wavefunction coefficients. A time-dependence of the orbitals arises only if a substantial modification of the orbital space is required.

Another choice is to set the constraint operator equal to the single-particle Hamiltonian, $\hat{Q}(t) = \hat{h}(t)$, which is similar to the quantum-mechanical interaction picture. Changes implied by the single-particle term are then processed by the orbitals. Furthermore, it is possible to choose a constraint such that the time-dependent orbitals are the natural orbitals of the system, i.e., the set of orbitals which diagonalize the single-particle density matrix, see Ref. [88].

In general, different formulations of the MCTDHF equations lead to different numerical performance. The particular choice $\hat{Q}(t) = 0$ is expected to perform favorably if the solution of the orbital equation is the numerically most expensive part, which is the case in this work. This has been confirmed in our test calculations for helium, which showed that the propagation for $\hat{Q}(t) = \hat{h}(t)$ is roughly 10% slower [109].

Alternative formulation of the orbital equation. Out of the many possible alternative formulations of the orbital equation, we further state one which resembles the Fock equation known from classic time-dependent Hartree-Fock theory. For this, the whole right-hand side of Eq. (2.144) is combined to

$$i \frac{\partial}{\partial t} |\phi_n\rangle = \hat{\mathbf{P}} \sum_q \hat{M}_{nq} |\phi_q\rangle, \quad (2.145)$$

where the non-linear operator \hat{M}_{nq} is given by

$$\hat{M}_{nq} = \delta_{nq} \hat{h} + \sum_{prs} (\mathbf{D}^{-1})_{np} d_{pqrs} \hat{g}_{rs}. \quad (2.146)$$

The formulation (2.145) can be useful for the numerical solution, because its linear-like structure allows for the application of the Lanczos or Crank-Nicolson propagator 3.6). However, as it is still a non-linear equation, one must be careful in the adjustment of the step-size.

Inversion of the density matrix. In principle, the inversion of the single-particle density matrix can be a problematic step, because it is not guaranteed to be non-singular. In fact, the density matrix is positive *semi*-definite, meaning that its eigenvalues $d_k(t)$ —the occupation of the natural orbitals—may also attain zero. The corresponding density matrix in natural orbital representation,

$$\mathbf{D}_{\text{NO}}(t) = \begin{pmatrix} d_1(t) & & & \\ & d_2(t) & & \\ & & \ddots & \\ & & & d_M(t) \end{pmatrix}, \quad (2.147)$$

is then not of full rank and hence not invertible. The practical solution to this problem is to alter a general density matrix $\mathbf{D}(t)$ according to [151]

$$\mathbf{D}(t) \rightarrow \mathbf{D}(t) + \varepsilon \exp\left(\frac{1}{\varepsilon} \mathbf{D}(t)\right), \quad (2.148)$$

where ε is a small number, say of the order 10^{-10} . This ensures that the density matrix is positive definite and the inverse can be formed. As the regularization affects only the unoccupied orbitals, and these only marginally, it has no practically relevant influence on the results of the MCTDHF propagation.

2.5.7 Spin-unrestricted MCTDHF equations

In a similar way as before, one arrives at the equations of motion for the variational parameters of the spin-unrestricted MCTDHF ansatz. The only difference is that one has to deal with an action functional that depends on two sets of time-dependent orbitals, one for α -spin and one for β -spin,

$$\begin{aligned} S &= S[\{C_I(t)\}, \{|\phi_{p\alpha}(t)\rangle\}, \{|\phi_{p\beta}(t)\rangle\}] \\ &= \int dt \left\{ \langle \Psi | \hat{H} - i \frac{\partial}{\partial t} | \Psi \rangle - \sum_{kl,\sigma} \mu_{kl,\sigma}(t) (\langle \phi_{k\sigma} | \phi_{l\sigma} \rangle - \delta_{kl}) \right\}. \end{aligned} \quad (2.149)$$

In the spin-unrestricted case, the orthogonality constraint must be imposed only among orbitals with identical spin, since α - and β -spin-orbitals are already orthogonal, $\langle \phi_{k\alpha} | \phi_{l\beta} \rangle = 0$. The expectation value can be expressed through the spin-resolved density matrices and electron integrals introduced in Sect. 2.1,

$$\langle \Psi | \hat{H} - i \frac{\partial}{\partial t} | \Psi \rangle = \sum_{pq,\sigma} D_{pq}^\sigma \left[h_{pq}^\sigma - \left(i \frac{\partial}{\partial t} \right)_{pq}^\sigma \right] + \sum_{pqrs,\sigma\tau} d_{pqrs}^{\sigma\tau} g_{pqrs}^{\sigma\tau}. \quad (2.150)$$

From here, the derivation proceeds in an analogous way as in the spin-restricted case and leads to the *spin-unrestricted orbital equations*,

$$i \frac{\partial}{\partial t} |\phi_{n\alpha}\rangle = \hat{\mathbf{P}}^\alpha \left\{ \hat{h}(t) |\phi_{n\alpha}\rangle + \sum_{pqrs,\tau} [(\mathbf{D}^\alpha)^{-1}]_{np} d_{pqrs}^{\alpha\tau} \hat{g}_{rs}^\tau |\phi_{q\alpha}\rangle \right\}, \quad (2.151)$$

$$i \frac{\partial}{\partial t} |\phi_{n\beta}\rangle = \hat{\mathbf{P}}^\beta \left\{ \hat{h}(t) |\phi_{n\beta}\rangle + \sum_{pqrs,\tau} [(\mathbf{D}^\beta)^{-1}]_{np} d_{pqrs}^{\beta\tau} \hat{g}_{rs}^\tau |\phi_{q\beta}\rangle \right\}, \quad (2.152)$$

and the coefficient equation,

$$i \frac{\partial}{\partial t} C_{I_\alpha I_\beta}(t) = \sum_{J_\alpha J_\beta} \langle I_\alpha I_\beta | \hat{H}(t) | J_\alpha J_\beta \rangle C_{J_\alpha J_\beta}(t), \quad (2.153)$$

where, for convenience, we set both constraint operators $\hat{Q}^\alpha(t)$ and $\hat{Q}^\beta(t)$ equal to zero. The spin-unrestricted MCTDHF equations have, to our knowledge, not been published in the literature in this explicit formulation.

2.5.8 Limiting cases

The two limiting cases of the MCTDHF formalism are time-dependent full configuration interaction and time-dependent Hartree-Fock theory. The first one, TD-FCI, is obtained by setting $M = N_b$. The projection operator $\hat{\mathbf{P}} = \mathbf{1} - \sum_m |\phi_m\rangle\langle\phi_m|$ in

the orbital equation then vanishes in the space spanned by the single-particle basis, and one obtains

$$i \frac{\partial}{\partial t} C_I(t) = \sum_J \langle I | \hat{H}(t) - \hat{Q}(t) | J \rangle C_J(t), \quad (2.154)$$

$$i \frac{\partial}{\partial t} |\phi_n(t)\rangle = \hat{Q}(t) |\phi_n(t)\rangle. \quad (2.155)$$

These are the time-dependent full configuration interaction equations in a representation induced by the constraint operator $\hat{Q}(t)$. By setting $\hat{Q}(t) = 0$, one immediately recovers the TD-FCI equation (2.60), whereas the choice $\hat{Q}(t) = \hat{h}_0$ yields the equations of motion corresponding to the Dirac picture.

The other limit, TD-HF, is arrived if the determinant basis is comprised of only a single determinant, which is obtained for $M = N/2$ and $N_\alpha = N_\beta$ in the spin-restricted case, and for $M_\alpha = N_\alpha$ and $M_\beta = N_\beta$ in the spin-unrestricted case. We consider only the spin-restricted case in the following. For a single determinant, the two-particle density matrix is related to the single-particle density matrix by [59]

$$d_{pqrs} = D_{pq} D_{rs} - \frac{1}{2} D_{ps} D_{qr}. \quad (2.156)$$

Insertion into the orbital equation readily leads to

$$i \frac{\partial}{\partial t} |\phi_n\rangle = \hat{\mathbf{P}} \left\{ \hat{h}(t) |\phi_n\rangle + \sum_{rs} D_{rs} \hat{g}_{rs} |\phi_n\rangle - \frac{1}{2} \sum_{rq} D_{qr} \hat{g}_{rn} |\phi_q\rangle \right\}, \quad (2.157)$$

and, by further using the diagonal representation of the density matrix in Hartree-Fock orbitals for a closed-shell system, $D_{ij} = 2\delta_{ij}$, to

$$i \frac{\partial}{\partial t} |\phi_n\rangle = \hat{\mathbf{P}} \left\{ \hat{h}(t) |\phi_n\rangle + \sum_r 2 \hat{g}_{rr} |\phi_n\rangle - \sum_r \hat{g}_{rn} |\phi_r\rangle \right\}. \quad (2.158)$$

This differs from the usual Hartree-Fock equation only in the projection operator, which, however, can be transformed away by choosing the constraint operator equal to Fock operator (which is the operator acting in curly brackets). This results in the time-dependent Hartree-Fock equations,

$$i \frac{\partial}{\partial t} |\phi_n\rangle = (\hat{h}(t) + \sum_r 2 \hat{g}_{rr}) |\phi_n\rangle - \sum_r \hat{g}_{rn} |\phi_r\rangle, \quad (2.159)$$

as given, for instance, in Ref. [174].

2.5.9 Comparison of spin-restricted and spin-unrestricted treatments

At the end of this section, we briefly discuss the properties and differences of the spin-restricted and spin-unrestricted MCTDHF approaches. For this purpose, we consider the example of the hydrogen molecule and focus on the question, whether the different MCTDHF approximations are *size-consistent*, i.e., whether for increasing distance R of the hydrogen nuclei the ideal energy of $E(H_2) = 2E(H) = -1 \text{ Ha}$ is approached. For the single-determinant Hartree-Fock scheme, a similar but more detailed analysis is given in Ref. [119].

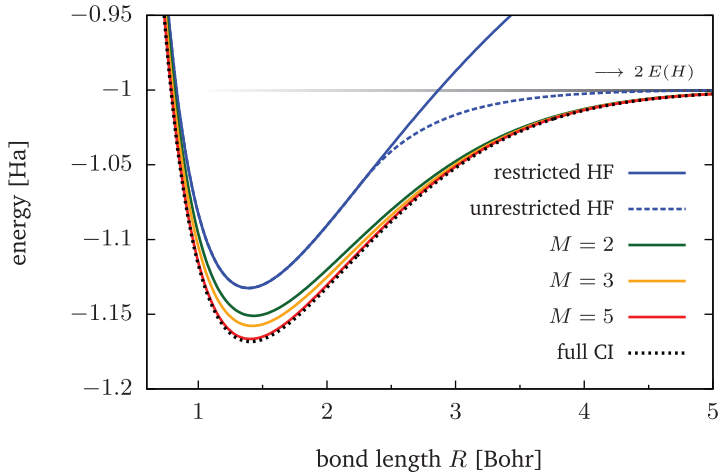


Fig. 12. Energy of the hydrogen molecule plotted against the distance R of the nuclei. In contrast to the spin-restricted Hartree-Fock calculations, the spin-unrestricted HF results is able to model the dissociation limit of two separated hydrogen atoms. For larger numbers of MCTDHF orbitals M , restricted and unrestricted approximations yield the same results and with increasing M converge against the full CI solution. The calculations use a 6-31 G^{**} Gaussian basis set.

In Fig. 12, we plot the energies of the hydrogen molecule against the bond length R . The calculations have been carried out with a 6-31 G^{**} Gaussian basis set of size $N_b = 12$ [175]. One notices that the spin-restricted Hartree-Fock result does not yield the correct result of $2E(H)$ in the dissociation limit. This well-known fact is caused by the use of a single orbital and implies that spin-restricted Hartree-Fock is not size-consistent. In contrast, due to its larger variational freedom, the spin-unrestricted approach is able to recover the correct qualitative behavior and also the correct dissociation energy. It fails, however, to reproduce the exact form of the wavefunction, which is a singlet, and instead leads to an unrestricted determinant which is not a spin eigenfunction. This drawback is cured by the more accurate MCTDHF wavefunctions, which all exhibit a similar convergence behavior. The spin-unrestricted calculations converged against the restricted result for any of the random initial states we have examined. With increasing number of orbitals M , the energies tend against the full CI result depicted by the dotted curve. The $M = 5$ result already agrees well with the reference and predicts a bond length of $R = 1.405$ Bohr, which comes perfectly close to the exact value of $R = 1.398$ Bohr [176].

The agreement of the spin-restricted and spin-unrestricted approaches is caused by the simple structure of the wavefunction. For more complex systems, and particularly if the number of α - and β -electrons differs, the unrestricted ansatz can be expected to be more accurate and show similar advantages as for the single-determinant Hartree-Fock results in the example.

3 Numerical implementation of MCTDHF and RASCI

The present section summarizes the two employed numerical methods—MCTDHF and TD-RASCI. In the following, we present the main ideas underlying their implementation: we begin with the introduction of appropriate basis sets for describing photoionization in section 3.1 and the related transformation routines in section 3.2. Sections 3.3 and 3.4 cover the representation of Slater determinants and the solution

of the configuration interaction equations, while Sect. 3.5 deals with the solution of the MCTDHF orbital equation. The applied time-stepping algorithms are summarized in Sect. 3.6, and Sect. 3.7 collects several methods for the analysis of the wavefunction. Finally, the closing Sect. 3.10 gives an overview of the structure of the MCTDHF code.

3.1 Basis sets

For exactly solvable problems in quantum mechanics, the wavefunction can be completely specified in the form of analytical functions. For the majority of only numerically accessible systems, however, one needs to represent the wavefunction in terms of known functions, which is most often accomplished by a linear expansion of the form

$$|\phi(t)\rangle = \sum_j c_j(t) |\psi_j\rangle. \quad (3.1)$$

Such a representation is exact if the basis functions $\{|\psi_j\rangle\}$ form a complete system and thus span the full single-particle Hilbert space. In numerical applications, one is naturally restricted to a finite basis and Eq. (3.1) presents an approximation, the quality of which crucially depends on the size of the basis and on the actual choice for the $\{|\psi_j\rangle\}$.

As shown in Sect. 2.1.4, by introduction of a basis, operators get mapped onto discrete matrices termed *electron integrals*. Of special importance are the one-electron Hamiltonian matrix elements,

$$h_{pq}(t) = \int \psi_p^*(\mathbf{r}) \left\{ -\frac{1}{2} \nabla^2 + v(\mathbf{r}) + \hat{v}_{\text{em}}(t) \right\} \psi_q(\mathbf{r}) d\mathbf{r}, \quad (3.2)$$

which are hermitian, $h_{pq} = h_{qp}^*$, and the *two-electron integrals*,

$$g_{pqrs} = \int \psi_p^*(\mathbf{r}) \psi_q(\mathbf{r}) \frac{1}{|\mathbf{r} - \mathbf{r}'|} \psi_r^*(\mathbf{r}') \psi_s(\mathbf{r}') d\mathbf{r} d\mathbf{r}'. \quad (3.3)$$

It is of great relevance for the practical use of a basis set that these integrals can be calculated efficiently. Especially the two-electron integrals constitute a bottleneck in many applications, since their calculation and storage, in general, requires an effort that scales as $\mathcal{O}(N_b^4)$. For the present work, which is dealing with large basis sizes N_b in order to adequately describe the continuum states, it is therefore of major importance to utilize basis sets which offer an improved scaling behavior.

In the following, we collect the basis sets implemented and used in this work, and particularly discuss their application as well as strengths and weaknesses for the treatment of photoionization processes. The electron integrals and further details of most of the presented basis sets are given in appendix B.

3.1.1 Gaussian- and Slater-type orbitals

Two kinds of basis sets are most prominent in quantum chemistry, *Slater-type orbitals* (STOs) and *Gaussian-type orbitals* (GTOs). Slater-type orbitals are defined by

$$\psi_{nlm\zeta}^{\text{STO}}(\mathbf{r}) = N_{n,\zeta} r^{n-1} e^{-\zeta r} Y_{lm}(\theta, \varphi), \quad (3.4)$$

where $N_{n,\zeta}$ denotes a normalization factor. They were introduced by Slater in 1930 as an alternative to exact hydrogen-like eigenfunctions which allow for a simplified evaluation of the electron integrals [177]. STOs exhibit the correct asymptotic behavior

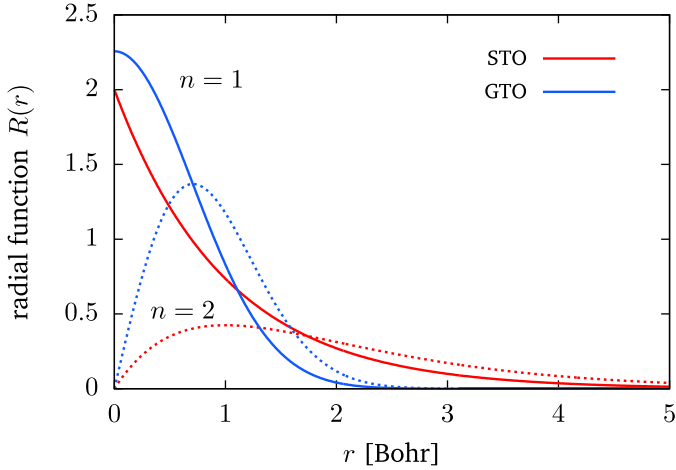


Fig. 13. Radial parts of Slater- and Gaussian-type orbitals for the main quantum number $n = 1$ (solid curves) and $n = 2$ (dotted curves) and for exponents $\zeta = 1$, $\alpha = 1$, respectively.

and also satisfy the cusp condition at the position of the nuclei [178]. Unlike the common hydrogenic orbitals, they have no radial nodes and are therefore not orthogonal. In a typical quantum chemical calculation, a chosen number of STOs is placed at the atomic centers in order to model the electrons localized there. As the calculation of three- and four-center two-electron integrals occurring in general molecules cannot be performed analytically, STOs are primarily used in atomic or diatomic calculations when high accuracy is required [137].

Gaussian-type orbitals have been introduced by Boys in 1950 [179] and are given by

$$\psi_{nlm\alpha}^{\text{GTO}}(\mathbf{r}) = N_{n,\alpha} r^{n-1} e^{-\alpha r^2} Y_{lm}(\theta, \varphi). \quad (3.5)$$

They differ from STOs only in the exponent and the normalization constant $N_{n,\alpha}$. GTOs are non-orthogonal as well and also possess a nodeless radial part, but neither satisfy the correct asymptotic behavior nor the cusp condition. Therefore, a larger number of GTOs is usually required as compared to STOs to obtain a similar accuracy. The principal reason for nevertheless using GTOs is given by the Gaussian product theorem, which allows for the reduction of the general four-center two-electron integral to a two-center integral and by this for a tremendous simplification. For a detailed survey on the various types of Gaussian basis sets, their application and the calculation of the electron integrals, we refer to [180]. An online library of orbital coefficients n and α optimized for the use in electronic structure methods can be found in Ref. [175].

Figure 13 illustrates the radial functions of Gaussian- and Slater-type orbitals for the main quantum numbers $n = 1$ and $n = 2$ and exponents $\zeta = 1$ and $\alpha = 1$. Both kinds of orbitals are well localized around the origin of the coordinate system, and tend outwards with increasing main quantum number. From the figure, one immediately notices why GTOs and STOs are not the appropriate choice for describing highly excited or continuum states: the representation of a single plane-wave, for example, would already require a rather large and carefully designed basis set (note, however, that such attempts exist [181]). GTOs and STOs are occasionally used in photoionization studies, but with the focus lying more on bound state excitations of the atom or molecule rather than on the ionization process, see Refs. [161, 182, 183].

3.1.2 Spherical DVR expansion

The accurate description of continuum states requires a basis set which, on the one hand, is flexible in describing general wave packets moving away from the nucleus. On the other hand, it should span an extensive region in coordinate space, such that the wave packet does not hit the boundary during the propagation time. These conditions can be satisfied with a basis set of the form

$$\psi_{nlm}(\mathbf{r}) = \frac{\chi_n(r)}{r} Y_{lm}(\theta, \varphi), \quad (3.6)$$

which is composed of products of radial basis functions χ_n and spherical harmonics Y_{lm} . The use of a spherical coordinate system is an appropriate choice for photoionization studies of atoms, since the wavefunction is often smooth in the angular coordinates⁸. In the radial direction, one requires a basis set which is able to describe the ionizing wavepacket over large distances with constant accuracy. Several alternatives are available for this task, such as B-splines [139, 185], plane waves [186], finite differences [138], finite elements or Sturmian functions [47]. In this work, we employ a *discrete variable representation*, which is briefly outlined in the following.

Discrete variable representation. The discrete variable representation (DVR) has been introduced to quantum physics by Lill et al. [187]. It is a method which constructs, in a very general way, a basis transformation from a finite set of functions to a grid-like representation, in which the representation of any local operator is approximately diagonal. The DVR thus provides two main advantages: first, the construction of the electron integrals is greatly simplified and second, the diagonality often leads to a rather sparse representation of the Hamiltonian matrix.

A discrete variable representation is constructed from a complete set of functions $\{p_k(r)\}$ defined on an interval $[a, b]$ according to the formula

$$\chi_k(r) = \sqrt{w_k} \sum_{n=0}^{N-1} p_n^*(r_k) p_n(r). \quad (3.7)$$

The real quantities r_k and w_k denote the abscissas and weights of an appropriate quadrature rule, which should give an accurate estimation of integrals such as

$$\int_a^b w(r) p_i^*(r) p_j(r) dr = \sum_{k=0}^{N-1} w_k w(r_k) p_i^*(r_k) p_j(r_k), \quad (3.8)$$

where $w(r)$ is a positive weight function. Common choices for the functions $\{p_k(r)\}$ are orthogonal polynomials, sine functions, or the eigenfunctions of a Hermitian operator. One can show that the DVR basis $\{\chi_k(r)\}$ defined in Eq. (3.7) has several convenient properties. Probably the most important one is that local operators $f(r)$, when evaluated with the quadrature rule, possess a diagonal representation,

$$f_{ij} = \langle \chi_i | f(r) | \chi_j \rangle = f(r_i) \delta_{ij}, \quad (3.9)$$

in which the matrix elements are simply given by the function values at the grid points. The DVR therefore resembles a grid defined by the (in general unequally spaced) points r_k . The representation of non-local operators like the kinetic energy

⁸ The reason for this smoothness is that photo-electrons are created predominantly in the vicinity of the origin, and, when moving outwards into the continuum, experience a broadening of the tangential structure [184].

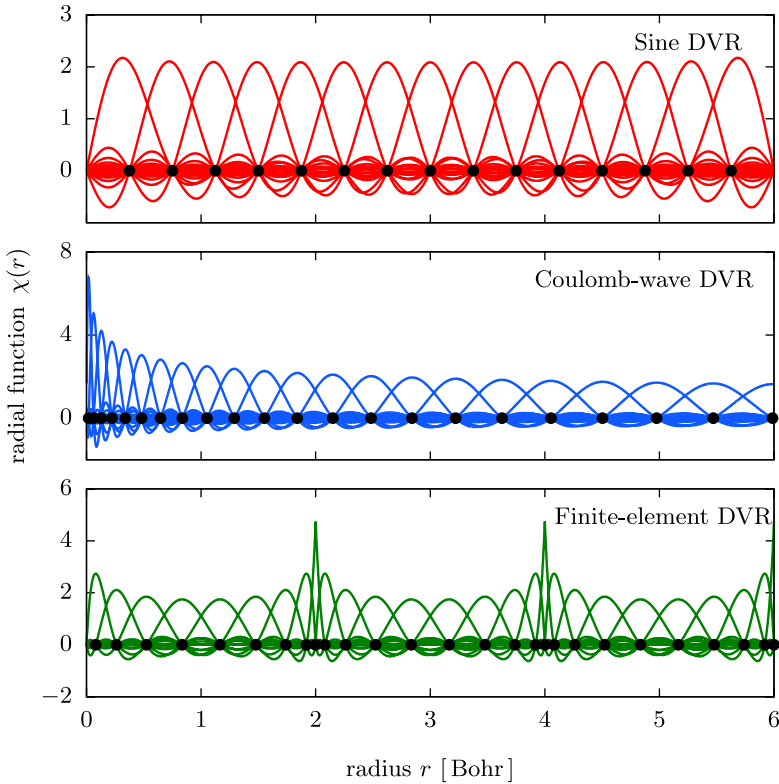


Fig. 14. Illustration of three different discrete variable representation (DVR) basis sets which have been implemented for this work. *Top:* sine DVR constructed over an equally spaced grid. *Middle:* Coulomb-wave DVR with a denser grid near the origin which becomes equally spaced grid in the continuum. *Bottom:* finite-element DVR constructed over a set of Gauss-Lobatto grids. Three finite-elements of length 2 Bohr are depicted.

follows directly from the definition (3.7), and usually leads to full matrices. This differs from the procedure applied in a finite differences approach, where derivatives are approximated by function values on a few adjacent grid points, and is one reason for the increased accuracy of DVR-based approaches.⁹

In Fig. 14, we give a comparison of three DVR basis sets which have been implemented in the course of this work, the sine DVR, the Coulomb-wave DVR (CWDVR), and the finite-element DVR (FEDVR). The intention here is to get a visual impression of these basis sets, while the mathematical details can be found in appendix B. The sine DVR shown at the top of the figure is based on particle-in-a-box eigenfunctions, and has equally spaced abscissas [188]. It has been recently applied in our MCTDHF study on the one-dimensional helium atom [109]. The CWDVR shown in the middle is constructed using the zeros of the positive-energy Coulomb eigenfunctions [189]. The resulting grid is unequally spaced with a more dense distribution near the origin—taking into account the faster oscillations occurring in the vicinity of the core—and a grid spacing that becomes equidistant for large distances. The actual distribution of the grid points can be adjusted through the atomic charge Z , which determines the

⁹ This completely delocalized representation is also encountered when calculating the derivatives with the Fourier transformation. In fact, the special DVR which is obtained by using an equidistant grid is mathematically identical to a discrete Fourier transform [88].

grid-spacing at the origin, and the energy E of the Coulomb wave, which controls the spacing at large distances. In the figure, the CWDVR is depicted for the parameters $Z = 50$ and $E = 2$.

Finite-element discrete variable representation. Finally, the plot at the bottom of Fig. 14 shows the FEDVR basis set which is discussed here more in detail due to its frequent use in this work; again, supplementary material can be found in appendix B. The FEDVR employs a division of the coordinate space in a chosen number of finite elements, where in each element Legendre polynomials are used for the basis functions $\{p_j(r)\}$. For this choice, Eq. (3.7) is a polynomial as well and can be expressed in terms of Lagrange polynomials,

$$\chi_n(r) = \frac{1}{\sqrt{w_n}} \prod_{j \neq n} \frac{r - r_j}{r_n - r_j}, \quad (3.10)$$

where r_n denotes a grid consisting of Gauss-Lobatto abscissas and w_n the corresponding integration weights. A Gauss-Lobatto grid has the property that grid points are placed at the element boundaries. The Lagrange polynomials constructed over such a boundary grid point, the so-called *bridge functions*, have a different normalization than the polynomials in Eq. (3.10), which ensures the continuity of the basis functions across the boundary. The FEDVR basis is highly convenient in describing general functions, and, in addition, offers a great freedom in placing the finite elements. Furthermore, it has the advantage that the representation of derivative operators is given by banded matrices. As will be explained below in Sect. 3.2.4, this is a key property in the solution of the Poisson equation. The FEDVR is therefore used in most parts of this work.

Representation of the two-electron integrals. A great advantage of the spherical DVR basis is the sparse representation of the two-electron integrals, which enables the usage of a large number of basis functions. In the following, we shortly present the results for the two-electron integrals, while the detailed derivation is given in paragraph B.2.2 of the appendix. The calculation proceeds by taking a multipole expansion of the Coulomb interaction, through which the radial and angular coordinates disentangle, and a subsequent integration of the factorized integrals, and leads to

$$G_{k_1 l_1 m_1, k_2 l_2 m_2, k_3 l_3 m_3, k_4 l_4 m_4} = \delta_{k_1 k_2} \delta_{k_3 k_4} \delta_{m_1 - m_2, m_4 - m_3} \\ \times \sum_{l=\max(|l_1 - l_2|, |l_3 - l_4|)}^{\min(l_1 + l_2, l_3 + l_4)} \frac{4\pi}{2l + 1} y_{l_1 m_1, l m_1 - m_2, l_2 m_2} \bar{y}_{l_3 m_3, l m_4 - m_3, l_4 m_4} P_{k_1 k_2, k_3 k_4}^{(l)}. \quad (3.11)$$

The favorable property of this expression is the diagonality with respect to the radial indices k_1, k_2 and k_3, k_4 , respectively, which allows for the usage of large grids. The quantities y and \bar{y} are *Gaunt coefficients* defined as the integral of the product of three spherical harmonics [113],

$$y_{l_1 m_1, l m, l_2 m_2} = \int Y_{l_1 m_1}^*(\Omega) Y_{l m}(\Omega) Y_{l_2 m_2}(\Omega) d\Omega, \quad (3.12)$$

$$\bar{y}_{l_1 m_1, l m, l_2 m_2} = \int Y_{l_1 m_1}^*(\Omega) Y_{l m}^*(\Omega) Y_{l_2 m_2}(\Omega) d\Omega. \quad (3.13)$$

They can be evaluated analytically in terms of Wigner-3j coefficients, see Eq. (B.24) in the appendix. Further, the coefficient $P_{k_1 k_2, k_3 k_4}^{(l)}$ in Eq. (3.11) originates from the

radial integration,

$$P_{k_1 k_2, k_3 k_4}^{(l)} = \int \chi_{k_1}(r) \chi_{k_2}(r) \frac{r_{<}^l}{r_{>}^{l+1}} \chi_{k_3}(r') \chi_{k_4}(r') dr dr', \quad (3.14)$$

with the definitions $r_{<} := \min(r, r')$ and $r_{>} := \max(r, r')$, and its straightforward calculation using the properties of the DVR yields

$$P_{k_1 k_2 k_3 k_4}^{(l)} = \delta_{k_1 k_2} \delta_{k_3 k_4} \frac{\min(r_{k_1}, r_{k_3})^l}{\max(r_{k_1}, r_{k_3})^{l+1}}. \quad (3.15)$$

However, as has been pointed out by McCurdy et al. [190], due to the derivative singularity of the integrand at $r = r'$, Eq. (3.14) is evaluated more accurately by employing the corresponding Poisson equation which, after some algebra, leads to

$$P_{k_1 k_2, k_3 k_4}^{(l)} = \delta_{k_1 k_2} \delta_{k_3 k_4} p_{k_3 k_4}^{(l)}(r_{k_1}). \quad (3.16)$$

The function $p_{k_3 k_4}^{(l)}(r_{k_1})$ is the solution of the radial Poisson equation and is defined in Eq. (B.45) of the appendix. Note again the diagonality of the radial integrals, which is a highly convenient property of the DVR basis. For a very similar application of the Poisson equation, see also Sect. 3.2.4.

3.1.3 Mixed basis set

In the following, we describe an extension of the FEDVR basis which is of major importance for obtaining appropriate initial states in restricted active space calculations. Therefore, let us shortly recapitulate the problem already stated in Sect. 2.4.6: full configuration interaction calculations are invariant under unitary transformations of the single-particle basis, i.e., the discretized subspace of the Hilbert space is the same for a basis set $\{|\psi_k\rangle\}$ as well as for any unitarily transformed set

$$|\tilde{\psi}_j\rangle = \sum_k b_{jk} |\psi_k\rangle. \quad (3.17)$$

The choice of the single-particle basis therefore only depends on numerical considerations, and in general, basis sets leading to a sparse Hamiltonian are preferable. On the other hand, in a restricted active space treatment where only a part of the full CI space is accessible, a unitary transformation of the single-particle basis results in another restricted active space that is not necessarily identical to the original one. This can be seen most easily for the extreme case of a single determinant, where the variation of the orbital basis obviously changes the determinant. As is well known, there exists a unique set of orbitals leading to the best single determinant—in the sense of giving the lowest energy—which is obtained by solving the Hartree-Fock equations. This demonstrates a principle that is generally valid in RAS calculations: the more the restricted space deviates from the full CI space, the better the single-particle basis needs to be adapted in order to give an adequate description of the wavefunction. Therefore, to be confident, RAS calculations are usually carried out in a well-adapted basis, regardless of the accuracy of the many-body space. Typical choices are Hartree-Fock orbitals or the orbitals obtained from a multiconfigurational Hartree-Fock calculation [64, 119].

However, the usability of such optimized basis sets is limited in the treatment of photoionization, because with increasing basis size N_b , the creation and storage of the two-electron integrals in the Hartree-Fock basis becomes a tedious task requiring at

least an effort of $\mathcal{O}(N_b^4)$. In effect, the advantages of the grid-like FEDVR treatment are completely lost.

To circumvent this, we introduce a mixed basis set, i.e., a basis which consists of (at least) two types of different orbitals. Mixed basis sets have been applied several times in the literature, see, e.g., Ref. [108] for a basis of GTOs and FEDVR functions, or Ref. [186] for a basis of GTOs and plane waves. In this work, we apply a mixed basis consisting of Hartree-Fock eigenfunctions and FEDVR functions. The Hartree-Fock functions are localized only in a small region \mathcal{B}_1 around the nucleus, while the remaining space \mathcal{B}_2 is described by the grid-like basis (for an illustration of the spaces see Fig. 10 on page 211). Thus, we obtain both a good description of the ground state, which is assumed to lie entirely in \mathcal{H}_1 , as well as of the continuum, and this at a moderate effort.

For the construction of the mixed basis, we first solve the (single- or multi-configurational) Hartree-Fock equations in \mathcal{B}_1 using the spherical FEDVR basis $\{|\psi_k\rangle\}$, and by this obtain optimized orbitals in the form

$$|\phi_j\rangle = \sum_k b_{1,jk} |\psi_k\rangle, \quad (3.18)$$

with an $M \times N_b$ -matrix \mathbf{b}_1 , where M labels the number of occupied orbitals. The virtual orbitals are usually delocalized and do not resemble excited atomic orbitals. To obtain appropriate *pseudo-orbitals*, we employ the single-particle Hamiltonian eigenstates which are further orthonormalized to the bound Hartree-Fock states. Subsequently, these orbitals are used to extend the transformation matrix in Eq. (3.18) to a unitary $N_b \times N_b$ -matrix, which transforms the spherical FEDVR basis to the optimized orbitals in the subspace \mathcal{B}_1 . In the total basis \mathcal{B} , the unitary matrix is given by

$$\mathbf{b} = \begin{pmatrix} \mathbf{b}_1 & 0 \\ 0 & \mathbf{1} \end{pmatrix}, \quad (3.19)$$

and is used to transform the electron integrals to the optimized orbitals according to the formulas in Sect. 3.2. The arising mixed basis is illustrated in Fig. 15 for the example of beryllium, in which the $1s$ and $2s$ Hartree-Fock orbitals are occupied. Note that the localized orbitals in the region $r > 20$ Bohr essentially remain unchanged, whereas the orbitals inside $r \leq 20$ Bohr are given by Hartree-Fock eigenfunctions for the occupied orbitals, and appropriate pseudo-orbitals for the virtual states.

3.1.4 Angular DVR

As an interesting alternative to the spherical harmonic expansion, one can use a discrete variable representation in the angular coordinates. In the same way as for the one-dimensional DVR sets, an angular DVR is constructed according to formula (3.7) by using spherical harmonics and a grid Ω_γ of points and associated weights w_γ on the unit sphere,

$$\Gamma_\gamma(\Omega) = \sqrt{w_k} \sum_{lm} Y_{lm}^*(\Omega_\gamma) Y_{lm}(\Omega). \quad (3.20)$$

Two kinds of quadrature grids have been discussed in the literature, leading to different DVRs: the *extended-Legendre DVR* of Sukiasyan and Meyer employs a product grid consisting of an equally spaced grid, in azimuthal direction, and abscissas of the Gauss-Legendre integration, in polar direction [191], whereas the *Lebedev DVR*—introduced by Haxton—uses the grids of octahedral symmetry derived by Lebedev and Laikov [192, 193]. Both grids are depicted in Fig. 16. The lines from the origin to a

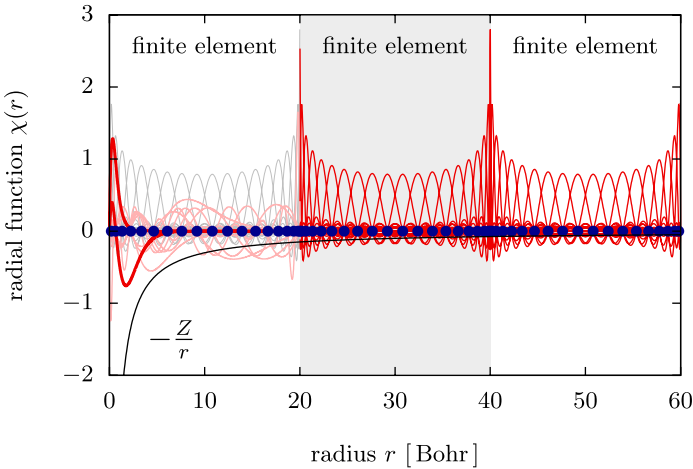


Fig. 15. Radial part of the single-particle basis used for the TD-RASCI calculations, which consists of a combination of Hartree-Fock orbitals (obtained for beryllium) in the vicinity of the atom (left element), and FEDVR basis functions in the continuum (the two elements on the right). In each element, the basis functions are constructed over a Gauss-Lobatto grid with 20 points. In the first element, the 1s and 2s Hartree-Fock orbitals are emphasized. Figure from Ref. [75].

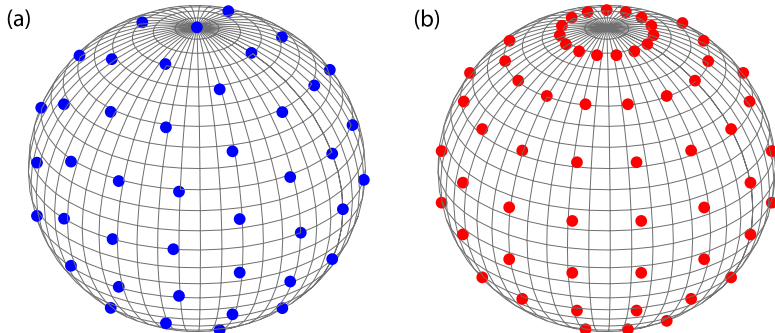


Fig. 16. Quadrature grids on the two-dimensional unit sphere used to construct angular DVRs: (a) Lebedev grid of octahedral symmetry. (b) Extended Legendre grid consisting of an equidistant grid in azimuthal and a Gauss-Legendre grid in polar direction.

point on the sphere define the directions in which the radial grid points are placed. The resulting three-dimensional grid is much denser at the origin and becomes sparse at large distances from the core. For further details on the construction of these spherical DVR basis sets, we refer to [192].

The great advantage of the angular DVR is that, when used in conjunction with a radial DVR $\{\chi_i(r)\}$, the representation of spatial functions becomes completely diagonal,

$$\langle \chi_k(r) \Gamma_\gamma(\Omega) | f(\mathbf{r}) | \chi_l(r) \Gamma_\nu(\Omega) \rangle = f(r_k, \Omega_\gamma) \delta_{kl} \delta_{\gamma\nu}. \quad (3.21)$$

Particularly, the two-electron integrals reduce to two-fold indexed quantities,

$$g_{k_1\gamma_1, k_2\gamma_2, k_3\gamma_3, k_4\gamma_4} = \delta_{k_1 k_2} \delta_{\gamma_1 \gamma_2} \delta_{k_3 k_4} \delta_{\gamma_3 \gamma_4} g_{k_1\gamma_1, k_3\gamma_3}, \quad (3.22)$$

where the diagonal element $g_{k_1\gamma_1, k_3\gamma_3}$ can be properly calculated using the Poisson equation [73]. This form can give notable advantages in storage as well as in the basis transformations considered in Sect. 3.2.

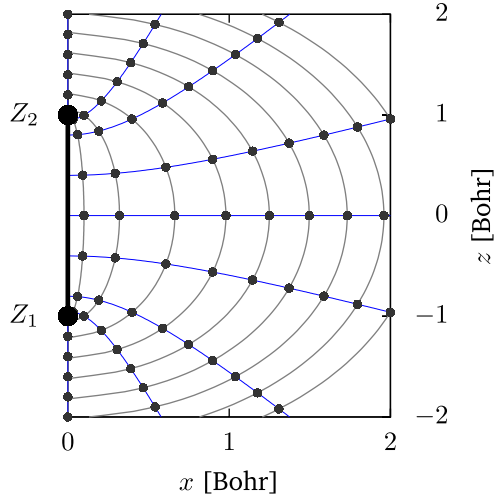


Fig. 17. Example of the coordinate lines of the prolate spheroidal system. Gray lines are drawn for varying η and fixed ξ , blue lines for varying ξ and fixed η . The dots denote the intersection points on which the wavefunction can be discretized. ξ -coordinate lines (gray) are drawn for $\xi = 1.005, 1.05, 1.2, 1.4, \dots$, η -coordinate lines (blue) for $\eta = 0, \pm 0.4, \pm 0.8, \pm 0.95, \pm 1$.

3.1.5 Prolate spheroidal DVR expansion

Prolate spheroidal coordinates constitute a particularly convenient choice for the description of diatomic molecules. They are defined by [194, 195]

$$\begin{aligned} x &= a\sqrt{(\xi^2 - 1)(1 - \eta^2)} \cos \varphi, \\ y &= a\sqrt{(\xi^2 - 1)(1 - \eta^2)} \sin \varphi, \\ z &= a\xi\eta, \end{aligned}$$

and can be obtained by rotating an ellipse around the focal axis (i.e., by varying the angle φ). Figure 17 illustrates the coordinate lines in the x - z plane. As the angular coordinates (η, φ) define a point on the three-dimensional unit sphere, one can apply a partial wave expansion,

$$\psi_{klm}(\mathbf{r}) = \frac{\chi(\xi)}{\xi} Y_{lm}(\arccos(\eta), \varphi), \quad (3.23)$$

where the radial part is described by a FEDVR basis. In contrast to the spherical case, the expansion (3.23) is not orthogonal in spheroidal coordinates. The prolate spheroidal DVR basis is not applied in this work, but has been included in the MCTDHF code to treat diatomic molecules. It is able to reproduce benchmark results for the ground state energy of the hydrogen molecule [73] and other diatomic molecules, which proves the correctness of the implementation.

3.2 Basis transformations

Basis transformations present a key operation in the implementation of the MCTDHF method. The problem is the following: suppose one is given an orthonormal single-particle basis set $\{|\psi_j\rangle\}$ of size N_b as well as the corresponding electron integrals.

Now, when performing a transformation into another orthonormal basis set $\{|\phi_n\rangle\}$ of size $M \leq N_b$ according to

$$|\phi_n\rangle = \sum_{j=1}^{N_b} b_{nj} |\psi_j\rangle, \quad (3.24)$$

how do the electron integrals look like in the new basis? We give the easy answer in the following for single- and two-particle operators. Thereafter, we present more efficient transformation schemes for the two-electron integrals employing both a Cholesky decomposition and the Poisson equation and, finally, consider the influence of a basis change on the many-body wavefunction.

3.2.1 Single-electron integrals

For a single-particle operator \hat{h} with matrix elements $h_{jk}^{(0)} = \langle \psi_j | \hat{h} | \psi_k \rangle$ in the old basis, the matrix elements $h_{mn} = \langle \phi_m | \hat{h} | \phi_n \rangle$ in the new basis are readily obtained by insertion of Eq. (3.24),

$$h_{jn}^{(1)} = \langle \psi_j | \hat{h} | \phi_n \rangle = \sum_{k=1}^{N_b} b_{nk} h_{jk}^{(0)}, \quad (3.25)$$

$$h_{mn} = \langle \phi_m | \hat{h} | \phi_n \rangle = \sum_{j=1}^{N_b} b_{mj}^* h_{jn}^{(1)}. \quad (3.26)$$

The transformation has been divided into two steps for later convenience. We further need the result of a renewed transformation of one index back to the original basis set,

$$h_{jn}^{(3)} = \sum_{m=1}^M \langle \psi_j | \phi_m \rangle \langle \phi_m | \hat{h} | \phi_n \rangle = \sum_{m=1}^M b_{mk} h_{mn}, \quad (3.27)$$

which later arises in the derivation of the MCTDHF equations through application of the projection operator $\sum_m |\phi_m\rangle \langle \phi_m|$. The preceding equations can also be written more compactly in matrix notation,

$$\begin{aligned} \mathbf{h}^{(1)} &= \mathbf{h}^{(0)} \mathbf{b}, \\ \mathbf{h}^{(2)} &= \mathbf{b}^\dagger \mathbf{h}^{(0)} \mathbf{b}, \\ \mathbf{h}^{(3)} &= \mathbf{b} \mathbf{b}^\dagger \mathbf{h}^{(0)} \mathbf{b}. \end{aligned}$$

Note that $\mathbf{h}^{(1)} = \mathbf{h}^{(3)}$ holds if \mathbf{b} is a unitary matrix. Otherwise, e.g., for $M < N_b$, information is lost in the back-transformation. For general basis sets, the effort of the complete transformation scales as $\mathcal{O}(N_b^2 M)$. For a banded matrix $\mathbf{h}^{(0)}$, as it is obtained for the spherical DVR basis, the number of operations is reduced to $\mathcal{O}(N_b M)$.

3.2.2 Two-electron integrals

The transformation of two-electron operators proceeds in a similar way, except that one has to deal with product basis states $|\psi_i \psi_j\rangle \in \mathcal{H}_2$ and matrix elements

$$g_{ijkl}^{(0)} = (\psi_i \psi_k | \hat{g} | \psi_j \psi_l). \quad (3.28)$$

The corresponding transformation matrix in the two-particle space is formally given by the outer product $\mathbf{b} \otimes \mathbf{b}$ of the two transformation matrices. The transformation is accomplished after the following steps:

$$g_{ijrs}^{(2)} = \sum_{k=1}^{N_b} b_{rk}^* \sum_{l=1}^{N_b} b_{sl} g_{ijkl}^{(0)} \quad (3.29)$$

$$g_{iqrs}^{(3)} = \sum_{j=1}^{N_b} b_{qj} g_{ijrs}^{(2)}, \quad (3.30)$$

$$g_{pqrs} = \sum_{i=1}^{N_b} b_{pi}^* g_{iqrs}^{(3)}, \quad (3.31)$$

$$g_{iqrs}^{(5)} = \sum_{p=1}^M b_{pi} g_{pqrs}. \quad (3.32)$$

Note that we again included the back-transformation step leading to $g^{(5)}$. By defining matrices in the product space,

$$[\mathbf{g}^{(0)}]_{(ik),(jl)} := (\psi_i \psi_k | \hat{g} | \psi_j \psi_l) = g_{ijkl}^{(0)}, \quad (3.33)$$

one can, alternatively, write the preceding formulas as

$$\mathbf{g}^{(2)} = (\mathbf{1} \otimes \mathbf{b})^\dagger \mathbf{g}^{(0)} (\mathbf{1} \otimes \mathbf{b}), \quad (3.34)$$

$$\mathbf{g}^{(3)} = (\mathbf{1} \otimes \mathbf{b})^\dagger \mathbf{g}^{(0)} (\mathbf{b} \otimes \mathbf{b}), \quad (3.35)$$

$$\mathbf{g} = (\mathbf{b} \otimes \mathbf{b})^\dagger \mathbf{g}^{(0)} (\mathbf{b} \otimes \mathbf{b}), \quad (3.36)$$

$$\mathbf{g}^{(5)} = (\mathbf{b} \otimes \mathbf{1}) (\mathbf{b} \otimes \mathbf{b})^\dagger \mathbf{g}^{(0)} (\mathbf{b} \otimes \mathbf{b}). \quad (3.37)$$

Again, it is $\mathbf{g}^{(3)} = \mathbf{g}^{(5)}$ for a unitary matrix \mathbf{b} . The total effort of the two-electron transformation grows as $\mathcal{O}(N_b^4 M)$ for general basis sets¹⁰. Significant improvements can be obtained by using basis sets with sparse two-electron integrals. For example, the spherical DVR basis leads to an effort of roughly $\mathcal{O}(N_b^2 N_{\text{ang}}^2 M)$, while the angular DVR basis, due to its diagonal two-electron integrals, even approaches $\mathcal{O}(N_b^2 M)$.

3.2.3 Low-rank approximations

The scaling of the two-integral transformation constitutes a serious bottleneck in many applications. For MCTDHF calculations, where usually $M \ll N_b$, particularly the evaluation of Eq. (3.34) is problematic. Therefore, several methods have been designed to reduce this effort, among them low-rank approximations [70, 197], Cholesky decompositions [198, 199], density-fitting methods [200], and tensor decomposition

¹⁰ Taking the symmetries (2.27) – (2.28) into account, the prefactor might in principle be reduced by up to a factor of eight [196]. In real applications, however, the corresponding speedup is often not that large due to a more complicated index structure.

schemes [201]. Basically, all methods utilize linear dependencies in the two-electron integral matrix to approximately express it in a form similar to

$$g_{ijkl}^{(0)} \approx \sum_{\lambda=1}^L u_{\lambda,ij} u_{\lambda,kl}, \quad (3.38)$$

which is an exact representation for $L = N_b^2$. The practical efficiency of this decomposition strongly depends on the magnitude of L . Given it can be chosen substantially smaller than N_b^2 , while at the same time the two-electron integrals are represented properly, it is advantageous to transform the factors separately and combine them in the new basis,

$$g_{pqrs} = \sum_{\lambda=1}^L \left(\sum_{ij} b_{pi}^* b_{qj} u_{\lambda,ij} \right) \cdot \left(\sum_{kl} b_{rk}^* b_{sl} u_{\lambda,kl} \right). \quad (3.39)$$

This procedure scales in the same amount as L single-particle transformations. Regarding the required size of L , it has been shown in Ref. [199] for the special class of even-tempered Gaussian basis sets that $L \approx N_b$ holds asymptotically. According to our experience, this feature also holds for several other basis sets having a dense two-electron integral matrix. Therefore, the use of low-rank approximations reduces the effort of the two-electron integral transformation to approximately $\mathcal{O}(MN_b^3)$, i.e., by one order of magnitude as compared to the direct approach given in Eqs. (3.29)–(3.32).

A straightforward way to obtain the factors \mathbf{u}_λ is through an eigenvalue decomposition,

$$[\mathbf{g}^{(0)}]_{(ij),(kl)} = \sum_{\lambda=1}^{N_b^2} \bar{u}_{\lambda,(ij)} \delta_\lambda \bar{u}_{\lambda,(kl)}, \quad (3.40)$$

where the eigenvalues δ_λ are non-negative due to the positive-semidefiniteness of the two-electron integral matrix. By retaining only the L eigenvalues larger than a chosen cutoff and defining new eigenvectors

$$u_{\lambda,(ij)} = \sqrt{\delta_\lambda} \bar{u}_{\lambda,(ij)}, \quad (3.41)$$

one immediately arrives at the desired form of Eq. (3.38). We note that the specified procedure is essentially identical to the Cholesky decomposition approach which, however, takes advantage of the definiteness of the matrix and is typically faster by a factor of about three [199].

As an example, we apply the eigenvalue decomposition scheme to a basis of *even-tempered* Slater-type orbitals of the form [202]

$$\psi_{nlm}^{\text{STO}}(\mathbf{r}) = N_{l,\zeta_{nl}} r^l e^{-\zeta_{nl}r} Y_{lm}(\theta, \varphi), \quad (3.42)$$

where the exponents are given by the geometric progression

$$\zeta_{nl} = \alpha_l (\beta_l)^n. \quad (3.43)$$

Here, $\alpha_l = 0.8$ and $\beta_l = 1.2$ is chosen. The results are shown in Fig. 18 for angular momenta $l = 0$ and $l = 1$ and basis sizes up to $N_b = 30$. For both cutoff parameters, $\eta = 10^{-6}$ and $\eta = 10^{-10}$, one observes that the tensor rank L is notably smaller than N_b^2 , which leads to a speedup of the transformation routines of up to a factor of five. This trend is continued for increasing N_b , and becomes particularly important for basis sets consisting of hundreds of basis functions.

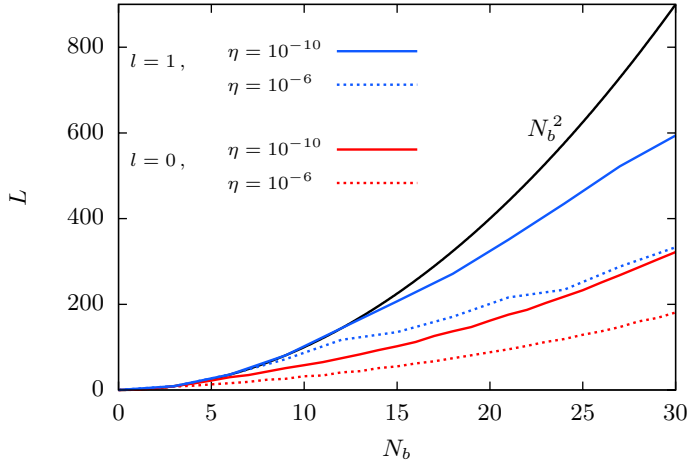


Fig. 18. Eigenvalues of the two-electron matrix larger than a cutoff of $\eta = 10^{-6}$ and $\eta = 10^{-10}$, respectively, for a basis set consisting of even-tempered Slater-type orbitals with angular momenta $l = 0$ and $l = 1$. One observes that the rank L grows distinctly slower than N_b^2 . This linear dependency can be used to efficiently improve the performance of the two-electron matrix transformation.

Low-rank approximations have the disadvantage that they do not work well for sparse two-electron integrals. Further, the straightforward procedure given before is hardly applicable to the large basis sizes required in photoionization (where $N_b \gtrsim 1000$), as the eigenvalue decomposition takes an effort of $\mathcal{O}(N_b^6)$. Therefore, in the following, we present another approach to reduce the transformation costs which is based on the Poisson equation.

3.2.4 Poisson equation

The use of the Poisson equation has a long tradition in quantum chemistry as a means to efficiently calculate electron integrals of the Coulomb interaction [203]. For the derivation, we begin by rewriting Eq. (3.29) as

$$g_{ijrs}^{(2)} = \int \psi_i^*(\mathbf{r}) \psi_j(\mathbf{r}) g_{rs}(\mathbf{r}) d\mathbf{r}, \quad (3.44)$$

with the *mean-field integrals*¹¹

$$g_{rs}(\mathbf{r}) = \int \phi_r^*(\mathbf{r}') \frac{1}{|\mathbf{r} - \mathbf{r}'|} \phi_s(\mathbf{r}') d\mathbf{r}', \quad (3.45)$$

Using straightforward numerical quadrature, the evaluation of a single integral would scale quadratically in the number of grid points. By application of the Laplace operator and making use of the equation

$$\Delta \frac{1}{|\mathbf{r} - \mathbf{r}'|} = -4\pi \delta(\mathbf{r} - \mathbf{r}'), \quad (3.46)$$

one obtains the Poisson equation

$$\Delta g_{rs}(\mathbf{r}) = -4\pi \phi_r^*(\mathbf{r}) \phi_s(\mathbf{r}). \quad (3.47)$$

¹¹ They are also named *Coulomb-integrals* for $r = s$ and *exchange-integrals* for $r \neq s$.

The direct integration has thus been replaced by the task of solving of a differential equation. The main advantage of this alternative formulation is that the Poisson equation can be solved with an effort that scales at best linearly in the number of grid points [140]. Once the Coulomb/exchange-integrals are at hand, the calculation of $g^{(2)}$ in Eq. (3.44) requires an effort that is again linear in the number of grid points. Altogether, we have thus obtained a huge reduction as compared to the direct evaluation of Eq. (3.45).

It remains to actually solve the Poisson equation. We sketch the procedure for the spherical DVR basis and refer to Sect. B.2.2 in the appendix for the mathematical details. According to Eq. (3.6), in the spherical DVR the orbitals are represented by

$$\phi_r(\mathbf{r}) = \sum_{klm} b_{r,klm} \frac{\chi_k(r)}{r} Y_{lm}(\theta, \varphi). \quad (3.48)$$

Similarly, we are seeking a representation for the mean-field integrals of the form

$$g_{rs}(\mathbf{r}) = \sum_{klm} g_{rs,klm} \frac{\chi_k(r)}{r} Y_{lm}(\theta, \phi). \quad (3.49)$$

Insertion of both these equations into the Poisson equation (3.47) yields the equation

$$\sum_{k'} \Delta_{klm,k'lm} g_{rs,k'lm} = -4\pi \rho_{rs,klm}, \quad (3.50)$$

where

$$\Delta_{klm,k'lm} = \int \chi_k(r) \frac{\partial^2}{\partial r^2} \chi_{k'}(r) dr - \delta_{kk'} \frac{l(l+1)}{r_k^2} \quad (3.51)$$

is the matrix representation of the Laplace operator, and

$$\rho_{rs,klm} = \frac{1}{r_k \sqrt{w_k}} \sum_{l_1 m_1, l_2 m_2} b_{r,kl_1 m_1}^* b_{s,kl_2 m_2} \bar{y}_{l_1 m_1, l_2 m_2} \quad (3.52)$$

the discretized charge density which involves the Gaunt coefficient introduced in Eq. (3.13). Equation (3.50) constitutes a number of $M^2 N_{\text{ang}}$ linear systems for the coefficients $g_{rs,klm}$ which, in order to satisfy the boundary condition, need to be further augmented by eigenfunctions of the homogeneous Laplace equation.

At this point one can understand the advantages of a banded derivative matrix: a general radial basis would require an effort of $\mathcal{O}(N_{\text{rad}}^3)$ for the solution of a single linear system. For the FEDVR basis, in contrast, one can apply specialized band-matrix solvers the effort of which scales only with $\mathcal{O}(N_{\text{rad}})$, i.e., linearly in the number of radial grid points. The total scaling is then dominated by the calculation of the $\rho_{rs,klm}$ on the right-hand side of Eq. (3.50), which requires $\mathcal{O}(M^2 N_b N_{\text{ang}}^2)$ operations¹². Altogether, we obtained a significant reduction as compared to the direct approach in Eq. (3.29).

Another advantage of the previous scheme is that one also gains a technique to calculate two-electron integrals of essentially any basis set of the form

$$\psi_{klm}(\mathbf{r}) = R_{klm}(r) Y_{lm}(\theta, \phi). \quad (3.53)$$

This can be accomplished by expanding the general radial function $R_{klm}(r)$ into a FEDVR basis, and then solving the Poisson equation with the corresponding expansion coefficients. In the program, this idea is utilized for a basis consisting of energy eigenfunctions of the single-particle Hamiltonian.

¹² The scaling refers to a direct evaluation of the term $\rho_{rs,klm}$. However, through the use of fast spherical-harmonic transforms [204], one is likely to obtain a faster algorithm.

3.2.5 Fourier transform method

Another way to arrive at an evaluation of the Coulomb/exchange-integrals is through the use of a Fourier transformation. To this aim, we rewrite Eq. (3.45) in the following way,

$$\begin{aligned} g_{rs}(\mathbf{r}) &= \int \frac{1}{|\mathbf{r} - \mathbf{r}'|} \phi_r^*(\mathbf{r}') \phi_s(\mathbf{r}') d\mathbf{r}' \\ &= \int d\mathbf{r}' \frac{1}{(2\pi)^3} \int d\mathbf{k} \frac{4\pi}{k^2} e^{i\mathbf{k}(\mathbf{r}-\mathbf{r}')} \phi_r^*(\mathbf{r}') \phi_s(\mathbf{r}') \\ &= \frac{1}{2\pi^2} \int d\mathbf{k} \frac{e^{i\mathbf{k}\mathbf{r}}}{k^2} \underbrace{\int d\mathbf{r}' e^{-i\mathbf{k}\mathbf{r}'} \phi_r^*(\mathbf{r}') \phi_s(\mathbf{r}')}_{=\rho_{rs}(\mathbf{k})}. \end{aligned} \quad (3.54)$$

Here we made use of the Fourier back-transformation of the Coulomb repulsion,

$$\frac{1}{|\mathbf{r} - \mathbf{r}'|} = \frac{1}{(2\pi)^3} \int d\mathbf{k} \frac{4\pi}{k^2} e^{i\mathbf{k}(\mathbf{r}-\mathbf{r}')}. \quad (3.55)$$

The calculation of the mean-field terms is thus obtained by a Fourier transformation of the product of two orbitals, a multiplication in Fourier space by $1/k^2$, and a final back-transformation to coordinate space. Note that this approach—here performed in 3D—can be readily extended to other dimensions and other interaction types.

The practical application of this formula crucially depends on the type of the basis set. First, the basis set should be able to appropriately represent its own Fourier transform, as well as its Fourier transform divided by k^2 . As a counter-example, consider the simplest choice of a single Gaussian: its Fourier transform gives a Gaussian in momentum space with different width, and in general can not be modeled through the Gaussian itself. The required flexibility to model its own Fourier transform is given, e.g., by basis sets defined on Cartesian or radial grids. As usual in this connection, a great advantage is gained for the case of equally-spaced Cartesian grids, where one can apply a Fast-Fourier-Transform (FFT) and arrives at the mean-field integrals in $\mathcal{O}(N_b \log N_b)$ evaluations. Often, however, rather dense grids are necessary due to the singularity of $1/k^2$. In the case of non-equidistant grids, such as implied by a three-dimensional Cartesian FEDVR, one needs to apply a Discrete-Fourier-Transform (DFT) the calculation of which scales as $\mathcal{O}(N_b^2)$, and thus would have obtained no advantage over the direct formula (3.29). On the other hand, for delocalized basis sets, such as eigenfunctions of the single-particle Hamiltonian, the effort scales quadratically as well and yields a great reduction over the direct formula (a good representation in Fourier space is presumed).

In order to apply these principles to an expansion into a spherical product basis,

$$\phi_r(\mathbf{r}) = \sum_{lm} \frac{R_{lm}(r)}{r} Y_{lm}(\theta, \phi), \quad (3.56)$$

an insertion of the well-known spherical-harmonic expansion of plane waves into Eq. (3.54), followed by a short calculation leads to

$$g_{rs}(\mathbf{r}) = \sum_{lm, l_r m_r, l_s m_s} \frac{4\pi}{(2l+1)} \bar{y}_{l_r m_r, lm, l_s m_s} Y_{lm}(\theta, \phi) \int dr' \frac{r'_<^l}{r'_>^{l+1}} R_{l_r m_r}^*(r') R_{l_s m_s}(r'). \quad (3.57)$$

Interestingly, this is just the usual Slater integral! Consequently, through a direct evaluation one gains no advantage over a direct multipole expansion of the Coulomb term. Note that during the derivation, the integral

$$\int dk j_l(kr) j_l(kr') = \frac{\pi}{2(2l+1)} \frac{r_<^l}{r_>^{l+1}} \quad (3.58)$$

has been used¹³. However, the separated representation given by Eq. (3.58) also offers a chance for improvement: instead of analytically calculating the integral and arriving at a full matrix, one could also make use of a Fast-Bessel-Transform in order to bring down the quadratical scaling of Eq. (3.57) with respect to the radial coordinate. In addition, as mentioned in the last subsection, the angular integral could be evaluated more efficiently using a Fast-Spherical-Harmonic-Transform [204]. However, in this work, we followed none of these approaches, in favor of the Poisson equation.

3.2.6 Effects on the many-particle wavefunction

Suppose we are given a wavefunction specified by a full CI expansion in a single-particle basis $\{|\psi_i\rangle\}$,

$$|\Psi\rangle = \sum_I C_I |\psi_{i_1} \cdots \psi_{i_N}\rangle. \quad (3.59)$$

By changing to a new basis set $\{|\phi_j\rangle\}$, the Slater determinants get transformed according to

$$|\phi_{j_1} \cdots \phi_{j_N}\rangle = \sum_I (\mathbf{b} \otimes \cdots \otimes \mathbf{b})_{j_1 \cdots j_N, i_1 \cdots i_N} |\psi_{i_1} \cdots \psi_{i_N}\rangle, \quad (3.60)$$

and a general wavefunction in the new determinant basis is given by

$$|\tilde{\Psi}\rangle = \sum_I D_J |\phi_{j_1} \cdots \phi_{j_N}\rangle. \quad (3.61)$$

Is it possible to represent the wavefunction $|\Psi\rangle$ also in the new determinant basis, i.e., to obtain coefficients D_J such that $|\tilde{\Psi}\rangle = |\Psi\rangle$? The answer can be readily found by considering the coefficients

$$D_{j_1, \dots, j_N} = \sum_I (\mathbf{b}^\dagger \otimes \cdots \otimes \mathbf{b}^\dagger)_{j_1 \cdots j_N, i_1 \cdots i_N} C_{i_1, \dots, i_N}. \quad (3.62)$$

Insertion into (3.61) then reveals that the wavefunctions are identical, if

$$(\mathbf{b}^\dagger \otimes \cdots \otimes \mathbf{b}^\dagger)(\mathbf{b} \otimes \cdots \otimes \mathbf{b}) = \mathbf{1}, \quad (3.63)$$

i.e., if \mathbf{b} is a unitary matrix. Full CI spaces are, therefore, invariant under unitary rotations of the orbitals, and the same is true for MCTDHF Hilbert spaces at a fixed time-point.

In contrast, for restricted active space expansions, an orbital transformation in general leads to a set of determinants which spans a different Hilbert space than the original determinants, so that Eq. (3.61) may not be solvable. In order to retain

¹³ Taken from <http://functions.wolfram.com/Bessel-TypeFunctions/SphericalBesselJ/21/02/02/>.

the RAS Hilbert space, one has to restrict the unitary transformation \mathbf{b} . For two restricted active spaces, it is immediately obvious that transformations of the form

$$\mathbf{b} = \begin{pmatrix} \mathbf{b}_1 & 0 \\ 0 & \mathbf{b}_2 \end{pmatrix}, \quad (3.64)$$

where the unitary matrices \mathbf{b}_1 and \mathbf{b}_2 act only on the first and second subspace, respectively, conserve the RAS structure. Further, the requirement that \mathbf{b} is unitary shows that this is the only possible choice for the transformation matrix, since insertion of further off-diagonal elements would directly lead to non-normalized row- and column-vectors and thus would destroy the unitarity.¹⁴

3.3 Slater determinants

Slater determinants are one of the most important components of the MCTDHF and TD-RASCI methods. They are commonly represented in two ways, either by specifying the occupied orbitals,

$$|I\rangle = |\phi_{i_1} \dots \phi_{i_N}\rangle, \quad (3.65)$$

or in occupation number representation,

$$|\mathbf{n}\rangle = |n_1 \dots n_{N_b}\rangle, \quad (3.66)$$

where n_k labels the occupation of the orbital $|\phi_k\rangle$. Both approaches have their advantages and disadvantages. In the code, the occupation number formalism is used almost exclusively. The determinants are encoded in a bit-wise representation¹⁵, which simplifies the application of the elementary annihilation and creation operators,

$$a_p^\dagger |n_1 \dots n_p \dots n_{N_b}\rangle = \delta_{n_p,0} \Gamma_p^\mathbf{n} |n_1 \dots 1_p \dots n_{N_b}\rangle, \quad (3.67)$$

$$a_p |n_1 \dots n_p \dots n_{N_b}\rangle = \delta_{n_p,1} \Gamma_p^\mathbf{n} |n_1 \dots 0_p \dots n_{N_b}\rangle, \quad (3.68)$$

with the phase factors introduced in Eq. (2.19). For the efficient use in calculations of matrix elements, one needs to be able to address the newly created determinants on the right-hand sides in an efficient way. Subsection 3.3.2 deals with that task.

3.3.1 Determinants as products of spin strings

Particles with different spin projection can be discriminated by experiment. Further, the Hamiltonian used in this work, Eq. (1.2), commutes with the spin operators, such that the particles remain in the spin state σ in which they are initially prepared. As a consequence, the particles with different spin can be fundamentally considered distinguishable, and the determinants can be represented as a direct product of *spin strings* corresponding to α - and β -spin functions [59],

$$\begin{aligned} |I\rangle &= |\phi_{i_1,\alpha} \dots \phi_{i_{N_\alpha},\alpha} \phi_{i_{(N_\alpha+1)},\beta} \dots \phi_{i_{(N_\alpha+N_\beta)},\beta}\rangle \\ &= |\phi_{i_1^\alpha,\alpha} \dots \phi_{i_{N_\alpha}^\alpha,\alpha}\rangle |\phi_{i_{i_1}^\beta,\beta} \dots \phi_{i_{N_\beta}^\beta,\beta}\rangle \\ &= |I_\alpha\rangle |I_\beta\rangle. \end{aligned} \quad (3.69)$$

¹⁴ This consideration can also be extended to the case of non-orthogonal basis transformations, see Ref. [59].

¹⁵ Using `std::vector<bool>` in the MCTDHF code and `boost::dynamic_bitset` in the TD-RASCI code.

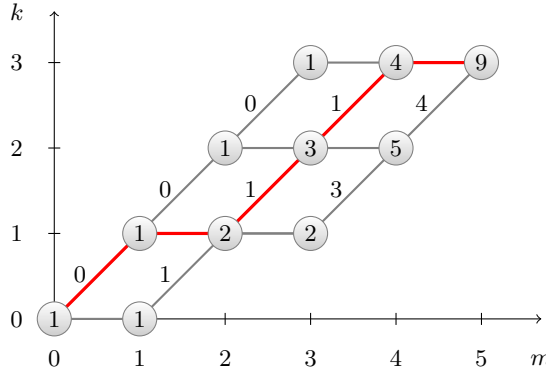


Fig. 19. Graphical scheme to resolve the address of a Slater determinant for $N = 3$ particles in $M = 5$ orbitals, taken from [59]. The path drawn in red illustrates the representation of the determinant $|\mathbf{n}\rangle = |1, 0, 1, 1, 0\rangle$. Its address is obtained by summing the weights at the diagonal connection lines, $\text{add}(|\mathbf{n}\rangle) = 0 + 1 + 1 = 2$.

This separation can bring a significant advantage in the calculation of matrix elements, and is particularly useful in the direct CI approach detailed later in Sect. 3.4.2.

3.3.2 Addressing determinants

The address $\text{add}(|\mathbf{n}\rangle)$ of a determinant $|\mathbf{n}\rangle$ is a unique number in the consecutive index set $\{0, 1, \dots, N_{\text{det}} - 1\}$. In principle, the address can be found straightforwardly through a linear search in the determinant space, a procedure which scales as $\mathcal{O}(N_{\text{det}})$. This, however, quickly becomes inefficient for large Hilbert spaces. A by far better method is therefore to use binary search algorithms as implemented, e.g., in ordered associative arrays, which reduce the effort to $\mathcal{O}(\log N_{\text{det}})$ comparisons. Another alternative which has been applied in this work constructs the address directly from the occupation number vector [59]. The basic idea is to represent determinants as paths in a diagram and introduce an ordering of these paths. For N electrons in M orbitals, a determinant can—in addition to the representations (3.65) and (3.66)—be represented by a number of M ordered pairs (m, k) , where m is the orbital index and k the number of electrons occupying the orbitals up to m . This defines a path in an $(N + 1) \times (M + 1)$ diagram which starts at the vertex $(0, 0)$ and ends at (M, N) . The vertices are connected either by horizontal lines from (m, k) to $(m + 1, k)$ corresponding to unoccupied orbitals, or by diagonal lines from (m, k) to $(m + 1, k + 1)$ for occupied orbitals. Figure 19 depicts the set of possible paths for three particles in five orbitals, where the lowest two orbitals must be occupied by at least one electron.

To construct the address, one introduces for each allowed vertex (m, k) a weight $W_{m,k}$ which is recursively defined by

$$W_{m,k} = W_{m-1,k} + W_{m-1,k-1}, \quad (3.70)$$

and $W_{0,0} = 1$. The weights at non-allowed vertices are set to zero. Note that Eq. (3.70) agrees with the recursion formula for binomial coefficients, however, with different boundary conditions. Next, one introduces for each connection line originating from vertex (m, k) an arc weight which is given by $Y_{m,k}^0 = 0$ for a horizontal line and by

$$Y_{m+1,k+1}^1 = W_{m+1,k+1} - W_{m,k}, \quad (3.71)$$

for a diagonal line. In terms of these, the address of a determinant can be constructed as

$$\text{add}(|n_1, n_2, \dots, n_M\rangle) = \sum_{m=1}^M Y_{m,k_m}^{n_m} \quad (3.72)$$

$$= \sum_{m=1}^M \delta_{n_m, 1} W_{m-1, k_m}, \quad (3.73)$$

where $k_m = \sum_{i=1}^m n_i$. In practice, one therefore has to set up the vertex weights once at the beginning of the simulation, and then use them to address the whole determinant space.

The advantage of the graphical scheme is that it can be applied equally well to full CI and RASCI determinant spaces. Further, an extension to address bosonic configurations is straightforward. Alternative addressing schemes, such as the ones in presented in Refs. [205, 206], provide closed formulas which are conveniently applicable to FCI spaces, but require further effort for the extension to restricted active space configurations.

3.4 TD-CI equation

With the techniques introduced in the previous section, we are now able to derive efficient schemes to numerically solve the time-dependent configuration interaction equation, Eq. (2.64),

$$i\dot{\mathbf{C}}(t) = \mathbf{H}(t) \mathbf{C}(t). \quad (3.74)$$

The essential operation that needs to be carried out here is the matrix-vector multiplication on the right-hand side. For its evaluation, one can basically choose between two different approaches, either *conventional CI*, where the representation of the Hamiltonian and other operators is determined once and stored in sparse matrices, or *direct CI*, which proceeds by evaluating only the action of the Hamiltonian onto the state vector,

$$\boldsymbol{\sigma}(t) = \mathbf{H}(t) \mathbf{C}(t). \quad (3.75)$$

In general, conventional CI involves an overhead through the need to construct and store the operator matrices, but the matrix-vector products are evaluated rapidly. The direct method, on the other hand, takes longer for the calculation of $\boldsymbol{\sigma}(t)$, but the initialization of the matrices is avoided completely. The decision between the two methods depends on the actual application. For example, in time-independent quantum chemistry, direct CI is the *de facto* standard since usually only a few matrix-vector multiplications are required for the iterative schemes to converge. Direct CI is also a convenient choice for MCTDHF calculations, where the time-dependent basis leads to a Hamiltonian which needs to be constructed anew at each time-step. For the solution of the time-dependent CI equation, in contrast, conventional CI is advantageous as typically a large number of matrix-vector products needs to be carried out. We cover both algorithms in the following, starting with conventional TD-CI.

3.4.1 Conventional TD-CI

The conventional CI approach proceeds by calculating the contribution from single- and two-particle operators in the second-quantization Hamiltonian (2.24),

$$\hat{H} = \sum_{pq} h_{pq} \hat{a}_p^\dagger \hat{a}_q + \frac{1}{2} \sum_{pqrs} g_{pqrs} \hat{a}_p^\dagger \hat{a}_r^\dagger \hat{a}_s \hat{a}_q, \quad (3.76)$$

as well as for other required operators such as the dipole matrices. The task is to evaluate the matrix elements

$$H_{nm} = \langle \mathbf{n} | \hat{H}(t) | \mathbf{m} \rangle \quad (3.77)$$

for each pair of determinants. A straightforward approach would loop over all these pairs and evaluate the value using the Slater-Condon rules. This, however, scales with $\mathcal{O}(N_{\text{det}})$ and becomes unfeasible for large determinant bases.

Therefore, it is more convenient to use an approach which is based on the orbital indices. There, for the single-particle term, one has to loop over the orbital indices (p, q) as well as over the set of determinants $|\mathbf{n}\rangle$. For each determinant, the address $n = \text{add}(|\mathbf{n}\rangle)$ is calculated, and the excitation operators are applied to produce the new state

$$\hat{a}_p^\dagger \hat{a}_q |\mathbf{n}\rangle = \xi |\mathbf{n}_p^q\rangle, \quad (3.78)$$

where the phase factor $\xi \in 0, \pm 1$ is easily calculated from the definition of the excitation operators, Eqs. (2.18) and (2.20). In case the excited determinant is non-zero, its address $m = \text{add}(|\mathbf{n}_p^q\rangle)$ is calculated, and the Hamiltonian is updated according to

$$H_{nm} \rightarrow H_{nm} + \xi h_{pq}. \quad (3.79)$$

Similarly, for the two-electron part, one has to loop over the orbital indices (p, q, r, s) and the determinants $|\mathbf{n}\rangle$, and repeatedly apply the four-operator product

$$\hat{a}_p^\dagger \hat{a}_r^\dagger \hat{a}_s \hat{a}_q |\mathbf{n}\rangle = \xi |\mathbf{n}_{pr}^{qs}\rangle. \quad (3.80)$$

If the doubly-excited determinant $|\mathbf{n}_{pr}^{qs}\rangle$ is non-zero, its address m is evaluated and the contribution is added to the Hamiltonian,

$$H_{nm} \rightarrow H_{nm} + \xi g_{pqrs}. \quad (3.81)$$

Due to the occurrence of at most two-particle operators, the Hamiltonian is usually sparse and therefore effectively stored in a sparse matrix format. Sometimes, however, it can be more convenient to apply dense matrix algebra which allows for a faster performance of matrix-vector products and also for the complete diagonalization. Such a case can be encountered in the TD-RASCI method, when the restricted active space constraints lead to a non-sparse Hamiltonian, or for the finite temperature calculations in Sect. 5.1.2.

3.4.2 Direct TD-CI

The direct CI algorithm is used in the MCTDHF program, where the Hamiltonian, due to the time-dependent orbitals, changes at each propagation step and the construction of a sparse matrix would therefore be inefficient. The algorithm we describe in the following is called the *minimal operation-count* method and is taken from Ref. [59]. The strategy is to calculate separately the one- and two-particle contributions in the different spin subspaces,

$$\boldsymbol{\sigma}(t) = \boldsymbol{\sigma}^\alpha(t) + \boldsymbol{\sigma}^\beta(t) + \boldsymbol{\sigma}^{\alpha\alpha}(t) + \boldsymbol{\sigma}^{\alpha\beta}(t) + \boldsymbol{\sigma}^{\beta\beta}(t). \quad (3.82)$$

The single-particle contributions are easily evaluated as

$$\boldsymbol{\sigma}_{I_\alpha I_\beta}^\alpha(t) = \sum_{J_\alpha J_\beta} \sum_{pq} h_{pq}^\alpha(t) \langle I_\alpha I_\beta | \hat{a}_{p\alpha}^\dagger \hat{a}_{q\alpha} | J_\alpha J_\beta \rangle C_{J_\alpha J_\beta}(t) \quad (3.83)$$

$$= \sum_{J_\alpha} \sum_{pq} h_{pq}^\alpha(t) \langle I_\alpha | \hat{a}_{p\alpha}^\dagger \hat{a}_{q\alpha} | J_\alpha \rangle C_{J_\alpha I_\beta}(t), \quad (3.84)$$

and similarly for the β component. The advantage here is that the loop is performed only over the number N_α of α -strings, which is usually small compared to the total number of determinants ($N_{\text{det}} = N_\alpha \cdot N_\beta$). The practical evaluation of Eqs. (3.83) proceeds by determination and storage of the expectation values in a single spin-space, e.g., for the one-particle α -component,

$$K_{I_\alpha J_\alpha}^\alpha(t) = \sum_{pq} h_{pq}(t) \langle I_\alpha | \hat{a}_{p\alpha}^\dagger \hat{a}_{q\alpha} | J_\alpha \rangle, \quad (3.85)$$

and a subsequent contraction with the coefficients vector,

$$\sigma_{I_\alpha I_\beta}^\alpha(t) = \sum_{J_\alpha} K_{I_\alpha J_\alpha}^\alpha(t) C_{J_\alpha I_\beta}. \quad (3.86)$$

The total effort for this operation scales as $\mathcal{O}(N_\alpha(N_b - N_\alpha)N_{\text{det}})$, where N_α is the number of α -spin-orbitals. In the same way, the two-particle component with identical spin projection α (and similarly β) is calculated by

$$K_{I_\alpha J_\alpha}^{\alpha\alpha} = \sum_{pqrs} g_{pqrs} \langle I_\alpha | \hat{a}_{p\alpha}^\dagger \hat{a}_{r\alpha}^\dagger \hat{a}_{s\alpha} \hat{a}_{q\alpha} | J_\alpha \rangle, \quad (3.87)$$

$$\sigma_{I_\alpha I_\beta}^{\alpha\alpha}(t) = \sum_{J_\alpha} K_{I_\alpha J_\alpha}^{\alpha\alpha} C_{J_\alpha I_\beta}(t), \quad (3.88)$$

which requires an effort of $\mathcal{O}(N_\alpha^2(N_b - N_\alpha)^2 N_{\text{det}})$. The two-particle term with mixed spin projections,

$$\sigma_{I_\alpha I_\beta}^{\alpha\beta}(t) = \sum_{J_\alpha J_\beta} \sum_{pqrs} g_{pqrs}^{\alpha\beta} \langle I_\alpha | \hat{a}_{p\alpha}^\dagger \hat{a}_{q\alpha} | J_\alpha \rangle \langle I_\beta | \hat{a}_{r\beta}^\dagger \hat{a}_{s\beta} | J_\beta \rangle C_{J_\alpha J_\beta}(t), \quad (3.89)$$

is most easily treated by rewriting it in the form

$$\sigma_{I_\alpha I_\beta}^{\alpha\beta}(t) = \sum_{pq} \sigma_{I_\alpha I_\beta, pq}^{\alpha\beta}(t), \quad (3.90)$$

where

$$\sigma_{I_\alpha I_\beta, pq}^{\alpha\beta}(t) = \sum_{J_\beta} \left[\langle I_\alpha | \hat{a}_{p\alpha}^\dagger \hat{a}_{q\alpha} | J_\alpha \rangle C_{J_\alpha J_\beta} \right] \left[\sum_{rs} \langle I_\beta | \hat{a}_{r\beta}^\dagger \hat{a}_{s\beta} | J_\beta \rangle \right]. \quad (3.91)$$

With the terms in brackets being evaluated separately and subsequently contracted over I_β , the required effort scales as $\mathcal{O}(N_\alpha N_\beta (N_b - N_\alpha)(N_b - N_\beta)N_{\text{det}})$.

Using the previously introduced algorithm, the total operation count of the multiplication of the Hamiltonian matrix with the coefficient vector is given by the theoretically required minimum, thence the name minimal operation-count method [59].

3.5 MCTDHF orbital equation

In the present section, we discretize the orbital equation in terms of a single-particle basis set, which is an essential step for the numerical solution. Subsequently, we focus on how to reduce the stiffness of the arising differential equation in order to increase the efficiency of its solution.

3.5.1 Basis representation of the spin-restricted equations

Starting point for the derivation of the discretized orbital equation is the expansion of the M time-dependent MCTDHF orbitals $\{|\phi_n(t)\rangle\}$ into an, in general, non-orthogonal basis set $\{|\psi_k\rangle\}$ of size N_b ,

$$|\phi_m(t)\rangle = \sum_{k=1}^{N_b} b_{nk}(t) |\psi_k\rangle. \quad (3.92)$$

Insertion of this ansatz into the spin-restricted orbital equation (2.144),

$$i \frac{\partial}{\partial t} |\phi_n\rangle = \hat{\mathbf{P}} \left\{ \hat{h}(t) |\phi_n\rangle + \sum_{pqrs} (\mathbf{D}^{-1})_{np} d_{pqrs} \hat{g}_{rs} |\phi_q\rangle \right\}, \quad (3.93)$$

and projection onto $\langle \psi_k |$ leads to the equations of motion for the variational parameters $b_{nk}(t)$,

$$\begin{aligned} i \sum_l \langle \psi_k | \psi_l \rangle \dot{b}_{nl} &= \left(\langle \psi_k | - \sum_m^M \sum_{ij}^{N_b} b_{mi} b_{mj}^* \langle \psi_k | \psi_i \rangle \langle \psi_j | \right) \\ &\quad \times \left\{ \sum_l^{N_b} \hat{h} |\psi_l\rangle b_{nl} + \sum_{pqrs}^M (\mathbf{D}^{-1})_{np} d_{pqrs} \sum_{ijl}^{N_b} \langle \psi_i | \hat{g} | \psi_j \rangle b_{ri}^* b_{sj} b_{ql} |\psi_l\rangle \right\}. \end{aligned} \quad (3.94)$$

Using the definitions of Sect. 3.2 and the notation $S_{kl} = \langle \psi_k | \psi_l \rangle$ for the overlap matrix, the previous equation can also be written more compactly as

$$i \sum_l^{N_b} S_{kl} \dot{b}_{nl} = h_{nk}^{(1)} - \sum_l^{N_b} S_{kl} h_{nl}^{(3)} + \sum_{pqrs}^M (\mathbf{D}^{-1})_{np} d_{pqrs} \left(g_{kqrs}^{(3)} - \sum_l^{N_b} S_{kl} g_{lqrs}^{(5)} \right). \quad (3.95)$$

As the overlap matrix is non-singular, it can be inverted to arrive at the final explicit form,

$$i \dot{b}_{nk} = \sum_l^{N_b} (\mathbf{S}^{-1})_{kl} h_{nl}^{(1)} - h_{nk}^{(3)} + \sum_{pqrs}^M (\mathbf{D}^{-1})_{np} d_{pqrs} \left(\sum_l^{N_b} (\mathbf{S}^{-1})_{kl} g_{lqrs}^{(3)} - g_{kqrs}^{(5)} \right). \quad (3.96)$$

Note that, in practice, it may be advantageous to solve a linear system rather than to apply the inverse overlap matrix explicitly. This is particularly true if the overlap matrix has a special structure, e.g., is of tridiagonal form, since in general, the inversion does not conserve this structure. As an alternative to the inversion, one could also apply a Cholesky decomposition of the overlap matrix, which is possible due to its positive definiteness. In case of an orthonormal single-particle basis, the overlap matrix becomes the identity matrix and Eq. (3.96) reduces to

$$i \dot{b}_{nk} = h_{nk}^{(1)} - h_{nk}^{(3)} + \sum_{pqrs}^M (\mathbf{D}^{-1})_{np} d_{pqrs} \left(g_{kqrs}^{(3)} - g_{kqrs}^{(5)} \right). \quad (3.97)$$

Equations (3.96) and (3.97) govern, for a given set of electron integrals in the time-independent basis and the one- and two-particle matrix determined by the wavefunction coefficients, the temporal evolution of the expansion coefficients \mathbf{b} , and therefore the discretization of the time-dependent MCTDHF orbitals. For each step, the evaluation of the right-hand side requires a transformation of the electron integrals from the time-independent to the time-dependent basis according to the formulas given in Sect. 3.2. As discussed there in detail, particularly the transformation of the two-electron integrals is the most expensive part.

3.5.2 Basis representation of the spin-unrestricted equations

By applying the same procedure as in the previous subsection to the spin-unrestricted MCTDHF orbital equations (2.151) and (2.152), one readily obtains the corresponding basis representation, which we present for convenience only for an orthonormal single-particle basis,

$$i\dot{b}_{nk}^{\alpha} = h_{nk}^{\alpha,(1)} - h_{nk}^{\alpha,(3)} + \sum_{pqrs,\tau} [(\mathbf{D}^{\alpha})^{-1}]_{np} d_{pqrs}^{\alpha\tau} (g_{kqrs}^{\alpha\tau,(3)} - g_{kqrs}^{\alpha\tau,(5)}), \quad (3.98)$$

$$i\dot{b}_{nk}^{\beta} = h_{nk}^{\beta,(1)} - h_{nk}^{\beta,(3)} + \sum_{pqrs,\tau} [(\mathbf{D}^{\beta})^{-1}]_{np} d_{pqrs}^{\beta\tau} (g_{kqrs}^{\beta\tau,(3)} - g_{kqrs}^{\beta\tau,(5)}). \quad (3.99)$$

These equations involve the spin-resolved density matrices introduced in Sect. 2.1.6, as well as the spin-resolved electron integrals, which in the matrix notation of Sect. 3.2 are given by

$$h_{jn}^{\sigma,(1)} = \sum_{k=1}^{N_b} b_{nk}^{\sigma} h_{jk}^{(0)}, \quad (3.100)$$

$$h_{mn}^{\sigma} = \sum_{j=1}^{N_b} b_{mj}^{\sigma *} h_{jn}^{\sigma,(1)} \quad (3.101)$$

$$h_{jn}^{\sigma,(3)} = \sum_{m=1}^M b_{mk}^{\sigma} h_{mn}^{\sigma}, \quad (3.102)$$

and

$$g_{ijrs}^{\tau,(2)} = \sum_{kl=1}^{N_b} b_{rk}^{\tau *} b_{sl}^{\tau} g_{ijkl}^{(0)}, \quad (3.103)$$

$$g_{iqrs}^{\sigma\tau,(3)} = \sum_{j=1}^{N_b} b_{qj}^{\sigma} g_{ijrs}^{\tau,(2)}, \quad (3.104)$$

$$g_{pqrs}^{\sigma\tau} = \sum_{i=1}^{N_b} b_{pi}^{\sigma *} g_{iqrs}^{\sigma\tau,(3)}, \quad (3.105)$$

$$g_{iqrs}^{\sigma\tau,(5)} = \sum_{p=1}^M b_{pi}^{\sigma} g_{pqrs}^{\sigma\tau}, \quad (3.106)$$

where, as throughout this work, $\sigma, \tau \in \{\alpha, \beta\}$.

The solution of the spin-unrestricted orbital equations proceeds in the same way as the solution of the spin-restricted equations, except that a larger number of transformations needs to be performed. As the most expensive step is the formation of the Coulomb/exchange-integrals $\{\mathbf{g}^{\alpha,(2)}\}$ and $\{\mathbf{g}^{\beta,(2)}\}$, respectively, the effort is approximately doubled as compared to the spin-restricted case.

3.6 Time propagation

Quantum-mechanical time-evolution assigns to a given wavefunction at time t_0 a new one at time t under preservation of the norm. Its action is thus expressed by a unitary time-evolution operator $\hat{U}(t, t_0)$ defined by the relation

$$|\Psi(t)\rangle = \hat{U}(t, t_0)|\Psi(t_0)\rangle. \quad (3.107)$$

The equation of motion and the initial condition follow directly from the time-dependent Schrödinger equation,

$$i\partial_t \hat{U}(t, t_0) = \hat{H}(t) \hat{U}(t, t_0), \quad (3.108)$$

$$\hat{U}(t_0, t_0) = \mathbf{1}. \quad (3.109)$$

By iterating the integral of Eq. (3.108), one can state the formal solution,

$$\hat{U}(t, t_0) = \sum_{n=0}^{\infty} U_n(t, t_0), \quad (3.110)$$

$$U_n(t, t_0) = (-i)^n \int_{t_0}^t dt_1 \int_{t_0}^{t_1} dt_2 \cdots \int_{t_0}^{t_n} dt_n \hat{H}(t_1) \cdots \hat{H}(t_n), \quad (3.111)$$

which is known as the *Dyson series* [207]. Alternatively, it can be written as

$$\hat{U}(t, t_0) = \hat{\mathcal{T}} \exp \left\{ -i \int_{t_0}^t \hat{H}(\bar{t}) d\bar{t} \right\}, \quad (3.112)$$

where the time-ordering operator $\hat{\mathcal{T}}$ orders later times to the left. However, the direct use of the Dyson series to determine $U(t, t_0)$ for numerical propagation is tedious, because truncation at a given order does not lead to a unitary operator¹⁶.

There are basically two ways to handle Eq. (3.112). On the one hand, there are methods which explicitly account for the time-ordering. Among these is the Magnus expansion that replaces Eq. (3.108) by a normal exponential $\hat{U}(t, t_0) = \exp \{\sum_n \Omega_n\}$, which, when truncating the sum at any level, yields a unitary and approximately time-ordered scheme [208, 209]. There is the (t, t') -method, which incorporates the time-ordering exactly by introducing a second time variable [210, 211]. And there is a recently introduced scheme that iterates the Dyson series up to convergence [212]. On the other hand, there are the more frequently encountered methods which neglect

¹⁶ This can be seen, most prominently, in the treatment of time-dependent perturbation theory as provided in most textbooks on quantum mechanics, e.g., Ref. [207].

the time-ordering. Their foundation is given by the following approximation to the time-evolution operator,

$$\begin{aligned}\hat{U}(t, t_0) &= \hat{\mathcal{T}} \exp \left\{ -i \int_{t_0}^t \hat{H}(\bar{t}) d\bar{t} \right\} \\ &\approx \hat{\mathcal{T}} \exp \left\{ -i \sum_{j=1}^{N_t} \hat{H}(t_j) \Delta t \right\} \\ &\approx \hat{\mathcal{T}} \exp \{-i \hat{H}(t_{N_t}) \Delta t\} \cdots \exp \{-i \hat{H}(t_1) \Delta t\} \\ &= \exp \{-i \hat{H}(t_{N_t}) \Delta t\} \cdots \exp \{-i \hat{H}(t_1) \Delta t\}. \end{aligned} \quad (3.113)$$

Here, the integral is evaluated via the trapezoidal rule using N_t intermediate time points $\{t_j\}$, and subsequently the exponential is factorized under neglect of commutators of higher order in Δt . As the resulting term (3.113) is already time-ordered, $\hat{\mathcal{T}}$ can be trivially applied. Methods of this kind include Chebyshev [213], Crank-Nicolson [214] and pseudo-spectral methods [215]. A quantitative comparison of several of these methods can be found in [216]. In the following, we summarize the methods which have been implemented and used during this work.

3.6.1 Eighth-order Dormand-Prince integrator

The eighth-order Dormand-Prince integrator is a member of the Runge-Kutta (RK) family of ordinary differential equation solvers which has been introduced by Hairer et al. [217]. RK methods are general-purpose integrators suitable for a large class of initial value problems of the form

$$\frac{\partial}{\partial t} \mathbf{y}(t) = f(\mathbf{y}(t), t), \quad \mathbf{y}(0) = \mathbf{y}_0. \quad (3.114)$$

Starting from the function $\mathbf{y}_n = \mathbf{y}(t_n)$ at time t_n , the propagated function $\mathbf{y}_{n+1} = \mathbf{y}(t_n + \Delta t)$ is obtained through [204]

$$\mathbf{y}_{n+1} = \mathbf{y}_n + \sum_{i=1}^s b_i \mathbf{k}_i, \quad (3.115)$$

where \mathbf{k}_i denote the results of s intermediate steps,

$$\mathbf{k}_1 = \Delta t f(\mathbf{y}_n, t_n), \quad (3.116)$$

$$\mathbf{k}_2 = \Delta t f(\mathbf{y}_n + a_{21} \mathbf{k}_1, t_n + c_2 \Delta t), \quad (3.117)$$

$$\mathbf{k}_3 = \Delta t f(\mathbf{y}_n + a_{31} \mathbf{k}_1 + a_{32} \mathbf{k}_2, t_n + c_3 \Delta t), \quad (3.118)$$

⋮

$$\mathbf{k}_s = \Delta t f(\mathbf{y}_n + a_{s,1} \mathbf{k}_1 + a_{s,2} \mathbf{k}_2 + \cdots + a_{s,s-1} \mathbf{k}_{s-1}, t_n + c_s \Delta t). \quad (3.119)$$

A Runge-Kutta method is therefore specified by the real weights b_i (for $i = 1, \dots, s$), the nodes c_i (for $i = 2, \dots, s$) and the coefficients a_{ij} , which for an explicit scheme

need to be defined for $1 \leq j < i \leq s$. These parameters are usually summarized in a table called *Butcher tableau*, which for the eighth-order Dormand-Prince method is given in Ref. [204].

The Dormand-Prince integrator is further an instance of the Runge-Kutta-Fehlberg methods, which use an adaptive step size to reduce the required numerical effort. The general idea is to advance the function by two methods with different accuracy, and then use a comparison of the propagated results to check the error and adjust the new time-step. Runge-Kutta-Fehlberg methods now aim at finding RK coefficients in a way that as few as possible function evaluations are required. In this relation, the Dormand-Prince integrator involves an eighth-order propagator as well as a combination of a fifth- and a third-order propagator and requires a total of twelve function evaluations. For further details we refer to Ref. [204], which presents also the basis of our numerical implementation.

Runge-Kutta methods have been successfully applied to solve the time-dependent Schrödinger equation [218, 219]. Due to the extensive number of intermediate steps, they are able to reasonably account for the effects of the time-ordering. On the other hand, in the form applied here, RK propagators are not unitary, i.e., the norm of the propagated wavefunction can differ from one; in practice, however, this appears to be only a minor problem¹⁷.

3.6.2 Short-iterative Lanczos propagator

The short-iterative Lanczos propagator [221] is a standard method widely used in simulations of photoionization processes [43, 88, 222]. It is an exponential-type propagator which aims at approximating the action of the time-evolution operator on the wavefunction,

$$|\Psi(t + \Delta t)\rangle = \exp\{-i\hat{H}(t)\Delta t\}|\Psi(t)\rangle. \quad (3.120)$$

The exact calculation of the matrix exponential scales cubically with the dimension of $\hat{H}(t)$, and is thus feasible only for small systems [223]. Moreover, it would make sense only for a time-independent or weakly time-dependent Hamiltonian, where large propagation steps can be taken. Therefore, in the Lanczos method, the matrix exponential is approximated in the *Krylov subspace*,

$$\{|\Psi(t)\rangle, \hat{H}(t)|\Psi(t)\rangle, \hat{H}(t)^2|\Psi(t)\rangle, \dots, \hat{H}(t)^L|\Psi(t)\rangle\} \subset \mathcal{H}_N. \quad (3.121)$$

The *Lanczos recursion* applies the Gram-Schmidt procedure to construct an orthonormal basis $\{|\Phi_k\rangle\}$ of the Krylov subspace according to

$$|\Phi_0\rangle = |\Psi(t)\rangle, \quad (3.122)$$

$$|\Phi_1\rangle = \frac{1}{\beta_0} \left(\hat{H}(t)|\Phi_0\rangle - \alpha_0|\Phi_0\rangle \right), \quad (3.123)$$

$$|\Phi_{j+1}\rangle = \frac{1}{\beta_j} \left(\hat{H}(t)|\Phi_j\rangle - \alpha_j|\Phi_j\rangle - \beta_{j-1}|\Phi_{j-1}\rangle \right), \quad (3.124)$$

where $|\Psi(t)\rangle$ is assumed to be normalized and the real coefficients are given by

$$\alpha_j = \langle \Phi_j | \hat{H}(t) | \Phi_j \rangle, \quad (3.125)$$

¹⁷ We note that there also exist symplectic RK schemes which carry out a unitary propagation [220].

$$\beta_j = \langle \Phi_{j-1} | \hat{H}(t) | \Phi_j \rangle = \| \hat{H}(t) | \Phi_j \rangle - \alpha_j | \Phi_j \rangle - \beta_{j-1} | \Phi_{j-1} \rangle \| . \quad (3.126)$$

The Hamiltonian is represented in the Krylov subspace by

$$\hat{H}_L(t) = \sum_{ij} |\Phi_i\rangle H_{L,ij}(t) \langle \Phi_j|, \quad (3.127)$$

with the symmetric tridiagonal matrix of dimension $(L+1) \times (L+1)$,

$$\mathbf{H}_L = \begin{pmatrix} \alpha_0 & \beta_0 & & \\ \beta_0 & \alpha_1 & \ddots & \\ \ddots & \ddots & \ddots & \beta_{L-1} \\ & \beta_{L-1} & \alpha_L & \end{pmatrix}. \quad (3.128)$$

The exponential of this matrix can easily be evaluated through an eigendecomposition, which usually requires a negligible effort as compared to the Lanczos recursion. The propagated wavefunction is then given by

$$|\Psi(t + \Delta t)\rangle = \sum_{k=0}^L \left(e^{-i\mathbf{H}_L(t)\Delta t} \right)_{0k} |\Phi_k\rangle. \quad (3.129)$$

The Lanczos propagator is explicitly unitary and accurate up to order $\mathcal{O}(\Delta t^L)$. In case the Hamiltonian is non-Hermitian, such as induced by a complex absorbing potential, one must instead apply the Lanczos-Arnoldi recursion which leads to a Hessenberg matrix rather than a tridiagonal matrix [88].

3.6.3 Generalized Crank-Nicolson propagator

The generalized Crank-Nicolson propagator constitutes an extension of the widely used Crank-Nicolson method to higher orders in time [214]. It starts by an expansion of the time-evolution operator in a $[s, s]$ -Padé series and a subsequent factorization of the arising polynomials,

$$\exp\{-i\hat{H}(t)\Delta t\} = \frac{1 - \frac{i\hat{H}(t)\Delta t}{2} - \frac{\hat{H}(t)^2\Delta t^2}{10} + \cdots + a_s \hat{H}(t)^s \Delta t^s}{1 + \frac{i\hat{H}(t)\Delta t}{2} - \frac{\hat{H}(t)^2\Delta t^2}{10} + \cdots + a_s^* \hat{H}(t)^s \Delta t^s} \quad (3.130)$$

$$= \prod_{j=1}^s \frac{1 + \frac{i\hat{H}(t)\Delta t}{z_j^{(s)}}}{1 - \frac{i\hat{H}(t)\Delta t}{z_j^{(s)*}}}. \quad (3.131)$$

The coefficients $z_j^{(s)}$ are found by solving for the zeros of the numerator, which can also be written in closed form with the help of the confluent hypergeometric function [224],

$$1 + \frac{1}{2}z + \frac{1}{10}z^2 + a_3 z^3 + \cdots + a_s z^s = {}_1F_1(-s, -2s, z) \equiv 0, \quad (3.132)$$

which is evaluated at $z = -i\hat{H}(t)\Delta t$ to obtain the numerator of Eq. (3.130). Table 2 collects the coefficients up to order $s = 4$. The ordinary Crank-Nicolson method is obtained for $s = 1$.

Table 2. Coefficients $z_j^{(s)}$ used in the generalized Crank-Nicolson method up to order $s = 4$.

s	$j = 1$	2	3	4
1	-2.00			
2	$-3.00 + i 1.73$	$-3.00 - i 1.73$		
3	-4.64	$-3.68 - i 3.51$	$-3.68 + i 3.51$	
4	$-4.21 + i 5.31$	$-5.79 + i 1.73$	$-5.79 - i 1.73$	$-4.21 - i 5.31$

The wavefunction $|\Psi^{(0)}\rangle = |\Psi(t)\rangle$ is then propagated by applying a series of s intermediate steps of the form

$$|\Psi^{(j)}\rangle = \frac{1 + \frac{i\hat{H}(t)\Delta t}{z_j^{(s)}}}{1 - \frac{i\hat{H}(t)\Delta t}{z_j^{(s)*}}} |\Psi^{(j-1)}\rangle, \quad (3.133)$$

until the wavefunction $|\Psi(t + \Delta t)\rangle = |\Psi^{(s)}\rangle$ is obtained. A single step constitutes a system of linear equations which involves the known wavefunction $|\Psi^{(j-1)}\rangle$ and has to be solved for the unknown $|\Psi^{(j)}\rangle$,

$$\left(1 - \frac{i\hat{H}(t)\Delta t}{z_j^{(s)*}}\right) |\Psi^{(j)}\rangle = \left(1 + \frac{i\hat{H}(t)\Delta t}{z_j^{(s)}}\right) |\Psi^{(j-1)}\rangle. \quad (3.134)$$

The propagated wavefunction is accurate up to order $\mathcal{O}(\Delta t^s)$. Due to the usually large dimension of the Hamiltonian matrix and its sparse structure, we use the biconjugate gradient stabilized method (BiCGstab) for the iterative solution of the linear system [225].

3.6.4 Imaginary time propagation

In order to apply the previous propagation methods to physical problems, one needs to specify a reasonable initial state. Such one is basically obtained via solution of the corresponding time-independent Schrödinger equation, which yields the eigenstates and eigenenergies of the system. Alternatively, selected eigenstates can also be obtained by using the method of *imaginary time propagation* (ITP), which requires only a working implementation of a real-time propagator and thus can save the overhead of solving the stationary problem.

In the ITP method, the real time t is replaced by an imaginary time variable $\tau = -it$, such that the time-evolution operator becomes

$$\hat{U}(\tau) = \exp\{-\hat{H}\tau\}. \quad (3.135)$$

Note that this is the exact form for a time-independent Hamiltonian, i.e., there appears no time-ordering as \hat{H} trivially commutes with itself at different imaginary times. Application of the imaginary time propagator onto a trial state $|\Phi_0\rangle$ leads to

$$\hat{U}(\tau)|\Phi_0\rangle = \hat{U}(\tau) \sum_k C_k |\Psi_k\rangle \quad (3.136)$$

$$= \sum_k C_k e^{-E_k \tau} |\Psi_k\rangle, \quad (3.137)$$

where we inserted the expansion into eigenstates $|\Psi_k\rangle$. Equation (3.137) reveals that $\hat{U}(\tau)$ is not unitary since the absolute values of the expansion coefficients are decreasing or increasing, depending on whether the corresponding energy value is positive or negative. The state with the lowest energy is decreasing the slowest (or increasing the fastest, respectively). Therefore, by repeatedly propagating the wavefunction and applying a renormalization of the coefficients after each step, only the state corresponding to the lowest energy survives. The ITP therefore converges to the system's ground state, unless the initial trial function was chosen orthogonal to the ground state.

Imaginary time propagation has been used in Ref. [226], and was found competitive to sparse matrix diagonalization using the implicitly restarted Lanczos-Arnoldi method. In the MCTDHF method, it presents a crucial step for the calculation of the initial ground state [88]. The results are essentially equivalent to those of MCHF calculations applied in quantum chemistry, but the two implementations differ considerably [59]. In addition to ITP, a scheme called *improved relaxation* exists, which can be used to obtain excited states from an MCTDHF calculation [88, 160]. Finally, we also mention the technique of *adiabatic switching*, which is similar in spirit to ITP but requires only a real-time evolution [227].

3.7 Analysis of the wavefunction

The quantum-mechanical calculations in this work basically proceed in three steps: (i) solution of the time-independent Schrödinger equation to obtain the ground state at time t_0 , (ii) propagation of this state under the action of a laser field up to the system time T , and (iii) extraction of the relevant observables from the many-body wavefunction $|\Psi(T)\rangle$. The present section is devoted to the third step, which is often considered to be the most intricate one [47]. This is particularly true for the MCTDHF wavefunction, where the time-dependent orbitals complicate the analysis.

In the following, we summarize various approaches to extract information appropriate for the MCTDHF and TD-RASCI methods. Most of them are well-known and collected in the MCTDH review of Beck et al. [88]. Others, such as the two-time spectral function and density matrices, are only rarely considered in the literature so far.

3.7.1 One- and two-particle observables

The calculation of expectation values of a one-particle operator $\hat{h}(t)$ is readily performed by using the single-particle density matrix,

$$\begin{aligned}\langle \hat{h}(t) \rangle &= \langle \Psi(t) | \hat{h}(t) | \Psi(t) \rangle \\ &= \sum_{pq} h_{pq}(t) \langle \Psi(t) | \hat{a}_p^\dagger \hat{a}_q | \Psi(t) \rangle \\ &= \sum_{pq} h_{pq}(t) D_{pq}(t).\end{aligned}\tag{3.138}$$

Similarly, one obtains the expectation value of a two-particle operator \hat{g} from the two-particle density-matrix,

$$\begin{aligned}\langle \hat{g} \rangle &= \frac{1}{2} \sum_{pqrs} g_{pqrs} \langle \Psi(t) | \hat{a}_p^\dagger \hat{a}_r^\dagger \hat{a}_s \hat{a}_q | \Psi(t) \rangle \\ &= \frac{1}{2} \sum_{pq} g_{pqrs} d_{pqrs}(t).\end{aligned}\tag{3.139}$$

This way several quantities are calculated in the MCTDHF program, such as the total energy and energy contributions, spatial and momentum expectation values, and others. If the single-particle basis size becomes large, as is often the case in TD-RASCI calculations, the storage of the two-particle density matrix presents a severe problem. It is then advantageous to calculate the needed matrix elements on-the-fly, or, alternatively, employ the many-body representation of the operator \hat{g} ,

$$\langle \hat{g} \rangle = \sum_{IJ} C_I^*(t) C_J(t) \langle I | \hat{g} | J \rangle. \quad (3.140)$$

For the efficient evaluation, one can use the techniques presented in Sect. 3.3.

3.7.2 Ionization yields

The extraction of ionization yields is of central interest to this work. In principle, the yields can be straightforwardly calculated via projection of the wavepacket $|\Psi(T)\rangle$ at the end of the propagation time T onto a specified subset of the Hamiltonian eigenstates $|\Phi_i\rangle$,

$$|\Psi'(T)\rangle = \sum_i' \langle \Phi_i | \Psi(T) \rangle | \Psi(T) \rangle | \Phi_i \rangle. \quad (3.141)$$

For instance, by performing the projection only onto the singly-ionized states, one could extract the singly-ionized part of the wavefunction and from that the ionization yields and other observables. This simple procedure, however, is in practice feasible only for one-particle systems. For others, first, the Hamiltonian is usually much too large to find all the required eigenstates, and second, even if they were somehow obtained, the selection of the relevant states presents a problem in its own right—as a common example, consider the problem of disentangling the singly- and doubly-ionized states, which in principle can be achieved through their asymptotic behavior, but which is not easy to manage in numerical calculations¹⁸.

The workaround is to perform the projection onto approximate eigenstates, which are typically constructed using plane waves or Coulomb functions [43]. There, the concept is to extract the yields from a long-propagated wavepacket at a large distance to the core, so as to diminish the influence of the ionic potential and obtain nearly asymptotic conditions. On the other hand, there also exist approaches which partially include correlations in the final states using, e.g., the J-matrix method [47] or a diagonalization in the radial degrees of freedom [105]. The importance of final state correlations is an actively debated topic at present. It seems, however, that the common sense tends towards the validity of the uncorrelated procedure, see Refs. [43, 229, 230].

In the present work an uncorrelated scheme is applied, in which an electron is considered ionized if it is located outside a distance R to the nucleus. This criterion, visualized in Fig. 20, presents a standard choice in the literature on photoionization [138, 231]. The corresponding single-ionization yield P_1 is given by

$$P_1(t) = \int_{r>R} D(\mathbf{r}, t) d\mathbf{r}, \quad (3.142)$$

where $D(\mathbf{r}, t)$ is the density matrix introduced in Eq. (2.44). Similarly, the double-ionization yield P_2 is obtained from the two-particle density matrix,

$$P_2(t) = \int_{r>R} \int_{r'>R_0} d(\mathbf{r}, \mathbf{r}', t) d\mathbf{r} d\mathbf{r}'. \quad (3.143)$$

¹⁸ Note that this problem is addressed in (exterior) complex scaling schemes [190, 228].

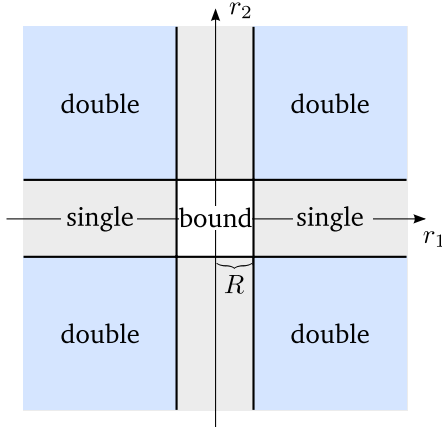


Fig. 20. Ionization criterion used in this work. An electron is considered ionized if it is located outside a distance R from the nucleus. Consequently, the coordinate space is decomposed into regions corresponding to bound states, single-ionization and double-ionization.

In practice, the yields are implemented by calculating the matrix representation of

$$I_{pq}^{(1)} = \langle \phi_p | \theta(r - R) | \phi_q \rangle, \quad (3.144)$$

$$I_{pqrs}^{(2)} = \langle \phi_p \phi_r | \theta(r - R) \theta(r' - R) | \phi_s \phi_q \rangle, \quad (3.145)$$

where θ is the Heaviside function, and then resorting to Eqs. (3.138) and (3.139). In a similar way, one can also calculate angle-resolved ionization yields by restricting the spatial integration to a specified solid angle.

3.7.3 Cross sections

In order to compare with experiments, the ionization yields have to be connected to cross sections. The total generalized cross section σ_N for N -photon absorption is defined as the proportionality constant between the ionization rate Γ_N and the photon flux I/ω [47],

$$\Gamma_N = \sigma_N \left(\frac{I}{\omega} \right)^N, \quad (3.146)$$

where I is the intensity of the field. The total transition probability P_N is obtained by integration over time,

$$P_N = \int_{-\infty}^{\infty} \Gamma_N(t) dt = \frac{\sigma_N}{\omega^N} \int_{-\infty}^{\infty} I(t)^N dt, \quad (3.147)$$

from which the cross section directly follows,

$$\sigma_N = \left(\frac{\omega}{I_0} \right)^N \frac{1}{T_{\text{eff},N}} P_N. \quad (3.148)$$

Here, T_{eff} is the effective time for an N -photon process [43],

$$T_{\text{eff},N} = \int_{-\infty}^{\infty} \left(\frac{I(t)}{I_0} \right)^N dt. \quad (3.149)$$

For a laser field with squared-sine envelope, it evaluates to

$$T_{\text{eff},1} = \int_0^T \sin^4 \left(\pi \frac{t}{T} \right) dt = \frac{3}{8} T, \quad (3.150)$$

$$T_{\text{eff},2} = \int_0^T \sin^8 \left(\pi \frac{t}{T} \right) dt = \frac{35}{128} T. \quad (3.151)$$

The previous results can be summarized by compact formulas for the single- and double-ionization cross sections [47],

$$\sigma_1 [\text{cm}^2] = 1.032 \cdot 10^{-4} \frac{\omega^2 P_1}{n I_0}, \quad (3.152)$$

$$\sigma_2 [\text{cm}^4 \text{s}] = 2.28 \cdot 10^{-23} \frac{\omega^3 P_2}{n I_0^2}, \quad (3.153)$$

where n represents the number of cycles in the pulse, ω is the frequency in eV and I_0 is the intensity in W/cm².

A comment on the validity of these formulas is in order. Due to the definition of the cross section as the transition amplitude in lowest non-vanishing order of perturbation theory, the peak intensity has to be sufficiently low in order to avoid processes induced by higher-order photon absorption. Further, only the direct process can be described, since sequential ionization leads to a transition probability growing quadratically in time, which prevents the definition of a time-independent cross section [47]. For corresponding expressions of cross sections appropriate for sequential ionization processes, see Ref. [43].

3.7.4 Time-independent picture of the MCTDHF method

The particular time-dependence of the MCTDHF expansion, though very compact and efficient, significantly complicates the analysis. For example, it can be a complicated task to calculate the occupation of atomic orbitals during the time-evolution. It is therefore convenient to possess an alternative time-independent MCTDHF expansion, which is received through

$$\begin{aligned} |\Psi(t)\rangle &= \sum_I C_I(t) |\phi_{i_1}(t) \cdots \phi_{i_N}(t)\rangle \\ &= \sum_J \left[\sum_I C_I(t) (\mathbf{b}(t) \otimes \cdots \otimes \mathbf{b}(t))_{i_1 \cdots i_N, j_1 \cdots j_N} \right] |\psi_{j_1} \cdots \psi_{j_N}\rangle \\ &= \sum_J \tilde{C}_J(t) |\psi_{j_1} \cdots \psi_{j_N}\rangle. \end{aligned} \quad (3.154)$$

In the second line, we inserted the basis expansion into a set of time-independent basis functions $\{\psi_k\}$ and let the expansion coefficients $\mathbf{b}(t)$ act only on the wavefunction coefficients $C_I(t)$. This leads to the full CI expansion corresponding to the MCTDHF wavefunction (3.154). However, as the full CI wavefunction is in most cases too complex to handle—this is just the reason why MCTDHF is usually employed—it might be more useful to consider the related one-particle density matrix, which is given by

$$\mathbf{D}^{(0)}(t) = \mathbf{b}^\dagger \mathbf{D}(t) \mathbf{b}. \quad (3.155)$$

Note that the transformation matrix \mathbf{b} is of dimension $M \times N_b$, such that the density matrix $\mathbf{D}^{(0)}$ has the dimension of the time-independent basis.

The diagonal elements of the density matrix now contain the occupation of the time-independent orbitals during the propagation. If necessary, one can further apply a unitary transformation to the time-independent basis in order to arrive at a more meaningful basis set, e.g., the Hartree-Fock orbitals.

3.7.5 Momentum spectra

Momentum spectra can be obtained from the density matrix by

$$D(\mathbf{p}, t) = \sum_{pq} D_{pq}(t) \phi_p^*(\mathbf{p}) \phi_q(\mathbf{p}), \quad (3.156)$$

where the Fourier transform of the basis functions is given by

$$\phi_p(\mathbf{p}) = \frac{1}{\sqrt{2\pi}} \int e^{-i\mathbf{pr}} \phi_p^*(\mathbf{r}) d\mathbf{r}. \quad (3.157)$$

For MCTDHF calculations, where the basis functions are time-dependent and expanded into a time-independent basis according to

$$\phi_p(\mathbf{r}, t) = \sum_i b_{pi}(t) \psi_i(\mathbf{r}), \quad (3.158)$$

it is sufficient to calculate the Fourier transform of the time-independent basis functions once, and then evaluate the spectrum through

$$D(\mathbf{p}, t) = \sum_{ij} D_{ij}^{(0)}(t) \psi_i^*(\mathbf{p}) \psi_j(\mathbf{p}), \quad (3.159)$$

where the density matrix $\mathbf{D}^{(0)}(t)$ in the time-independent basis has been introduced in the previous subsection.

In this work, we are usually concerned with the momentum spectrum of the ionized fraction of the wavefunction. This can be obtained by performing the Fourier transform only over the space outside the ionization radius, a procedure which has been suggested in Ref. [232].

3.7.6 Autocorrelation function

The autocorrelation function gives access to the excitation spectrum of the system induced by an external perturbation, and is defined as

$$S(t, t') = \langle \Psi(t) | \Psi(t') \rangle. \quad (3.160)$$

Its information content is most clearly revealed by considering a time-independent Hamiltonian and inserting the expansion of $|\Psi(0)\rangle$ into eigenstates,

$$\begin{aligned} S(t, t') &= \langle \Psi(0) | e^{-i\hat{H}(t'-t)} | \Psi(0) \rangle \\ &= \sum_{nm} C_m^* C_n \langle \Psi_m | e^{-i\hat{H}(t'-t)} | \Psi_n \rangle \\ &= \sum_n |C_n|^2 e^{iE_n(t-t')}. \end{aligned} \quad (3.161)$$

By taking the Fourier transform with respect to the relative time $\tau = (t - t')$, one obtains the spectrum,

$$\begin{aligned} S(E) &= \int e^{i(E+E_0)\tau} S(t, t') d\tau \\ &= \sum_n |C_n|^2 \int e^{i(E-(E_n-E_0))\tau} d\tau, \\ &\rightarrow \sum_n |C_n(T)|^2 \delta(E - (E_n - E_0)), \end{aligned} \quad (3.162)$$

where we further applied a frequency-shift by the ground state energy E_0 . The spectrum is peaked at the excitation energies, and the heights of the peaks render the occupation of the corresponding eigenstates. In case of a time-independent Hamiltonian, the autocorrelation function depends only on the relative time τ , whereas a time-dependent Hamiltonian also leads to a modulation along the center-of-mass coordinate $T = (t + t')/2$. Then, for instance, a Fourier transformation of $S(\tau, T)$ leads to the quantity $S(E, T)$, which gives the variation of the spectrum over time. The practical evaluation of the autocorrelation function is considered in appendix A.4.

The autocorrelation function has been used in a single-time formulation by Nest et al. [160] to determine excited states of atoms and molecules from an MCTDHF calculation. In Ref. [233], it is used to extract the photo-electron spectra of the hydrogen atom and the molecular hydrogen ion. In both applications, the system is propagated for an amount of time after the external perturbation has ended, and the excitation spectrum is determined via Eq. (3.162). The two-time version of the autocorrelation function has been considered in signal theory and is known as the *Wigner-Ville function* [234]. It bears some similarities to the definition of the Wigner distribution or non-equilibrium Green function [54]. We are, however, not aware of an application to extract information from quantum-mechanical many-body wavefunctions.

3.7.7 Two-time density matrix

A useful generalization of the autocorrelation function is given by the two-time density matrix,

$$D_{pq}(t, t') = \langle \Psi(t) | \hat{a}_p^\dagger \hat{b}_q | \Psi(t') \rangle. \quad (3.163)$$

Here it is assumed that $|\Psi(t)\rangle$ is composed of the orbitals $\{|\phi_p\rangle\}$ which are created/annihilated by $\hat{a}_p^{(\dagger)}$, while $\hat{b}_q^{(\dagger)}$ and $\{|\psi_q\rangle\}$ are the excitation operators and orbitals related to $|\Psi(t')\rangle$. The evaluation of Eq. (3.163) is detailed in appendix A.5. In principle, the two-time density matrix can be used to obtain the spectrum related to one-electron operators \hat{O} ,

$$O(t, t') = \langle \Psi(t) | \sum_{pq} \langle \phi_p | \hat{O} | \psi_q \rangle \hat{a}_p^\dagger \hat{b}_q | \Psi(t') \rangle \quad (3.164)$$

$$= \sum_{pq} \langle \phi_p | \hat{O} | \psi_q \rangle D_{pq}(t, t'). \quad (3.165)$$

Again, a transformation to center-of-mass and relative coordinates and a subsequent Fourier transformation lead to the spectrum. By taking \hat{O} to be a projection operator, for instance, one can extract the spectrum from a certain region in space, or concentrate on a specified angular momentum quantum number.

A particular application of the previous idea is given by the *flux formalism*, which has been introduced in the context of MCTDH by Jäckle and Meyer [235]. There, a sophisticated derivation leads to the consideration of the two-time expectation value of the complex absorbing potential operator \hat{W} , which is non-zero only in the asymptotic region and therefore extracts the spectrum of the ionized particle. The flux formalism has been recently applied by Haxton et al. to the photoionization of beryllium and molecular hydrogen [73, 74].

The two-time density matrix has a close relationship to the non-equilibrium Green function, which is basically defined as¹⁹

$$G_{pq}(t, t') \sim \langle \Psi_0 | \hat{a}_p^\dagger(t) \hat{a}_q(t') | \Psi_0 \rangle, \quad (3.166)$$

where $|\Psi_0\rangle$ is the ground state of the system. In contrast to the two-time density matrix in Eq. (3.163), here the creation- and annihilation operators are given in Heisenberg representation. As a short calculation for the example of a time-independent Hamiltonian shows, this fact has a direct influence on the information content. The two-time density matrix $D_{pq}(t, t')$ contains the information on the total energy E_{pq} of the state in which an electron has been excited from orbital p to orbital q . On the other hand, the non-equilibrium Green function $G_{pq}(t, t')$ oscillates with a frequency of $(E_{pq} - E_0)$ along the relative-time coordinate and thus contains the excitation and ionization energies, respectively.

The definition of the two-time density matrix can be readily extended to a larger number of excitations. For instance, one can employ the two-particle two-time density matrix to set up a corresponding flux formalism, which extracts the information only from the doubly-ionized fraction of the wavefunction. Work is in progress to reveal the capabilities of this interesting quantity.

3.7.8 Extended Koopmans theorem

The extended Koopmans theorem (EKT) presents a convenient method to obtain information on the ionization energies of an N -particle system without having to consider the $(N - 1)$ -particle system explicitly. It originates from the basic idea that the N -particle wavefunction remains valid if one particle is removed to infinity, and therefore already includes information on the ground state of the ion [236]. In second quantization, the $(N - 1)$ particle state can be set up through

$$|\Psi_{N-1}\rangle = \sum_p d_p \hat{a}_p |\Psi_N\rangle, \quad (3.167)$$

i.e., it is approximately expressed by a set of N_b Slater determinants of the $(N - 1)$ -particle Hilbert space which are believed to be of particular importance for the description of the ion. The expansion coefficients $\{d_k\}$ are found by requiring the energy of the ion to be minimal. The usual Raleigh-Ritz variation of the energy expression in the $(N - 1)$ -particle basis then leads to the generalized eigenvalue problem

$$\sum_q \langle \Psi_N | \hat{a}_p^\dagger \hat{H} \hat{a}_q | \Psi_N \rangle \Delta_q = \sum_q \varepsilon_q \langle \Psi_N | \hat{a}_p^\dagger \hat{a}_q | \Psi_N \rangle \Delta_q. \quad (3.168)$$

The negative eigenvalues $-\varepsilon_q = E_N - E_{N-1,q}$ are the ionization energies for removal of an electron from the orbital $|\psi_q\rangle$, and the eigenvectors

$$|\phi_q\rangle = \sum_j \Delta_{q,j} |\psi_j\rangle \quad (3.169)$$

¹⁹ The true definition actually involves a further constant $-i$ as well as the time-ordering operator on the Keldysh contour [54].

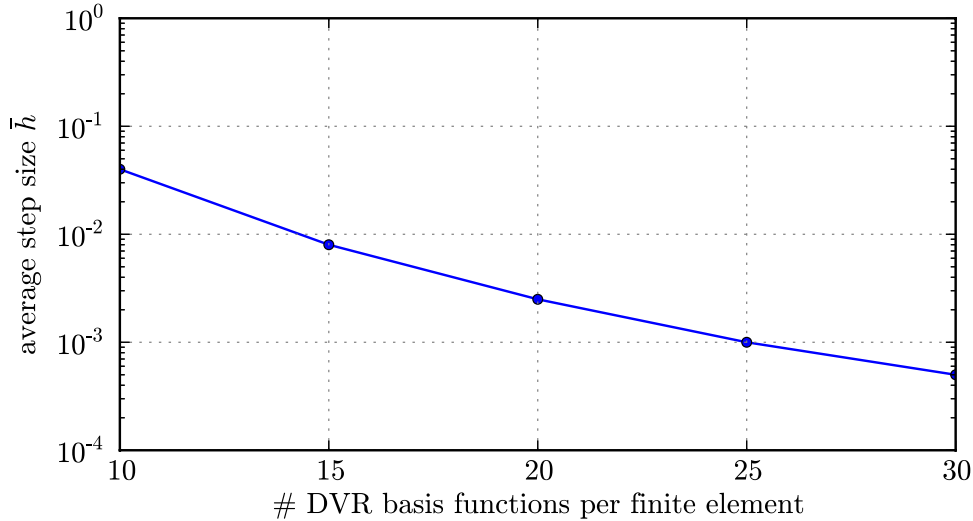


Fig. 21. Dependency of the step size on the number of DVR basis function per finite element without stiffness reduction. The angular basis contains spherical harmonics with azimuthal quantum numbers l up to 2.

yield the corresponding Dyson orbitals [237]. Using the fact that $|\Psi_N\rangle$ is further an eigenstate of the Hamiltonian, Eq. (3.168) can also be rewritten as [236]

$$\mathbf{F} \Delta = \varepsilon \mathbf{D} \Delta, \quad (3.170)$$

where, using the single- and two-particle density matrices of the ground state wavefunction, \mathbf{F} is given by

$$F_{ik} = \sum_q h_{iq} D_{kq} + \sum_{qrs} g_{iqrs} d_{kqrs}. \quad (3.171)$$

For a single-determinant ansatz, Eq. (3.170) reduces to the Hartree-Fock equation, in which case one recovers the standard Koopmans theorem.

3.8 Stiffness reduction

This subsection is devoted to the issue of stiffness as it may prevent application of the MCTDHF equations to complex systems. In the first part of the section, we will discuss the root cause of the problem and then present several methods which are commonly applied to this problem. In the second part, we will propose a domain-specific solution for this problem and outline a possible implementation.

3.8.1 Introduction

As observed in [238], the step size, which was used for the numerical integration of the MCTDHF equations, decreases, if we increase the size of the used basis set. This phenomenon is demonstrated in Fig. 21 for atomic helium. Due to its simplicity, we will use helium as the test case throughout this section, using the FEDVR/spherical harmonic basis for the numerical description. The radial basis extends over a range of

100 a.u. divided into 25 finite elements. The magnetic quantum number m is 0 for all basis functions throughout this section. The entire system is always propagated over a time range of 150 a.u. without any excitations. Since we did not change the physical system, this cannot be a property of the solution and must be a result of the numerical description. Such behavior, where the step size is determined by other factors rather than the solution, are commonly known as stiffness [204] in computational science. To illustrate the origin of the stiffness, we consider the time-dependent Schrödinger equation

$$i \frac{\partial}{\partial t} |\Psi(t)\rangle = \hat{H} |\Psi(t)\rangle \quad (3.172)$$

with a time-independent Hamiltonian \hat{H} . As is commonly known, the solution of Eq. (3.172) can always be written as an expansion

$$|\Psi(t)\rangle = \sum_k c_k e^{\frac{i}{\hbar} E_k t} |E_k\rangle \quad (3.173)$$

of the state $|\Psi(t)\rangle$ into energy eigenstates $|E_k\rangle$ with some initial expansion coefficients c_k . In numerical calculations, all eigenstates are always at least weakly occupied due to rounding errors, hence all eigenstates contribute to the solution. Despite the low occupancy of eigenstates with large energy eigenvalues in physical systems due to the lack of strong enough excitations, the used integration algorithm tries to resolve the highly-oscillating terms, which correspond to these eigenstates, in the expansion (3.173). According to the Nyquist-Shannon sampling theorem the maximal step size which can be used to resolve the oscillations is $h_{\max} \propto \frac{1}{E_{\max}}$, where E_{\max} is the largest absolute value of any of the E_k . If this condition is not satisfied, an explicit integration scheme would become numerical unstable. The used integrator with adaptive step size adjusts the step size accordingly to prevent this instability. In the case that we increase the size of the basis set and keep all physical parameters of the system constant, E_{\max} starts to rise and the step size has to be consequently decreased, resulting in the observed effect. In the following, we will examine several possible methods to prevent the effect of the stiffness.

3.8.2 Prior work

The natural approach to counter the numerical instability of explicit integrators is the application of stable algorithms. This is further complicated by the fact that the orbital equations are non-linear which rules out most methods. Nevertheless, some implicit integration schemes, such as implicit Runge-Kutta methods or BDF-integrators, are known to exhibit this property by damping the occurring errors, instead of accumulating them [204]. The common downside of these methods compared to explicit methods is that one needs to solve a system of equations in every integration step, which in the worst case might be non-linear. In either case, commonly used implementations need to calculate the Jacobian matrix

$$J := \left(\frac{\partial f_i(x_1, \dots, x_n)}{\partial x_j} \right) \quad (3.174)$$

of the system function f repeatedly during the integration process. While many approaches to evaluate the Jacobian matrix—like analytical derivation, finite differences [204, 239], and automatic differentiation [240, 241]—exist, one has to be aware, that each method has its downsides. To avoid obstacles like an increased maintenance

burden or numerical instability [239] one would need to carefully choose an algorithm, which might not be possible at all in general.

Even if we are able to theoretically calculate the Jacobian, we would need to populate all of its elements, implying at least one evaluation of the system function for each element. This would lead to several billion evaluations in some typical cases. Under the consideration that the system function is by far the most expensive part of an MCTHDF calculation, the runtime of the program would be greatly increased by the application of an implicit method for more complicated systems. Since this restricts the entire algorithm to simple systems, while greatly increasing the time spent on the implementation, we consider this approach impractical for our purposes.

3.8.3 Energy subspace projection method

In [238], we have proposed the energy subspace projection (ESP) method as a means to solve the stiffness issue at its root. The application of a domain-specific scheme allows a much handier approach than more generic methods. In the subsequent paragraphs, we will introduce the theoretical foundation of the scheme and present our implementation.

Introduction. To avoid the aforementioned problems of the generic methods described in the previous section, we propose a domain-specific solution, the energy subspace projection (ESP) method, as a possible solution. The major advantage of such an approach over a fully generic method is that one can tailor the scheme to the specific structure of this domain, which often makes the solution more suitable. As already shown in Sect. 3.8.1, the root cause of the stiffness are the high energy eigenvalues in the Hamiltonian. Since the corresponding expansion coefficients are—due to their non-physical origin—small in the majority of cases, it is a valid approximation to truncate the expansion (3.173) by discarding these coefficients. This directly eliminates the highly-oscillating terms in Eq. (3.173). From a linear algebra perspective, truncation is a projection onto the subspace spanned by the energy eigenvectors with desired eigenvalues, hence the name of the method. To our best knowledge, this is the first time that such a method was applied to a quantum mechanical problem.

As a simplification, we will first develop the method by applying our idea to the time-dependent Schrödinger equation

$$i \frac{\partial}{\partial t} \mathbf{c} = \mathbf{H} \mathbf{c}, \quad (3.175)$$

which was discretized using an arbitrary basis of size N_b , before we try to incorporate the scheme into the much more complex MCTDHF algorithm.

To proceed, we need to identify the spurious eigenvalues and their associated coefficients. In the general case this would require a quite sophisticated scheme, since one has to consider the occupation of the eigenstates, as we only can discard the lowly occupied states safely. Since in practice all energy levels above a certain threshold are lowly occupied, we decided to rely on the user to pick a suitable energy threshold E_{cutoff} , hence known as cutoff energy, using his knowledge of the physical system. While this method might ignore some of the spurious eigenvalues, the implementation is greatly simplified by this choice and performs quite well for all practical purposes. In what follows, it is assumed that the energy eigenvalues are sorted in increasing order. In practice this is not an issue, since almost all linear algebra tools already calculate the eigenvalues in this order. Due to the order, the cutoff energy directly corresponds to an index N_c for which the property

$$i \in [0, N_c] \iff E_i < E_{\text{cutoff}} \quad (3.176)$$

holds. It should be noted that we ignore the problem of negative eigenvalues with a large absolute value at this point, as we will see in Sect. C.1.2 that this case is difficult to handle and has barely any practical relevance. Using this cutoff index N_c , one can now define the truncation matrix $\tilde{\mathbf{L}}$, which reads

$$\tilde{\mathbf{L}} := \begin{pmatrix} \mathbb{1}_{N_c \times N_c} & 0 \\ 0 & 0 \end{pmatrix} \quad (3.177)$$

in block matrix representation. If applied to the coefficient vector $\tilde{\mathbf{c}}$, the truncation matrix precisely sets the spurious coefficients to zero, while preserving the desired coefficients. Since the expression $\mathbb{1} - \tilde{\mathbf{L}}$ will be used frequently below, it is convenient to define it as the remainder matrix

$$\tilde{\mathbf{R}} := \mathbb{1} - \tilde{\mathbf{L}}. \quad (3.178)$$

Since we apply these matrices to quantities which are represented in our arbitrarily chosen basis, we need to transform them back from the basis of energy eigenfunctions into the chosen basis via their corresponding basis transformation \mathbf{V} , which leads to the expressions

$$\mathbf{L} := \mathbf{V}^\dagger \tilde{\mathbf{L}} \mathbf{V} \quad (3.179)$$

and

$$\mathbf{R} := \mathbf{V}^\dagger \tilde{\mathbf{R}} \mathbf{V}. \quad (3.180)$$

Using the identity

$$\mathbb{1} = \mathbf{L} + \mathbf{R} \quad (3.181)$$

the right-hand side of equation (3.175) can be rewritten as

$$\mathbf{H}(\mathbf{L} + \mathbf{R})\mathbf{c} = \mathbf{H}\mathbf{L}\mathbf{c} + \rho(\mathbf{c}) \quad (3.182)$$

with a remainder term

$$\rho(\mathbf{c}) = \mathbf{H}\mathbf{R}\mathbf{c}. \quad (3.183)$$

If we discard the remainder term in Eq. (3.182), we have already achieved our goal to eliminate the spurious eigenvalues. The success of our approach can easily be verified on the helium test system, as shown in Fig. 22. As we see, the average step size remains constant, even if we increase the size of the basis set. This leads to a significant drop decrease of the runtime which is depicted in Fig. 23. This shows, that we gain a significant speedup of over an order of magnitude for large basis sets due to the reduced stiffness of the system. Figure 24 illustrates that the average step size is actually proportional to the inverse maximal energy—which should be roughly the cutoff energy—as already mentioned in Sect. 3.8.1. The plateau for small energies exists due to other effects like the real variation of the solution which demands a certain step size. This value will be even larger if we increase the size of the basis set further to treat more complex systems than helium. The implementation of the algorithm which we used to produce this results is described in Sect. C.1 together with an analysis of the introduced cutoff error.

3.8.4 Summary and extensions

In the preceding paragraphs, we were able to pinpoint the origin of the stiffness and developed a scheme, which is able to eliminate the stiffness, while avoiding the high costs of implicit integration methods. In addition, we were able to show that the truncation error introduced by this scheme can be neglected for most practical purposes if the threshold for the truncation is chosen accordingly. To conclude this section, we give some possible extensions, which might enhance the scope or increase

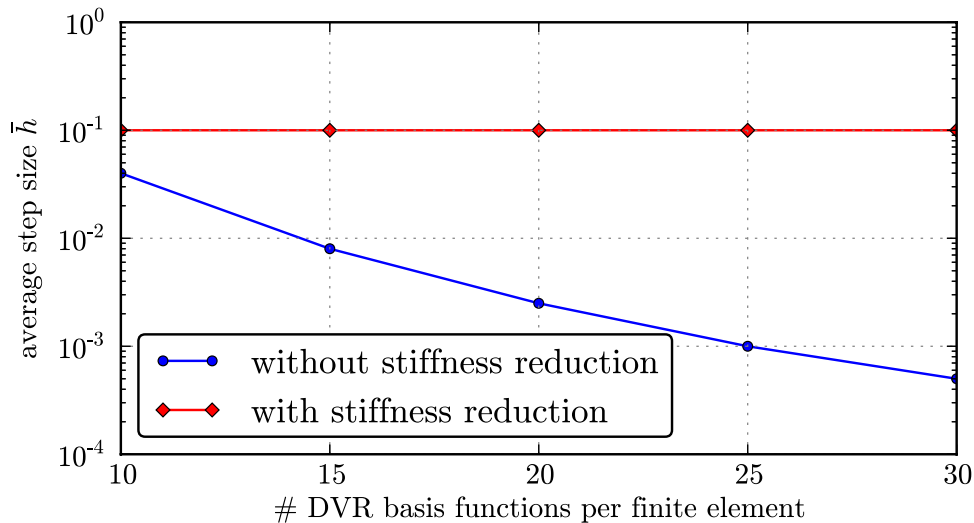


Fig. 22. Dependency of the step size on the number of DVR basis functions per finite element with and without stiffness reduction. The angular basis contains spherical harmonics with azimuthal quantum numbers l up to 2.

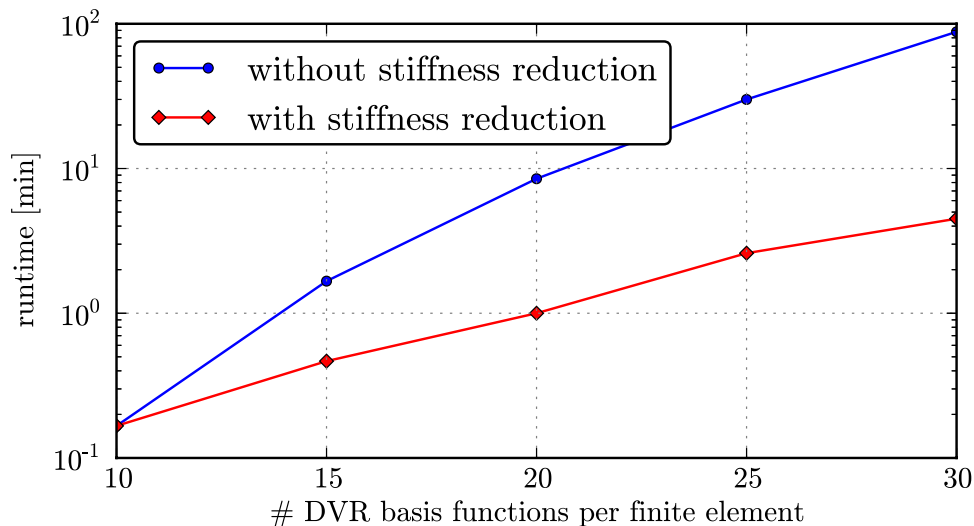


Fig. 23. Dependency of the runtime on the number of DVR basis functions per finite element with and without stiffness reduction. The angular basis contains spherical harmonics with azimuthal quantum numbers l up to 2.

the practicality of the method in different situations:

- While we decided to use a quite simple scheme to select the eliminated eigenvalues, one could imagine more sophisticated methods. For example, one could use the error estimator, which is presented in C.1.1, to incrementally purge energy eigenfunctions, from the lowest occupied to the highest occupied, as long as a user-specified error bound is undershot. This would allow the application of the method to systems with strongly changing occupations over a large region of energies.

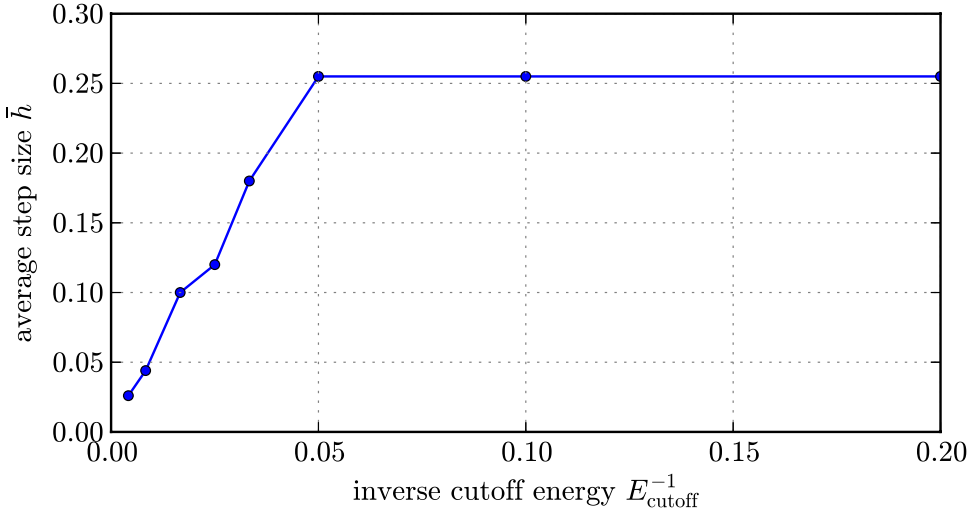


Fig. 24. Dependency of the step size on the inverse cutoff energy. The angular basis contains spherical harmonics with azimuthal quantum numbers l up to 4.

- Another improvement would be the restriction of the projector to a specific subspace. This can be important for large Hilbert spaces, if the spurious eigenvalues are only originating from a very small subspace. Therefore, it would be a waste of computational resources, to apply the scheme to the entire Hilbert space. A classic example is the description of atomic systems with localized basis sets, where the basis functions lie very dense in the small core region. On the other hand, the basis functions in the larger outer part of the space lie relatively sparse and do not contribute to the stiffness, while spanning the largest part of the Hilbert space. An experimental implementation of this feature shows very promising results for such systems.

3.9 Parallelization

In this section, we will outline a possible parallelization scheme for the MCTDHF equations and introduce the necessary tools to explore its characteristics. In the last part of this section, we will perform such a survey and will discuss the consequences.

3.9.1 Motivation

While the ESP method described in Sect. 3.8 tries to accelerate the MCTDHF scheme by improving the algorithm, a much more direct approach to accelerate the application would be the use of more computational resources in the form of parallelization. Due to the fact that virtually every modern computer has several processing units, parallelization is getting more and more important—even outside of the traditional high-performance computing (HPC) field—, since a serial program would waste valuable resources. As most cluster computers are distributed-memory systems we will focus on this kind of parallelization. While we can only give a short introduction into the field of parallelization due to spatial and temporal constraints, we deem the results too important to be ignored.

3.9.2 The algorithm

In order to speed up the MCTDHF calculations, we have implemented a parallelization scheme for distributed-memory clusters using the well-known Message Passing Interface (MPI). The basic idea of the scheme is the parallel calculation of all two-particle quantities during a time step. This is possible since all two-particle quantities are 4-tensors of the form A_{pqrs} and computations regarding different values of the multi-index (rs) are completely independent of each other. Hence, we can trivially distribute the work over all processes, by splitting the computation of all tensors over the multi-index (rs) . The only common dependency of all computations is the current state, which can be easily distributed to all processes at the beginning of a time step. To perform the computations, the set of processes is divided into a master process which controls the execution of all code and several worker processes which only perform parallel computations. During the execution of a parallelized region of code, the master node behaves in the same way as a worker node. The application of this scheme leads to the following steps, which are performed during each time step:

1. Broadcast the current state from the master process to all worker processes.
2. Calculate all single-particle quantities within the master process.
3. Transform the electron integrals partially within every process in parallel.
4. Calculate the two-particle contributions of the orbital and wavefunction equation partially within every process in parallel.
5. Reduce all partially calculated two-particle contributions within the master process. This yields the full two-particle contributions.
6. Combine the one-particle and two-particle contributions.

After the last step, the MCTDHF equations are integrated within the master process and the algorithm starts again at the first step.

3.9.3 Performance measurements

To test the behavior of our implementation on a real system, we used atomic helium as a test system. The ground state was propagated over 100 a.u. without any excitation. The FEDVR/spherical harmonics basis was used for the numerical description of the system. The radial basis extends over a range of 400 a.u. and is divided into 80 finite elements. Each finite element contains 15 DVR basis functions. The maximal azimuthal quantum number of the angular basis is $l_{max} = 2$, while all angular basis functions have a magnetic quantum number of $m = 0$. The calculations were carried out on the ice2-queue of the Norddeutscher Verbund für Hoch- und Höchstleistungsrechnen (HLRN). To compare the behavior of the algorithm under different circumstances, we used the usual performance metrics, namely the weak scaling behavior [242] and the Karp-Flatt metric [243]. As we are more interested in enabling the simulation of more complex systems rather than reducing the simulation time, we will not discuss the strong scaling behavior [244] at this point. In addition to the original sources, a short discussion of the performance metrics and their application can be found in Sect. C.2. To examine the weak scaling behavior, we chose the number of processors as $P = n^2 = M^2$.

Figure 25 shows the weak scaling behavior of the algorithm, with and without the ESP scheme, in comparison to the ideal behavior. We observe that the scaling behavior of our parallelization scheme is by no means ideal, even if we see a reasonable speedup. It is evident that application of the ESP scheme during the propagation, changes the scaling behavior of the MCTDHF scheme. To understand this, we look at the serial fraction of the algorithm, which was calculated with the Karp-Flatt

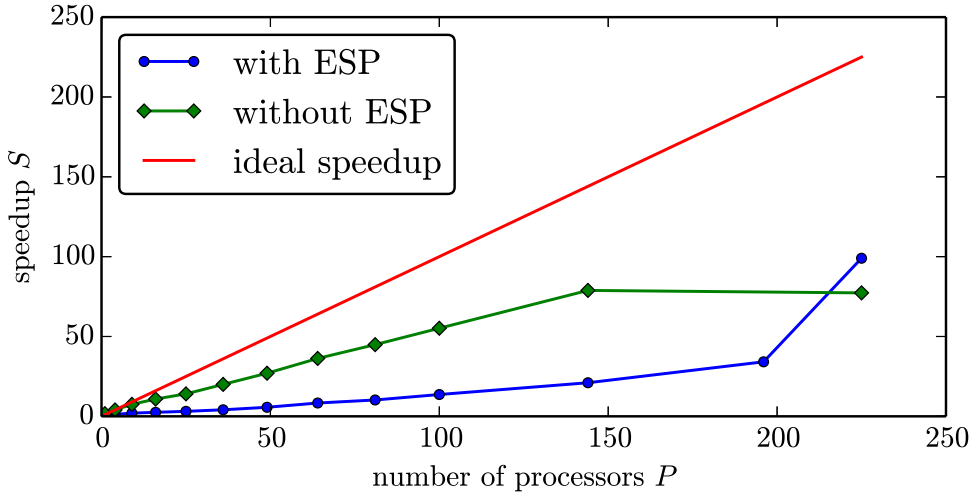


Fig. 25. Comparison of the speedups for the test system with the ideal speedup with and without the application of the ESP scheme. The algorithm was executed in a weak scaling fashion.

metric (C.18). The serial fraction is shown in Fig. 26 as a function of the number of processors. We observe that the serial fraction is almost zero, if we do not apply the ESP scheme, but starts at a larger value otherwise. This explains the inferior results, when using the ESP scheme in addition to the parallelization, as we spend more time in a non-parallelized portion of the algorithm. The decay of the serial fraction can be explained if we compare the asymptotical runtime of the ESP scheme with the asymptotical runtime of the parallelized portion. The calculation of the two-particle quantities lies in $O(M^2)$, whereas the EPS scheme lies in $O(M)$. Hence, the ratio between the time spent in the serial EPS algorithm and the time spent on the parallel calculation of two particle quantities drops with the number of orbitals M , and thereby with the number of processors P . This also explains the huge jump in the speedup for a large number of processors which we see in Fig. 25. Another feature of the algorithm is depicted in Fig. 26. We note that the serial fraction of the parallel algorithm—which was obtained using Eq. (C.17) and denoted as the parallel serial fraction—is roughly constant, even if the ESP scheme is not applied. The difference between the parallel serial fraction and the serial fraction is that the parallel serial fraction is calculated from an actual parallel run of the program, while the serial fraction is calculated with regard to a serial run. This shows us that the poor scaling in this case is caused by the remaining serial portions of the algorithm, which are identical to the calculation of the single-particle contributions. If we would parallelize these parts, we should observe a significant improvement of the scaling behavior.

3.9.4 Summary

In the previous paragraph, we have observed that we have successfully parallelized the MCTDHF program. While the obtained speedups are by no means optimal, due to the mentioned reasons, it is a success from a practical point of view. Due to the reduced runtime, we were able to treat much more complex system with increased accuracy. We hope to circumvent the causes of the mentioned shortcomings in the future by using a more elaborate parallelization scheme.

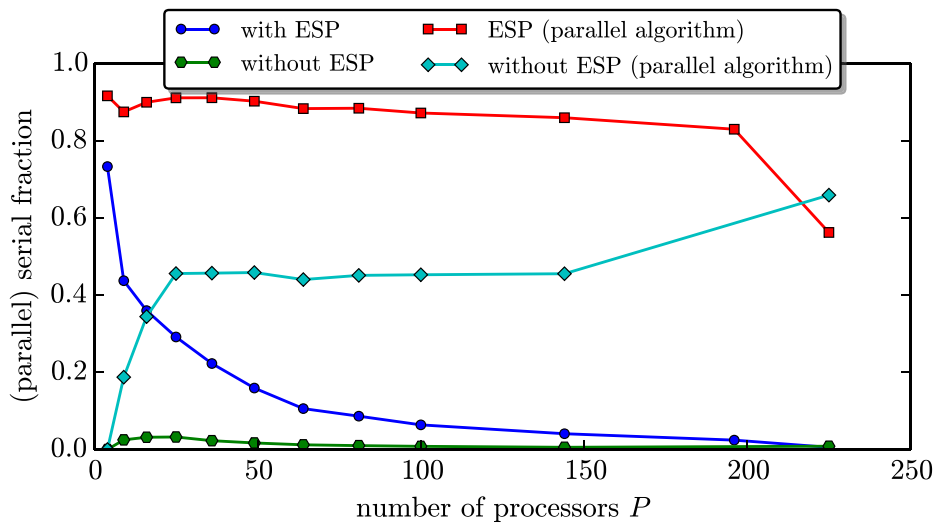


Fig. 26. (Parallel) serial fraction of the (parallel) algorithm in dependency of the number of processors for the test system. All quantities were computed from the speedups shown in Fig. 25.

3.10 Computational implementation of MCTDHF

In the following, we briefly summarize the main ideas underlying the computational implementation of the MCTDHF formalism and give some suggestions for the overall structure of a typical MCTDHF code. This is based on the experience with our own MCTDHF code, dubbed *Kiel MCTDHF*, which has been initiated by one of us (DH) in 2008. Since then, the code has evolved into a general and versatile tool for the ab-initio simulation of quantum-mechanical atoms and molecules, as well as several other physical systems.

3.10.1 Structure of a typical MCTDHF code

A main focus has been lying on a generic implementation, which allows for the application of the MCTDHF scheme to a diverse set of systems in a single framework. The main idea is the separation of single-particle basis, the many-particle basis and the generic MCTDHF implementation. A major advantage of this separation is that one can easily exchange either the single-particle or the many-particle basis—if this is necessary—while the implementation retains the possibility to use basis-specific properties to accelerate the computation of various quantities. This scheme leads to a chain of responsibilities where the generic MCTDHF implementation queries the many-particle basis for the specific quantities, which itself will delegate the basis-dependent portions of its work to the specific single-particle basis. The substitutability of all components is enforced by generic interfaces between each link in this chain.

The basic program flow of the resulting algorithm is shown in Fig. 27: At the beginning, the required parameters are collected from an initialization file or from the command line. Then, the single-particle basis and the electron integrals are constructed and the Slater determinants/permanents are initialized. Subsequently, the wavefunction and orbital expansion coefficients are propagated first in imaginary time,

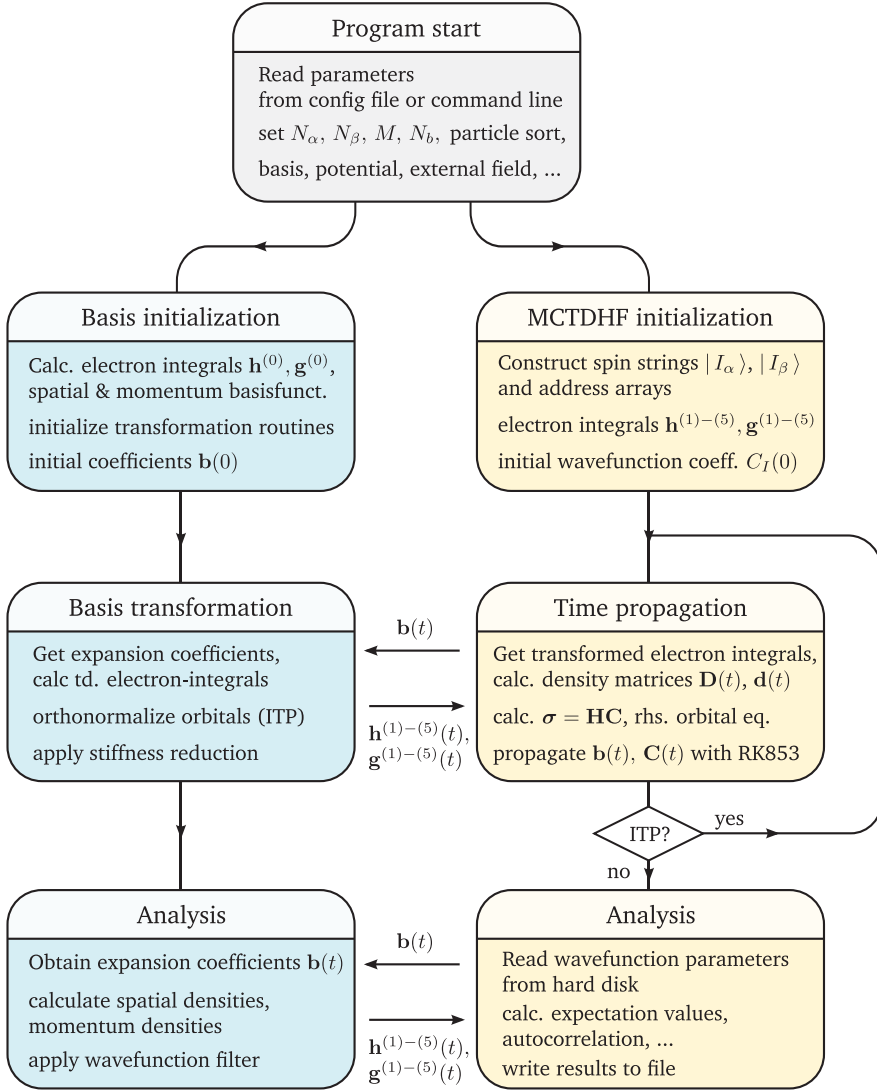


Fig. 27. Illustration of the program flow of the MCTDHF code. The main idea is the separation of single-particle basis routines and the generic MCTDHF implementation. By this, several basis sets can be implemented in a single framework, which allows the efficient treatment of a variety of one-, two- and three-dimensional systems. At the same time, for a given basis set one can implement a set of optimized transformation routines and therefore account for a special structure of the electron integrals.

and later in real time. For the evaluation of the Hamiltonian and the right-hand side of the orbital equation, the transformed electron integrals are required, which can be queried from the single-particle basis. The integration of the MCTDHF equations of motion is performed with any suitable ODE integrator. From our experience, the eighth-order Dormand-Prince integrator (here labeled RK853) leads to decent results both in accuracy and computational cost. During the propagation, the propagated MCTDHF wavefunction is stored on hard disk at selected time points. Subsequent to the real-time propagation, the simulation is analyzed using the methods of Sect. 3.7.

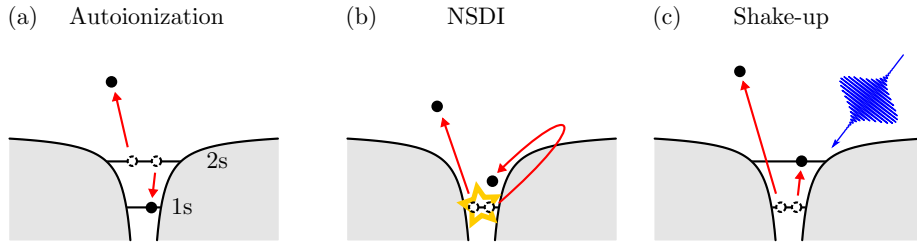


Fig. 28. Correlated processes in helium: (a) Autoionization, where the decay of a doubly-excited state (here the $2s^2$ state) results in ionization of one electron. (b) Non-sequential double-ionization (NSDI): a released electron oscillates in the field and returns to the helium ion, where it kicks out the second electron. (c) Shake-up process: the photoionization by a laser pulse leaves the atom in an excited state.

4 Photoionization of atoms

In the present chapter, we apply the MCTDHF and the TD-RASCI methods to simulations of photoionization processes of atoms. First, in Sect. 4.1, we study single- and double-ionization of helium. Thereafter, we consider the photoionization of beryllium in Sect. 4.2, and cover as well a pump-probe process. Finally, the cross section and momentum spectra of neon are calculated in Sect. 4.3.

4.1 Helium

Helium is the simplest and probably best-studied many-electron atom, which, as an instance of the three-body Coulomb problem, is not amenable to analytical solutions. Despite its simplicity, helium exhibits a variety of characteristic effects induced by electron correlations. Three important examples are depicted in Fig. 28: autoionization, in which the decay of a doubly-excited bound state leads to detectable resonances in the cross section; non-sequential double-ionization, which is usually explained by a process in which the first ionized electron returns to the parent ion and liberates the remaining bound electron; or shake-up processes, where after photoionization the atom is left in an excited state. All these processes require the accurate description of the Coulomb interaction between the electrons, which must be able to share the energy gathered by the absorption of a photon. Helium can therefore be considered as the prototype of a many-electron atom, the study of which is indispensable for an understanding of the processes in more complex atoms.

On the other hand, being merely a two-particle system, helium can be attacked by theoretical methods which are usually considerably easier as those for larger atoms. Direct methods are feasible also for extensive basis sizes and allow for the accurate simulation of photoionization processes. Accordingly, the last two decades have seen an ever growing number of computational studies on helium which mainly employ the time-dependent close-coupling method, see, e.g., Refs. [43, 47, 105]. A central topic has been the investigation of non-sequential double-ionization, which leads to the formation of the famous *knee structure* in the photoionization cross section [245]. The single-photon double-ionization is nowadays considered as being a well understood process [246, 247], and its occurrence is linked to the re-scattering process sketched in Fig. 28. In contrast, the situation is still much less clear for the two- and higher-photon double-ionization, which has attracted great theoretical interest in recent years and which is considered later in this section. Other topics of recent attention are the pump-probe ionization both for XUV-XUV [49, 50] as well as for XUV-IR [248]

Table 3. Helium ground state energies for different numbers M of time-dependent orbitals, and percentage of the covered correlation energy. The difference between our full configuration interaction result and the exact non-relativistic ground state energy is due to the angular basis, which includes partial waves only up to $l = 2$.

approximation	energy [Ha]	correlation
HF	-2.86168	0%
$M = 2$	-2.87800	40%
$M = 3$	-2.88471	56%
$M = 4$	-2.89127	72%
$M = 6$	-2.89821	89%
$M = 10$	-2.90041	94%
$M = 15$	-2.90101	96%
full CI	-2.90276	100%
exact [252]	-2.90372	

pump-probe pulses, the stabilization of ionization in intense XUV laser fields [249], or the attosecond streaking of electronic transitions [250].

4.1.1 Ground state properties

The calculation of the ground state energy of helium was one of the major struggles of early quantum mechanics. It was satisfactorily solved by Hylleraas in 1929, who applied the variational principle to an ansatz in terms of explicitly correlated functions and obtained an energy of 79.001 eV [251], which compares favorably to the experimental result of 79.005 eV [252]. An accessible survey on the analytical properties of the helium ground state wavefunction is given by Slater [253]. Nowadays, the non-relativistic energy of helium can be calculated with an accuracy of up to 50 digits [254], many of which are certainly of purely academic interest. In contrast, for the application to photoionization processes, the accuracy of the ground state is usually not in the primary focus of attention; instead, it is important that the relevant ionization channels are included into the calculation.

Ground state energy. We first consider the ground state energies, which are obtained by imaginary time propagation in the MCTDHF method and by Lanczos diagonalization in the configuration interaction calculations. In Table 3 the ground state energies are listed for various MCTDHF approximations and compared to the full CI result as well as to the exact non-relativistic energy. The disagreement between the exact and our full CI value is caused by the angular expansion in our calculations, which includes partial waves only up to $l = 2$. We further show the percentage of the covered correlation energy defined as the difference of the full CI and Hartree-Fock energy [255]. The general trend is obvious: by increasing the number M of time-dependent orbitals, the MCTDHF energy approaches the full CI reference result, until for $M = 15$, it reaches 96% of the correlation energy and differs only by a few mHa. The first correction to Hartree-Fock, $M = 2$, is already able to account for 40% of the correlation energy²⁰. Reasonably accurate values of around 90% of the correlation energy are obtained for $M \geq 6$.

²⁰ Note that this value is much larger for one-dimensional models of helium, where the $M = 2$ correction already yields 87% of the correlation energy [109].

Table 4. Comparison of helium ground state energies with the results of Froese-Fischer [144], which are obtained with MCTDHF orbitals with fixed angular symmetry. The second column specifies the type of the included orbitals which together add up to the number M of MCTDHF orbitals. All results agree perfectly, indicating the correctness of the present MCTDHF implementation.

approximation	orbitals	energy [Ha]	Froese-Fischer [144]
HF	1s	-2.86167999956	-2.861680
$M = 2$	2s	-2.8779968141	-2.877997
$M = 3$	3s	-2.8788708705	-2.878871
$M = 4$	4s	-2.8789900960	-2.878990
$M = 7$	4s, 1p	-2.8985542760	-2.898554
$M = 10$	4s, 2p	-2.9001503902	-2.900150

Angular momentum restricted energies. In most parts of this work we employ a general form of the MCTDHF orbitals,

$$|\phi_p(t)\rangle = \sum_{klm} b_{p,klm}(t) \frac{\chi_k(r)}{r} Y_{lm}(\theta, \varphi), \quad (4.1)$$

where the spatial part of the orbitals may be varied freely. However, as discussed in Sect. 2.5.4, it is also possible to use the more restrictive ansatz

$$|\phi_p(t)\rangle = \sum_k b_{p,k}(t) \frac{\chi_k(r)}{r} Y_{l_p m_p}(\theta, \varphi), \quad (4.2)$$

in which the angular part of the MCTDHF orbital $|\phi_p(t)\rangle$ is determined by a spherical harmonic with selected quantum numbers l_p and m_p . Although not utilized in the remainder of this work, in the present subsection it allows for the comparison with the MCHF results of Froese-Fischer using the same approach [144]. Since the imaginary-time propagation involves all the essential components of the MCTDHF algorithm, by this we can benchmark the MCTHDF implementation and demonstrate its correctness. Note that in practice, we obtain the effect of expansion (4.2) by applying the more general expansion given by Eq. (4.1) and setting all coefficients except $b_{p,k l_p m_p}(t)$ equal to zero during the ITP. A more efficient implementation would instead treat the arising integrals over spherical harmonics analytically and reduce the MCTDHF equations to equations for the radial part only.

Table 4 depicts the results of the calculations with fixed angular momenta. The symmetry of the employed orbitals is given in the second column: $n_s s$ here stands for the use of n_s orbitals with spherical s -symmetry, whereas $n_s s$, $n_p p$ indicates that further a number of $3n_p$ p -orbitals with angular momentum projection quantum numbers $m = 0, \pm 1$ are used. The orbitals add up to the total number of $M = n_s + 3n_p$ MCTDHF orbitals. The comparison with the results of Froese-Fischer shows a perfect agreement and, hence, ensures the correctness of our MCTDHF implementation. One further notices that the energies of the restricted angular momentum calculations lie above the ones listed in Table 3 obtained with the general ansatz, which is naturally caused by the diminished variational freedom.

Ionization energies. Several methodologies can be applied for the theoretical calculation of ionization energies. For instance, the atom can be subjected to a laser field of varying frequency and the instantaneous increase of the ionization yield can be observed. This, however, is cumbersome due to the time-propagation which must

Table 5. Ionization potential of the helium ground state as obtained from the extended Koopmans theorem and the Δ SCF method for different MCTDHF approximations.

approximation	EKT	Δ SCF
HF	24.979 eV	23.447 eV
$M = 2$	24.090 eV	23.891 eV
$M = 3$	24.268 eV	24.074 eV
$M = 4$	24.442 eV	24.253 eV
$M = 6$	24.627 eV	24.441 eV
$M = 10$	24.545 eV	24.501 eV
$M = 15$	24.562 eV	24.518 eV
exact [256]		24.587 eV

be performed many times. Alternatively, in a time-independent framework, one can calculate both the energies of the N -particle and $(N - 1)$ -particle ground state and subtract the two values, a method which is referred to as Δ SCF method [59]. Further, the same idea can be performed approximately by means of the extended Koopmans theorem (EKT) introduced in Sect. 3.7.8. The Δ SCF method is usually considered to be more accurate than the EKT as it accounts better for the ionic relaxation, but it involves the overhead of having to explicitly solve the Schrödinger equation of the $(N - 1)$ -particle system. In the case of helium, however, the ion is a hydrogen-like atom and neither the relaxation nor the explicit solution are relevant factors.

Table 5 lists the ionization potentials obtained with the EKT and Δ SCF methods as well as the experimental result for different MCTDHF approximations. Both approximations approach the experimental result as the number of time-dependent orbitals is increased. The ionization potentials from the Δ SCF method grow monotonically, i.e., just in the same way as the ground state energies from which they are obtained by subtraction of the ideal energy of $E_{\text{id}} = -2 \text{ Ha}$. The EKT results, on the other hand, the results from the EKT are closer to the true results but show an oscillating behavior. In the Hartree-Fock case, the ionization potential is overestimated, which is a well-known defect of the standard Koopmans theorem [119].

Two-particle radial densities. As compared to the integrated observables in the previous subsections, particle densities present more sensitive quantities which are suited to illustrate some characteristics of the MCTDHF method. We particularly focus on the two-particle radial density, which is obtained from the two-particle density via integration over the angular degrees of freedom,

$$d(r_1, r_2) = r_1^2 r_2^2 \int d(\mathbf{r}_1, \mathbf{r}_2) d\Omega_1 d\Omega_2. \quad (4.3)$$

The two-particle radial density offers the joint probability to find one particle at the radius r_1 and another one at r_2 . Note, however, that it is not normalized to unity but instead to $N(N - 1)/2$, see Eq. (2.40).

Figure 29 illustrates the radial densities in the vicinity of the nucleus for different MCTDHF approximations. In each plot, the red dashed lines depict the reference results from a full CI calculation. The curves are symmetric with respect to the diagonal $r_1 = r_2$ due to the particle exchange symmetry. The full CI result shows a slight pinch at the diagonal which implies a lower probability for two particles to be located at the same radius. From the Hartree-Fock curves, which do not exhibit this property, one observes that the description of this pinch requires a correlated treatment. Already the 4 determinants used for the $M = 2$ correction suffice to give

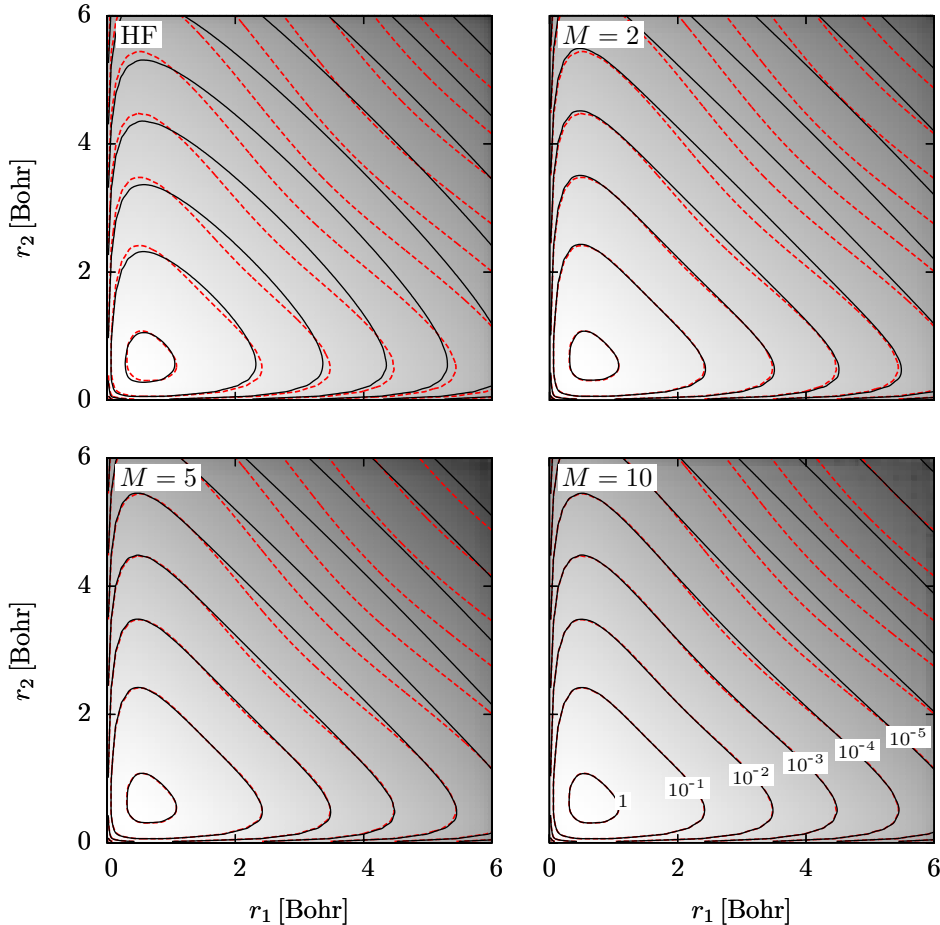


Fig. 29. Two-particle radial densities $d(r_1, r_2)$ of the helium ground state for various MCTDHF approximations compared to full CI results (red dashed curves). In each plot contour lines are drawn at $1, 10^{-1}, 10^{-2}$, etc. With increasing number of time-dependent orbitals, the MCTDHF results approach the full CI reference.

an accurate description up to the 10^{-1} contour line. With increasing correlation, the MCTDHF curves tend towards the full CI results, but especially in regions of small densities the convergence is slow. This is due to the fact that these parts contribute little to the total energies. The more accurate MCTDHF approximations improve the description mainly in regions of high density, as can be seen by closely observing the two largest contour lines which, from $M = 2$ to $M = 10$, converge to visual accuracy.

Although the time-dependent variational principle ensures this behavior to be optimal in an energetic sense, it can be inconvenient for some applications, e.g., for double-ionization processes considered later in this work. Instead, one could also think of alternative schemes which attribute larger importance to the improvement of the wavefunction in regions of small density far away from the origin, at the cost of obtaining a worse description close to the nucleus. Unfortunately, it is by no means trivial to reasonably modify the TDVP in order to achieve the desired features such as a better description of double-ionization. Work on this promising topic is in progress, see Sect. 5.1.5.

Table 6. Ground state energies for the atoms lithium to silicon obtained in Hartree-Fock approximation, compared to the results of Tatewaki et al. [257].

atom	charge Z	energy [Ha]	Ref. [257]
Li	3	-7.4327	-7.4327
Be	4	-14.573	-14.573
B	5	-24.529	-24.529
C	6	-37.689	-37.689
N	7	-54.401	-54.401
O	8	-74.811	-74.809
F	9	-99.411	-99.409
Ne	10	-128.547	-128.547
Na	11	-161.859	-161.858
Mg	12	-199.615	-199.614
Al	13	-241.877	-241.876
Si	14	-288.855	-288.854

Ground state energies of larger atoms. The present implementation of the MCTDHF method is in principle able to treat any atom in the periodic system. A satisfying performance can be obtained for the first- and second-row elements. To give an overview of its capabilities, we finally consider the ground state energies for the atoms from lithium to silicon that arise from a Hartree-Fock treatment. Our results were obtained with partial waves up to $l = 2$ and on a grid extending to $r = 30$ Bohr, and the FEDVR basis consisted of 10 finite elements with 10 basis functions in each element (except for 25 basis functions in the first element).

The results are collected in Table 6. For comparison, we use the numerical Hartree-Fock results of Tatewaki et al. [257], which agree favorably with ours. Again, this shows the correctness and accuracy of the MCTDHF code and also the appropriateness of the spherical DVR basis. For each of the considered atoms (and also for larger ones), we could now obtain improved results by performing more accurate multiconfigurational Hartree-Fock calculations, and further investigate the reaction to a laser pulse by propagating it in time. In this work, however, we restrict ourselves to the treatment of helium, beryllium and neon.

4.1.2 Single-photoionization cross sections

Cross sections present a central quantity in the study of photoionization. They are important in many fields of physics such as astrophysics, where they are used to determine the ionization characteristics of cosmic gases [258]. Recently, the two-photon ionization of helium has also been suggested as a measure for the coherence of SASE-generated FEL pulses [259, 260]. These applications require accurate values for the cross sections, and various techniques have been introduced for their calculation, among them sophisticated methods such as Stieljes imaging [261], complex scaling [262, 263] and exterior complex scaling [190, 230]. Here, we apply two explicitly time-dependent methods which are discussed in the following.

Cross sections via laser pulses. The first method that we consider models the situation found in experiments: The helium atom is prepared in the ground state and subjected to laser pulses with varying photon energy. For each photon energy, the ionization yield P_1 is recorded at the end of the pulse as the part of the wavefunction

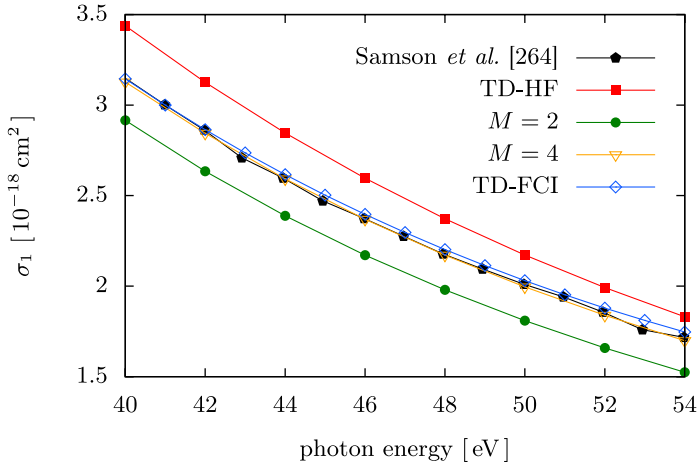


Fig. 30. Single-photoionization cross sections of helium for photon energies in the direct two-photon double-ionization regime, plotted for various MCTDHF approximations as well as full CI reference results and experimental measurements by Samson et al. [264]. One observes that the $M = 4$ approximation is able to accurately reproduce the measured result [76].

outside $R = 20$ Bohr. The yield is then related to the cross-section via

$$\sigma_1 [\text{cm}^2] = 1.032 \cdot 10^{-4} \frac{\omega^2 P_1}{n I_0}, \quad (4.4)$$

which is described in detail in Sect. 3.7.3. The laser pulse is assumed to be linearly polarized and to follow a squared-sine envelope,

$$\mathbf{E}(t) = \mathbf{E}_0 \sin(\omega t) \cdot \begin{cases} \sin^2\left(\frac{\pi t}{T}\right), & 0 \leq t \leq T, \\ 0, & \text{otherwise,} \end{cases} \quad (4.5)$$

with an intensity of $I_0 = 10^{13} \text{ W/cm}^2$ and a duration of $T = 100$ a.u. (≈ 2.4 fs). The results presented in the following have been published in Refs. [75, 76].

We first consider the energy range from $\omega = 40$ to 54 eV, which is the regime of two-photon non-sequential double-ionization. The single-ionization cross sections obtained from MCTDHF calculations are plotted in Fig. 30. Two curves are of major interest here: the black diamonds denote the high-precision measurements obtained by Samson et al. using a double ion chamber and a high-voltage spark discharge, which possess an estimated accuracy of 2% [264]. And the open blue diamonds which present the result of time-dependent full configuration interaction calculations using partial waves up to $l = 3$ and a FEDVR basis with finite elements of length 4 Bohr and 11 Gauss-Lobatto functions. Notably, the experimental and full CI results agree almost perfectly. The monotonic decrease with increasing photon energy is, for this setup, a well-known property of photoionization cross sections, which is reproduced already in simplified treatments such as the Born approximation [80].

The MCTDHF results have been obtained using the same single-particle basis as for the full CI calculation. The latter therefore serves as a reference, against which the MCTDHF results should converge in the limit of a large number M of time-dependent orbitals. One observes that the Hartree-Fock ($M = 1$) approximation overestimates the true result but is able to describe the behavior qualitatively correctly. On the other hand, the first correction, $M = 2$, yields cross sections which underestimate the true

results and also deviate nearly as much as the HF result. The true result is reproduced to high accuracy by the $M = 4$ calculation, which is depicted by the orange triangles, and also by all approximations with $M \geq 4$ not plotted here. The advantage of the MCTDHF approach is the greatly reduced effort: whereas the full CI calculations took approximately three days on a single processor, the MCTDHF approximation using $M = 4$ time-dependent orbitals requires only a few minutes. The MCTDHF method is therefore highly preferable for the calculations of the single-ionization cross sections in this range of photon energies.

Next, we present the results of the TD-RASCI method. As considered in detail in Sect. 2.4.6, the configuration space is divided into a region in the vicinity of the nucleus ($r < 20$ Bohr) and a region outside representing the continuum. The basic approximation we use is the TD-CIS ansatz, which includes only single-excitations out of the Hartree-Fock ground state $1s^2$ of 1S_0 symmetry,

$$|\Psi(t)\rangle = c_0(t)|\Phi_0\rangle + \sum_{ar} c_a^r(t)|\Phi_a^r\rangle. \quad (4.6)$$

This includes both transitions to excited Hartree-Fock orbitals in the bound region as well as ionization into the continuum. For the TD-RASCI method, we similarly allow only for single-excitations, but use a more accurate description of the ground state and the excited states. In order to do so, we apply a full CI expansion in a restricted subspace of the bound space, plus all single-excitations from the included determinants. The form of the full CI space is specified by the notation $(n_s s, n_p p, \dots)$, which indicates the single-particle basis used to construct the full CI determinants. For example, $(1s)$ corresponds to the TD-CIS approximation, $(2s)$ to the case where the full CI space consists of the four determinants obtained by distributing the two particles in the $1s$ and $2s$ orbitals, $(2s, 2p)$ to the case where further transitions to the $2p$ orbitals are allowed, and so on. The corresponding TD-RASCI wavefunction can be written as

$$|\Psi(t)\rangle = \sum_{\gamma} c_{\gamma}(t)|\Phi_{\gamma}\rangle + \sum_{ar} c_{\gamma,a}^r(t)|\Phi_{\gamma,a}^r\rangle, \quad (4.7)$$

where the states $|\Phi_{\gamma}\rangle$ determine the full CI space. Formally, it resembles a multi-reference CI expansion with restricted excitations, see Eq. (2.94).

In Fig. 31, we depict the cross section obtained with the TD-RASCI method in the $(10s, 3p)$ approximation. The experimental results of Samson et al. [264] and the TD-FCI results are the same as in the previous Fig. 30. As before, the TD-FCI calculations present the reference, against which an accurate calculation should converge. The TD-CIS results show the qualitatively correct behavior, but deviate from the exact result to an extent which is larger than for the Hartree-Fock approximation. The TD-HF method thus performs better than the TD-CIS method for this application. On the other hand, the results of the $(10s, 3p)$ approximation agree almost exactly with the TD-FCI results, which is remarkable, as the total required time of the TD-RASCI calculation is reduced by about a factor of twenty. The TD-RASCI approximation reveals the importance of electronic correlations even for this relatively simple process. As is stated already in Ref. [265], a correlated initial state is required to obtain accurate cross sections. The TD-RASCI method is able to provide such one while, at the same time, it reduces the effort by focusing only on the single-ionization.

Autoionizing states. Both numerical approaches, the MCTDHF and the TD-RASCI method, perform well for estimating the single-ionization cross sections in the energy range from 40 to 54 eV, since at these photon energies the dominant process is linear photoionization from the ground state to the continuum. We now consider the

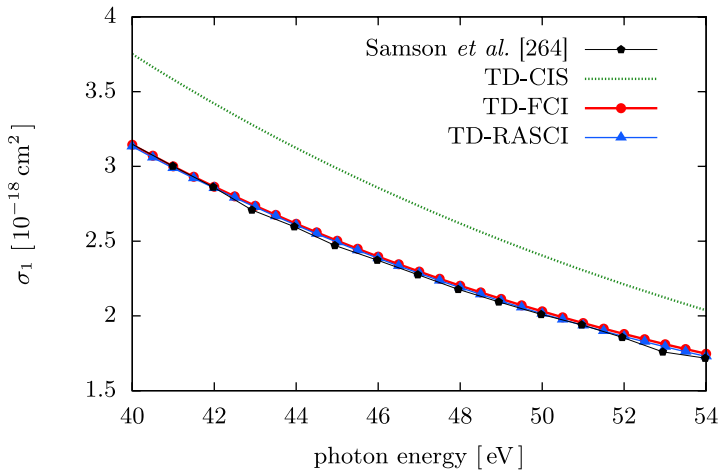


Fig. 31. Single-photoionization cross sections of helium obtained with the TD-RASCI schemes. The parameters are the same as in the previous figure. Figure from Ref. [75].

ionization for photon energies beyond 54 eV, where autoionization resonances enter the cross section. Generally, resonances are encountered if there is more than one channel for the electron to reach the ionized state, and these different pathways interfere. For photon energies above 60 eV, doubly-excited states of helium become occupied by the effect of the laser pulse and subsequently decay since they are coupled through the Coulomb interaction to a degenerate singly-ionized state. Autoionization resonances were observed and classified by Madden and Coddling [266], and their characteristic shape has been explained in a seminal paper by Fano [267]. Nowadays, they are precisely characterized by experimental [268, 269] and theoretical studies [228, 270].

Figure 32 presents the cross sections in the energy range from $\omega = 54$ to 80 eV for the MCTDHF and TD-RASCI approximations. Both calculations are compared to measurements of Samson et al. [264] and to theoretically calculated resonance positions by Scrinzi and Piraux, who used the complex scaling method [228]. The MCTDHF results are plotted in the upper picture. It is immediately obvious that the TD-HF ansatz fails to model the resonances, which is implied by the fact that it is unable to describe correlated doubly-excited states. However, the absolute values of the cross sections fit quantitatively better than for the lower energy range considered before. This is caused by the fact that for larger photon energies the Born approximation is valid, and consequently there is no need to accurately describe the ionic eigenstates. The $M = 2$ approximation, on the other hand, is able to describe the doubly-excited states, due to its correlated nature, and yields a distinct peak around 70 eV. However, it does not predict the other resonances. The same is true for the $M = 4$ approximation, which adds a certain structure to the shape of the resonance, but does not correct the resonance position.

The inset at the bottom of Fig. 32 depicts the results of the TD-RASCI calculations. The TD-CIS calculations plotted in green do not yield any resonance, which is not surprising since the wavefunction includes at most single-excitations and is therefore obviously unable to describe doubly-excited states. Beside that, the accuracy of the results is similar, but slightly worse, than for the TD-HF ansatz. The TD-RASCI approximation now allows to add selected determinants to the description. For instance, the addition of the $|2s, 2s\rangle$ determinant leads to the direct formation of the corresponding resonance in the cross section. Here, we apply the $(10s, 3p)$ approximation, which includes all doubly-excited states up to the $10s$ and $3p$ orbital. The results

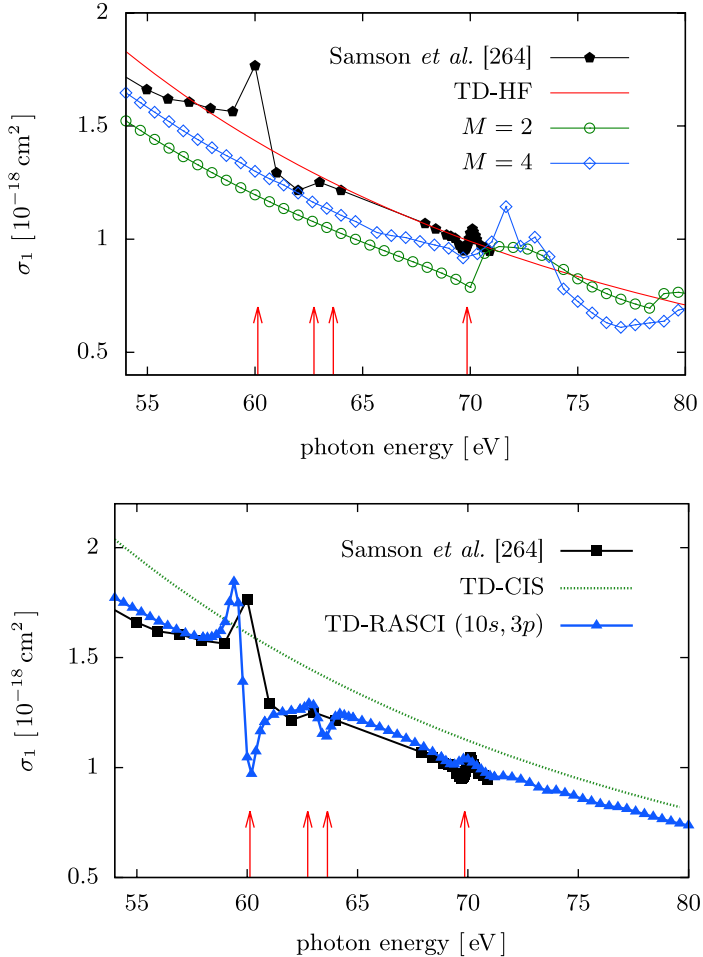


Fig. 32. Single-ionization cross sections of helium for the same field parameters as in Fig. 30. Shown are the results of MCTDHF (*top*) and TD-RASCI approximations (*bottom*). Black squares denote the experimental results of Samson et al. [264], and red arrows the resonance positions of 1P_o symmetry according to Scrinzi and Piraux [228]. Bottom figure from Ref. [75].

show a clear improvement over the TD-CIS results: all the measured resonances are well reproduced and appear at the correct position. This shows that the TD-RASCI method is able to describe the important ionization channels and yield exact results also for this more difficult scenario. At the same time, the effort is significantly reduced as compared to direct full CI calculations.

Cross sections via the autocorrelation function. In the previous method, several pulses with sharp photon energies are applied to the atom, and the response of the system is observed for each. Strong reactions are obtained when the frequency of the exciting pulse corresponds to an eigenfrequency, i.e., to the energy difference of the ground state and an excited state. Although this principle performs well, many separate computations are required in order to obtain results as shown before. In the following, we apply another principle which yields the cross section from a single calculation by means of the autocorrelation function [271]. For this technique, the

ground state $|\Psi_0\rangle$ of the system is disturbed by the dipole operator \hat{D} ,

$$|\tilde{\Psi}_0\rangle = \hat{D} |\Psi_0\rangle, \quad (4.8)$$

and the thus obtained initial state is propagated in time. The autocorrelation function then contains the relevant ingredients for the cross section, as the following calculation shows,

$$\begin{aligned} S(t) &= \langle \tilde{\Psi}_0 | \tilde{\Psi}(t) \rangle \\ &= \langle \Psi_0 | \hat{D}^\dagger e^{-i\hat{H}t} \hat{D} | \Psi_0 \rangle \\ &= \sum_{nm} \langle \Psi_0 | \hat{D}^\dagger | \Psi_n \rangle \langle \Psi_n | e^{-i\hat{H}t} | \Psi_m \rangle \langle \Psi_m | \hat{D} | \Psi_0 \rangle \\ &= \sum_n |\langle \Psi_n | \hat{D} | \Psi_0 \rangle|^2 e^{-iE_n t}. \end{aligned}$$

Note that in the third line, unity operators in terms of eigenstates $|\Psi_n\rangle$ of the system have been inserted. A Fourier transformation converts this into

$$S(E) = 2\pi \sum_n |\langle \Psi_n | \hat{D} | \Psi_0 \rangle|^2 \delta(E_n - E). \quad (4.9)$$

Upon comparison with the usual time-independent definition of the cross section, e.g. [65],

$$\sigma_1(E) = \frac{8\pi^2}{c} E \sum_n |\langle \Psi_{E,n}^- | \hat{D} | \Psi_0 \rangle|^2, \quad (4.10)$$

where $|\Psi_{E,n}^-\rangle$ denotes the approximated set of singly-ionized states with ingoing boundary conditions and the dipole operator is taken in length gauge, one notices that the autocorrelation function is proportional to the cross section,

$$\sigma_1 = \frac{4\pi}{c} E S(E). \quad (4.11)$$

Figure 33 presents the Fourier transform of the autocorrelation function for three MCTDHF approximations. The time propagation has been performed up to $T = 1000$ a.u., which provides a resolution of around 0.17 eV in energy space. The TD-HF approximation shows the series of excitations converging against the single ionization threshold around 24.6 eV, which are related to the excitation of a single bound electron to excited bound states. The autoionizing resonances caused by double-excitations can not be described by the TD-HF approximation, and their modeling requires the correlated $M = 2$ approximation. However, as already observed in Fig. 32, the position of the resonances is not quantitatively correct. In contrast, the $M = 6$ approximation in the lower panel shows two distinct peaks close to the reference positions, and is therefore able to resolve the autoionization states.

4.1.3 Two-photon double-ionization

Two-photon double-ionization (TPDI) has attracted much theoretical interest in the last decade. This is mainly caused by two reasons: first, perturbation theory, which proved to work well for the single-photon double-ionization, is much harder to apply and therefore favors the use of explicitly time-dependent approaches, which became

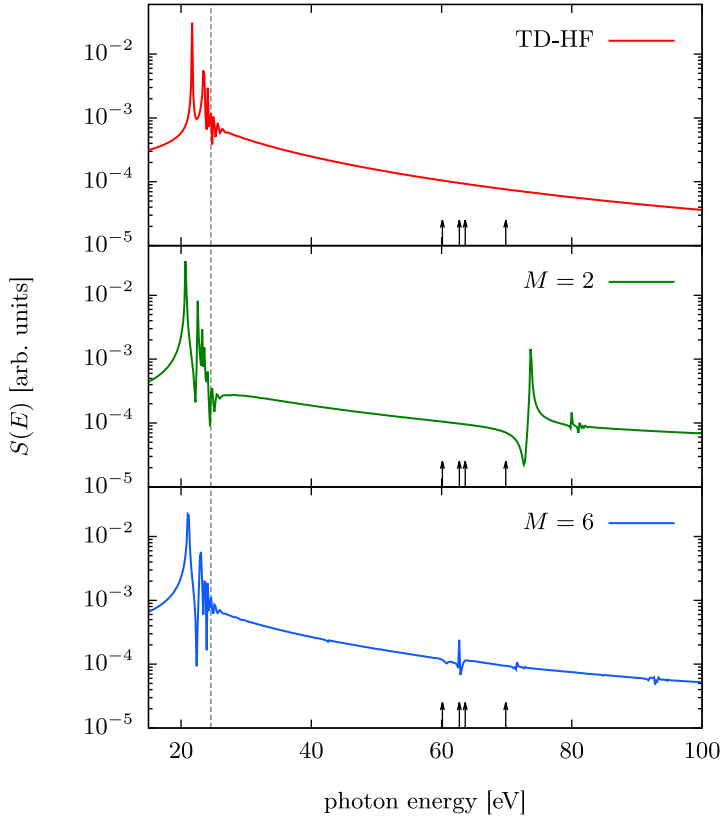


Fig. 33. Fourier transform of the autocorrelation function of helium for different MCTDHF approximations. The system was propagated for $T = 1000$ a.u. The dashed line marks the ionization potential of helium, while the black arrows denote the resonance positions of Ref. [228].

available to the required extent only in recent time. And second, the few experiments performed up to now [10, 272, 273] are hardly sufficient to conclusively distinguish between the different explanations, so that theory is literally on its own. The investigations performed so far utilize mostly time-dependent close-coupling approaches [43, 105, 274], perturbation theory [275–278], convergent close-coupling [279] or R-matrix Floquet methods [280]. A delicate question which is actively debated up to these days is whether the extraction of cross sections requires correlation in the doubly-ionized final states, or whether uncorrelated states are adequate, see also Sect. 3.7.2. The debate has been triggered by works of Nikolopoulos and Lambropoulos [275, 276] and Foumouo et al. [47], who, through projection on approximately correlated final states, obtained cross sections which were an order of magnitude larger than the hitherto existing results. Most delicately, Foumouo et al. also presented uncorrelated results which were acquired in the same framework, and those agree well with other uncorrelated treatments in the literature. Although this question is far from being answered, recent results using large grids [43, 274], exterior complex scaling techniques [230, 281] or analytical models [229] provide good arguments for the credibility of uncorrelated projection schemes.

In the present work, we focus on the direct or non-sequential regime which is characterized by the absorption of two photons with energies in the range from 39.5 to

54.4 eV. The lower energy bound gives the minimal energy required by two photons to overcome the double-ionization threshold of 79 eV (which is just the total energy). On the other hand, the upper energy bound of 54.4 eV marks the second ionization potential of helium, and for larger photon energies, the sequential double-ionization process becomes accessible. For double-ionization to occur in the direct process, the electrons must be able to share the energy via the Coulomb interaction. Different scenarios are possible for that, among them the shake-up mechanism, where during the ionization of the first electron the other one is excited to an energy level from which it can be ionized through another photon, or the re-collision process, in which one electron gathers two photons and kicks out the remaining electron. Using a recently introduced analytical model, Førre et al. identify the mechanism as a combined impact of the second photon and the ionized re-scattered electron, and rule out the absorption of two photons by a single electron and subsequent re-collision [229].

In the following, we investigate the non-sequential two-photon double-ionization using the MCTDHF method. Initially, these attempts have been made in the hope to obtain an equally appropriate description as for the single-ionization process. This would have allowed for simulations on much larger grids than those accessible by full CI calculations, and hence, e.g., for a detailed examination of the validity of the uncorrelated projection scheme. Unfortunately, it turned out that the MCTDHF scheme does not perform as accurately as expected. Nevertheless, the present investigation is valuable as it indicates the strengths and limitations of the MCTDHF method.

TPDI total cross sections. To obtain the total double-ionization cross sections from MCTDHF calculations, we follow the usual technique: helium is first prepared in the ground state and afterward subjected to a laser pulse with squared sine envelope of duration $T = 100$ a.u. and a peak intensity of $I = 10^{13}$ W/cm². The cross sections are then extracted from the wave packet at time T using the formula

$$\sigma_2[\text{cm}^4\text{s}] = 2.28 \cdot 10^{-23} \frac{\omega^3 P_2}{nI_0^2}, \quad (4.12)$$

which has been derived in Sect. 3.7.3. The calculations are performed for various MCTDHF approximations as well as for the TD-FCI method.

Figure 34 depicts the final result: shown are the TPDI cross sections versus photon energy for MCTDHF calculations with $M = 15$ time-dependent orbitals and TD-FCI reference calculations. They are compared to the theoretical results of Feist et al. obtained with the time-dependent close-coupling (TD-CC) method [43] and to measurements of Hasegawa et al. [272] and Sorokin et al. [10], who used FEL-generated laser pulses in conjunction with a nuclear-recoil reaction microscope. First, let us focus on the direct results: both the TD-FCI and the TD-CC results show a monotonic linear growth up to around $\omega = 48$ eV and then steeply increase towards the threshold at 54 eV. This qualitative behavior is observed by the majority of theoretical studies. The deviation of the two curves is caused by the different techniques to extract the cross sections. The TD-CC results use a projection on Coulomb waves, which is known to yield smaller results than the more simple spatial partitioning applied for the TD-FCI calculations [43]. Further, the pulses applied here are shorter and, consequently, have a larger bandwidth with FWHM ≈ 4 eV, hence the cross sections are effectively averaged over this range. The experimental value of Hasegawa et al. lies on the TD-CC curve, whereas the lower bound of the error bar of Sorokin et al. touches the results of the TD-FCI calculation.

The best MCTDHF approximation that we considered, $M = 15$, is able to qualitatively reproduce the increase against the threshold. It fails, however, in describing the behavior at smaller photon energies, and generally does not provide a quantitatively correct description throughout the considered energy range. Moreover, the

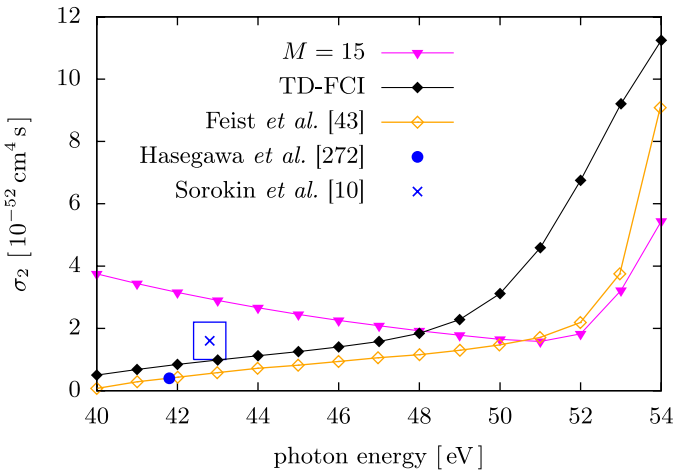


Fig. 34. Total cross sections for two-photon double-ionization of helium plotted against the photon energy. Shown are the results of the MCTDHF $M = 15$ approximation and of TD-FCI calculations performed using the same single-particle basis, the results of Feist et al. [43], as well as the experimental values by Hasegawa et al. [272] and Sorokin et al. [10] (the latter with error bars). Reproduced with permission from J. Chem. Phys. **134**(8), 084106 (2011) [76]. Copyright 2011 American Institute of Physics.

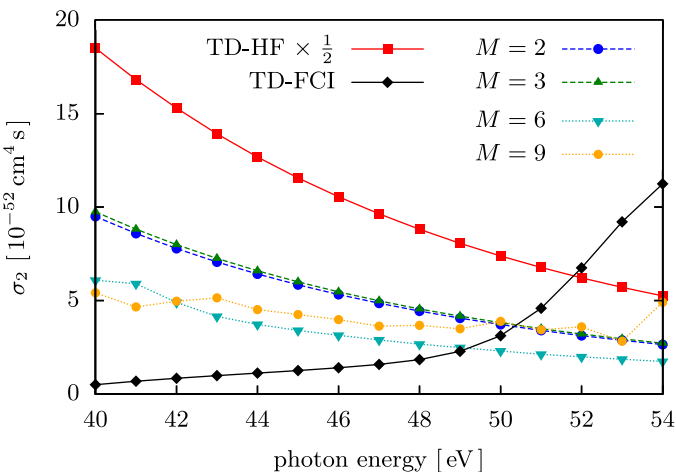


Fig. 35. Closer look at the convergence behavior of the double-ionization cross sections of helium with increasing number of MCTDHF orbitals. The successive approximations should, ideally, converge against the TD-FCI result. It requires at least the $M = 9$ approximation to—at least qualitatively—reproduce the increasing trend observed in the TD-FCI result. The TD-HF curve drastically overestimates the true cross section [76].

MCTDHF $M = 15$ calculations took 13 days on a single processor, whereas the exact results required only three days. The reason for this poor performance is considered later in the discussion.

Convergence properties. It is further instructive to have a closer look at the results of other MCTDHF approximations, which are illustrated in Fig. 35. There, we plot the TPDI cross sections starting from time-dependent Hartree-Fock and going up to the $M = 9$ approximation, together with the full CI result. It is obvious that TD-HF

is unable to model the TPDI: it overestimates the full CI reference by two orders of magnitude at 40 eV, and shows a monotonically decreasing trend throughout the considered energy range. The $M = 2$ and $M = 3$ curves, which almost agree with each other, improve on the absolute values but not on the qualitative behavior, and the same is also true for the $M = 6$ calculations. The $M = 9$ approximation is the first to stop this trend: it yields an almost horizontal line, with a slight increase towards the threshold.

Discussion. Why are the double-ionization results that dissatisfying when, at the same time, the single-ionization cross-sections are excellently reproduced? Why do the MCTDHF double-ionization cross sections follow this particular form, which exhibits an inverted trend as compared to the full CI results? To answer these questions, let us first consider the TD-HF approximation. With the wavefunction being described by a single, spin-restricted singlet-determinant, the two-particle reduced density matrix is completely determined by the product of the corresponding single-particle RDM [59],

$$d_{\text{HF}}(\mathbf{r}, \mathbf{r}', t) = \frac{1}{2} D(\mathbf{r}, t) D(\mathbf{r}', t). \quad (4.13)$$

For the ionization criteria used in this work, Eqs. (3.142) and (3.143), this leads to a double-ionization yield P_2 which is related to the single-ionization, P_1 , by

$$P_2 = \frac{P_1^2}{4}. \quad (4.14)$$

Hence, the monotonically decreasing structure of the TD-HF double-ionization cross section is a direct consequence of the corresponding behavior of the single-ionization results, compare again Fig. 30. In other words, there is no way to suppress the double-ionization, once single ionization occurs. In contrast, for the full CI method, the two-particle RDM wavefunction is, for $N = 2$ particles, the absolute square of the wavefunction,

$$d_{\text{FCI}}(\mathbf{r}, \mathbf{r}', t) = |\Psi(\mathbf{r}, \mathbf{r}', t)|^2. \quad (4.15)$$

If we then consider, for simplicity, an expansion in terms of a six-dimensional Cartesian grid, each grid point $(\mathbf{r}_i, \mathbf{r}_j)$ is exclusively determined by a single expansion parameter in the full CI wavefunction. Consequently, the representation of double-ionization is completely independent of the representation of single-ionization.

The MCTDHF wavefunction now settles in between these two limits. However, as confirmed numerically, the double-ionization yields of the low-order MCTDHF approximations are still highly influenced by the corresponding single-ionization yields, i.e., terms of the form (4.13) are dominant in the two-particle density matrix. While the MCTDHF method is, in principle, able to model the correlated two-particle density matrix it, however, utilizes most of its capabilities to obtain an adequate description in regions where the density is large. Processes that occur with a small particle density, such as the double-ionization are, therefore, mostly neglected in favor of an adequate description of the time-dependence of the ground state and excited states. This behavior is also confirmed by the two-particle radial densities in Fig. 29.

It is of crucial importance for future applications of the MCTDHF method to general photoionization processes to ameliorate this issue. A possible approach is addressed in Sect. 5.1.5.

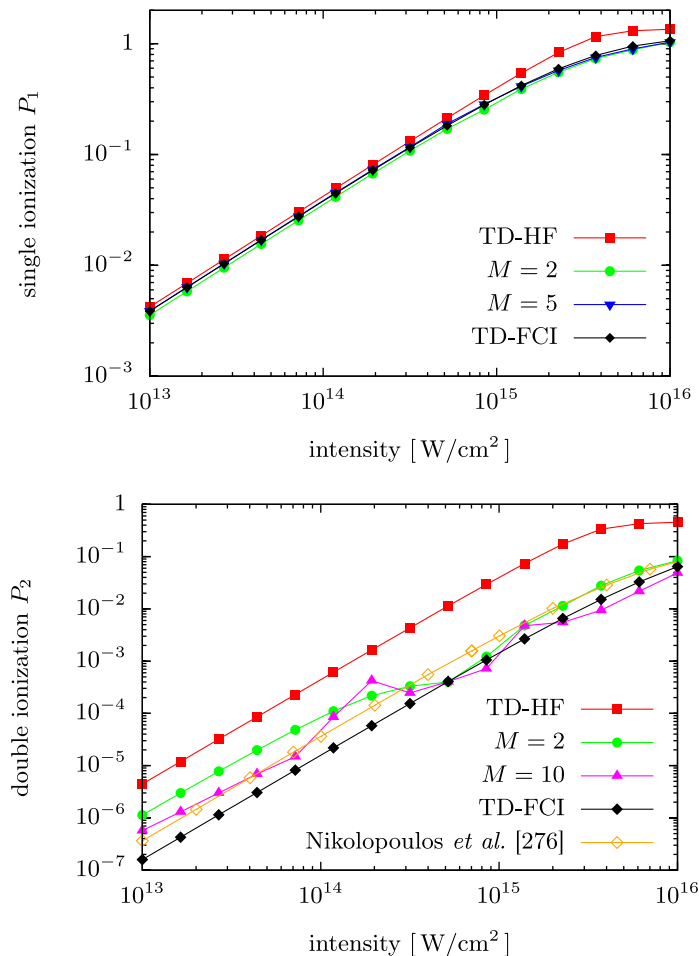


Fig. 36. Single- and double-ionization yield of helium versus intensity for a photon energy of 45 eV. Shown are results from different MCTDHF approximations and TD-FCI, as well as the double-ionization results of Nikolopoulos and Lambropoulos [276]. Reproduced with permission from J. Chem. Phys. **134**(8), 084106 (2011) [76]. Copyright 2011 American Institute of Physics.

4.1.4 Photoionization at $\omega = 45$ eV

In the following, we concentrate on the photoionization at a fixed photon energy of $\omega = 45$ eV and consider the intensity dependence, the time-evolution of the MCTDHF orbitals and of other observables.

Intensity dependence. The dependence of the ionization yields on the intensity of the laser pulse is plotted in Fig. 36. We first focus on the picture on top, which shows the single-ionization yield. At intensities lower than $I = 5 \cdot 10^{14} W/cm^2$, all depicted curves are given by straight lines with a slope of one, which corresponds to the prediction of perturbation theory [276]. Over the whole range of intensities, the TD-FCI reference results are well reproduced already with the first correction to TD-HF, $M = 2$, while the $M = 5$ approximation yields a virtually exact agreement in the logarithmic plot. Towards intensities of $I = 10^{16} W/cm^2$, one notices a

decreasing slope which implies the breakdown of perturbation theory, and which is overestimated by the TD-HF approximation. This behavior is caused by the depletion of the ground state, which becomes roughly half emptied. This transition to the ion leads to an increased ionization potential, which hampers the ionization of the second electron.

The lower picture of Fig. 36 depicts the results for the double-ionization. They are compared to TD-FCI reference calculations and to results of Nikolopoulos et al. [276] which, beside a systematic shift, agree well with each other. In the region where perturbation theory holds, the curves are given by straight lines with a slope of two. This is reasonable since two photons are required for the double-ionization, and hence the yield scales with I^2 . The TD-HF result shows a similar qualitative behavior as TD-FCI, but is more than one order of magnitude larger (note that they are again just the square of the single-ionization yields). The plotted MCTDHF results deviate from the expected straight lines. The $M = 2$ approximation lies roughly in between TD-HF and TD-FCI, and approaches the latter for intensities larger than $5 \cdot 10^{14} \text{ W/cm}^2$. The $M = 10$ results are closer to the TD-FCI reference and are, thus, generally more accurate. However, they show oscillations which qualitatively deviate from the exact result. Particularly, for the $M = 10$ approximation around the intensity $2 \cdot 10^{14} \text{ W/cm}^2$, a further increase of the intensity leads to an unphysical decrease of the ionization yield. This reveals the highly non-linear nature of the MCTDHF method. Another point worth mentioning is that the MCTDHF results become more accurate for increasing intensity. This is caused by the increased double-ionization yield which, in turn, leads to a better description by the MCTDHF method, as outlined above.

Time-dependence of the MCTDHF orbitals. Let us now focus on the evolution of the MCTDHF orbitals during the laser pulse. The orbitals are governed by the time-dependent variational principle, which ensures the optimal representation of the wavefunction at each time-step. The actual form of the orbitals, however, is not unique because of the invariance of the full CI wavefunction under unitary transformations. In fact, the orbitals heavily depend on the chosen MCTDHF constraint operator $\hat{Q}(t)$, see Sect. 2.5.6. For the following results we, therefore, restrict ourselves to the straightforward choice $\hat{Q}(t) = 0$. The helium atom is excited by a laser pulse with photon energy $\omega = 45 \text{ eV}$, duration $T = 100 \text{ a.u.}$ and intensity $I = 10^{14} \text{ W/cm}^2$.

Figure 37 depicts the MCTDHF orbitals for the time-dependent Hartree-Fock approximation as well as for the $M = 2$ and $M = 3$. It shows, from left to right, four pictures which illustrate the modulus squared of the orbitals at the time-points $t = 0, 50, 100$ and 150 a.u. , i.e., at the beginning, the maximum and the end of the pulse, as well as at a time 50 a.u. after the pulse has ended. The TD-HF approximation yields a rotationally symmetric s -orbital for the ground state at $t = 0$. Upon action of the laser pulse, the orbital accounts for the ionized electron and produces an outgoing wave packet of p -symmetry which, at $t = 150 \text{ a.u.}$, is well separated from the (still rotationally symmetric) ion. For the $M = 2$ approximation, the situation is different. Both orbitals reveal s -symmetry in the ground state, but only one—the upper one in the plot—reacts to the laser pulse giving rise to a p -electron. The other shows a small p -component only at the maximum of the pulse, which might be associated to double-ionization. This p -component becomes smaller as the electron travels out into the continuum and is not plotted anymore at later time-points, where again an orbital of mainly s -symmetry is observed that is more confined than the initial ground state. This can be interpreted as each of the two orbitals describing an electron—one orbital the outer photo-electron, and one the inner bound electron which screens the core potential. The laser pulse then mainly acts on the outer orbital and ionizes it, while

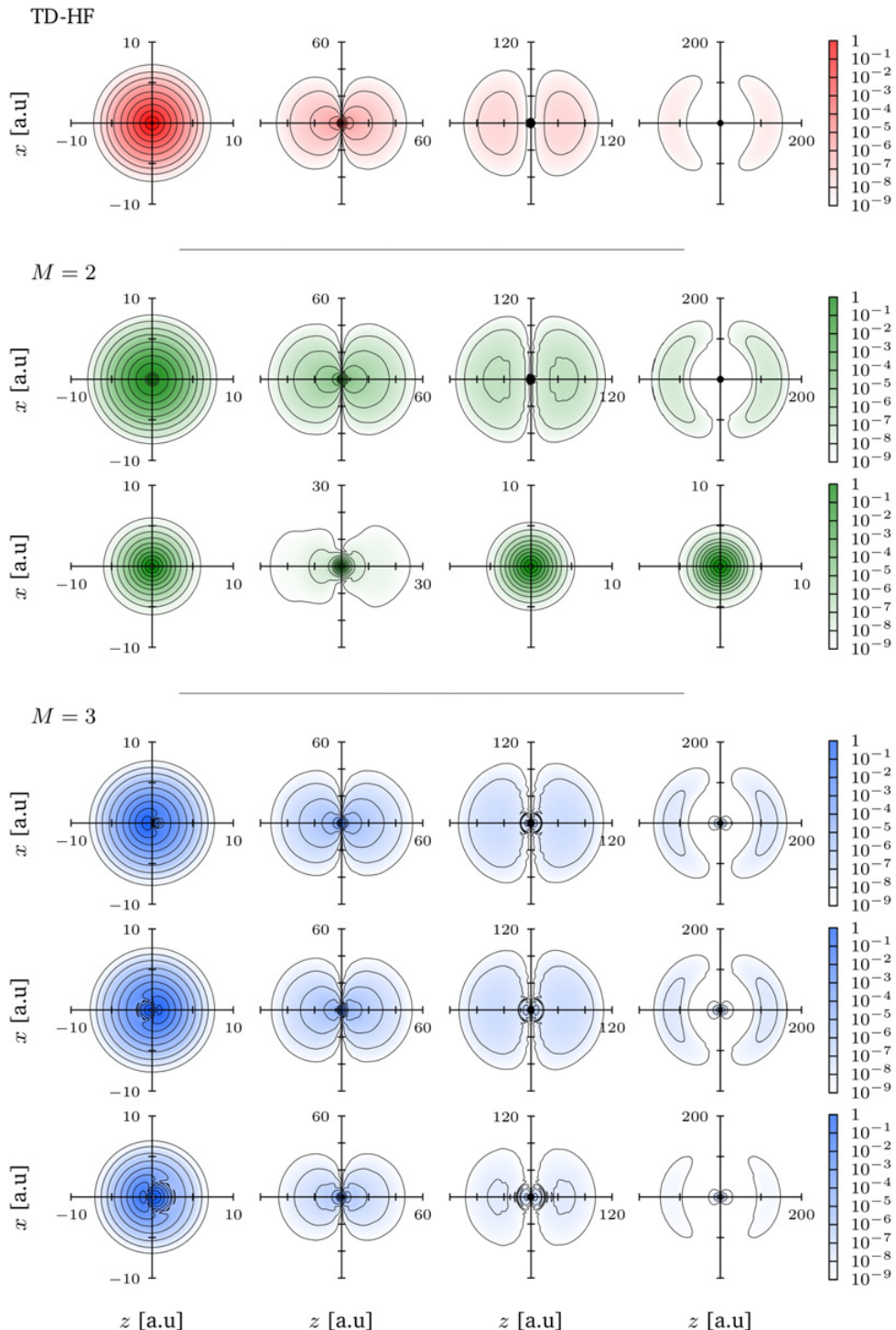


Fig. 37. Time-dependence of the MCTDHF orbitals for photoionization from the helium ground state. Plotted from left to right are the squared absolute values of the orbitals at the time-points $t = 0, 50, 100$ and 150 a.u. The time-dependent Hartree-Fock approximation (*top*), the two orbitals arising from the $M = 2$ approximation (*middle*) and the three $M = 3$ orbitals (*bottom*) are depicted.

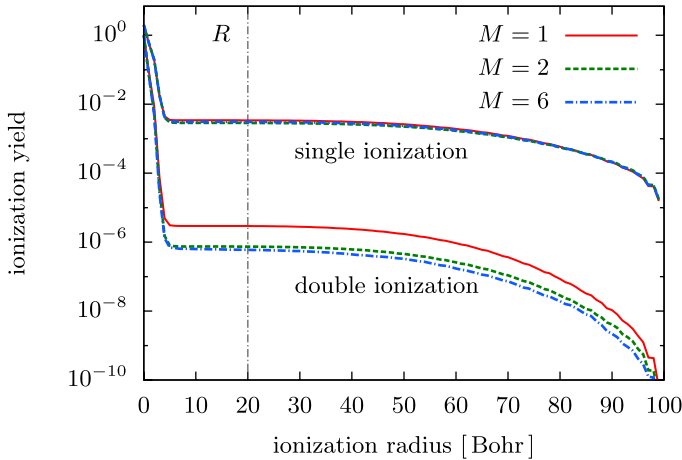


Fig. 38. Single and double-ionization yields of helium for selected MCTDHF approximations plotted against the radius, at which a particle is considered ionized. The line at $R = 20$ Bohr marks the value which is mainly used in this work. The laser pulse parameters are $\omega = 45$ eV and $I = 10^{13}$ W/cm 2 . Reproduced with permission from J. Chem. Phys. **134**(8), 084106 (2011) [76]. Copyright 2011 American Institute of Physics.

the inner orbital is used to represent the ion²¹. For the $M = 3$ approximation, each orbital consists of an s -component and a p -component, and the laser pulse produces an outgoing wavepacket for each of them. The two upper orbitals have very similar amplitudes, while the lower one is only slightly ionized. At $t = 150$ a.u., one also notices a p -component which remains in the vicinity of the nucleus, that can be related to the excitation of doubly-excited states or a shake-up process, where the initial p -components are elevated into higher orbitals.

For more complex cases, it is difficult to attribute a physical interpretation to the MCTDHF orbitals, particularly for the basis expansion applied in this work, in which different angular momentum states are allowed to be mixed. Furthermore, the connection between particles and MCTDHF orbitals is lost. This complicates the analysis of MCTDHF wavefunctions as well as the introduction of approximation schemes, as will be discussed in Sect. 5.1.5.

Influence of the choice of the ionization radius. A shortcoming of the definition of ionization, as used in this work [Eqs. (3.142) and (3.143)], is the arbitrariness of the ionization radius R . In Fig. 38, we thus examine its influence on the single- and double-ionization yields induced by a pulse with $\omega = 45$ eV, intensity $I = 10^{13}$ W/cm 2 and duration of $T = 100$ a.u. One can see that for all depicted MCTDHF approximations, there is a region between $r = 8$ and $r = 40$ Bohr in which the yields are almost constant. From this, one can expect that the distance of $R = 20$ Bohr which is used in most parts of this work presents a reasonable choice for the helium atom.

For a more detailed look, we further consider the radial density in Fig. 39. There, the snapshots of the radial density are shown for different times up to $t = 400$ a.u. (~ 10 fs). One notices a distinct wave packet moving away from the atom which is, at $t = 100$ a.u., mainly localized within a distance of 100 Bohr from the nucleus. At $t = 400$ a.u., a significant part of the wave packet starts to get reflected at the grid

²¹ A similar interpretation has been given by Dahlen and van Leeuwen for photoionization of one-dimensional helium with the time-dependent extended Hartree-Fock method [282], which closely resembles the $M = 2$ approximation.

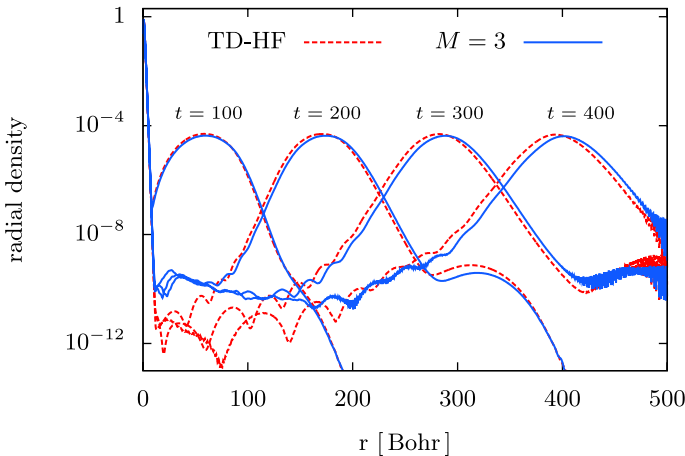


Fig. 39. Snapshots of the radial density for different times t from 100 to 400 a.u. following an application of a 45 eV pulse of intensity 10^{13} W/cm^2 onto the helium ground state. One clearly notices a wave packet leaving the atom, which moves slightly faster for the $M = 3$ approximation than for TD-HF. Reproduced with permission from J. Chem. Phys. **134**(8), 084106 (2011) [76]. Copyright 2011 American Institute of Physics.

boundary, and subsequently interferes with its outgoing part²². One further observes that the velocity of the wave packet, which is determined by the difference of the photon energy and the ionization potential, is larger in the $M = 3$ approximation than in TD-HF. This can be explained with the well-known fact that the Hartree-Fock approximation—or, more precisely, Koopmans theorem—overestimates the exact value of the ionization potential. The MCTDHF approximation improves on this, and the resulting smaller ionization potential leads to a larger electron excess energy.

Length vs. velocity gauge. The dipole approximation represents the most common way to model laser-atom interactions. It is valid if the wavelength of the laser field is much longer than the dimension of the atom, and amounts to neglecting the influence of electric quadrupole and magnetic dipole and higher terms on the target. The dipole approximation usually comes in two versions, either in the length gauge, where the coupling operator reduces to [79, 80]

$$\hat{v}_{\text{em}} = \mathbf{r} \mathbf{E}(t), \quad (4.16)$$

or the velocity gauge,

$$\hat{v}_{\text{em}} = \mathbf{p} \mathbf{A}(t). \quad (4.17)$$

Another choice which is used occasionally is the acceleration gauge or Kramers-Henneberger representation, as well as more general gauges [285]. The wavefunctions corresponding to different gauges are connected by a unitary transformation. As is considered in detail in Sect. 3.2.6, only full CI wavefunctions are invariant under unitary transformations, whereas approximated wavefunctions can differ in two representations. Therefore, the degree of agreement between results in the length and velocity gauge is sometimes used as a measure for the accuracy of the wavefunction.

Here, we consider the performance of the length and velocity gauge in the MCTDHF method. Figure 40 depicts the single- and double-ionization yields versus time

²² Such reflections could be easily avoided by applying exterior complex scaling [190, 283] or complex absorbing potentials [284].

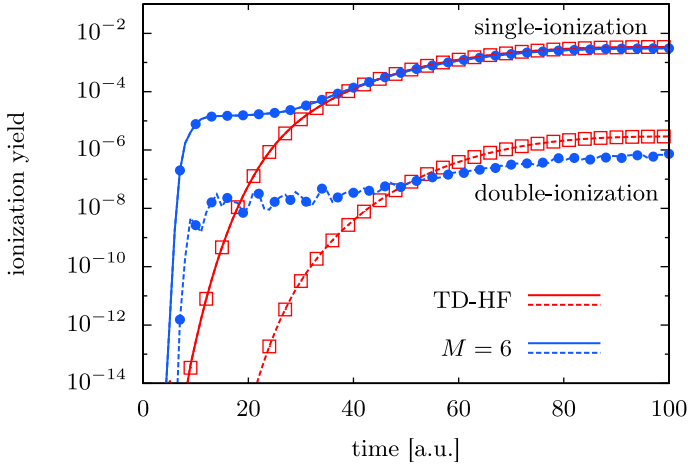


Fig. 40. Comparison of the results of length and velocity gauge for the single-ionization (solid lines) and double-ionization yields (dashed lines) of helium. Shown are the TD-HF and the $M = 6$ approximation. The results for the length gauge are plotted as lines, while those for the velocity gauge are shown as circular and square dots. Both gauges agree exactly.

calculated in the TD-HF and $M = 6$ approximation, for a laser pulse of duration $T = 100$ a.u. and intensity $I = 10^{13}$ W/cm². The lines show the results of the length gauge, the circles and squares those of the velocity gauge. From the dynamic of the ionization yields, it is again apparent that the single- and double-ionization are directly related for low-order MCTDHF approximations. The correlated $M = 6$ approximation, however, provides a mechanism to reduce the double-ionization and thus yields a notably slower increase for times $t > 50$ a.u. as compared to the TD-HF approximation. Furthermore, the $M = 6$ curves show a much earlier increase of the ionization and, therefore, a greater sensitivity also to laser fields of low intensity²³.

The results of the two gauges agree exactly for all depicted curves, and the same behavior is also observed for other MCTDHF approximations. This numerical observation can be explained by the fact that gauge transformations are represented exactly in the MCTDHF method. More precisely, a unitary gauge transformation acts in the momentarily spanned MCTDHF Hilbert space which, at a given time, corresponds to a full CI Hilbert space and, therefore, remains invariant. However, the numerical performance between the two gauges is different, and the length gauge is found to be about 30% faster than the velocity gauge. Correspondingly, for the MCTDHF approximation, the concept that the differences between the two gauges contains the information on the accuracy of the wavefunction does not apply. In contrast, in the TD-RASCI approximation, that was considered in Sect. 3.2.6, a gauge transformation can result in a different RAS Hilbert space and, therefore, the results of the length and velocity gauge, in general, differ. In the limit when the RAS Hilbert space approaches the full CI space, the wavefunction becomes exact and both gauges will yield the same results. The other direction of this implication, however, is not true, i.e., it is not valid to make predictions on the accuracy of the wavefunction from its behavior under a special unitary transformation. We therefore reject, supported also by Ref. [265], the concept of using the comparison between length and velocity gauge as a means to qualify the wavefunction.

²³ This concept, however, has also been questioned [265].

4.2 Beryllium

Beryllium is the simplest atom with two closed shells. The ionization energy of its $2s$ orbital is experimentally found to be 9.32 eV, and 123.35 eV for ionization from the $1s$ orbital [286]. Therefore, when considering photon-energies below the $1s$ -threshold, the large energetic separation of the two shells allows for a fixation of the $1s$ core-orbitals and, thus, for the reduction to an effective two-particle problem. In this spirit, several works have been performed focusing on single- and double-electron photoionization. Most of them employ a time-independent approach, using, e.g., the R-matrix method [287], the relativistic random-phase approximation [288], hyperspherical calculations [289], or Multiconfigurational Hartree-Fock [145]. The time-dependent treatments are usually performed with the close-coupling approach [107, 290] or a mixed-basis approach [108], both of which attain a reduction by freezing the $1s$ orbitals (or, occasionally, the $2s$ orbitals).

In contrast, the methods applied here present true many-particle calculations in the sense that all electrons are active. For the TD-RASCI approach, we use a similar ansatz as before in helium: after solving the Hartree-Fock equations and orthogonalizing the remaining ideal orbitals, we include 10 s -orbitals and 2 p -orbitals, which may be arbitrarily occupied by the 4 electrons. The only restriction is that we allow only for single-excitations from the $1s$ orbitals, which is reasonable, as for the considered photon energy range and intensity double excitations from the $1s$ shell are negligible. By this, we obtain a RASCI ground state energy of $E = -14.618$ Ha, which has to be compared to the HF energy of $E = -14.573$ Ha and to the exact energy $E = -14.667$ Ha [291]. We further present results from MCTDHF calculations. A very similar MCTDHF study has been published recently by Haxton et al. [74].

4.2.1 Ground state energy

In analogy with the investigation in section 4.1.1, we first examine the ground state energy of beryllium for different levels of the MCTDHF approximation. Since the bound density is contained in a small region by the Coulomb potential, we can afford to use a small radial grid of 30 atomic units for these calculations. The radial dimension is divided into 10 elements, each containing 20 FEDVR basis functions. The number of angular basis functions is adjusted to assure the convergence of the results, cf. Table 7. In addition, the fraction of correlation energy that is covered by the MCTDHF approximation, with regard to the exact ground state energy of $E_0^{\text{exact}} = -14.667$ Ha [292] was calculated. We observe that the amount of correlations rises rapidly, in the range $M \in [2, 7]$. After $M = 7$, the convergence slows down and, after $M = 10$, the amount of correlation reaches a value of roughly 90% and is almost constant. This is consistent with the results for helium shown in section 4.1.1. A remarkable difference between both results is the amount of correlation due to the first correction beyond the Hartree-Fock approximation. While the first correction in the case of helium already adds 40% of the total correlation energy, it only covers 15% of all correlations, in the beryllium case. This is most likely due to the more complex structure of the beryllium ground state. Another important observation is that it is necessary to adapt the angular basis when the level of approximation is varied. This is caused by the richer angular structure of the ground state, which is produced by the increasing correlations.

4.2.2 Single-ionization cross section

As a first check of the TD-RASCI method, we calculate the photoionization cross sections using an explicitly time-dependent approach, as was considered in the

Table 7. Ground state energy of beryllium and the amount of covered correlations for different numbers of orbitals M . The maximal azimuthal quantum number and the maximal magnetic quantum number are adjusted to assure the convergence of the energy, if necessary.

l_{\max}	m_{\max}	M	$E_0[\text{eV}]$	correlations (%)
2	1	2	-14.573	0
		3	-14.587	15
		4	-14.605	34
		5	-14.612	41
		6	-14.619	49
		7	-14.634	65
		8	-14.646	78
3	2	9	-14.653	85
		10	-14.655	87
		11	-14.656	88
		12	-14.657	89
		13	-14.657	89
		14	-14.658	90
4	3	15	-14.658	90
		16	-14.659	91

previous section on helium. We note, however, that the application of a time-dependent method is usually not the most efficient way for obtaining cross sections. In fact, accurate results can be obtained already with time-independent methods which require a much reduced effort. However, the cross sections provide an indispensable test for the accuracy of the approach, as one can directly identify the states and ionization channels included in the wavefunction. These can then be exploited for problems requiring an explicitly time-dependent description, such as the X-ray–IR photoionization considered below.

The top picture of Fig. 41 shows the cross-sections obtained with TD-RASCI for photon energies in the range $\omega = 20$ to 85 eV, in which the single photoionization is the dominant process. The duration of the applied sine-squared laser pulse is 400 a.u. and its intensity is 10^{12} W/cm 2 . We compare our theoretical results to measurements performed in two works of Wehlitz et al. [293, 294]. Further, we depict the theoretical cross sections of Laulan and Bachau, which have been calculated with the time-dependent close-coupling method and fixed $1s$ orbitals [107]. As before in helium, the curves show a monotonically decreasing behavior. The TD-CIS results already give a good qualitative agreement with the experimental results which becomes better for larger photon energies. By adding double-excitations up to the $(10s, 2p)$ orbitals in the TD-RASCI approximation, we are able to reproduce the experimental results almost perfectly. Particularly, the all-active electron calculations perform superior to the fixed-core results of Laulan and Bachau [107]. The corresponding MCTDHF results are depicted in the lower panel of Fig. 41. The TD-HF calculations already reproduce the measurements to within a few percent accuracy, and thus perform better than the TD-CIS approximation. The correlated $M = 4$ approximation, on the other hand, gives only a slight improvement over the TD-HF curve.

In Fig. 42, we consider the resonances in between the $\text{Be}^+(2p)$ and $\text{Be}^+(3s)$ thresholds. In order to obtain a higher resolution, the calculations have been performed with a pulse duration of $T = 800$ a.u. (~ 20 fs). The reference results are taken from a time-independent R-matrix study of Kim et al. [287]. The TD-CIS approximation predicts cross sections of the correct order of magnitude, but is not adequate

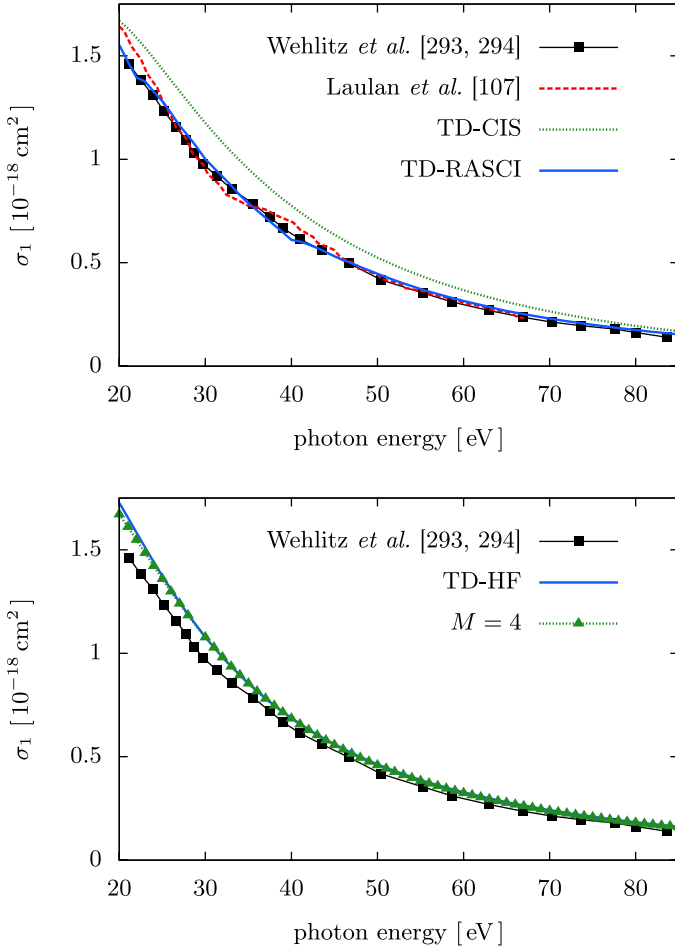


Fig. 41. Single-photoionization cross section for beryllium. *Top:* comparison of TD-RASCI calculations with the experiments of Wehlitz [293, 294] and the theoretical calculations of Laulan and Bachau [107]. Figure from Ref. [75]. *Bottom:* cross sections from MCTDHF calculations. Shown are the results of TD-HF and the $M = 4$ approximation.

to model the resonances. This is not surprising as the required doubly-excited states are missing in the wavefunction; the results are shown here only for reference. At the same time, the TD-RASCI method determines the overall structure correctly and, particularly, the first three resonances are well reproduced. Due to the limited bandwidth, however, our time-dependent approach does not resolve the threshold region around 20 eV. To obtain more accurate results, much longer propagation times and probably also larger TD-RASCI expansions would be necessary²⁴. We stress that the missing resolution towards the threshold does not mean that the related states do not exist. In fact, any of the orbitals up to 10s and 2p may get occupied and are, therefore, consistently included in the calculation.

²⁴ Alternatively, one could set up a corresponding time-independent RASCI approach which is, however, not the goal of the present work.

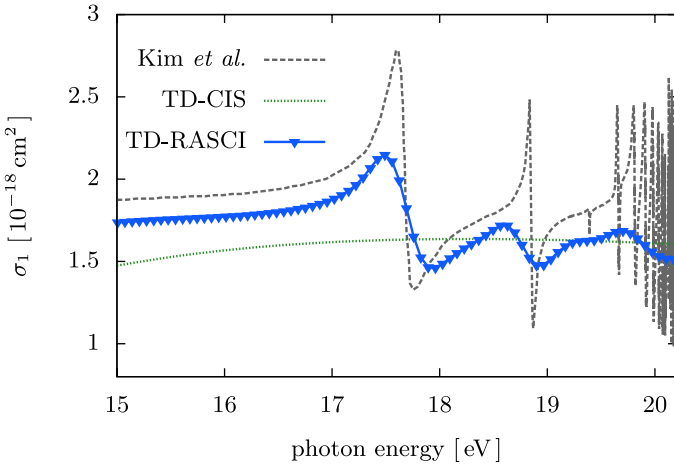


Fig. 42. Single-photoionization cross section for beryllium between the $\text{Be}^+(2p)$ and $\text{Be}^+(3s)$ thresholds. TD-CIS and TD-RASCI calculations are compared to the R-matrix results of Kim et al. [287]. Figure from Ref. [75].

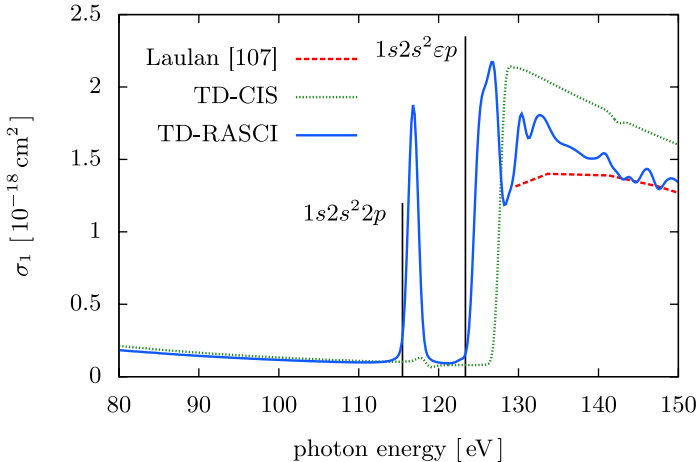


Fig. 43. Photoionization cross-section of beryllium around the $1s$ threshold. The (red) dashed line shows the results of Laulan and Bachau [107] obtained through a time-dependent method and fixation of the $2s$ orbitals, the (green) dotted and solid (blue) curves are our TD-RASCI and TD-CIS results. The vertical black lines mark the resonance and ionization energy according to the NIST database [286]. Figure from Ref. [75].

4.2.3 Core-electron ionization

The previous investigation considered ionization from the $2s$ shell. In the following, we take a closer look at the ionization of the core electrons. Figure 43 presents the cross sections for photon energies in between $\omega = 80$ and 150 eV, i.e., around the onset of the ionization of the $1s$ orbital at 123.35 eV. Here, a pulse duration of $T = 200$ a.u. is used. Again, we compare our results to those of Laulan and Bachau [107] where, this time, the two $1s$ electrons are considered active and the $2s$ shell is kept “frozen”. We note again that, in contrast, the TD-RASCI method (and TD-CIS as a special case of it) treats ionization from both shells on the same footing. It is, therefore, able to adequately describe the transition region where the ionization from the $1s$ -shell

becomes dominant. In TD-CIS, the ionization of the $1s$ orbitals occurs at an energy of $\omega = 128.72$ eV, which is the ionization energy obtained in Hartree-Fock through the Koopmans theorem. Note that the reason for this agreement is the missing coupling between the bound and singly-excited states, due to the Brioullin theorem [59]. The more accurate $(10s, 2p)$ TD-RASCI wavefunction is able to shift the onset energy closer towards the exact position to around 125 eV. The same holds for the $1s\ 2s^2\ 2p$ -resonance which, unlike the resonances considered so far, is already contained in the TD-CIS approximation, as the corresponding excited state is obtained from the ground state by a single excitation from $1s$ to $2p$. Again, the TD-RASCI approximation corrects the resonance position and achieves almost the exact result. Above the $1s$ threshold, one encounters a large number of densely lying resonances caused by the further excitation of the electrons from the $2s$ shell which have been studied in detail by Voky et al. using the time-independent R-matrix method [295]. In contrast to the results of Laulan and Bachau, which show a smooth monotonically decreasing curve, the TD-RASCI method again reproduces the occurrence and position of the resonances which are populated in shake-up processes.

4.2.4 X-ray–IR pump-probe ionization

So far, in our time-dependent study of beryllium we considered only stationary quantities such as total cross sections. In the following, we investigate a pump-probe process which, in contrast to the previous applications, is accessible only by an explicitly time-dependent treatment. We consider the following scenario: beryllium in its ground state is ionized by an X-ray pulse with a photon energy of 200 eV, an intensity of 10^{12} W/cm² and a squared sine envelope with a duration of 20 cycles. At the same time, a single-cycle IR pulse with a wavelength of 780 nm and an intensity of 10^{11} W/cm² acts on the system. Following the usual streak camera principle, the delay δ between the X-ray and the IR pulse is varied and observables such as the ionization yields and momentum spectra are recorded as a function of δ .

For the TD-RASCI calculations, we use three different levels of accuracy: in the basic approximation, referred to as $(2s)$, only the Hartree-Fock determinant and its single-excitations are included, i.e., it corresponds to a TD-CIS approximation. We further apply more accurate models in which we allow for double excitation up to the orbital ns [denoted (ns)] and additionally up to the mp orbital [denoted (ns, mp)]. For example, $(5s, 3p)$ labels the CISD wavefunction with double excitations allowed up to the $5s$ and $3p$ orbitals, and additionally all single-excitations of these determinants. The presented calculations require between half an hour on a single processor for the $(2s)$ approximation and two days for the $(5s, 3p)$ approximation.

Figure 44 illustrates the time-dependent ionization yield for three different delays δ of the pump and probe pulses and the $(2s)$ as well as the more sophisticated $(5s, 3s)$ approximation. As expected, all calculations show a steep rise of the yields during the action of the X-ray pulse. As suggested by Fig. 41, the total yield is larger for the single-active electron approximation. One further obtains relative differences for the three delays, which can be observed most obviously for the delay $\delta = T_{\text{IR}}$, where the X-ray field begins right after the IR pulse has passed. In the TD-CIS approximation $(2s)$, at this time, a significant portion has been ionized by the IR pulse, and accordingly the total yield is larger and also differs for the three delays. For the $(5s, 3p)$ approximation, the influence of the IR field on the ionization is much reduced and all three delays show a comparable ionization yield. This is caused by the fact that the more sophisticated TD-RASCI ansatz is able to model more accurately the polarization of the atom which is induced by the IR field.

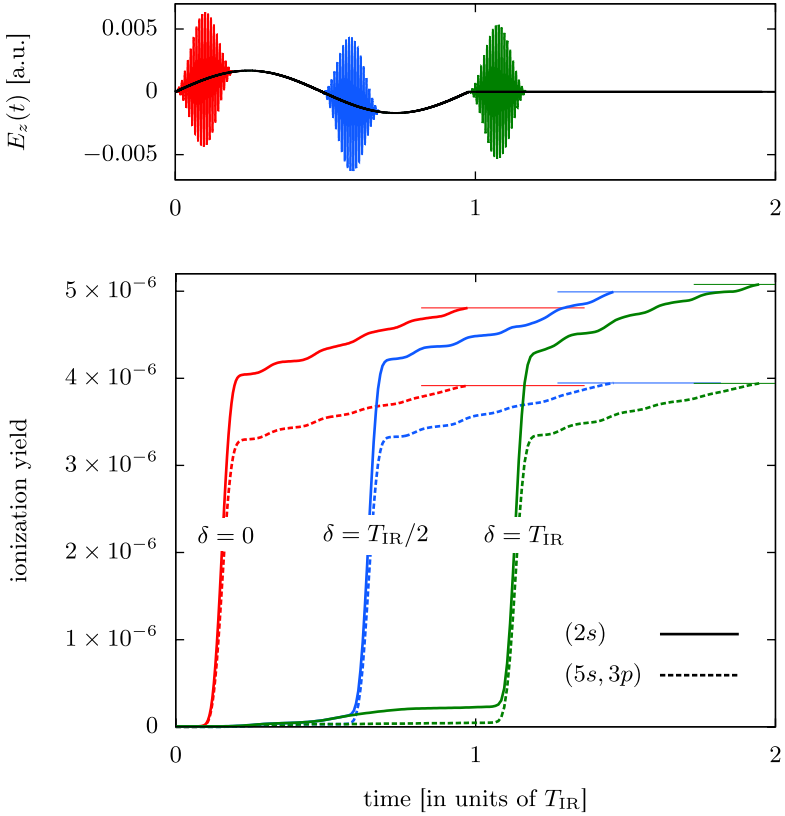


Fig. 44. Total ionization yield of beryllium subjected to X-ray pump and IR probe pulses with three different delays shown in the top figure. The results are plotted from a single-active electron calculation (2s) and the more accurate (5s, 3p) TD-RASCI approximation (see text). For better comparison, the horizontal lines at the end of the pulses mark the total ionization yield. Figure from Ref. [75].

The angular distribution of the ionized part of the wavefunction is depicted in Fig. 45, for the two delays $\delta = 0$ and $\delta = T_{IR}$. As before, the ionization yield is determined for each angle as the norm of the wavefunction outside a distance $r = 20$ Bohr from the nucleus. For the delay $\delta = 0$, the photo-electron is excited to high angular momentum states which cause the peculiar structure of the angular distribution. This structure becomes largely damped upon inclusion of more s -orbitals into the expansion. Further, the use of more p -orbitals leads to a considerable asymmetry between forward ($\theta = 0$) and backward ($\theta = \pi$) direction. For the delay $\delta = T_{IR}$, the X-ray pulse acts after the IR pulse has passed leading to ionization predominantly to lower partial waves and, therefore, to a smoother distribution. Nevertheless, one observes a noticeable influence on the ionization yields. The best TD-RASCI approximation, (5s, 3p), again gives an ionization yield which is reduced by a factor of roughly 2.5, as compared to the TD-CIS curve and, further, predicts enhanced ionization in forward direction. This is remarkable as there is no IR field acting on the atom, and one could also expect a symmetric distribution as it is obtained in the normal photoionization. Hence, it appears that the IR field induces electronic motion which remains after the pulse has passed and affects the photoionization process. The detailed investigation of the characteristics of this special photoionization process is an interesting subject for future work.

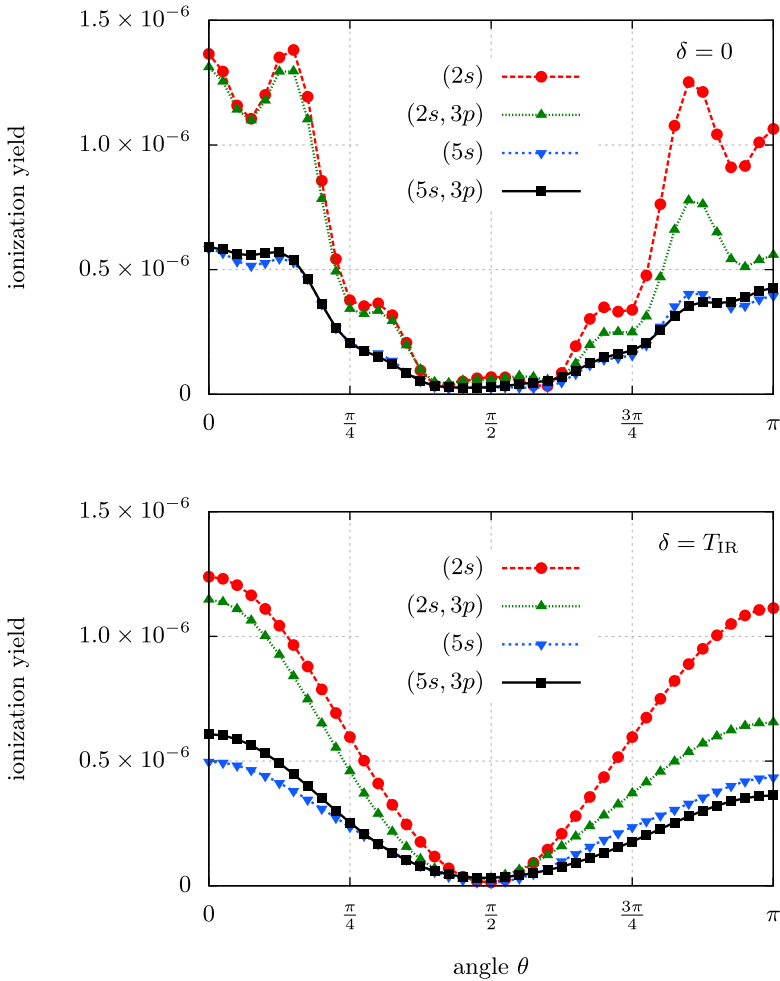


Fig. 45. Angular distribution of the photoionization yield of beryllium subjected to an X-ray pump and an IR probe pulse with the delay δ indicated in the figures. Plotted are the results of different RAS approximations (see text). Figure from Ref. [75].

4.3 Neon

Neon is a common target in photoionization studies and has been investigated several times in the previous half century. Generally, its closed-shell structure facilitates the application of theoretical approaches, and several methods such as perturbation theory [296], Hartree-Fock [297] or random-phase methods [298], R-matrix theory [65] or the Stieltjes-Chebyshev moment technique [299] have been used to calculate total or state-resolved cross sections. In addition, a variety of experimental studies have measured the cross sections, e.g., Refs. [300–302]. Neon has further been the recent subject of experimental studies on FEL-induced non-sequential double ionization [10], the angular correlation of the emitted photo- and Auger-electrons in the K-shell ionization [303] as well as on the interatomic Coulombic decay of electronic states in the neon dimer [304]. Another interesting effect is the time-delay between the photo-emission from the 2s and 2p shell [30]. In this work, we address the task of calculating

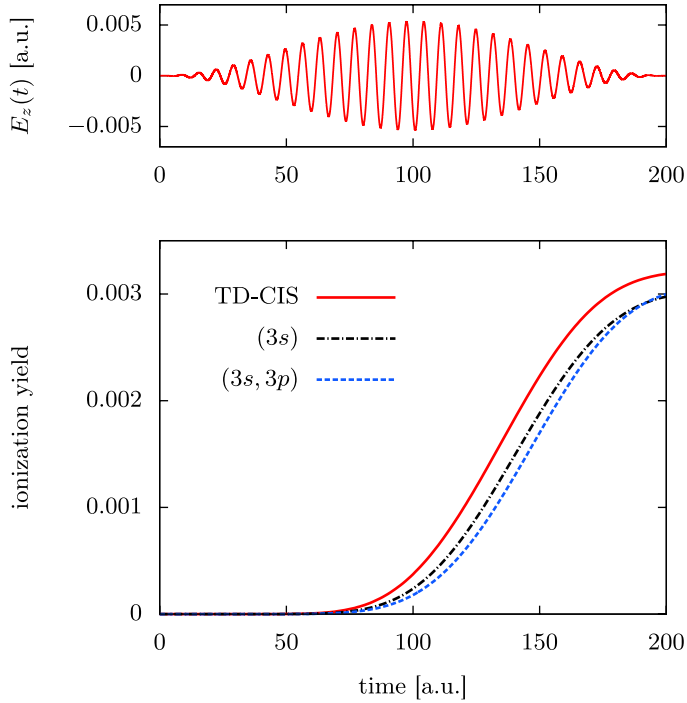


Fig. 46. Ionization yield plotted versus time for photoionization from the ground state of neon subjected to the laser field shown in the top panel. The photon energy is 25 eV and the intensity 10^{12} W/cm^2 . The TD-CIS method predicts a slightly larger ionization yield than the (3s) and (3s, 3p) approximations (see text). Figure from Ref. [77].

the total and angle-resolved photoionization yields and spectra. The presented results have been published in Ref. [77].

4.3.1 Single-photoionization cross sections

For the neon atom, we apply the basic form of the TD-RASCI wavefunction used before, that is, we consider single-ionization where only one particle is allowed in the continuum—the region outside $r = 20$ Bohr. For the wavefunction in the inner region we use three approximations: (i) TD-CIS, where only the Hartree-Fock ground state plus all single-excitations are included, (ii) the (3s)-approximation where double-excitations up to the $3s$ orbital are allowed, and (iii) the (3s, 3p) approximation where double-excitations to the $3s$ orbital and, further, to the $3p$ orbitals are allowed. The single-particle basis consists of partial waves up to $l = 3$ and a radial grid that extends up to 400 Bohr. The grid has finite elements of length 4 Bohr which include 10 basis functions each, except for the first element which contains 20 basis functions. The total number of Slater determinants used to describe the wavefunction is $N_{\text{det}} = 32447$, for the TD-CIS approximation, $N_{\text{det}} = 237922$, for the (3s) approximation, and $N_{\text{det}} = 454151$, for the (3s, 3p) approximation. The neon atom is propagated for $T = 200$ a.u. under the action of a laser pulse with a sine-squared envelope (also with duration T). The calculations take in between 90 minutes on a single processor for the TD-CIS approximation and 48 hours for the (3s, 3p) approximation.

Figure 46 depicts the ionization dynamics for photoionization from the neon ground state with the 25 eV pulse shown in the top panel. A particle is considered

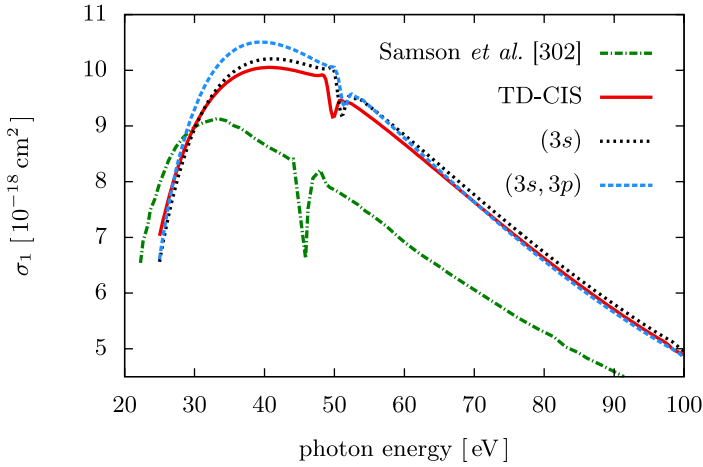


Fig. 47. Total single-photoionization cross section of neon versus photon energy for photoionization from the ground state. The duration of the squared-sine envelope of the laser field is $T = 200$ a.u. and the intensity is 10^{12} W/cm 2 . The dotted-dashed curve depicts the experimental results of Samson et al. [77, 302].

ionized if it is located outside a radius of 20 Bohr from the nucleus. All three TD-RASCI approximations show the same qualitative behavior: a steep rise around $t = 100$ a.u., which is delayed with respect to the field, due to the time the electron needs to travel to $r = 20$ Bohr, followed by a saturation around the end of the pulse. The TD-CIS approximation produces the largest yield and a slightly earlier rise than the more advanced TD-RASCI approximations.

We now turn to the photoionization cross sections σ_1 , which are calculated from the ionization yield P_1 with formula (3.152). The ionization yield P_1 is determined as the norm of the wavefunction outside $r = 20$ Bohr at the end of the pulse. In Fig. 47, we plot the single-photoionization total cross section against the photon energy, for a laser pulse with duration 200 a.u. and an intensity of 10^{12} W/cm 2 . All three approximations produce cross sections which rise around the Hartree-Fock ionization energy of 23.15 eV. One further obtains a monotonic decrease for larger photon energies. Around 50 eV, we observe the $2s\ 2p^6\ 3s$ resonance, the exact location of which is 45.547 eV, according to Ref. [305]. The more accurate approximations shift the position of the resonance in the wrong direction. Further, when comparing the calculated cross section to experimental results of Samson et al. [302], we observe that the theoretical results are 10% larger than the measured values. The reason for these discrepancies is still open, considering the very good performance of TD-RASCI in estimating the cross sections in the previous applications.

4.3.2 Momentum distribution

The momentum distribution of the ionized particle for a photon energy of 70 eV is depicted in Fig. 48. The momentum is calculated by a Fourier transform of the ionized part of the wavefunction ($r > 20$ Bohr). The left picture shows the two-dimensional momentum distribution which arises from the $(3s, 3p)$ approximation. Due to the linear polarization of the laser it is symmetric with respect to rotations around the z -axis. One clearly notices two rings which correspond to ionization from the $2s$ and $2p$ shells. The inner ring around 30 eV exhibits p -symmetry and stems from the ionization from the $2s$ -orbital. The outer ring at 50 eV corresponds to the ionization from the $2p$

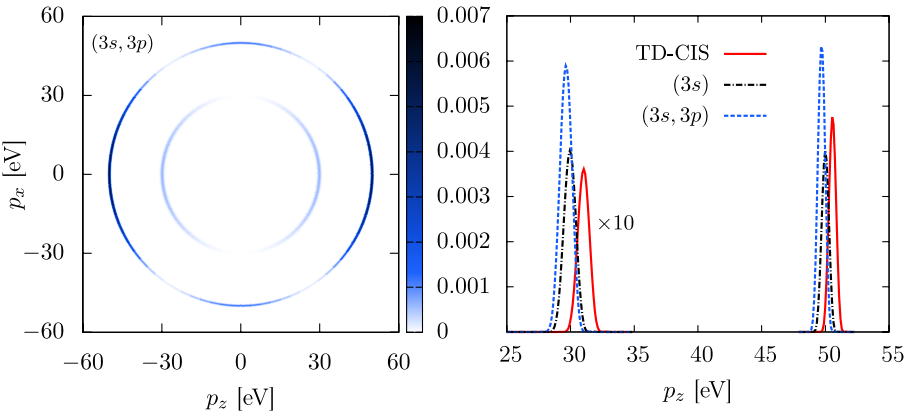


Fig. 48. Photoelectron momentum distribution for a photon energy of 70 eV. *Left:* momentum distribution for the $(3s, 3p)$ approximation. One clearly notices two rings which correspond to ionization from the $2s$ -orbital (inner ring) and the $2p$ -orbital (outer ring). *Right:* momentum distribution in forward direction for the three TD-RASCI approximations. The peaks which correspond to ionization from the $2s$ shell are multiplied by a factor of 10. Figure from Ref. [77].

orbitals and is dominantly of d -symmetry, but also has a contribution of s -symmetry, as can be seen from the distribution not going down to zero, but remaining at a finite value. The right panel shows the momenta from the three approximations in forward direction along the z -axis, i.e., $\theta = 0$. It is immediately obvious that the accuracy of the wavefunction has a distinct impact on the spectra. The TD-CIS results yield the highest photo-electron momentum. With increasing accuracy of the wavefunction, both peaks shift towards a lower momentum. Interestingly, the $2s$ -peak shows a larger relative shift than the peak corresponding to the $2p$ ionization. This indicates the importance of a correlated description, and is likely to have a major impact in the calculation of pump-probe processes using the streak camera principle.

5 Outlook and conclusions

In this final section, we will first give an outlook on possible extensions to the thus far described formalisms and an overview on other systems that were treated with these schemes. Subsequently, we will close this review with a summary of the obtained insights.

5.1 Further extensions of the methods

In the following, we discuss several extensions of the MCTDHF and TD-RASCI formalisms as provided so far, including the treatment of bosons, systems at finite temperatures and mixtures of different particle species. For each of them, we present example calculations making use of the numerical techniques developed in Sect. 3. Furthermore, we propose an idea of combining MCTDHF calculations with the restricted active space concept to efficiently simulate photoionization processes.

5.1.1 Bosonic particles

The methods introduced so far were applied to fermions, but can be easily extended to the treatment of bosons. To arrive there, one has to replace the Slater determinants by their bosonic analogues—permanents—which have been introduced in Sect. 2.1.2. A variety of bosonic systems has been studied using the multiconfigurational time-dependent Hartree method for bosons (MCTDHB), introduced by Alon et al. [154], or by similar but less sophisticated approaches, like the multi-orbital mean-field method [306]. Among the problems studied so far are the dynamics of double-well systems [307], the properties of a bosonic Josephson junction [308] or the fragmentation of Bose-Einstein condensates [309]. The latter has also been studied by Heimsoth and Bonitz using the unrestricted Hartree-Fock method for bosons [173]. Recently, also the multi-layer MCTDH method has been adopted for the simulation of bosons [310].

As has been pointed out by Alon et al., the MCTDHB orbital equations remain essentially unchanged, as compared to those derived for fermions [97]. In the coefficient equation, one only has to adapt the calculation of matrix elements between permanents, which are performed with the bosonic version of the Slater-Condon rules [206]. In the case of a single permanent, and for contact interaction, the MCTDHB equations become identical to the Gross-Pitaevskii equation.

As an example, we apply the MCTDHB method to describe a Bose-Einstein condensate on a one-dimensional ring, which is subjected to an external periodic driving field. The following results are based on Ref. [311]. The Hamiltonian is given by

$$\hat{H} = \sum_p \frac{p^2}{2} \hat{a}_p^\dagger \hat{a}_p + \sum_{|p-q|=1} v_{pq}(t) \hat{a}_p^\dagger \hat{a}_q + \frac{U}{2} \sum_{pqrs} g_{pqrs}, \quad (5.1)$$

with the two-electron integrals for contact interaction,

$$g_{pqrs} = \frac{1}{2\pi} \delta_{p+r,q+s}, \quad (5.2)$$

and the matrix elements of the driving field,

$$v_{pq}(t) = \delta_{p,q+1}(E_+ e^{-i\omega t} + E_- e^{i\omega t}) + \delta_{p,q-1}(E_+ e^{i\omega t} + E_- e^{-i\omega t}). \quad (5.3)$$

For a sufficiently small interaction strength, the initial ground state can be assumed being completely condensed in the zero angular momentum mode. The system then constitutes a possible realization of a bosonic orbital Josephson junction, given that the amplitudes E_\pm of the driving potential are sufficiently small, and the driving frequency ω is close to the energy difference between the initial $l = 0$ mode and the two outer modes, $l = 1$ and $l = -1$. The parameters we choose here, $E_+ = 0.7$, $E_- = 0.3$, and $\omega = 0.5$ a.u., satisfy this criterion. We consider $N = 40$ particles and take a particle interaction of

$$U = \frac{0.5}{N-1}, \quad (5.4)$$

which can be shown to yield chaotic motion in the mean-field limit via the calculation of the Ljapunov exponent [311]. Such dynamical instabilities notoriously cause mean-field predictions to fail and, therefore, require accurate many-body approaches.

Figure 49 shows the time-dependence of the occupation of the $l = 0$ angular momentum mode for different levels of MCTDHB approximations. In the beginning of the propagation, up to roughly $t = 100$ a.u., the results of all approximations agree well with each other. Thereafter, first the Gross-Pitaevskii ($M = 1$) approximation starts to deviate and predicts large oscillations of the occupation number.

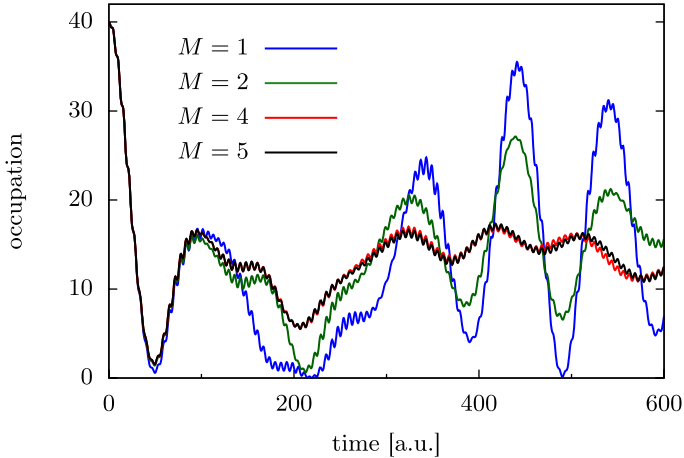


Fig. 49. Occupation of the ground state mode for a Bose-Einstein condensate with $N = 40$ particles on a one-dimensional ring. The $M = 1$ approximation uses a single time-dependent orbital and corresponds to the Gross-Pitaevskii approximation. By including a higher number of time-dependent orbitals, the MCTDHB method essentially recovers the exact dynamics of the condensate, as can be seen by the convergence of the $M = 4$ and $M = 5$ results.

The $M = 2$ correction shows a similar behavior which, however, deviates later (around $t = 200$ a.u.) and yields smaller amplitudes. Particularly at times $t > 300$ a.u., the $M = 4$ and $M = 5$ approximations predict a much smaller variation of the occupation number which oscillates around $N = 15$. Further, since both approximations agree well with each other over the whole considered time frame, it can be suggested that convergence has been achieved and the result is close to the exact one. For more details and further results, see Ref. [311].

5.1.2 Finite temperatures

In the main part of this work, the description of physical systems has been given in terms of pure states, as detailed in section 2.1. The present formalism, however, can also be extended to quantum statistics, where the system is described by a density operator given, in its spectral representation, by

$$\hat{\rho} = \sum_i p_i |\Psi_i\rangle\langle\Psi_i|. \quad (5.5)$$

The summation is performed over the complete set of eigenstates of $\hat{\rho}$, and the coefficients $p_i \in [0, 1]$ determine the probability for the system to be in the eigenstate $|\Psi_i\rangle$, where $\sum_i p_i = 1$. Expectation values of an operator \hat{O} are then computed by tracing over the density operator,

$$\begin{aligned} \langle \hat{O} \rangle &= \text{Tr} \{ \hat{O} \hat{\rho} \} \\ &= \sum_j \langle \Psi_j | \hat{O} \sum_i p_i |\Psi_i\rangle \langle \Psi_i | \Psi_j \rangle \end{aligned} \quad (5.6)$$

$$= \sum_i p_i \langle \Psi_i | \hat{O} | \Psi_i \rangle. \quad (5.7)$$

In the canonical ensemble, the equilibrium density operator is given by

$$\hat{\rho}_{\text{can}} = \frac{1}{Z_{\text{can}}} e^{-\beta \hat{H}}, \quad (5.8)$$

where $\beta = (k_B T)^{-1}$ denotes the inverse temperature, and the partition function is defined by

$$Z_{\text{can}} = \text{Tr} \{ e^{-\beta \hat{H}} \}. \quad (5.9)$$

Through expansion of the exponential in a Taylor series, one notices that the eigenfunctions of the density operator are exactly the eigenfunctions of the Hamiltonian, and that the coefficients in Eq. (5.5) consequently evaluate to

$$p_i = \frac{e^{-\beta E_i}}{\sum_j e^{-\beta E_j}}, \quad (5.10)$$

where E_i is the energy of the eigenstate $|\Psi_i\rangle$. Therefore, once the Hamiltonian is completely diagonalized, one has immediate access to the properties of the system at finite temperatures, a task which can be straightforwardly solved with the configuration interaction method.

The previous approach has been applied to describe fermionic few-particle systems in one- and two-dimensional harmonic oscillators. The 1D results have been published in Ref. [312], where they are mainly used to benchmark the configuration path-integral Monte-Carlo (CPIMC) method of Schoof, Bonitz et al., which performs a statistical sampling of Eq. (5.7) in a Slater determinant basis. Here, we consider, as an example, electrons (with Coulomb interaction) in a two-dimensional harmonic oscillator potential, described by a Hamiltonian of the form

$$\hat{H} = \sum_{i=1}^N \left\{ \frac{\mathbf{p}_i^2}{2} + \frac{\mathbf{r}_i^2}{2} \right\} + \frac{\lambda}{2} \sum_{i \neq j} \frac{1}{|\mathbf{r}_i - \mathbf{r}_j|}. \quad (5.11)$$

This system shows interesting physics including the cross over from Fermi gas to Fermi liquid and Wigner crystal-type behavior at very strong coupling, even for finite electron numbers, as was found using path integral Monte Carlo simulations, e.g. [313, 314] and references therein, but here we concentrate on moderate coupling. Note that, instead of atomic units, harmonic oscillator units are used here, in which the energy and length scales are given in units of $E_0 = \hbar\Omega$ and $x_0 = \sqrt{\hbar/m\Omega}$, respectively, where Ω is the trap frequency [315]. In particular, we focus on the case of $N = 6$ electrons which form a closed shell in 2D. The single-particle basis consists of Fock-Darwin states, i.e., harmonic oscillator eigenfunctions in polar coordinates, and has a size of $N_b = 15$. The corresponding electron integrals are calculated using the Talmi transformation [316]. We include determinants with spin and angular momentum projection of $S_z = 0$ and $L_z = 0$, respectively, which leads to a total dimension of $N_{\text{det}} = 16451$ of the full CI space. The corresponding Hamiltonian can, therefore, be conveniently diagonalized on a desktop computer. In addition to full CI, we also consider approximations with reduced excitations, where only a number of n_h holes is allowed in the reference determinant, which is chosen as the (zero-temperature) Hartree-Fock ground state. Note that $n_h = 1$ corresponds to the CIS scheme, $n_h = 2$ to the CISD scheme and so on, until for $n_h = 6$ full CI is recovered.

Figure 50 depicts the energies of the system for varying inverse temperature β and coupling parameter λ . The left inset illustrates the change of the energy with temperature for restricted-excitation schemes, from CIS to full CI. For $\beta > 3$ one notices a convergence against the ground state energy, whereas for smaller β , i.e., larger temperatures²⁵, the energies steeply increase until $\beta \approx 0.1$. For even smaller

²⁵ In the present units, $\beta = \hbar\Omega/k_B T$.

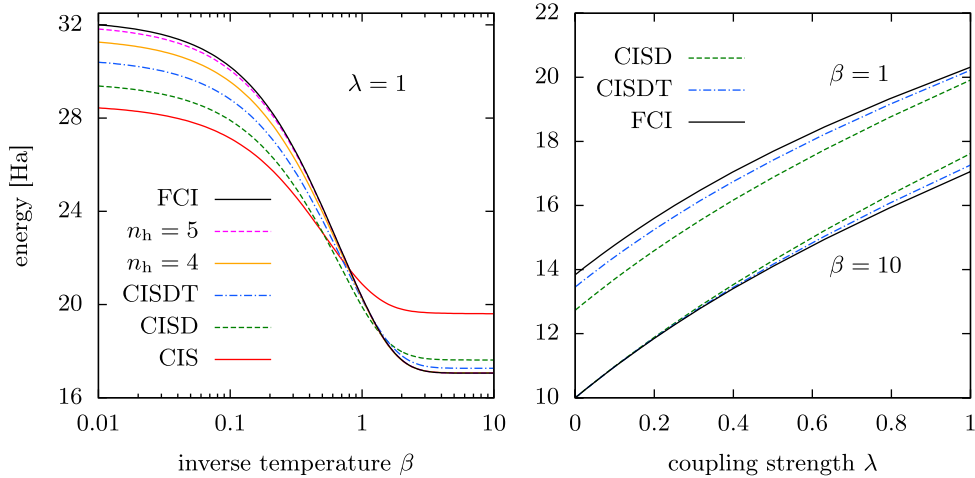


Fig. 50. Energies for $N = 6$ electrons in a two-dimensional harmonic oscillator at finite temperatures. *Left:* energy plotted against the inverse temperature β for various restricted-excitation schemes from CIS to full CI, for a coupling strength of $\lambda = 1$. *Right:* energy against the coupling parameters for $\beta = 1$ and $\beta = 10$. For all calculations, a single-particle basis of $N_b = 15$ Fock-Darwin states is used.

β , the curves show only a slight increase and, moreover, seem to converge. This is caused by the small single-particle basis, and corresponds to the fact that, at such high temperatures, each orbital is occupied. The different approximations yield a similar qualitative behavior and approach the full CI result with increasing number of allowed excitations. In the right inset of Fig. 50, the change of the energies with the coupling strength is plotted for two inverse temperatures. The value $\beta = 10$ corresponds to the ground state of the system and, in accordance with the Rayleigh-Ritz variational principle, the full CI result lies strictly below the CISD and CISDT results. Moreover, the approximations agree well with the full CI reference for small coupling strengths, $\lambda < 0.3$, as the Hartree-Fock determinant there becomes exact. This is different for the case of larger temperatures, $\beta = 1$, where the disagreement of CISD and CISDT is larger and the full CI curve lies above the results of the approximate calculations. Further, the disagreement remains even for vanishing interaction, which shows that the accuracy depends not only on the quality of the eigenfunctions (which are exact for $\lambda = 0$), but also on the dimension of the Hilbert space. In a similar way, the inclusion of determinants with other spin and angular momentum quantum numbers would affect the results.

We finally note that there also exist approximate techniques, which replace the complete diagonalization by an iterative procedure using, e.g., the Lanczos algorithm [317]. Further, specialized treatments have been set up to treat finite temperatures within the MCTDH approximation [318].

5.1.3 Systems with different particle species

The methods of this review are straightforwardly extended to systems containing different species of particles, i.e., distinguishable particles. The idea of the corresponding mathematical description has already been given in connection with the unrestricted treatment of particles with different spin projections. For N_A (N_B) particles of species A (B), one has to deal with a combination of two Hilbert spaces \mathcal{H}_A and \mathcal{H}_B .

The Hamiltonian acting on the Cartesian-product Hilbert space $\mathcal{H} = \mathcal{H}_A \times \mathcal{H}_B$ is

$$\hat{H} = \hat{H}_{AA} + \hat{H}_{BB} + \hat{H}_{AB}, \quad (5.12)$$

where \hat{H}_{AA} (\hat{H}_{BB}) comprises the terms which solely act on the subspace \mathcal{H}_A (\mathcal{H}_B),

$$\hat{H}_{AA} = \sum_{pq} h_{pq}^{(AA)} \hat{a}_p^\dagger \hat{a}_q + \frac{1}{2} \sum_{pqrs} g_{pqrs}^{(AA)} \hat{a}_p^\dagger \hat{a}_r^\dagger \hat{a}_s \hat{a}_q, \quad (5.13)$$

$$\hat{H}_{BB} = \sum_{pq} h_{pq}^{(BB)} \hat{b}_p^\dagger \hat{b}_q + \frac{1}{2} \sum_{pqrs} g_{pqrs}^{(BB)} \hat{b}_p^\dagger \hat{b}_r^\dagger \hat{b}_s \hat{b}_q. \quad (5.14)$$

Here, \hat{a}_q^\dagger and \hat{a}_q (\hat{b}_q^\dagger and \hat{b}_q) denote the creation and annihilation operators for orbitals $|a_k\rangle$ ($|b_k\rangle$) belonging to particle species A (B). They obey the usual fermionic/bosonic commutation relations within the subspaces and commute for different subspaces because the particle species are distinguishable. This also implies that orbitals belonging to different species are orthogonal, $\langle a_p | b_q \rangle = 0$. The electron integrals are defined as in Eqs. (2.25) and (2.26), however, possibly with different forms for the operators.

The term \hat{H}_{AB} introduces the coupling between the two Hilbert spaces,

$$\hat{H}_{AB} = \sum_{i=1}^{N_A+N_B} \hat{O}_i + \sum_i \sum_j^{N_B} \hat{T}_{ij}, \quad (5.15)$$

and is, for generality, written in first quantization. The one- and two-particle operators \hat{O} and \hat{T} define the single-particle and interaction terms which are determined by the physical problem at hand. In second quantization, the right-hand side of Eq. (5.15) could be written as²⁶

$$\sum_{pq} \left(O_{pq}^{(AB)} \hat{a}_p^\dagger \hat{b}_q + O_{pq}^{(BA)} \hat{b}_p^\dagger \hat{a}_q \right) + \sum_{pqrs} \left(T_{pqrs}^{(AB)} \hat{a}_p^\dagger \hat{b}_r^\dagger \hat{b}_s \hat{a}_q + T_{pqrs}^{(BA)} \hat{b}_p^\dagger \hat{a}_r^\dagger \hat{a}_s \hat{b}_q \right), \quad (5.16)$$

where the electron integrals are defined by

$$\hat{O}_{pq}^{(AB)} = \langle a_p | \hat{O} | b_q \rangle, \quad (5.17)$$

$$\hat{T}_{pqrs}^{(AB)} = \langle a_p b_r | \hat{T} | b_s a_q \rangle. \quad (5.18)$$

The wavefunction is then set up in terms of basis states of the combined Hilbert space \hat{H} , which are given by tensor products of the basis states of the two original Hilbert spaces,

$$|\Psi\rangle = \sum_{I_A J_B} C_{I_A, J_B}(t) |a_{i_1} \cdots a_{i_{N_A}}\rangle |b_{j_1} \cdots b_{j_{N_B}}\rangle. \quad (5.19)$$

Note that for an MCTDHF ansatz, the orbitals forming the configurations are furthermore time-dependent. From here, the procedure to derive the equations of motion is straightforward and exemplified in the derivation of the spin-unrestricted MCTDHF equations: For each set of time-dependent orbitals, one has to take one functional derivative and require it to vanish. Further, the derivation of the coefficient equation remains unchanged, and yields the MCTDHF coefficient equations as well as the formally identical full CI and TD-RASCI equations.

²⁶ By this, however, we restrict ourselves to a certain algebraic form of the operators. Other forms are possible and arise, e.g., in electron-photon interactions.

The previous approach (and its extension to a larger number of particle species) covers a broad range of physically relevant scenarios, including

- Different spin projections as encountered in the spin-unrestricted MCTDHF method in Sect. 2.5.7.
- Dynamics beyond the Born-Oppenheimer approximation. The introduced method thereby resembles the nuclear-electronic orbital (NEO) approach by Hammes-Schiffer and coworkers [319]. Time-dependent applications have been considered by Haxton et al. [73] and Nest et al. [165], however, using a different formulation.
- Mixtures of fermions and bosons, for which Alon and coworkers have derived MCTDHF equations [320]. Possible applications include, e.g., the BCS-BEC transition and the formation of excitons, of an exciton superfluid or crystal, e.g. [321, 322].
- The quantum-field theoretical treatment of laser fields, as considered in a less formal context by Buth and Santra [323].
- Electron-phonon interactions in solids, for an example, see Steinhoff et al. [324] and references therein.

These few examples may suffice to highlight the manifold of interesting directions into which the present MCTDHF and TD-RASCI theories can be developed. They might thereby evolve into an important alternative to and benchmark method (at least for small systems) for quantum-kinetic treatments, which currently often provide the only manageable approach.

Non-Born-Oppenheimer dynamics of hydrogen. To give an example of the previous formalism, we briefly consider the non-Born-Oppenheimer (BO) treatment of hydrogen, which presents an exactly solvable system through the usual separation in center-of-mass and relative coordinates. The corresponding Hamiltonian is given by

$$\hat{H} = -\frac{1}{2m_p}\nabla_p^2 - \frac{1}{2}\nabla_e^2 - \frac{1}{|\mathbf{r}_p - \mathbf{r}_e|}, \quad (5.20)$$

where \mathbf{r}_e (\mathbf{r}_p) labels the electronic (protomic) coordinate and $m_p \approx 1836$ is the proton mass in atomic units. The wavefunction is set up as a product of a time-dependent electronic and protomic orbital,

$$\Psi(\mathbf{r}_e, \mathbf{r}_p, t) = \psi_i(\mathbf{r}_e, t)\psi_j(\mathbf{r}_p, t), \quad (5.21)$$

and thus corresponds to a Hartree-Fock ansatz. Propagation of the system in imaginary time yields the ground state with energy $E_0 = -0.4664 \text{ Ha}$, which has to be compared to the exact value of -0.4997 Ha obtained by using the reduced mass $\mu = m_e m_p / (m_e + m_p)$. The results for the ground state densities are shown in Fig. 51a and b. One clearly notices that the proton density is spatially extended, which differs from the situation in the clamped-nuclei approximation where it corresponds to a delta-peak. Subsequent to the imaginary time-propagation, the system is excited by a linearly polarized dipole kick of strength $\eta = 10^{-3} \text{ a.u.}$ and duration $\tau = 10^{-3} \text{ a.u.}$ The excitation is well in the perturbative regime and thus yields the linear response of the system.

The expectation value of the z -coordinate is shown in Fig. 51c. The values of the protomic and electronic coordinates oscillate in opposite directions, with the amplitude of the proton being a factor of $1/m_p \approx 5 \cdot 10^{-4}$ smaller than that of the electron. The black dashed curve depicts the exact result obtained by solution of the single-particle Schrödinger equation in the relative frame (using the Coulomb potential $-1/r$). One observes that the electron coordinates of exact and non-BO treatments behave qualitatively similar, but exhibit a different frequency, as becomes particularly obvious at

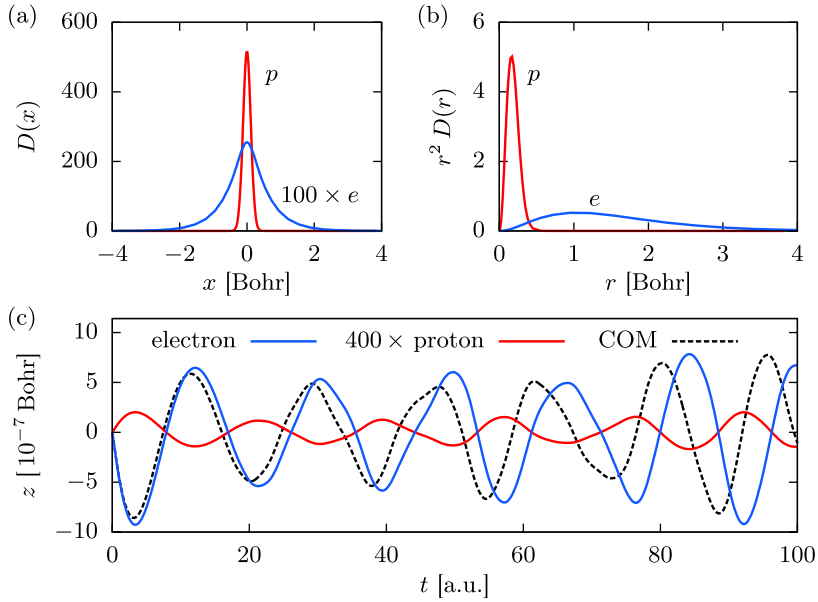


Fig. 51. Non-Born-Oppenheimer treatment of hydrogen. (a) Spherically symmetric electronic (e) and protonic (p) ground state density. For better visibility, the electronic density is multiplied by a factor of 100. (b) Radial ground state densities. (c) Expectation value of the z -position upon excitation by a dipole kick. COM labels the exact result obtained in center-of-mass and relative coordinates.

later times. The deviation of the non-BO curves is due to the Hartree-Fock description which, in the canonical particle coordinates, yields only a first-order approximation to the Coulomb interaction term. This could be improved either by using a more accurate MCTDHF ansatz to the wavefunction (5.21), or by working in the better suited center-of-mass coordinate system²⁷. The present approach could also be straightforwardly applied to larger atoms and molecules, which is, however, not in the focus of this work.

5.1.4 Multilayer MCTDHF

As another possible extension we mention the extension of the multilayer MCTDH scheme [325] to fermions which would lead to multilayer MCTDHF. This scheme allows to construct generic and compact basis functions, which would not suffer from the inherent symmetry of the traditional product ansatz. As a result, one can describe states with much richer structure with a minimum of basis functions.

5.1.5 New approaches for the treatment of photoionization

In this work, we mainly considered two approaches for the simulation of photoionization problems—the TD-RASCI and the MCTDHF method. As was investigated

²⁷ Here, COM coordinates are the natural choice, in which, due to the separation, already the $M = 1$ approximation yields exact results. For general systems, however, the appropriate choice for the coordinates is far from being obvious and is an actively studied topic [152].

in detail in Sect. 4, both perform well for analyzing certain aspects of photoionization and present successful theories which can compete with other well-established methods of many-body quantum mechanics. There are, however, also scenarios where simulations either become computationally difficult, or do not behave as expected. In the following, we briefly discuss some possible improvements, which are expected to allow for a more efficient description of photoionization in the future.

First, let us recall that MCTDHF employs the attractive idea of time-dependent orbitals and is—in principle—capable of providing any state needed during the propagation. For real applications, in contrast, we have seen that it uses a good part of its resources to model the bound states, such that the representation of the doubly-ionized states, for instance, is poor. Furthermore, being a non-linear approximation, there is no guarantee that the results for a certain observable quickly get better by increasing the number of orbitals M . On the other hand, the TD-RASCI ansatz can be adjusted to include the important states, which then behave as expected due to the linear expansion. Due to this feature, the TD-RASCI method performs superior for most of the applications in this work. However, as a static method, it requires to select the included states before the calculation, and it is often not clear in advance which states will be important for the physical process.

The strategy we propose here combines the MCTDHF and TD-RASCI treatment and was first proposed in Ref. [66]. It starts by the determination of the restricted active space. In TD-RASCI, the corresponding product Hilbert spaces are given by full CI spaces. However, one can employ any available determinant scheme, such as the MCTDHF method. This leads to a RAS-MCTDHF wavefunction that consists of products of time-dependent Slater determinants, each of which is optimized in a separate subspace of the total Hilbert space²⁸. [A similar concept has been presented in Ref. [158]]. For convenience, let us consider the basic example of two partitions, one in the vicinity of the atom (\mathcal{B}_1) and one in the continuum (\mathcal{B}_2), which is shown in Fig. 10 on page 211. The corresponding wavefunction, if both product wavefunctions are described by MCTDHF expansions, is given by

$$|\Psi(t)\rangle = \sum_{\substack{N_1, N_2 \\ N_1 + N_2 = N}} \sum_{I_{N_1}} \sum_{J_{N_2}} C_{I_{N_1} J_{N_2}}(t) |I_{N_1}, t\rangle |J_{N_2}, t\rangle, \quad (5.22)$$

where N_1 (N_2) denotes the particle number in subspace \mathcal{B}_1 (\mathcal{B}_2) and $|I_{N_1}\rangle$ ($|J_{N_2}\rangle$) the corresponding determinants, which are modeled by M_1 (M_2) time-dependent orbitals. This ansatz combines the advantages of the original methods: As for the TD-RASCI approach, the total number of determinants can be significantly reduced. Additionally, due to the much smaller number of time-dependent orbitals, the dimension of the involved subspaces is further reduced as compared to the TD-RASCI approach, and the effort of the orbital equation is lowered as the time-dependent orbitals must be optimized in smaller single-particle spaces. The principal advantage over the usual MCTDHF ansatz is that the wavefunction can be varied in the spatial partitions separately, and thus exclusively treat the arising processes there. By this, one can ensure that the continuum region is described with a certain accuracy and prevent the method from using the available resources to model the bound state. We expect this to be of major importance in the description of photoionization processes.

Three possible scenarios arise from this ansatz: either to use time-dependent orbitals only for the bound space, only for the continuum or for both spaces. All three

²⁸ Note that this is way different than the selected configurations scheme employed in MCTDH calculations [157]. There, instead of the single-particle basis, the time-dependent orbitals are partitioned, and the preservation of the constraints leads to projection operators which, according to Ref. [156], slow down the propagation.

choices can have their advantages. Using time-dependent orbitals for the bound states, for instance, leads to a reduction of the size of the determinant space and, at the same time, should give an adequate description in a region close to the nucleus where the multiconfigurational Hartree-Fock idea performs well. The second alternative, using time-dependent orbitals for the continuum, is likely to perform even better. This is due to the fact that continuum electrons are often only weakly correlated and, therefore, a small number of time-dependent orbitals might already yield accurate results. Finally, through the use of time-dependent orbitals in both spaces one could obtain a combination of the aforementioned advantages. Further, the approach can be extended to a larger number of partitions. By this, for instance, one can divide the coordinate space into several regions and apply an ansatz which becomes less correlated with increasing distance to the nucleus. Work is in progress in order to reveal the value of this promising idea.

5.2 Application to lattice models

While this review focused on atomic and molecular systems, the introduced methods are also applicable to completely distinct systems. Here, we will consider, as an example, an application of MCTDHF to lattice models, such as the Hubbard model. Such lattice Hamiltonians with localized particles (on-site interaction) have become quite popular in condensed matter physics since they allow for a drastic simplification of the many-electron problem and a number of exact results. Recently, these models have also been studied in cold atomic and molecular gases where such systems can be directly produced with the help of optical lattices.

We have recently implemented the Hubbard basis for the MCTDHF scheme²⁹. The first benchmark calculations show that the MCTDHF scheme is well applicable to Hubbard systems with a small number of particles before, eventually, the exponential growth of the computational cost with N inhibits any reasonable utilization. Especially, MCTDHF was able to treat a system featuring a single doublon (localized double occupation of fermions)—a distinct correlation effect—very well, as we were able to use a large number of sites and propagate the system over a long time. On the other hand, MCTDHF exhibits the same weaknesses as for the atomic systems. This problem is depicted in Fig. 52 which shows the time-dependence of the density on the first site—counting from the left to the right—of an eight site Hubbard model at half filling. The system is prepared in a strong nonequilibrium state where all eight particles are confined to the four leftmost sites. All possible levels of the MCTDHF approximation are shown. It should be noted that the good agreement of all approximations with the exact result arises from the lack of correlations in the initial state. As time passes, correlations are being build up, and the curves start to diverge. At around $t = 30$, the approximate results start to deviate significantly from the exact result. While we might have expected this, the obvious absence of convergence with M at later times is alarming. This behavior is clearly shown by the density drop shortly after $t = 40$, where all approximations exhibit the same incorrect density excursion and no convergence is visible at all. Overall, this calculation depicts the same Hartree-Fock-like behavior of MCTDHF which we already observed for atomic systems. This also reveals that this problem of convergence in MCTDHF is a fundamental one and not restricted to atomic systems. While the depicted results are rather discouraging, recent calculations indicate that other quantities show a better convergence, particularly for their long-time behavior. Due to this behavior, we regard the Hubbard model as a good benchmarking tool for the MCTDHF scheme, as

²⁹ This work was carried out in close collaboration with Sebastian Hermanns.

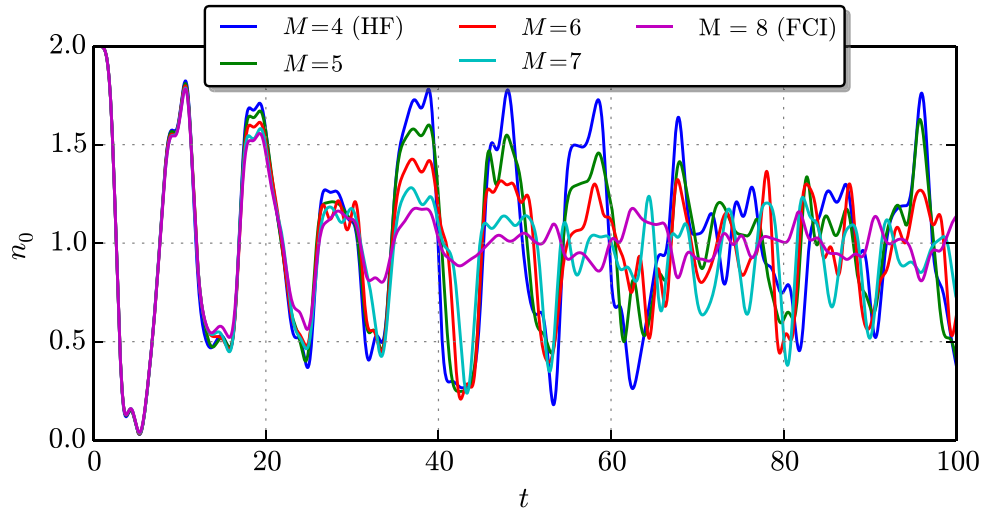


Fig. 52. Time-dependent variation of the occupation of the first site for an eight site Hubbard model with eight particles (half filling). The occupation is shown for different levels of the MCTDHF approximation [from Hartree-Fock (HF) to Full Configuration Interaction (FCI)]. Until around $t = 20$ the approximations are strictly ordered, with Hartree-Fock on the top and Full CI at the bottom. Time is in units of the inverse hopping constant.

one can investigate the advantages and weaknesses of the scheme in great detail on a simple test case which is trivial to implement.

Another non-atomic application of the MCTDHF scheme was recently carried out by Brabec et al. [326] by applying the scheme to the harmonic quantum dot and, more recently, to the breathing mode of strongly interacting electrons in quantum dots [170], see also [169, 171, 327, 328].

5.3 Concluding remarks

The present review was concerned with two theoretical approaches for efficient simulations of photoionization processes in many-electron atoms and molecules—time-dependent restricted active space configuration interaction (TD-RASCI) and multi-configurational time-dependent Hartree-Fock (MCTDHF). Whereas MCTDHF has already been well established in the literature, the TD-RASCI method has been derived only recently [66, 75, 77] and further developed in this review.

Both methods approach the many-particle time-dependent Schrödinger equation by representing the wavefunction in a configuration basis of the many-particle Hilbert space, and both follow their particular strategy to avoid the *curse of dimensionality*, i.e., the combinatorial growth of the dimension of the Hilbert space with increasing system size. The MCTDHF method, on the one hand, reduces the size of the configuration basis by allowing the Slater determinants to be time-dependent. Their evolution is determined by the time-dependent variational principle which ensures the optimal representation of the wavefunction at each time-point. On the other hand, TD-RASCI aims at neglecting those configurations which are expected to be of minor importance for the physical problem at hand, and retaining only a selected subset that can be handled in numerical simulations. In order to be efficient, TD-RASCI requires an appropriate reference determinant which, in this work, is constructed by means of a mixed basis set. It uses Hartree-Fock eigenfunctions, in the vicinity of the atom,

and localized basis sets, in the continuum, which makes it possible to handle large basis sizes.

Particular consideration has been devoted to the adjustments needed to efficiently simulate photoionization processes, which require an adequate description of both, the bound states and the scattering states. A variety of appropriate numerical methods sets has been employed for this task, which were summarized in Sect. 3. We introduced the crucial concept of localized single-particle basis state, which are indispensable for the treatment of large single-particle basis sets, and concentrated on how to efficiently perform basis transformations by use of the Poisson equation. Subsequently, we considered the implementation of the full CI method in its conventional, as well as the direct formulation. For the numerical solution of the orbital equations, we introduced a stiffness reduction scheme, which reduces the effort of the time-propagation by usually more than one order of magnitude. Further, we presented the employed methods for the numerical integration of the MCTDHF and TD-RASCI equations of motion and summarized the computer implementation and the principles underlying the distributed-memory parallelization.

The introduced multiconfiguration methods have been applied to the simulation of photoionization processes of atoms in Sect. 4. The main focus of these computations was on the calculation of cross sections, which allows for the comparison with existing experimental and theoretical results and, therefore, provides an indispensable test for the capabilities of the simulation methods. We observed that, for most scenarios, the single-ionization cross sections can be accurately reproduced using the MCTDHF and the TD-RASCI methods, both of which take only a fraction of the effort of time-dependent full configuration interaction (TD-FCI) calculations. Especially TD-RASCI performs well in describing Fano resonances which require the inclusion of doubly-excited states in the calculation. These resonances display one of the most basic effects of electronic correlations and are of major importance in a variety of physical processes.

The MCTDHF method has been further applied to describe the two-photon double-ionization of helium and was able to qualitatively reproduce the characteristics of the reference TD-FCI result. The reasons for the quantitative disagreement have been identified in detail, and a scheme was suggested how to improve the MCTDHF method by combining it with the TD-RASCI principle. Further, as an application which requires an explicitly time-dependent method, we have considered a two-color pump-probe scheme in beryllium and, using the TD-RASCI method, calculated the angle-resolved ionization yields for different relative timings of the X-ray pump and IR probe fields. We observed a distinct influence of the IR field on the polarization of the atom which is significantly reduced in more accurate TD-RASCI approximations and, thus, confirms the significance of a correlated description.

In addition, we outlined several approaches for useful further extensions of the TD-RASCI and MCTDHF methods. For instance, in Sect. 5.1, we presented a formalism how to handle different particle species and discussed the various possible applications, many of which have not taken advantage of multiconfiguration methods so far. Further, in Sect. 5.1.5, we suggested a strategy to combine the advantages of MCTDHF and TD-RASCI schemes, which is expected to perform favorably for simulations of photoionization processes. In Sect. 3.7, we highlighted the use of the two-time autocorrelation and density matrix which, in the framework of MCTDHF, have been considered only in special formulations, up to now. Work is in progress to identify their value in pump-probe schemes and other applications. Moreover, we briefly outlined the simulation of bosonic particles and how to treat systems at finite temperatures and performed proof-of-principle calculations for both these examples. This summary indicates the great generality of the introduced multiconfiguration

methods and demonstrates their excellent capabilities for the simulation of general few- and many-particle quantum systems.

We gratefully acknowledge the collaboration with Martin Heimsoth and Sebastian Hermanns during the extension of the MCTDHF method to bosonic particles and Hubbard clusters, respectively. Further, we acknowledge stimulating discussions with Martin Axt, Sebastian Bauch, Andreas Buchleitner, Thomas Brabec, D.J. Haxton, S. Hermanns, L.B. Madsen, C.W. McCurdy and Matthias Nest. The work which is presented in this review is supported by the Deutsche Forschungsgemeinschaft via project BO1366-9 and the Bundesministerium für Bildung und Forschung (BMBF) via Verbundprojekt FSP 302–Freie-Elektronen-Laser. Computational resources were supplied by the Norddeutscher Verbund für Hoch- und Höchstleistungsrechnen (HLRN), Grant No. shp0006.

Appendix A. Determinant formulas

In the following, we collect some of the formulas involving matrix elements of Slater determinants that are required for the analysis of the wavefunction. Therefore, we make repeated use of the definition (2.12).

A.1 Slater determinant overlap

First, we calculate the overlap between two Slater determinants $|I\rangle$ and $|J\rangle$ built with non-orthogonal orbitals. Let us denote the set of orbitals used to construct $|I\rangle$ by $|\phi_i\rangle$, the orbitals of $|J\rangle$ by $|\psi_j\rangle$, and their overlap by $S_{ij} = \langle\phi_i|\psi_j\rangle$. Making use of the determinant definition and the group property of permutations, one obtains

$$\begin{aligned} \langle I|J\rangle &= \frac{1}{N!} \sum_{P,P' \in S^N} (-1)^{P \circ P'} \langle \phi_{P'(i_1)} | \psi_{P(j_1)} \rangle \cdots \langle \phi_{P'(i_N)} | \psi_{P(j_N)} \rangle \\ &= \sum_{P \in S^N} (-1)^P \langle \phi_{i_1} | \psi_{P(j_1)} \rangle \cdots \langle \phi_{i_N} | \psi_{P(j_N)} \rangle \\ &= \begin{vmatrix} S_{i_1 j_1} & \cdots & S_{i_1 j_N} \\ \vdots & & \vdots \\ S_{i_N j_1} & \cdots & S_{i_N j_N} \end{vmatrix} = \det(S^{IJ}). \end{aligned} \quad (\text{A.1})$$

The overlap between the Slater determinants is thus given by the determinant of the overlaps of the occupied orbitals. The latter is efficiently evaluated using methods of numerical linear algebra, e.g., the QR-decomposition, which typically require an effort of $\mathcal{O}(N^3)$. For orthogonal basis sets, $\langle\phi_i|\psi_j\rangle = \delta_{ij}$ S_{ii} , Eq. (A.1) becomes

$$\langle I|J\rangle = \prod_{k=1}^N S_{i_k i_k} \delta_{i_k, j_k},$$

which reduces to

$$\langle I|J\rangle = \prod_{k=1}^N \delta_{i_k, j_k} = \delta_{I,J},$$

for the case of an orthonormal basis set.

A.2 Matrix elements of single-excitations

Next, we focus on single-excitations between non-orthogonal Slater determinants. Let the creation and annihilation operators associated with $|\phi_i\rangle$ be denoted by $\hat{\phi}_i^{(\dagger)}$, and those of $|\psi_j\rangle$ by $\hat{\psi}_j^{(\dagger)}$. By letting the creator act to the left and the annihilator to the right, one obtains

$$\begin{aligned}\langle I | \hat{\phi}_p^\dagger \hat{\psi}_q | J \rangle &= \Gamma_p^I \Gamma_q^J \langle I_p | J_q \rangle \\ &= \Gamma_p^I \Gamma_q^J \det(S^{I_p J_q}) \\ &= \Gamma_p^I \Gamma_q^J \det(S_{\#_p^I \#_q^J}^{IJ}),\end{aligned}\quad (\text{A.2})$$

where $|I_p\rangle$ denotes the determinant $|I\rangle$ from which the orbital p has been removed. Further, the matrix S_{ij}^{IJ} is obtained from S^{IJ} by removing the i -th row and the j -th column (the determinant of S_{ij}^{IJ} is also called the *minor* of S^{IJ}). We also made use of the phase factors already defined in Eq. (2.19),

$$\Gamma_p^I = \prod_{j=1}^p (-1)^{n_j^I}, \quad (\text{A.3})$$

and the *counting index*,

$$\#_p^I = \sum_{j < p} n_j^I. \quad (\text{A.4})$$

The corresponding expressions for an orthogonal basis set read

$$\langle I | \hat{\phi}_p^\dagger \hat{\psi}_q | J \rangle = \Gamma_p^I \Gamma_q^J \prod_{\substack{k=1 \\ i_k \neq p, j_k \neq q}}^N S_{i_k i_k} \delta_{i_k, j_k}, \quad (\text{A.5})$$

and

$$\langle I | \hat{\phi}_p^\dagger \hat{\psi}_q | J \rangle = \Gamma_p^I \Gamma_q^J \prod_{\substack{k=1 \\ i_k \neq p, j_k \neq q}}^N \delta_{i_k, j_k}, \quad (\text{A.6})$$

for orthonormal basis sets.

A.3 Matrix elements of double-excitations

Similarly, we calculate the matrix element of double excitation operators:

$$\begin{aligned}\langle I | \hat{\phi}_p^\dagger \hat{\phi}_r^\dagger \hat{\psi}_s \hat{\psi}_q | J \rangle &= \Gamma_{pr}^I \Gamma_{qs}^J \langle I_{pr} | J_{qs} \rangle \\ &= \Gamma_{pr}^I \Gamma_{qs}^J \det(S^{I_{pr} J_{qs}}) \\ &= \Gamma_{pr}^I \Gamma_{qs}^J \det(S_{\#_p^I \#_q^J, \#_r^I \#_s^J}^{IJ}).\end{aligned}\quad (\text{A.7})$$

The matrix $S_{ij,kl}^{IJ}$ is obtained by removing the k -th row and the l -th column from S_{ij}^{IJ} , and the phase factors are given by

$$\Gamma_{pr}^I = (1 - \delta_{p,r}) \Gamma_p^I \Gamma_r^I.$$

A.4 Autocorrelation

The autocorrelation function is defined by

$$\begin{aligned} S(t, t') &= \langle \Psi(t) | \Psi(t') \rangle \\ &= \sum_{IJ} C_I^*(t) C_J(t') \langle I(t) | J(t') \rangle, \end{aligned}$$

and its information content and application is discussed in [3.7.6](#). For Slater determinants constructed from a set of orthonormal orbitals (with respect to different times), the evaluation is trivial and leads to

$$S(t, t') = \sum_I C_I^*(t) C_I(t'). \quad (\text{A.8})$$

For the case of a non-orthogonal single-particle basis, on the other hand, one can directly use Eq. ([A.1](#)) to obtain

$$S(t, t') = \sum_{IJ} C_I^*(t) C_J(t') \det(S^{IJ}). \quad (\text{A.9})$$

A.5 Two-time density matrix

The two-time density matrix is defined by

$$D(\mathbf{r}t, \mathbf{r}'t') = N \int \Psi^*(\mathbf{r}, \mathbf{r}_2, \dots, \mathbf{r}_N, t) \Psi(\mathbf{r}', \mathbf{r}_2, \dots, \mathbf{r}_N; t') d\mathbf{r}_2 \dots d\mathbf{r}_N, \quad (\text{A.10})$$

and has been discussed in Sect. [3.7.7](#). In second quantization, the corresponding expression for the two-time density matrix is given by [\[59\]](#)

$$\begin{aligned} D_{pq}(t, t') &= \langle \Psi(t) | \hat{\phi}_p^\dagger \hat{\psi}_q | \Psi(t') \rangle \\ &= \sum_{IJ} C_I^*(t) C_J(t') \langle I, t | \hat{\phi}_p^\dagger \hat{\psi}_q | J, t' \rangle. \end{aligned}$$

We can now directly invoke Eq. ([A.2](#)) to obtain

$$D_{pq}(t, t') = \sum_{IJ} C_I^*(t) C_J(t') \Gamma_p^I \Gamma_q^J \det(S^{I_p J_q}), \quad (\text{A.11})$$

which is the way the two-time density is calculated in the computer program^{[30](#)}.

Appendix B. Basis sets

Basis sets are an important ingredient in quantum-mechanical calculations, as they provide the connection between the mathematical concepts and real applications.

³⁰ An alternative that uses the formalism of biorthogonal orbitals and sparse-matrix arithmetic has been given by Haxton [\[73\]](#).

Quantum-mechanical methods are typically formulated in terms of abstract single-particle orbitals $|\phi_i(t)\rangle$ which can be approximated through discretization. In most applications, this is accomplished using a linear expansion of the form

$$|\phi_i(t)\rangle = \sum_{j=1}^{N_b} c_{ij}(t) |\psi_j\rangle, \quad (\text{B.1})$$

where $|\psi_j\rangle$ denotes a set of square-integrable basis functions of size N_b . The previous expansion is rather general and, depending upon the analytical form of the basis functions, comprises several different approaches like spectral methods, finite differences, and finite elements in a single notation.

The appropriate selection of a certain basis set is a crucial step in the calculation, which strongly depends on the system at hand and the occurring physical processes. In quantum chemistry, Gaussian- and Slater-type orbitals are widely used since they are able to capture a lot of the static properties of atoms and molecules³¹. For photoionization, however, they are only of limited use, since the continuum states are poorly described by functions localized mainly around the atoms, so their use would lead to completely biased results. In the following, we collect the basis sets employed in this work which are appropriate for treating photoionization processes. They have been selected for their flexibility in describing general functions, and, even more important, for the property of leading to a sparse representation of the two-electron integrals which is crucial when using large basis sets³².

B.1 Discrete variable representation

The discrete variable representation (DVR)³³ constitutes a method that constructs, in a very general way, a basis transformation from a finite set of functions to a grid-like representation in which the representation of any local operator is approximately diagonal. The DVR thus provides two main advantages: first, the construction of the electron integrals is greatly simplified and second, the diagonality often leads to a rather sparse representation of the Hamiltonian matrix.

The standard DVR construction starts with a set of functions $p_j(x)$ defined on an interval $[a, b]$, which are orthonormal with respect to a weight function $w(x)$,

$$\int_a^b w(x) p_i(x) p_j(x) dx = \delta_{ij}. \quad (\text{B.2})$$

It is further assumed that an appropriate numerical quadrature rule is specified by a set of N abscissas x_k and integration weights w_k , by which one can approximate the integral of a function $f(x)$ as

$$\int_a^b w(x) f(x) dx \approx \sum_{n=0}^{N-1} w_n f(x_n). \quad (\text{B.3})$$

³¹ See chapter 3 of Ref. [329] for an introduction to the variety of basis sets for computational chemistry.

³² There are several other interesting basis sets which have been successfully applied to photoionization, but which are not covered in the following. Among them are finite differences [138], B-splines [139], wavelets [330], and Sturmian functions [47].

³³ DVR was introduced to quantum mechanics in 1982 by Lill, Parker and Light [187], based on previous work by Dickinson and Certain [331] and Harris [332].

The abscissas and weights may now be used to define the new basis

$$\chi_k(x) = \sqrt{w_k} \sum_{n=0}^{N-1} p_n^*(x_k) p_n(x), \quad (\text{B.4})$$

which is called a *discrete-variable representation* (DVR) basis. The corresponding transformation matrix, $U_{kn} = \sqrt{w_k} p_n(x_k)$, is unitary, as long as the quadrature rule evaluates the overlap integral exactly, since then

$$[\mathbf{U}^\dagger \mathbf{U}]_{ij} = \sum_{k=0}^{N-1} w_k p_i^*(x_k) p_j(x_k) = \delta_{ij}. \quad (\text{B.5})$$

By setting $x = x_j$ in Eq. (B.4) and using the completeness relation, one obtains the important property

$$\chi_k(x_j) = \frac{\delta_{kj}}{\sqrt{w_j}}, \quad (\text{B.6})$$

from which quickly follows the diagonal representation of local operators $f(x)$,

$$\int \chi_i(x) f(x) \chi_j(x) dx = \sum_{k=0}^{N-1} w_k \chi_i(x_k) f(x_k) \chi_j(x_k) \quad (\text{B.7})$$

$$= f(x_i) \delta_{ij}. \quad (\text{B.8})$$

Note that this relation is, in a strict mathematical sense, only true if the integrand is evaluated exactly. In any other case, Eq. (B.7) presents an approximation, the quality of which depends on the applied quadrature rule.

A classic choice for the basis functions p_i are orthogonal polynomials, for which the existence of an associated Gauss quadrature guarantees the exactness of Eq. (B.3) when $f(x)$ is a polynomial of degree $2N - 1$ or less [204]. In this case, Eq. (B.4) is a polynomial as well and may alternatively be represented by Lagrange interpolating polynomials

$$\chi_k(x) = \frac{1}{\sqrt{w_k}} \prod_{j=0}^{N-1} \frac{x - x_j}{x_k - x_j}. \quad (\text{B.9})$$

The corresponding abscissas x_k and weights w_k are determined through the zeros of the function $p_{N+1}(x)$ [204]. Important choices for the orthogonal polynomials include Legendre-, Hermite-, and Laguerre polynomials. There are further a lot of non-classical nt examples like harmonic oscillator-, sine- or Fourier functions which can be used to construct a DVR, see Refs. [88, 188].

If the variety of existing DVRs turns out to be not appropriate, one can also follow an alternative approach and define abscissas x_i which are adjusted to the physical problem at hand. One way to generate these is through a diagonalization of the position operator in the basis of single-particle Hamiltonian eigenfunctions. Next, one has to select a numerical quadrature and thus the weights w_i . In the absence of another reasonable choice, one can use here the trapezoidal formula, which—though not as accurate as Gaussian integration—is likely to perform well due to the optimized abscissas, which are dense in regions where the wavefunction oscillates and sparse where it is smooth. The corresponding basis functions are given by the Lagrange polynomials (B.9). In the following, we briefly consider the sine- and finite-element DVR implemented in this work.

B.1.1 Sine DVR

The sine DVR is constructed using the eigenfunctions of a one-dimensional box potential with infinite walls³⁴. It is defined on an equally spaced grid with $N+1$ points,

$$x_j = x_0 + j\Delta x, \quad j \in \{0, \dots, N\}, \quad (\text{B.10})$$

where the grid spacing is

$$\Delta x = \frac{x_N - x_0}{N}, \quad (\text{B.11})$$

and the weights are constant

$$w_j = \sqrt{\Delta x}. \quad (\text{B.12})$$

The sine DVR bears several similarities to a discrete Fourier transform, however, with the difference that the functions vanish at the boundary. We only state here the kinetic energy matrix elements, which are enough for a numerical implementation,

$$T_{ij} = (-1)^{i-j} \frac{\pi^2}{4(x_N - x_0)^2} \begin{cases} \frac{(2N^2+1)}{3} - \frac{1}{\sin^2(\frac{\pi j}{N})}, & \text{for } i = j \\ \frac{1}{\sin^2(\frac{\pi(i-j)}{2N})} - \frac{1}{\sin^2(\frac{\pi(i+j)}{2N})}, & \text{otherwise} \end{cases} \quad (\text{B.13})$$

and refer to the original work [188] and Ref. [88] for further information.

B.1.2 Finite-element DVR

The previously mentioned DVRs share the property that derivative operators like the kinetic energy operator lead to dense matrices. In contrast, the finite-element DVR (FEDVR) provides a kinetic energy matrix with a banded structure, which turns out to be a very convenient factor in the solution of the Poisson equation, see Sect. 3.2.4. Regarding the construction of the FEDVR, we mention only the basic thoughts, whereas we refer to Refs. [333–336] for the details. First, the coordinate space is divided into a chosen number N_e of finite elements. In each element e , a grid of Gauss-Lobatto nodes x_k^e and corresponding integration weights w_k^e is set up using, for instance, the methods of Ref. [204]. We denote the number of grid-points in element e by n_e . Gauss-Lobatto nodes have the property that grid points are situated at the boundary of the finite element which accounts for the continuity of the wavefunction across two elements. The basis functions are constructed as Lagrange polynomials over the grid points in a chosen finite element,

$$\chi_k^e(x) = \frac{f_k^e(x)}{\sqrt{w_k^e}}, \quad \text{for } k \in \{1, \dots, n_e - 2\}, \quad (\text{B.14})$$

where the *Lobatto shape functions* are defined by

$$f_k^e(x) = \prod_{l \neq k} \frac{x - x_l^e}{x_k^e - x_l^e}. \quad (\text{B.15})$$

Further, at the boundary points of the finite element, i.e., at the grid-point $x_{n_e-1}^e = x_0^{e+1}$, one defines a *bridge function* by

$$\chi_{n_e-1}^e(x) = \frac{f_{n_e-1}^e(x) + f_0^{e+1}(x)}{\sqrt{w_{n_e-1}^e + w_0^{e+1}}}, \quad (\text{B.16})$$

which connects the finite elements e and $(e+1)$. For an illustration, see Fig. 53.

³⁴ This has been introduced by Colbert and Miller [188].

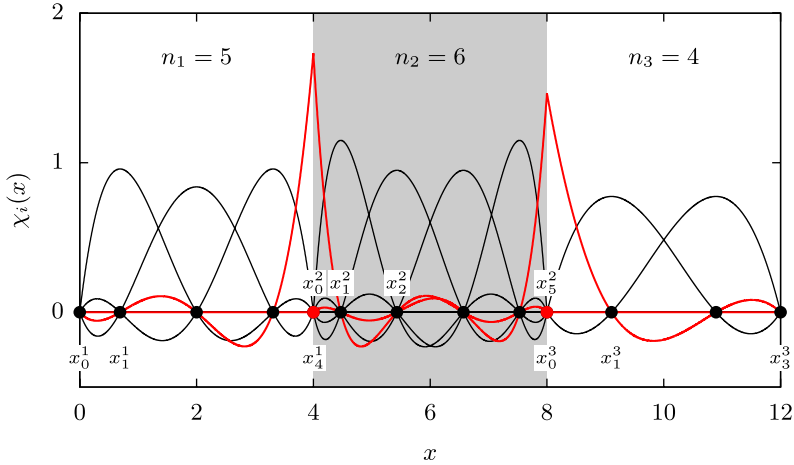


Fig. 53. FEDVR basis for three finite-elements of length 4 and a Gauss-Lobatto grid consisting of (5, 6, 4) points. The bridge functions connecting different elements are drawn in red color. Note that the first and last FEDVR functions have been removed in order to satisfy the usual boundary conditions of the wavefunction.

The FEDVR then satisfies the usual property of DVR, a diagonal representation of local operators,

$$V_{ij}^{ef} = \int \chi_i^e(x) f(x) \chi_j^f(x) dx = \delta_{ef} \delta_{ij} f(x_i^e). \quad (\text{B.17})$$

The kinetic energy elements can be easily evaluated via analytic differentiation of the basis functions,

$$T_{ij}^{ef} = -\frac{1}{2} \int \chi_i^e(x) \frac{d^2}{dx^2} \chi_j^f(x) dx \quad (\text{B.18})$$

$$= \delta_{ef} \frac{1}{2\sqrt{w_i^e w_j^f}} \sum_{k=1}^{N_e} w_k^e \frac{df_i^e(x_k)}{dx} \frac{df_j^f(x_k)}{dx}, \quad (\text{B.19})$$

for two inner-element functions. The expressions when boundary functions are involved look very similar and can be found, e.g., in Ref. [335]. Note that, instead of working with a multi-index, in practice it is more convenient to introduce a single index $i \in \{0, \dots, N_b - 1\}$, which indicates the global Gauss-Lobatto points $\{x_i\}$ as well as the corresponding FEDVR basis functions $\{\chi_i(x)\}$. The FEDVR basis can then be handled in the same way as the general DVRs introduced before.

B.2 Spherical coordinates

Spherical coordinates are a convenient choice for rotationally symmetric systems like atoms. This is because for many physical processes, the wavefunction is smooth in the angular coordinates and can be described by a few basis functions.

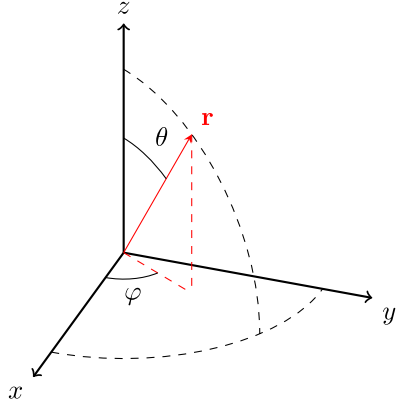


Fig. 54. Spherical coordinate system used in this work.

Spherical coordinates (r, θ, φ) are commonly defined by

$$\begin{aligned} x &= r \sin \theta \cos \varphi = r \sqrt{\frac{2\pi}{3}} \left(Y_{1-1}(\theta, \varphi) - Y_{11}(\theta, \varphi) \right), \\ y &= r \sin \theta \sin \varphi = r \sqrt{\frac{2\pi}{3}} i \left(Y_{1-1}(\theta, \varphi) + Y_{11}(\theta, \varphi) \right), \\ z &= r \cos \theta = r \sqrt{\frac{4\pi}{3}} Y_{10}(\theta, \varphi), \end{aligned}$$

see also Fig. 54. The Laplacian is given by

$$\Delta = \frac{\partial^2}{\partial r^2} + \frac{2}{r} \frac{\partial}{\partial r} + \frac{1}{r^2 \sin \theta} \frac{\partial}{\partial \theta} \sin \theta \frac{\partial}{\partial \theta} + \frac{1}{r^2 \sin^2 \theta} \frac{\partial^2}{\partial \varphi^2}, \quad (\text{B.20})$$

and the volume element is $dV = r^2 \sin \theta dr d\varphi d\theta$.

B.2.1 Gaunt coefficients

Gaunt coefficients repeatedly arise for partial wave expansions in spherical coordinates. They are defined as the integral of the product of three spherical harmonics over the solid angle,

$$y_{l_1 m_1, l_2 m_2, l_3 m_3} = \int Y_{l_1 m_1}^*(\theta, \varphi) Y_{l_2 m_2}(\theta, \varphi) Y_{l_3 m_3}(\theta, \varphi) \sin \theta d\theta d\varphi. \quad (\text{B.21})$$

We further define the related quantity

$$\bar{y}_{l_1 m_1, l_2 m_2, l_3 m_3} = \int Y_{l_1 m_1}^*(\theta, \varphi) Y_{l_2 m_2}^*(\theta, \varphi) Y_{l_3 m_3}(\theta, \varphi) \sin \theta d\theta d\varphi \quad (\text{B.22})$$

$$= (-1)^{m_2} g_{l_1 m_1, l_2 - m_2, l_3 m_3}. \quad (\text{B.23})$$

The integral (B.21) has been evaluated by Racah using the Wigner-Eckhart theorem and is given by [113]

$$y_{l_1 m_1, l_2 m_2, l_3 m_3} = \sqrt{\frac{(2l_1 + 1)(2l_2 + 1)(2l_3 + 1)}{4\pi}} \begin{pmatrix} l_1 & l_2 & l_3 \\ 0 & 0 & 0 \end{pmatrix} \begin{pmatrix} l_1 & l_2 & l_3 \\ m_1 & m_2 & m_3 \end{pmatrix}. \quad (\text{B.24})$$

The introduced Wigner-3j symbols ($\langle \dots \rangle$) are closely related to the Clebsch-Gordan coefficients. Their explicit form is given in Ref. [113].

In the numerical implementation, the Wigner coefficients are evaluated once and stored on disk using the index transformation of Rasch and Yu [337] which was found to be more efficient than using recursion relations [338]. Note that for large angular momentum quantum numbers ($l \gtrsim 30$), quad precision is required for the accurate calculation of the Wigner-3j symbols.

B.2.2 Partial wave expansion with radial DVR basis

The spherical DVR basis is the basis set considered in most parts of this work. It is constructed as a product of a radial DVR basis and spherical harmonics,

$$\psi_{klm}(\mathbf{r}) = \frac{\chi_k(r)}{r} Y_{lm}(\theta, \varphi). \quad (\text{B.25})$$

In the following, we state the corresponding electron integrals.

One-electron integrals. Equation (B.25) defines an orthonormal basis, as can be seen from the overlap integral,

$$\begin{aligned} S_{klm, k'l'm'} &= \int \frac{\chi_k(r)}{r} \frac{\chi_{k'}(r)}{r} r^2 dr \int Y_{lm}^*(\theta, \varphi) Y_{l'm'}(\theta, \varphi) \sin \theta d\theta d\varphi \\ &= \delta_{kk'} \delta_{ll'} \delta_{mm'}. \end{aligned} \quad (\text{B.26})$$

The kinetic energy integral is calculated as

$$T_{klm, k'l'm'} = \delta_{ll'} \delta_{mm'} \left(T_{kk'} + \delta_{kk'} \frac{l(l+1)}{2r_k^2} \right), \quad (\text{B.27})$$

where $T_{kk'}$ denotes the kinetic energy integral in the DVR basis. The diagonal potential energy matrix is evaluated to

$$V_{klm, k'l'm'} = -\frac{Z}{r_k} \delta_{kk'} \delta_{ll'} \delta_{mm'}, \quad (\text{B.28})$$

where Z denotes the charge of the atomic nucleus. Further, the dipole matrix elements are given by

$$X_{klm, k'l'm'} = \delta_{kk'} r_k \sqrt{\frac{2\pi}{3}} \left(y_{lm, 1-1, l'm'} - y_{lm, 11, l'm'} \right), \quad (\text{B.29})$$

$$Y_{klm, k'l'm'} = \delta_{kk'} r_k \sqrt{\frac{2\pi}{3}} i \left(y_{lm, 1-1, l'm'} - y_{lm, 11, l'm'} \right), \quad (\text{B.30})$$

$$Z_{klm, k'l'm'} = \delta_{kk'} r_k \sqrt{\frac{4\pi}{3}} y_{lm, 10, l'm'}. \quad (\text{B.31})$$

Two-electron integrals. For the calculation of the two-electron integrals,

$$\begin{aligned} G_{k_1 l_1 m_1, k_2 l_2 m_2, k_3 l_3 m_3, k_4 l_4 m_4} \\ = \iint \psi_{k_1 l_1 m_1}^*(\mathbf{r}) \psi_{k_2 l_2 m_2}(\mathbf{r}) \frac{1}{|\mathbf{r} - \mathbf{r}'|} \psi_{k_3 l_3 m_3}^*(\mathbf{r}') \psi_{k_4 l_4 m_4}(\mathbf{r}') d\mathbf{r} d\mathbf{r}', \end{aligned} \quad (\text{B.32})$$

we insert the multipole expansion of the inter-electronic distance,

$$\frac{1}{|\mathbf{r} - \mathbf{r}'|} = \sum_{l=0}^{\infty} \frac{4\pi}{2l+1} \frac{r_-^l}{r_>^{l+1}} \sum_{m=-l}^l Y_{lm}(\Omega) Y_{lm}^*(\Omega'), \quad (\text{B.33})$$

where, as usual, we defined $r_- = \min(r, r')$ and $r_> = \max(r, r')$. This straightforwardly leads to

$$G_{k_1 l_1 m_1, \dots, k_4 l_4 m_4} = \delta_{m_1 - m_2, m_4 - m_3} \sum_{l=\max(|l_1 - l_2|, |l_3 - l_4|)}^{\min(l_1 + l_2, l_3 + l_4)} \frac{4\pi}{2l+1} y_{l_1 m_1, l m_1 - m_2, l_2 m_2} \\ \times \bar{y}_{l_3 m_3, l m_4 - m_3, l_4 m_4} P_{k_1 k_2, k_3 k_4}^{(l)}. \quad (\text{B.34})$$

Here, we introduced the radial integral

$$P_{k_1 k_2, k_3 k_4}^{(l)} = \int \chi_{k_1}(r) \chi_{k_2}(r) \frac{r_-^l}{r_>^{l+1}} \chi_{k_3}(r') \chi_{k_4}(r') dr dr', \quad (\text{B.35})$$

the efficient evaluation of which is to be discussed in the following.

Solution of the Poisson equation. As was pointed out by Hartree [144], the calculation of the radial integral, Eq. (B.35), is hampered by the derivative singularity at $r = r'$. However, it can be accurately evaluated by making use of the Poisson equation, which is further convenient since the effort of the numerical quadrature, which scales quadratically with the number of radial grid points, can be lowered to only a linear effort. Here we follow closely the work of McCurdy et al., who applied the Poisson equation to FEDVR and B-spline basis sets [185]. Their procedure starts by defining the function

$$p_{k_3 k_4}^{(l)}(r) = r \int dr' \chi_{k_3}(r') \frac{r_-^l}{r_>^{l+1}} \chi_{k_4}(r') \\ = \int dt \chi_{k_3}(t) \left(\frac{t}{r}\right)^l \chi_{k_4}(t) + \int dt \chi_{k_3}(t) \left(\frac{r}{t}\right)^{l+1} \chi_{k_4}(t),$$

in terms of which the radial integral can be written as

$$P_{k_1 k_2, k_3 k_4}^{(l)} = \int \chi_{k_1}(r) \chi_{k_2}(r) \frac{1}{r} p_{k_3 k_4}^{(l)}(r) dr. \quad (\text{B.36})$$

Differentiation of $p_{k_3 k_4}^{(l)}(r)$ with respect to r shows that it satisfies the radial part of the Poisson equation,

$$\left(\frac{\partial^2}{\partial r^2} - \frac{l(l+1)}{r^2} \right) p_{k_3 k_4}^{(l)}(r) = -\frac{2l+1}{r} \chi_{k_3}(r) \chi_{k_4}(r), \quad (\text{B.37})$$

with the boundary conditions

$$p_{k_3 k_4}^{(l)}(r) \Big|_{r=0} = 0, \quad (\text{B.38})$$

$$p_{k_3 k_4}^{(l)}(r) \Big|_{r=r_{\max}} = \frac{1}{r_{\max}^l} \int_0^{r_{\max}} \chi_{k_3}(t) \chi_{k_4}(t) t^l dt \quad (\text{B.39})$$

$$= \left(\frac{r_{k_3}}{r_{\max}} \right)^l \delta_{k_3 k_4}. \quad (\text{B.40})$$

Representation of Eq. (B.37) in the radial basis leads to the matrix equation

$$\sum_{k'} \underbrace{\left(2T_{kk'} + \delta_{kk'} \frac{l(l+1)}{r_k^2} \right)}_{=: \Delta_{kk'}^{(l)}} p_{k_3 k_4, k'}^{(l)} = \frac{2l+1}{r_k \sqrt{w_k}} \delta_{kk_3} \delta_{k_3 k_4}, \quad (\text{B.41})$$

where $T_{kk'}$ is the kinetic energy integral in the DVR basis. It defines the particular solution of the radial Poisson equation,

$$p_{k_3 k_4}^{(l), \text{in}}(r) = \delta_{k_3 k_4} \sum_{k'} p_{k_3 k_4, k'}^{(l)} \frac{\chi_{k'}(r)}{r}, \quad (\text{B.42})$$

which, remarkably, is diagonal in the indices of the radial basis functions. Due to the construction of the DVR, the particular solution vanishes at the last grid point r_{\max} . To satisfy the boundary condition, one further must add the homogeneous solution of Eq. (B.37),

$$p_{k_3 k_4}^{(l), \text{hom}}(r) = \alpha_{k_3 k_4} r^{l+1}. \quad (\text{B.43})$$

Via comparison with Eq. (B.40), the coefficient is determined to

$$\alpha_{k_3 k_4} = \delta_{k_3 k_4} \frac{r_{k_3}^l}{r_{\max}^{2l+1}}. \quad (\text{B.44})$$

The total solution of the radial Poisson equation is then given by

$$p_{k_3 k_4}^{(l)}(r) = \delta_{k_3 k_4} \left(p_{k_3 k_4}^{(l), \text{in}}(r) + \frac{r_{k_3}^l}{r_{\max}^{2l+1}} r^{l+1} \right). \quad (\text{B.45})$$

Through insertion of this result in Eq. (B.36) one can obtain the radial integrals,

$$P_{k_1 k_2, k_3 k_4}^{(l)} = \delta_{k_1 k_2} \delta_{k_3 k_4} p_{k_3 k_4}^{(l)}(r_{k_1}), \quad (\text{B.46})$$

and with Eq. (B.34) finally the two-electron integrals in the spherical DVR basis.

Appendix C. Computational aspects

This appendix focuses on some computational aspects in order to provide a better grasp of the more subtle aspects of an implementation and a better understanding of the computational background.

C.1 Implementation of the energy subspace projection method

In the first part of this section of the appendix, we will analyse the behavior of the cutoff error which is introduced by the energy subspace projection (ESP) method and discuss its impact on the realization of the scheme. In the second part, we will discuss an actual implementation of the scheme using the example of MCTDHF.

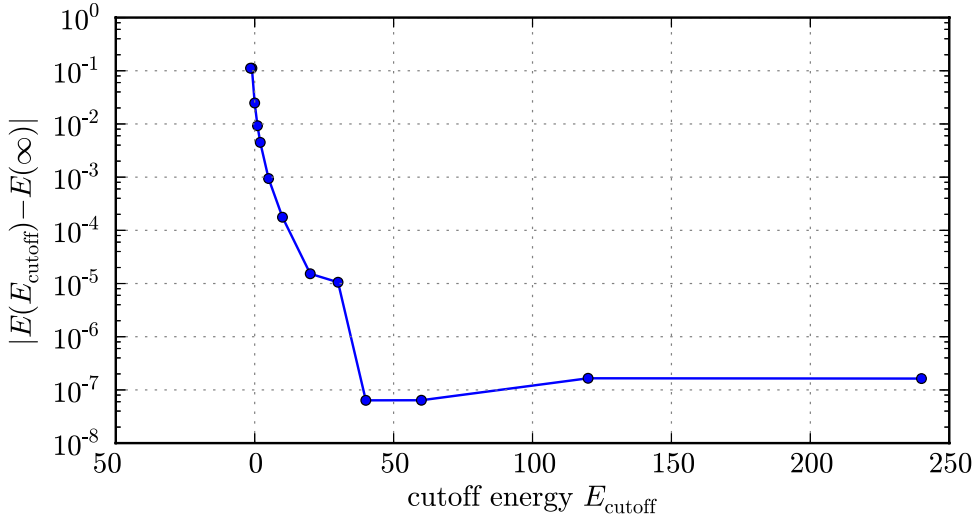


Fig. 55. Error in the ground state energy in dependency on the cutoff energy E_{cutoff} . Each finite element contains 15 DVR basis functions. The angular basis is constructed from spherical harmonics with azimuthal quantum numbers l up to 4.

C.1.1 Error analysis

Since the ESP scheme is an approximate procedure, it is important that we have an understanding of the circumstances when it can be used without compromising the accuracy of the calculations. The only additional error source in the ESP method is the truncation, which is described by the remainder term (3.183). Using any vector norm $\|\cdot\|$ and a corresponding compatible matrix norm, we can deduce the following estimate for the truncation error,

$$\begin{aligned}
 \epsilon(c) &= \|\rho(c)\| \\
 &= \|\mathbf{H}Rc\| \\
 &\leq \|\mathbf{H}\| \|Rc\| \\
 &= \|\mathbf{H}\| \|V^\dagger \tilde{\mathbf{R}}Vc\| \\
 &= \|\mathbf{H}\| \|\tilde{\mathbf{R}}\tilde{c}\|,
 \end{aligned} \tag{C.1}$$

from the remainder term. The expression $\|\tilde{\mathbf{R}}\tilde{c}\|$ exposes that the error is solely determined by the eliminated expansion coefficients. Therefore, the approximation remains valid as long as all truncated eigenstates are only lowly occupied, as expected.

Error estimators like (C.1) are good to get an intuition for the error source and are often necessary to develop more sophisticated schemes. Yet it is often not viable to use them as a method to obtain the error in practice since, in most cases, not all quantities are known³⁵. Therefore, it is necessary to perform empirical tests to explore the real error properties. We have performed these tests for the helium test system using different metrics for the induced error. The first metric used is the difference between the ground state energy for some value of E_{cutoff} and the ground state energy in the exact limit $E_{\text{cutoff}} \rightarrow \infty$. The dependency of this metric on the cutoff energy is shown in Fig. 55. The error remains small until the cutoff energy reaches the energy 40 a.u., which roughly corresponds to the point after which higher occupied

³⁵ Or are at least not feasible to calculate.

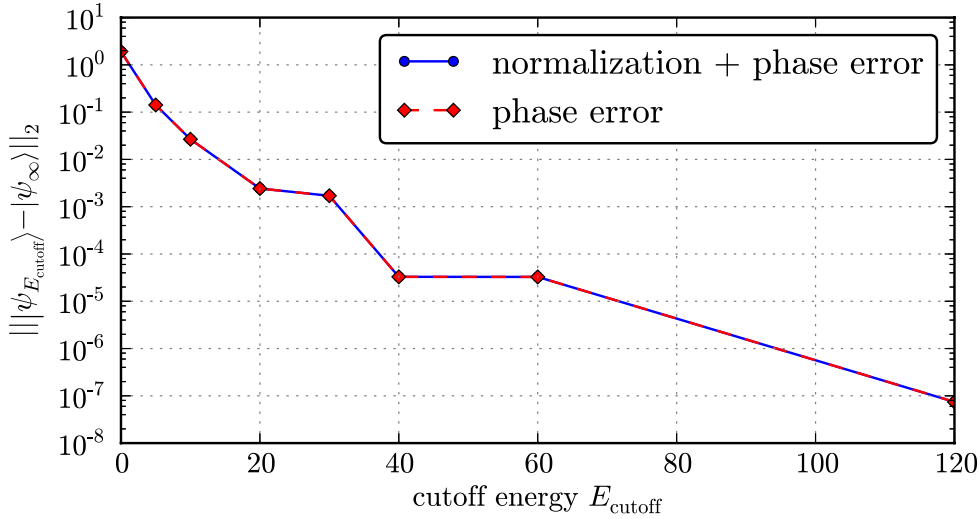


Fig. 56. L_2 error of the state at the end of the propagation versus cutoff energy E_{cutoff} . Each finite element contains 15 DVR basis functions. The angular basis is constructed from spherical harmonics with azimuthal quantum numbers l up to 4.

energy eigenstates are purged. After this point, the error starts to rise rapidly as we purge more and more occupied energy eigenstates. Since the maximal eigenvalue of the Hamiltonian is usually significantly larger than 40 a.u., it is evident that we can considerably reduce the stiffness without having to trade off accuracy for performance.

The L_2 error

$$\| |\psi_{E_{\text{cutoff}}} \rangle - |\psi_\infty \rangle \|_2 \quad (\text{C.2})$$

of the state at the end of the propagation, which we use as a second error metric, shows a quite similar behavior, as we can deduce from Fig. 56. Another feature shown in Fig. 56 is the comparison of the total error to the pure error in the phase. It is evident that the error in the normalization can be neglected in comparison to the error in the phase, as both graphics cannot be visually discriminated. The phase error was calculated by explicitly normalizing the densities before the L_2 error is calculated. While it is true that we can ignore the normalization error in most cases, it should be noted that this might not be true if the propagation time is very long, since the normalization decreases during every time step due to the truncation. In these cases, one should account for the error by either explicitly normalizing the state or by taking into account the error during the calculation of all observables.

C.1.2 Implementation

In this section, we will cover the more technical aspects of the ESP method, and its application to the MCTDHF equations³⁶. Since the stiffness—at least in the MCTDHF scheme—results from large eigenvalues in the single-particle Hamiltonian, we need to apply the ESP scheme to the orbital equation. Although this equation does not exactly have the form of (3.172), it is sufficiently close, for a successful application. From a practical point of view, it is convenient to apply the truncation matrix \mathbf{L} either to the Hamiltonian or to the orbital expansion coefficients. Since this would

³⁶ While we will restrict the discussion to the MCTDHF equations, some aspects of the implementation are of value also for more general cases.

simply result in a new Hamiltonian or new expansion coefficients, we can reuse the existing code for the calculation of the right-hand side of the MCTDHF equations in this case.

We chose to apply the truncation matrix to the expansion coefficients for two reasons. First, the Hamiltonian is time-dependent in many common applications of MCTDHF. Therefore, we would need to re-apply the truncation matrix to the Hamiltonian in every time step, which requires at least the costly evaluation of one matrix-matrix product. Hence, we only recommend this approach if the Hamiltonian is time-independent and we can reuse the evaluated result. The second reason is the fact that the orbital equation does also contain other terms apart from the one-particle contributions. If we would apply the truncation matrix solely to the single-particle Hamiltonian, we would introduce an inconsistent approximation to the equation. In theory, one could apply the scheme to all operators within the orbital equation consistently, but this is much more demanding than the application to the expansion coefficients, since we would need to evaluate complex tensor contractions. On the other hand, the application of the truncation matrix on the expansion coefficients only involves a cheap matrix-vector product and the approximation is consistently included in every term automatically. Let \mathbf{b}_j be the expansion coefficient vector of the j -th orbital, then the new coefficients read

$$\mathbf{b}'_j = \mathbf{L}\mathbf{b}_j. \quad (\text{C.3})$$

To speedup the computation of (C.3), we can exploit the structure of the truncation matrix \mathbf{L} . If we only discard a few eigenvalues, the truncation matrix in the energy representation (3.177) has merely a few non-zero entries. After inserting the definition (3.179) of \mathbf{L} into equation (C.3), which results in the expression

$$\mathbf{b}'_j = \mathbf{V}^\dagger \tilde{\mathbf{L}} \mathbf{V} \mathbf{b}_j, \quad (\text{C.4})$$

we can insert another $\tilde{\mathbf{L}}$, obtaining

$$\mathbf{b}'_j = \mathbf{V}^\dagger \tilde{\mathbf{L}} \tilde{\mathbf{L}} \mathbf{V} \mathbf{b}_j. \quad (\text{C.5})$$

This is possible, because

$$\tilde{\mathbf{L}}^2 = \tilde{\mathbf{L}} \quad (\text{C.6})$$

holds for the truncation matrix $\tilde{\mathbf{L}}$. Applying the truncation matrix on one transformation matrix each, we can rewrite (C.5) as

$$\mathbf{b}'_j = \left(\mathbf{V}'^\dagger (\mathbf{V}' \mathbf{b}_j) \right) \quad (\text{C.7})$$

with

$$\mathbf{V}' = \tilde{\mathbf{L}} \mathbf{V}. \quad (\text{C.8})$$

\mathbf{V}' is an $N_c \times N_b$ matrix effectively, since most of the elements of \mathbf{V} are set to zero by $\tilde{\mathbf{L}}$. If we apply this matrix to the coefficient vector according to the associativity implied by (C.7) we can reduce the computational cost from N_b^2 to $2N_c N_b$.

In the case of only a few discarded eigenvalues, we can apply a similar scheme by substituting \mathbf{L} using

$$\mathbf{L} = \mathbb{1} - \mathbf{R} \quad (\text{C.9})$$

and subsequently applying the same decomposition to \mathbf{R} . This leads to the equation

$$\mathbf{b}'_j = \left(\mathbb{1} - \mathbf{V}''^\dagger \mathbf{V}'' \right) \mathbf{b}_j = \mathbf{b}_j - \left(\mathbf{V}''^\dagger (\mathbf{V}'' \mathbf{b}_j) \right) \quad (\text{C.10})$$

with

$$\mathbf{V}'' = \tilde{\mathbf{R}}\mathbf{V}, \quad (\text{C.11})$$

which can be easily evaluated in a similar manner.

As already mentioned above, the handling of negative energies with large absolute values was discarded to simplify the implementation, since such values never occurred for the systems examined in this review. The reason is that the ground state energy of the single-particle Hamiltonian provides—by definition—a lower bound for all energy eigenvalues. A quick estimate for atomic systems shows that the ground state energy lies within the energy range specified by typical cutoff energies E_{cutoff} , except for heavier atoms and ions. Using the absolute value of the ground state energy of a hydrogen-like system

$$|E_0| = \frac{Z^2}{2} \quad (\text{C.12})$$

one arrives at the condition

$$|E_0| = \frac{Z^2}{2} \leq E_{\text{cutoff}}, \quad (\text{C.13})$$

for allowed atomic numbers Z . The maximal value of Z , which satisfies (C.13) is

$$Z_{\max} = \lfloor \sqrt{2E_{\text{cutoff}}} \rfloor. \quad (\text{C.14})$$

For most of the simulations presented in this review, a cutoff $E_{\text{cutoff}} = 60$ (≈ 1640 eV) was chosen corresponding to a maximal atomic number $Z_{\max} = 10$. Since such large systems are out of the scope of this review, this problem is ignored³⁷.

C.2 Parallelization – Performance metrics

Since we cannot observe the behavior of a parallelized application in real time, we need metrics which allow us to perform a “post-mortem” analysis of the algorithm. In the following sections, we will present some metrics, which are commonly applied during the empirical analysis of parallel algorithms. An ubiquitous quantity in these calculations is the speedup

$$S(n, p) := \frac{T(n, p)}{T(n, 1)}, \quad (\text{C.15})$$

which is defined as the ratio of the runtime $T(n, p)$ of the algorithm for a given problem size n on p processors and the runtime $T(n, 1)$ of the algorithm for the same size on one processor.

Strong scaling and Amdahl’s law. One of the first proposed use cases for parallel algorithms was the reduction of the runtime, which was needed to solve a given problem by applying more computational resources. The property of an algorithm which is coupled with this use case is the so called strong scaling behavior. Strong scaling behavior is defined as the behavior of $S(n, p)$ regarding p for $n = \text{const}$. That a good strong scaling behavior is not a goal which can be easily achieved gets evident if one examines Amdahl’s law [244]

$$S(n, p) \leq \frac{1}{f(n) + \frac{1-f(n)}{p}}, \quad (\text{C.16})$$

³⁷ Another point which should be considered is that the negative energy levels are highly occupied, if one starts from the ground state. Therefore, the ESP scheme—at least in its current form—would not be applicable in this common case anyway.

a model for the strong scaling behavior of parallel algorithms proposed by Amdahl in 1967. Here $f(n)$ denotes the inherently serial fraction of the sequential program. For a large number of processors—which is the interesting use case for parallel algorithms—the right-hand side of equation (C.16) behaves almost like $\frac{1}{f}$ as a function of the serial fraction. Due to the sharp slope of $\frac{1}{f}$ around $f = 0$, even a slight increase in the serial fraction will restrict the speedup to a very small value. Hence it is a very demanding task to apply this approach to most problems, except for the most simple ones.

Weak scaling and Gustafson's law. To counter the problems arising from Amdahl's law, Gustafson [242] argued that, in most use cases, the problem size is not restricted by external means. Therefore, one could increase the problem size, while applying more resources to keep the time that is needed to solve the problem constant. This leads to the notion of the weak scaling behavior which is defined as the behavior of $S(n, p)$ regarding p for some problem size $n(p)$ satisfying $\frac{n(p)}{p} = \text{const.}$ The weak scaling behavior of a parallel algorithm can be modeled by Gustafson's law,

$$S(n, p) \leq p + s(n, p)(1 - p), \quad (\text{C.17})$$

where $s(n, p)$ denotes the serial fraction of the parallel algorithm. Due to the linear slope of the right-hand side of equation (C.17), Gustafson's law is much more forgiving in comparison to Amdahl's law if we introduce serial parts into a parallel algorithm³⁸.

Karp-Flatt metric. Since both, Amdahl's law and Gustafson's law, do not include effects due to parallel overhead, one may use the Karp-Flatt metric [243]

$$e(n, p) = \frac{\frac{1}{S(n, p)} - \frac{1}{p}}{1 - \frac{1}{p}}, \quad (\text{C.18})$$

an empirical metric for the serial fraction which can be used to expose such effects.

References

1. A. Einstein, Phys. Z. **18**, 121 (1917)
2. J.P. Gordon, H.J. Zeiger, C.H. Townes, Phys. Rev. **99**, 1264 (1955)
3. A.L. Schawlow, C.H. Townes, Phys. Rev. **112**, 1940 (1958)
4. T.H. Maiman, Nature **187**, 493 (1960)
5. P.A. Franken, A.E. Hill, C.W. Peters, G. Weinreich, Phys. Rev. Lett. **7**, 118 (1961)
6. M.J. Weber, *Handbook of Lasers* (CRC Press, 2000)
7. D.A.G. Deacon, L.R. Elias, J.M.J. Madey, GJ Ramian, HA Schwettman, T.I. Smith, Phys. Rev. Lett. **38**, 892 (1977)
8. J. Ullrich, A. Rudenko, R. Moshammer, Ann. Rev. Phys. Chem. **63**, 635 (2012)
9. F. Grüner, S. Becker, U. Schramm, T. Eichner, M. Fuchs, R. Weingartner, D. Habs, J. Meyer-ter Vehn, M. Geissler, M. Ferrario, et al., App. Phys. B: Lasers Opt. **86**, 431 (2007)
10. A.A. Sorokin, M. Wellhöfer, S.V. Bobashev, K. Tiedtke, M. Richter, Phys. Rev. A **75**, 051402 (2007)
11. J.P. Cryan, J.M. Gownia, J. Andreasson, A. Belkacem, N. Berrah, C.I. Blaga, C. Bostedt, J. Bozek, C. Buth, L.F. DiMauro, L. Fang, O. Gessner, M. Guehr, J. Hajdu, M.P. Hertlein, M. Hoener, O. Kornilov, J.P. Marangos, A.M. March, B.K. McFarland,

³⁸ Due to this fact, this approach to parallelism seems very promising. Since we can always increase the size of the basis sets to get a more accurate description or to simulate more complex system, one should always be able to use this approach.

- H. Merdji, V.S. Petrović, C. Raman, D. Ray, D. Reis, F. Tarantelli, M. Trigo, J.L. White, W. White, L. Young, P.H. Bucksbaum, R.N. Coffee, Phys. Rev. Lett. **105**, 083004 (2010)
12. H.N. Chapman, P. Fromme, A. Barty, T.A. White, R.A. Kirian, A. Aquila, M.S. Hunter, J. Schulz, D.P. DePonte, U. Weierstall, et al., Nature **470**, 73 (2011)
 13. J. Ullrich, R. Moshammer, A. Dorn, R. Dörner, L.P.H. Schmidt, H. Schmidt-Böcking, Reports Progr. Phys. **66**, 1463 (2003)
 14. P.M. Paul, E.S. Toma, P. Breger, G. Mullot, F. Augé, P. Balcou, H.G. Muller, P. Agostini, Science **292**, 1689 (2001)
 15. M. Hentschel, R. Kienberger, C. Spielmann, GA Reider, N. Milosevic, T. Brabec, P. Corkum, U. Heinzmann, M. Drescher, F. Krausz, Nature **414**, 509 (2001)
 16. L. Gallmann, C. Cirelli, U. Keller, Ann. Rev. Phys. Chem. **63**, 447 (2012)
 17. M. Drescher, M. Hentschel, R. Kienberger, M. Uiberacker, V. Yakovlev, A. Scrinzi, T. Westerwalbesloh, U. Kleineberg, U. Heinzmann, F. Krausz, Nature **419**, 803 (2002)
 18. E. Goulielmakis, M. Uiberacker, R. Kienberger, A. Baltuska, V. Yakovlev, A. Scrinzi, T. Westerwalbesloh, U. Kleineberg, M. Drescher, Science **305**, 1267 (2004)
 19. M. Uiberacker, T. Uphues, M. Schultze, A.J. Verhoeft, V. Yakovlev, M.F. Kling, J. Rauschenberger, N.M. Kabachnik, H. Schröder, M. Lezius, Nature **446**, 627 (2007)
 20. P.B. Corkum, Phys. Rev. Lett. **71**, 1994 (1993)
 21. M. Lewenstein, Ph. Balcou, M.Yu. Ivanov, A. L'Huillier, P.B. Corkum, Phys. Rev. A **49**, 2117 (1994)
 22. R. Santra, A. Gordon, Phys. Rev. Lett. **96**, 73906 (2006)
 23. M.F. Kling, M.J.J. Vrakking, Ann. Rev. Phys. Chem. **59**, 463 (2008)
 24. E. Goulielmakis, M. Schultze, M. Hofstetter, V.S. Yakovlev, J. Gagnon, M. Uiberacker, A.L. Aquila, E.M. Gullikson, D.T. Attwood, R. Kienberger, F. Krausz, U. Kleineberg, Science **320**, 1614 (2008)
 25. K. Zhao, Q. Zhang, M. Chini, Y. Wu, X. Wang, Z. Chang, Opt. Lett. **37**, 3891 (2012)
 26. S. Bauch, M. Bonitz, Phys. Rev. A **78**, 043403 (2008)
 27. P. Tzallas, E. Skantzakis, L.A.A. Nikolopoulos, G.D. Tsakiris, D. Charalambidis, Nat. Phys. **7**, 781 (2011)
 28. B. Schütte, S. Bauch, U. Fröhling, M. Wieland, M. Gensch, E. Plönjes, T. Gaumnitz, A. Azima, M. Bonitz, M. Drescher, Phys. Rev. Lett. **108**, 253003 (2012)
 29. S. Bauch, M. Bonitz, Phys. Rev. A **85**, 053416 (2012)
 30. M. Schultze, M. Fieß, N. Karpowicz, J. Gagnon, M. Korbman, M. Hofstetter, S. Neppl, A.L. Cavalieri, Y. Komninos, T. Mercouris, et al., Science **328**, 1658 (2010)
 31. A.S. Kheifets, I.A. Ivanov, Phys. Rev. Lett. **105**, 233002 (2010)
 32. S. Nagele, R. Pazourek, J. Feist, K. Doblhoff-Dier, C. Lemell, K. Tókési, J. Burgdörfer, J. Phys. B: Atomic, Molec. Opt. Phys. **44**, 081001 (2011)
 33. L.R. Moore, M.A. Lysaght, J.S. Parker, H.W. van der Hart, K.T. Taylor, Phys. Rev. A **84**, 061404 (2011)
 34. P. Eckle, A.N. Pfeiffer, C. Cirelli, A. Staudte, R. Dörner, H.G. Muller, M. Büttiker, U. Keller, Science **322**, 1525 (2008)
 35. E. Goulielmakis, Z.H. Loh, A. Wirth, R. Santra, N. Rohringer, V.S. Yakovlev, S. Zherebtsov, T. Pfeifer, A.M. Azzeer, M.F. Kling, et al., Nature **466**, 739 (2010)
 36. E.E. Krasovskii, M. Bonitz, Phys. Rev. Lett. **99**, 247601 (2007)
 37. E.E. Krasovskii, M. Bonitz, Phys. Rev. A **80**, 053421 (2009)
 38. F.H.M. Faisal, J. Phys. B: Atomic Mol. Phys. **6**, L89 (1973)
 39. H.R. Reiss, Phys. Rev. A **22**, 1786 (1980)
 40. M.V. Ammosov, N.B. Delone, V.P. Krainov, Soviet. Phys. JETP **23**, 924 (1986)
 41. N. Camus, B. Fischer, M. Kremer, V. Sharma, A. Rudenko, B. Bergues, M. Kübel, N.G. Johnson, M.F. Kling, T. Pfeifer, J. Ullrich, R. Moshammer, Phys. Rev. Lett. **108**, 073003 (2012)
 42. P. Krause, T. Klamroth, P. Saalfrank, J. Chem. Phys. **123**, 074105 (2005)
 43. J. Feist, S. Nagele, R. Pazourek, E. Persson, B.I. Schneider, L.A. Collins, J. Burgdörfer, Phys. Rev. A **77**, 043420 (2008)

44. M. Rontani, C. Cavazzoni, D. Bellucci, G. Goldoni, J. Chem. Phys. **124**, 124102 (2006)
45. R. Bellman, *Adaptive Control Processes: A Guided Tour* (Princeton University Press, 1961)
46. J. Colgan, M.S. Pindzola, Phys. Rev. Lett. **108**, 053001 (2012)
47. E. Foumouo, G.L. Kamta, G. Edah, B. Piraux, Phys. Rev. A **74**, 063409 (2006)
48. M. Walter, J. Briggs, J. Phys. B: Atomic, Molec. Optical Phys. **32**, 2487 (1999)
49. J. Feist, S. Nagele, C. Ticknor, B.I. Schneider, L.A. Collins, J. Burgdörfer, Phys. Rev. Lett. **107**, 93005 (2011)
50. A. Palacios, T.N. Rescigno, C.W. McCurdy, Phys. Rev. Lett. **103**, 253001 (2009)
51. S. Bauch, K. Balzer, M. Bonitz, EPL **91**, 53001 (2010)
52. R. van Leeuwen, Phys. Rev. Lett. **82**, 3863 (1999)
53. K. Pernal, O. Gritsenko, E.J. Baerends, Phys. Rev. A **75**, 012506 (2007)
54. M. Bonitz, D. Semkat (eds.), *Introduction to Computational Methods in Many Body Physics* (Rinton Press, Princeton, 2006)
55. N.E. Dahlen, R. van Leeuwen, Phys. Rev. Lett. **98**, 153004 (2007)
56. D.A. Mazziotti, Phys. Rev. Lett. **93**, 213001 (2004)
57. K.C. Kulander, Phys. Rev. A **38**, 778 (1988)
58. S. Kvaal, J. Chem. Phys. **136**, 194109 (2012)
59. T. Helgaker, P. Joergensen, J. Olsen, *Molecular Electronic Structure Theory* (Wiley, New York, 2000)
60. S.R. White, A.E. Feiguin, Phys. Rev. Lett. **93**, 76401 (2004)
61. K.H. Marti, B. Bauer, M. Reiher, M. Troyer, F. Verstraete, New J. Phys. **12**, 103008 (2010)
62. G.H. Booth, A.J.W. Thom, A. Alavi, J. Chem. Phys. **131**, 054106 (2009)
63. K.C. Kulander, B.W. Shore, J. Optical Soc. Amer. B **7**, 502 (1990)
64. L. Greenman, P.J. Ho, S. Pabst, E. Kamarchik, D.A. Mazziotti, R. Santra, Phys. Rev. A **82**, 023406 (2010)
65. P.G. Burke, K.T. Taylor, J. Phys. B: Atomic, Molec. Optical Phys. **8**, 2620 (1975)
66. D. Hochstuhl, *Multiconfiguration Methods for the Numerical Simulation of Photoionization Processes of Many-Electron Atoms*, Ph.D. thesis, University of Kiel, 2013
67. M.A. Lysaght, P.G. Burke, H.W. van der Hart, Phys. Rev. Lett. **101**, 253001 (2008)
68. X. Guan, O. Zatsarinny, K. Bartschat, B.I. Schneider, J. Feist, C.J. Noble, Phys. Rev. A **76**, 053411 (2007)
69. X. Guan, C.J. Noble, O. Zatsarinny, K. Bartschat, B.I. Schneider, Phys. Rev. A **78**, 053402 (2008)
70. J. Caillat, J. Zanghellini, M. Kitzler, O. Koch, W. Kreuzer, A. Scrinzi, Phys. Rev. A **71**, 012712 (2005)
71. T. Kato, H. Kono, Chem. Phys. Lett. **392**, 533 (2004)
72. M. Nest, T. Kläroth, P. Saalfrank, J. Chem. Phys. **122**, 124102 (2005)
73. D.J. Haxton, K.V. Lawler, C.W. McCurdy, Phys. Rev. A **83**, 063416 (2011)
74. D.J. Haxton, K.V. Lawler, C.W. McCurdy, Phys. Rev. A **86**, 013406 (2012)
75. D. Hochstuhl, M. Bonitz, Phys. Rev. A **86**, 053424 (2012)
76. D. Hochstuhl, M. Bonitz, J. Chem. Phys. **134**, 084106 (2011)
77. D. Hochstuhl, M. Bonitz, J. Phys. Conf. Ser. **427**, 012007 (2013)
78. E. Schrödinger, Ann. Physik **385**, 437 (1926)
79. C.C. Gerry, P.L. Knight, *Introductory Quantum Optics*, Vol. 73 (Cambridge University Press, 2004)
80. I. Hertel, C. Schulz, *Atome, Moleküle und Optische Physik 1* (Springer, Berlin Heidelberg, 2008)
81. M. Born, R. Oppenheimer, Ann. Physik **389**, 457 (1927)
82. H.J. Kull, *Laserphysik: Physikalische Grundlagen des Laserlichts und Seine Wechselwirkung mit Materie* (Oldenbourg Wissenschaftsverlag, 2010)
83. P. Pyykko, Chem. Rev. **88**, 563 (1988)
84. R. Pauncz, *Spin Eigenfunctions: Construction and Use* (Plenum Press, New York, 1979)

85. J. Von Neumann, *Mathematical Foundations of Quantum Mechanics*, Vol. 2 (Princeton University Press, 1996)
86. G. Teschl, *Mathematical methods in quantum mechanics: with applications to Schrödinger operators*, Vol. 99 (American Mathematical Society, 2009)
87. A.L. Fetter, J.D. Walecka, *Quantum Theory of Many-Particle Systems* (Dover Publications, 2003)
88. M.H. Beck, A. Jäckle, GA Worth, H.D. Meyer, Phys. Rep. **324**, 1 (2000)
89. J.C. Slater, Phys. Rev. **34**, 1293 (1929)
90. E.U. Condon, Phys. Rev. **36**, 1121 (1930)
91. P.O. Löwdin, Phys. Rev. **97**, 1474 (1955)
92. R.K. Nesbet, *Variational Principles and Methods in Theoretical Physics and Chemistry* (Cambridge University Press, 2003)
93. P. Kramer, M. Saraceno, *Geometry of the Time-Dependent Variational Principle in Quantum Mechanics* *Geometry of the Time-Dependent Variational Principle in Quantum Mechanics*, Vol. 140 (1981)
94. P.A.M. Dirac, *Note on exchange phenomena in the Thomas atom* *Mathematical Proceedings of the Cambridge Philosophical Society*, Vol. 26 (Cambridge University Press, 1930)
95. J. Frenkel, *Wave Mechanics* (Clarendon Press, Oxford, 1934)
96. A.D. McLachlan, Molec. Phys. **8**, 39 (1964)
97. O.E. Alon, A.I. Streltsov, L.S. Cederbaum, J. Chem. Phys. **127**, 154103 (2007)
98. I. Shavitt, Mole. Phys. **94**, 3 (1998)
99. J. Olsen, P. Jørgensen, J. Simons, Chem. Phys. Lett. **169**, 463 (1990)
100. E. Rossi, G.L. Bendazzoli, S. Evangelisti, D. Maynau, Chem. Phys. Lett. **310**, 530 (1999)
101. F. Becca, A. Parola, S. Sorella, Phys. Rev. B **61**, 16287 (2000)
102. F. Deuretzbacher, K. Bongs, K. Sengstock, D. Pfannkuche, Phys. Rev. A **75**, 013614 (2007)
103. G.D. Purvis III, R.J. Bartlett, J.Chem. Phys. **76**, 1910 (1982)
104. S.R. White, R.L. Martin, J. Chem. Phys. **110**, 4127 (1999)
105. S. Laulan, H. Bachau, Phys. Rev. A **68**, 013409 (2003)
106. J. Colgan, M.S. Pindzola, F. Robicheaux, J. Phys. B: Atom., Molec. Opt. Phys. **37**, L377 (2004)
107. S. Laulan, H. Bachau, Phys. Rev. A **69**, 033408 (2004)
108. F.L. Yip, C.W. McCurdy, T.N. Rescigno, Phys. Rev. A **81**, 053407 (2010)
109. D. Hochstuhl, S. Bauch, M. Bonitz, J. Phys.: Conf. Ser. **220**, 012019 (2010)
110. B. Roos, Chem. Phys. Lett. **15**, 153 (1972)
111. J.C. Slater, *Quantum Theory of Molecules and Solids* (McGraw-Hill, 1967)
112. M. Tinkham, *Group Theory and Quantum Mechanics* (Dover Publications, 2003)
113. G.B. Arfken, H.J. Weber, *Mathematical Methods for Physicists*, Sixth edition (New York Academic, 2005)
114. P.O. Löwdin, Rev. Mod. Phys. **36**, 966 (1964)
115. R.K. Nesbet, J. Math. Phys. **2**, 701 (1961)
116. W. Duch, J. Karwowski, Comput. Phys. Rep. **2**, 93 (1985)
117. H.F. Schaefer, F.E. Harris, J. Comput. Phys. **3**, 217 (1968)
118. C.B. Mendl, G. Friesecke, *Angular Momentum and Spin Diagonalization on Atomic Subshells: Algorithm and Complexity* (2011)
119. A. Szabo, N.S. Ostlund, *Modern Quantum Chemistry: Introduction to Advanced Electronic Structure Theory* (Courier Dover Publications, 1996)
120. S.A. Blundell, K. Joshi, Phys. Rev. B **81**, 115323 (2010)
121. T. Vänskä, D. Sundholm, M. Lindberg, Phys. Rev. A **75**, 023621 (2007)
122. J. Olsen, B.O. Roos, P. Jørgensen, H.J.A. Jensen, J. Chem. Phys. **89**, 2185 (1988)
123. C.B. Mendl, Comput. Phys. Comm. **182**, 1327 (2011)
124. K.J. Schafer, B. Yang, L.F. DiMauro, K.C. Kulander, Phys. Rev. Lett. **70**, 1599 (1993)
125. C.I. Blaga, F. Catoire, P. Colosimo, G.G. Paulus, H.G. Muller, P. Agostini, L.F. DiMauro, Nat. Phys. **5**, 335 (2009)

126. M. Awasthi, Y.V. Vanne, A. Saenz, A. Castro, P. Decleva, Phys. Rev. A **77**, 063403 (2008)
127. M. Lein, Phys. Rev. Lett. **94**, 53004 (2005)
128. G. Lagmago Kamta, A.F. Starace, Phys. Rev. A **65**, 053418 (2002)
129. N. Rohringer, A. Gordon, R. Santra, Phys. Rev. A **74**, 043420 (2006)
130. A. Gordon, F.X. Kärtner, N. Rohringer, R. Santra, Phys. Rev. Lett. **96**, 223902 (2006)
131. S. Pabst, L. Greenman, P.J. Ho, D.A. Mazziotti, R. Santra, Phys. Rev. Lett. **106**, 053003 (2011)
132. M. Spanner, S. Patchkovskii, Phys. Rev. A **80**, 063411 (2009)
133. X.M. Tong, C.D. Lin, J. Phys. B: Atom., Molec. Opt. Phys. **38**, 2593 (2005)
134. J. Mauritssen, M.B. Gaarde, K.J. Schafer, Phys. Rev. A **72**, 13401 (2005)
135. A.K. Kazansky N.M. Kabachnik, J. Phys. B: Atom., Molec. Opt. Phys. **43**, 035601 (2010)
136. A.K. Kazansky, N.M. Kabachnik, Phys. Rev. A **72**, 052714 (2005)
137. F. Jensen, *Introduction to Computational Chemistry*, Vol. 2 (Wiley, New York, 1999)
138. J.S. Parker, E.S. Smyth, K.T. Taylor, J. Phys. B: Atom., Molec. Opt. Phys. **31**, L571 (1998)
139. H. Bachau, E. Cormier, P. Decleva, J.E. Hansen, F. Martin, Reports Progr. Phys. **64**, 1815 (2001)
140. S. Goedecker, O.V. Ivanov, Solid State Comm. **105**, 665 (1998)
141. C. McKenna, H.W. van der Hart, J. Phys. B: Atom., Molec. Opt. Phys. **37**, 457 (2003)
142. A.C. Brown, S. Hutchinson, M.A. Lysaght, H.W. van der Hart, Phys. Rev. Lett. **108**, 063006 (2012)
143. D.R. Hartree, W. Hartree, B. Swirles, Phil. Trans. Royal Soc. London. Ser A, Math. Phys. Sci. **238**, 229 (1939)
144. C.F. Fischer, *The Hartree-Fock Method for Atoms. A Numerical Approach* (Wiley, New York, 1977)
145. H.P. Saha, C.D. Caldwell, Phys. Rev. A **40**, 7020 (1989)
146. S. Fritzsch, A.N. Grum-Grzhimailo, E.V. Gryzlova, N.M. Kabachnik, J. Phys. B: Atom. Molec. Optical Phys. **41**, 165601 (2008)
147. E. Dalgaard, J. Chem. Phys. **72**, 816 (1980)
148. D.L. Yeager, P. Jørgensen, Chem. Phys. Lett. **65**, 77 (1979)
149. R. McWeeny, Inter. J. Quant. Chem. **23**, 405 (1983)
150. H.D. Meyer, U. Manthe, L.S. Cederbaum, Chem. Phys. Lett. **165**, 73 (1990)
151. U. Manthe, H.-D. Meyer, L.S. Cederbaum, J. Chem. Phys. **97**, 3199 (1992)
152. H.D. Meyer, F. Gatti, G.A. Worth, *Multidimensional Quantum Dynamics* (Wiley-VCH, 2010)
153. J. Zanghellini, M. Kitzler, T. Brabec, A. Scrinzi, J. Phys. B: Atom. Molec. Opt. Phys. **37**, 763 (2004)
154. O.E. Alon, A.I. Streltsov, L.S. Cederbaum, Phys. Rev. A **77**, 033613 (2008)
155. T. Tung Nguyen-Dang, M. Peters, Sen-Ming Wang, E. Sinelnikov, F. Dion, J. Chem. Phys. **127**, 174107 (2007)
156. G.A. Worth, H.D. Meyer, L.S. Cederbaum, W. Domcke, D.R. Yarkony, H. Köppel, Conical Intersections: Electr. Struc. Dyn. Spectr., 583 (2004)
157. H.-D. Meyer, Wiley Interdisciplinary Rev: Comput. Molec. Sci. **2**, 351 (2012)
158. H. Miyagi, L.B. Madsen, Phys. Rev. A **87**, 062511 (2013)
159. G. Jordan, J. Caillat, C. Ede, A. Scrinzi, J. Phys. B: Atom. Molec. Optical Phys. **39**, S341 (2006)
160. M. Nest, R. Padmanaban, P. Saalfrank, J. Chem. Phys. **126**, 214106 (2007)
161. T. Klamroth, M. Nest, Phys. Chem. Chem. Phys. **11**, 349 (2009)
162. T. Kato, H. Kono, J. Chem. Phys. **128**, 184102 (2008)
163. T. Kato, H. Kono, M. Kanno, Y. Fujimura, K. Yamanouchi, Laser Phys. **19**, 1712 (2009)
164. T. Nguyen-Dang, M. Peters, S. Wang, F. Dion, Laser Phys. **19**, 1521 (2009)
165. M. Nest, Chem. Phys. Lett. **472**, 171 (2009)
166. S. Kvaal, Phys. Rev. A **84**, 022512 (2011)

167. M. Bonitz, D. Hochstuhl, S. Bauch, K. Balzer, *Contrib. Plasma Phys.* **50**, 54 (2010)
168. S. Bauch, D. Hochstuhl, K. Balzer, M. Bonitz, *J. Phys.: Conf. Ser.* **220**, 012013 (2010)
169. J.W. Abraham, K. Balzer, D. Hochstuhl, M. Bonitz, *Phys. Rev. B* **86**, 125112 (2012)
170. C. McDonald, G. Orlando, J.W. Abraham, D. Hochstuhl, M. Bonitz, T. Brabec, *Phys. Rev. Lett.* **111**, 256801 (2013)
171. J.W. Abraham, M. Bonitz, C. McDonald, G. Orlando, T. Brabec, *New J. Phys.* **16**, 013001 (2014)
172. C.D. Sherrill, M.S. Lee, M. Head-Gordon, *Chem. Phys. Lett.* **302**, 425 (1999)
173. M. Heimsoth, M. Bonitz, *Physica E: Low-dimensional Syst. Nanostr.* **42**, 420 (2010)
174. A. Dalgarno, G.A. Victor, *Proc. Royal Soc. London Series A. Math. Phys. Sci.* **291**, 291 (1966)
175. K.L. Schuchardt, B.T. Didier, T. Elsethagen, L. Sun, V. Gurumoorthi, J. Chase, J. Li, T.L. Windus, *J. Chem. Info. Model.* **47**, 1045 (2007)
176. R.L. DeKock, H.B. Gray, *Chem. Structure and Bonding* (University Science Books, 1989)
177. J.C. Slater, *Phys. Rev.* **36**, 57 (1930)
178. T. Kato, *Comm. Pure Appl. Math.* **10**, 151 (1957)
179. S.F. Boys, *Proc. Royal Soc. London. Ser. A. Math. Phys. Sci.* **200**, 542 (1950)
180. S. Huzinaga, *Comput. Phys. Reports* **2**, 281 (1985)
181. A. Faure, J.D. Gorfinkel, L.A. Morgan, J. Tennyson, *Comput. Phys. Comm.* **144**, 224 (2002)
182. X. Li, S.M. Smith, A.N. Markevitch, D.A. Romanov, R.J. Levis, H.B. Schlegel, *Phys. Chem. Chem. Phys.* **7**, 233 (2005)
183. P. Krause, T. Klamroth, P. Saalfrank, *J. Chem. Phys.* **127**, 034107 (2007)
184. H.G. Muller, *Laser Phys.* **9**, 138 (1999)
185. C.W. McCurdy, F. Martín, *J. Phys. B: Atomic, Molec. Optical Phys.* **37**, 917 (2004)
186. L. Füsti-Molnar, P. Pulay, *J. Chem. Phys.* **116**, 7795 (2002)
187. J.V. Lill, G.A. Parker, J.C. Light, *J. Chem. Phys.* **85**, 900 (1986)
188. D.T. Colbert, W.H. Miller, *J. Chem. Phys.* **96**, 1982 (1992)
189. L.Y. Peng, A.F. Starace, *J. Chem. Phys.* **125**, 154311 (2006)
190. C.W. McCurdy, M. Baertschy, T.N. Rescigno, *J. Phys. B: Atom, Molec. Optical Phys.* **37**, R137 (2004)
191. S. Sukiasyan, H.D. Meyer, *J. Phys. Chem. A* **105**, 2604 (2001)
192. D.J. Haxton, *J. Phys. B: Atomic, Molec. Optical Phys.* **40**, 4443 (2007)
193. V.I. Lebedev, D.N. Laikov, *Doklady Math.* **59** (1999)
194. L. Tao, C.W. McCurdy, T.N. Rescigno, *Phys. Rev. A* **79**, 012719 (2009)
195. L. Tao, C.W. McCurdy, T.N. Rescigno, *Phys. Rev. A* **82**, 023423 (2010)
196. J.N. Hurley, D.L. Huestis, W.A. Goddard III, *J. Phys. Chem.* **92**, 4880 (1988)
197. A. Jäckle, H.D. Meyer, *J. Chem. Phys.* **104**, 7974 (1996)
198. N.H.F. Beebe, J. Linderberg, *Inter. J. Quant. Chem.* **12**, 683 (1977)
199. S. Wilson, *Comput. Phys. Comm.* **58**, 71 (1990)
200. F. Aquilante, L. Gagliardi, T.B. Pedersen, R. Lindh, *J. Chem. Phys.* **130**, 154107 (2009)
201. U. Benedikt, A.A. Auer, M. Espig, W. Hackbusch, *J. Chem. Phys.* **134**, 4118 (2011)
202. R.C. Raffenetti, *J. Chem. Phys.* **59**, 5936 (1973)
203. A.D. Becke, R.M. Dickson, *J. Chem. Phys.* **89**, 2993 (1988)
204. W.H. Press, S.A. Teukolsky, W.T. Vetterling, B.P. Flannery, *Numerical Recipes Third Edition: The Art of Scientific Computing* (Cambridge University Press, 2007)
205. P.J. Knowles, N.C. Handy, *Chem. Phys. Lett.* **111**, 315 (1984)
206. A.I. Streltsov, O.E. Alon, L.S. Cederbaum, *Phys. Rev. A* **81**, 022124 (2010)
207. T. Fließbach, *Lehrbuch zur Theoretischen Physik. 3. Quantenmechanik* (Spektrum Akademischer Verlag, 2000)
208. S. Blanes, F. Casas, J.A. Oteo, J. Ros, *Phys. Rep.* **470**, 151 (2009)
209. M. Klaiber, D. Dimitrovski, J.S. Briggs, *Phys. Rev. A* **79**, 043402 (2009)
210. U. Peskin, N. Moiseyev, *J. Chem. Phys.* **99**, 4590 (1993)
211. M. Heimsoth, C.E. Creffield, L.D. Carr, F. Sols, *New J. Phys.* **14**, 075023 (2012)
212. M. Ndong, H. Tal-Ezer, R. Kosloff, C.P. Koch, *J. Chem. Phys.* **132**, 064105 (2010)

213. H. Tal-Ezer, R. Kosloff, *J. Chem. Phys.* **81**, 3967 (1984)
214. W. van Dijk, F.M. Toyama, *Phys. Rev. E* **75**, 036707 (2007)
215. S.A. Chin, C.R. Chen, *J. Chem. Phys.* **117**, 1409 (2002)
216. C. Leforestier, R.H. Bisseling, C. Cerjan, M.D. Feit, R. Friesner, A. Guldberg, A. Hammerich, G. Jolicard, W. Karrlein, H.D. Meyer, N. Lipkin, O. Roncero, R. Kosloff, *J. Comput. Phys.* **94**, 59 (1991)
217. E. Hairer, S.P. Nørsett, G. Wanner, *Solving Ordinary Differential Equations: Nonstiff Problems*, Vol. 1 (Springer Verlag, 1993)
218. J.C. Tremblay, T. Carrington Jr., *J. Chem. Phys.* **121**, 11535 (2004)
219. K. Kormann, S. Holmgren, H.O. Karlsson, *J. Chem. Phys.* **128**, 184101 (2008)
220. Th. Monovasilis, Z. Kalogiratou, T.E. Simos, *Comput. Phys. Commu.* **181**, 1251 (2010)
221. Tae Jun Park, J.C. Light, *J. Chem. Phys.* **85**, 5870 (1986)
222. Q. Jie, D. Liu, *J. Phys. A: Math., General* **39**, 1691 (2006)
223. C. Moler, C. Van Loan, *SIAM Rev.* **45**, 3 (2003)
224. M. Abramowitz, I.A. Stegun, *Handbook of Mathematical Functions: With Formulas, Graphs, Mathematical Tables* (Dover Publications, 1965)
225. Y. Saad, *Numerical Methods for Large Eigenvalue Problems* (Manchester University Press, 1992)
226. L. Lehtovaara, J. Toivanen, J. Eloranta, *J. Comput. Phys.* **221**, 148 (2007)
227. S. Hermanns, K. Balzer, M. Bonitz, *Phys. Scr.* **2012**, 014036 (2012)
228. A. Scrinzi, B. Piraux, *Phys. Rev. A* **58**, 1310 (1998)
229. M. Førre, S. Selstø, Raymond Nepstad, *Phys. Rev. Lett.* **105**, 163001 (2010)
230. A. Palacios, T.N. Rescigno, C.W. McCurdy, *Phys. Rev. A* **77**, 032716 (2008)
231. J.S. Parker, L.R. Moore, K.J. Meharg, D. Dundas, K.T. Taylor, *J. Phys. B: Atom. Molec. Optical Phys.* **34**, L69 (2001)
232. L.B. Madsen, L.A.A. Nikolopoulos, T.K. Kjeldsen, J. Fernández, *Phys. Rev. A* **76**, 063407 (2007)
233. L.A.A. Nikolopoulos, T.K. Kjeldsen, L.B. Madsen, *Phys. Rev. A* **75**, 063426 (2007)
234. W. Martin, P. Flandrin, *Acoust, Speech, Signal Proc. IEEE Trans.* **33**, 1461 (1985)
235. A. Jäckle, H.D. Meyer, *J. Chem. Phys.* **105**, 6778 (1996)
236. D. Vanfleteren, D. Van Neck, P.W. Ayers, R.C. Morrison, P. Bultinck, *J. Chem. Phys.* **130**, 194104 (2009)
237. D.W. Smith, O.W. Day, *J. Chem. Phys.* **62**, 113 (1975)
238. C. Hinz, Investigation of many-particle processes in Beryllium using the Multiconfigurational time-dependent Hartree-Fock method, Master's thesis, University of Kiel, 2013
239. P.E. Gill, W. Murray, M.H. Wright, *Practical Optimization* (Academic Press, 1981)
240. L.B. Rall, *Automatic Differentiation: Techniques and Applications*, Vol. 120, Lect. Notes Computer Sci. (Springer, Berlin, 1981)
241. M. Jerosolimski, L. Levacher, A new method for fast calculation of Jacobian matrices: automatic differentiation for power system simulation. In *Power Industry Computer Application Conference*, Conference Proceedings, 411 (1993)
242. J.L. Gustafson, *Commun. ACM* **31**, 532 (1988)
243. A.H. Karp, H.P. Flatt, *Commun. ACM* **33**, 539 (1990)
244. G.M. Amdahl, In *Proc. of the April 18-20, 1967, Spring Joint Computer conference*, ACM, 483 (1967)
245. B. Walker, B. Sheehy, L.F. DiMauro, P. Agostini, K.J. Schafer, K.C. Kulander, *Phys. Rev. Lett.* **73**, 1227 (1994)
246. J.S. Briggs, V. Schmidt, *J. Phys. B: Atom. Molec. Optical Phys.* **33**, R1 (2000)
247. L. Avaldi, A. Huetz, *J. Phys. B: Atom. Molec. Optical Phys.* **38**, S861 (2005)
248. S. Chen, C. Ruiz, A. Becker, *Phys. Rev. A* **82**, 033426 (2010)
249. T. Birkeland, R. Nepstad, M. Førre, *Phys. Rev. Lett.* **104**, 163002 (2010)
250. R. Pazourek, J. Feist, S. Nagel, J. Burgdörfer, *Phys. Rev. Lett.* **108**, 163001 (2012)
251. E.A. Hylleraas, *Z. Phys. A Hadrons Nuclei* **54**, 347 (1929)
252. J.S. Sims, S.A. Hagstrom, *Inter. J. Quan. Chem.* **90**, 1600 (2002)

253. J.C. Slater, *Quantum Theory of Atomic Structure* (McGraw-Hill, 1964)
254. C. Schwartz, Inter. J. Mod. Phys. E **15**, 877 (2006)
255. P.O. Löwdin, Phys. Rev. **97**, 1509 (1955)
256. S.D. Bergeson, A. Balakrishnan, K.G.H. Baldwin, T.B. Lucatorto, J.P. Marangos, T.J. McIlrath, T.R. O'Brian, S.L. Rolston, C.J. Sansonetti, J. Wen, et al., Phys. Rev. Lett. **80**, 3475 (1998)
257. H. Tatewaki, T. Koga, Y. Sakai, A.J. Thakkar, J. Chem. Phys. **101**, 4945 (1994)
258. M. Yan, H.R. Sadeghpour, A. Dalgarno, Astrophys. J. **496**, 1044 (1998)
259. R. Mitzner, A.A. Sorokin, B. Siemer, S. Roling, M. Rutkowski, H. Zacharias, M. Neeb, T. Noll, F. Siewert, W. Eberhardt, et al., Phys. Rev. A. **80**, 025402 (2009)
260. R. Moshammer, Th. Pfeifer, A. Rudenko, Y.H. Jiang, L. Foucar, M. Kurka, K.U. Kühnle, C.D. Schröter, J. Ullrich, O. Herrwerth, M.F. Kling, X.-J. Liu, K. Motomura, H. Fukuzawa, A. Yamada, K. Ueda, K.L. Ishikawa, K. Nagaya, H. Iwayama, A. Sugishima, Y. Mizoguchi, S. Yase, M. Yao, N. Saito, A. Belkacem, M. Nagasono, A. Higashiya, M. Yabashi, T. Ishikawa, H. Ohashi, H. Kimura, T. Togashi, Optics Exp. **19**, 21698 (2011)
261. P.W. Langhoff, C.T. Corcoran, J. Chem. Phys. **61**, 146 (1974)
262. A. Scrinzi, N. Elander, J. Chem. Phys. **98**, 3866 (1993)
263. A. Stark, A. Saenz, J. Phys. B: Atom., Molec. Optical Phys. **44**, 035004 (2011)
264. J.A.R. Samson, Z.X. He, L. Yin, A. Haddad, J. Phys. B: Atom., Molec. Optical Phys. **27**, 887 (1994)
265. P. Lambropoulos, L.A.A. Nikolopoulos, New J. Phys. **10**, 025012 (2008)
266. R.P. Madden, K. Codling, Phys. Rev. Lett. **10**, 516 (1963)
267. U. Fano, Phys. Rev. **124**, 1866 (1961)
268. M. Domke, C. Xue, A. Puschmann, T. Mandel, E. Hudson, D.A. Shirley, G. Kandl, C.H. Greene, H.R. Sadeghpour, H. Petersen, Phys. Rev. Lett. **66**, 1306 (1991)
269. K. Schulz, G. Kandl, M. Domke, J.D. Bozek, P.A. Heimann, A.S. Schlachter, J.M. Rost, Phys. Rev. Lett. **77**, 3086 (1996)
270. A. Bürgers, D. Wintgen, J.M. Rost, J. Phys. B: Atom., Molec. Optical Phys. **28**, 3163 (1995)
271. E.J. Heller, Accounts Chem. Res. **14**, 368 (1981)
272. H. Hasegawa, E.J. Takahashi, Y. Nabekawa, K.L. Ishikawa, K Midorikawa, Phys. Rev. A **71**, 023407 (2005)
273. M. Kurka, J. Feist, D.A. Horner, A. Rudenko, Y.H. Jiang, K.U. Kühnle, L. Foucar, T.N. Rescigno, C.W. McCurdy, R. Pazourek, S. Nagele, M. Schulz, O. Herrwerth, M. Lezius, M.F. Kling, M. Schöfle, A. Belkacem, S. Düsterer, R. Treusch, B.I. Schneider, L.A. Collins, J. Burgdörfer, C.D. Schröter, R. Moshammer, J. Ullrich, New J. Phys. **12**, 073035 (2010)
274. R. Nepstad, T. Birkeland, M. Førre, Phys. Rev. A **81**, 063402 (2010)
275. L.A.A. Nikolopoulos, P. Lambropoulos, J. Phys. B: Atom., Molec. Optical Phys. **34**, 545 (2001)
276. L.A.A. Nikolopoulos, P. Lambropoulos, J. Phys. B: Atom. Molec. Optical Phys. **40**, 1347 (2007)
277. D.A. Horner, F. Morales, T.N. Rescigno, F. Martin, C.W. McCurdy, Phys. Rev. A **76**, 030701 (2007)
278. D.A. Horner, C.W. McCurdy, T.N. Rescigno, Phys. Rev. A **78**, 043416 (2008)
279. I.A. Ivanov, A.S. Kheifets, Phys. Rev. A **75**, 033411 (2007)
280. L. Feng, H.W. van der Hart, J. Phys. B: Atom. Molec. Optical Phys. **36**, L1 (2002)
281. A. Palacios, T.N. Rescigno, C.W. McCurdy, Phys. Rev. A **79**, 033402 (2009)
282. N.E. Dahlen, R. van Leeuwen, Phys. Rev. A **64**, 023405 (2001)
283. A. Scrinzi, Phys. Rev. A **81**, 053845 (2010)
284. U.V. Riss, H.D. Meyer, J. Phys. B: Atom. Molec. Optical Phys. **28**, 1475 (1995)
285. H. Bauke, C.H. Keitel, Phys. Rev. E **80**, 016706 (2009)
286. A. Kramida, W.C. Martin, J. Phys. Chem. Ref. Data **26**, 1185 (1997)
287. D.S. Kim, S.S. Tayal, H.L. Zhou, S.T. Manson, Phys. Rev. A **61**, 062701 (2000)

288. H.C. Chi, K.N. Huang, Phys. Rev. A **43**, 4742 (1991)
289. B. Zhou, C.D. Lin, Phys. Rev. A **51**, 1286 (1995)
290. J. Colgan, M.S. Pindzola, F.J. Robicheaux, D.C. Griffin, M. Baertschy, Phys. Rev. A **65**, 042721 (2002)
291. J. Komasa, W. Cencek, J. Rychlewski, Phys. Rev. A **52**, 4500 (1995)
292. J. Komasa, W. Cencek, J. Rychlewski, Phys. Rev. A **52**, 4500 (1995)
293. R. Wehlitz, J.B. Bluett, S.B. Whitfield, Phys. Rev. A **66**, 012701 (2002)
294. R. Wehlitz, D. Lukic, J.B. Bluett, Phys. Rev. A **71**, 012707 (2005)
295. L. Voky, H.E. Saraph, W. Eissner, Z.W. Liu, H.P. Kelly, Phys. Rev. A **46**, 3945 (1992)
296. T.N. Chang, Phys. Rev. A **16**, 1171 (1977)
297. K.G. Sewell, Phys. Rev. **138**, A418 (1965)
298. W.R. Johnson, K.T. Cheng, Phys. Rev. A **20**, 978 (1979)
299. K. Gokhberg, V. Vysotskiy, L.S. Cederbaum, L. Storchi, F. Tarantelli, V. Averbukh, J. Chem. Phys. **130**, 064104 (2009)
300. G.V. Marr, J.B. West, Atom. Data Nucl. Data Tables **18**, 497 (1976)
301. W.F. Chan, G. Cooper, X. Guo, C.E. Brion, Phys. Rev. A **45**, 1420 (1992)
302. J.A.R. Samson, W.C. Stolte, J. Electr. Spectros. Related Phenomena **123**, 265 (2002)
303. A.L. Landers, F. Robicheaux, T. Jahnke, M. Schöffler, T. Osipov, J. Titze, S.Y. Lee, H. Adaniya, M. Hertlein, P. Ranitovic, I. Bocharova, D. Akoury, A. Bhandary, Th. Weber, M.H. Prior, C.L. Cocke, R. Dörner, A. Belkacem, Phys. Rev. Lett. **102**, 223001 (2009)
304. N. Sisourat, H. Sann, N.V. Kryzhevoi, P. Kolorenč, T. Havermeier, F. Sturm, T. Jahnke, H.-K. Kim, R. Dörner, L.S. Cederbaum, Phys. Rev. Lett. **105**, 173401 (2010)
305. E.B. Saloman, C.J. Sansonetti, J. Phys. Chem. Ref. Data **33**, 1113 (2004)
306. O.E. Alon, A.I. Streltsov, L.S. Cederbaum, Phys. Lett. A **362**, 453 (2007)
307. A.I. Streltsov, O.E. Alon, L.S. Cederbaum, Phys. Rev. Lett. **99**, 030402 (2007)
308. K. Sakmann, Exact quantum dynamics of a bosonic Josephson junction, *Many-Body Schrödinger Dynamics of Bose-Einstein Condensates* (Springer, 2011), p. 65
309. A.I. Streltsov, O.E. Alon, L.S. Cederbaum, Phys. Rev. Lett. **100**, 130401 (2008)
310. L. Cao, S. Kronke, O. Vendrell, P. Schmelcher, J. Chem. Phys. **139**, 134103 (2013)
311. M. Heimsoth, D. Hochstuhl, C.E. Creffield, L.D. Carr, F. Sols, New J. Phys. **15**, 103006 (2013)
312. T. Schoof, M. Bonitz, A. Filinov, D. Hochstuhl, J.W. Dufty, Contrib. Plasma Phys. **51**, 687 (2011)
313. A. Filinov, Yu.E. Lozovik, M. Bonitz, Physica Status Solidi (b) **221**, 231 (2000)
314. A. Filinov, M. Bonitz, Yu.E. Lozovik, Phys. Rev. Lett. **86**, 3851 (2001)
315. K. Balzer, M. Bonitz, J. Phys. A: Math. Theor. **42**, 214020 (2009)
316. L.M. Robledo, Phys. Rev. C **81**, 044312 (2010)
317. J. Jaklic, P. Prelovsek, Phys. Rev. B **49**, 5065 (1994)
318. U. Manthe, F. Matzkies, Chem. Phys. Lett. **252**, 71 (1996)
319. S.P. Webb, T. Iordanov, S. Hammes-Schiffer, J. Chem. Phys. **117**, 4106 (2002)
320. O.E. Alon, A.I. Streltsov, L.S. Cederbaum, Phys. Rev. A. **76**, 062501 (2007)
321. J. Böning, A. Filinov, M. Bonitz, Phys. Rev. B **84**, 075130 (2011)
322. J. Schleede, A. Filinov, M. Bonitz, H. Fehske, Contrib. Plasma Phys. **52**, 819 (2012)
323. C. Buth, R. Santra, Phys. Rev. A. **75**, 033412 (2007)
324. A. Steinhoff, P. Gartner, M. Florian, F. Jahnke, Phys. Rev. B **85**, 205144 (2012)
325. U. Manthe, J. Chem. Phys. **128**, 164116 (2008)
326. J. Zanghellini, M. Kitzler, T. Brabec, A. Scrinzi, J. Phys. B: Atom Molec. Optical Phys. **37**, 763 (2004)
327. S. Bauch, K. Balzer, Henning C., M. Bonitz, Phys. Rev. B **80**, 054515 (2009)
328. R. Schmitz, S. Krönke, L. Cao, P. Schmelcher, Phys. Rev. A **88**, 043601 (2013)
329. J.M. García de la Vega, B. Miguel, L.A. Montero, L.A. Díaz, R. Bader, *Introduction to advanced topics of computational chemistry* (Facultad de Química, Universidad de La Habana, 2003)
330. N. Vence, R. Harrison, P. Krstić, Phys. Rev. A **85**, 033403 (2012)

331. A.S. Dickinson, P.R. Certain, *J. Chem. Phys.* **49**, 4209 (1968)
332. D.O. Harris, G.G. Engerholm, W.D. Gwinn, *J. Chem. Phys.* **43**, 1515 (1965)
333. T.N. Rescigno, C.W. McCurdy, *Phys. Rev. A* **62**, 032706 (2000)
334. B.I. Schneider, L.A. Collins, S.X. Hu, *Phys. Rev. E* **73**, 036708 (2006)
335. K. Balzer, S. Bauch, M. Bonitz, *Phys. Rev. A* **81**, 022510 (2010)
336. K. Balzer, S. Bauch, M. Bonitz, *Phys. Rev. A* **82**, 033427 (2010)
337. J. Rasch, A. Yu, *SIAM J. Scientific Comput.* **25**, 1416 (2004)
338. J.H. Luscombe, M. Luban, *Phys. Rev. E* **57**, 7274 (1998)